Physics Reports 596 (2015) 1–86

Contents lists available at ScienceDirect

Physics Reports

journal homepage: www.elsevier.com/locate/physrep

Recent developments in fusion and direct reactions with weakly bound nuclei☆

L.F. Canto [a,b], P.R.S. Gomes [b], R. Donangelo [a,c], J. Lubian [b], M.S. Hussein [d,e,f,*]

[a] Instituto de Física, Universidade Federal do Rio de Janeiro, C.P. 68528, 21941-972 Rio de Janeiro, RJ, Brazil
[b] Instituto de Física, Universidade Federal Fluminense, Av. Litorânea S-N, 24210-340 Niteroi, RJ, Brazil
[c] Instituto de Física, Facultad de Ingeniería, C.C. 30, 11000 Montevideo, Uruguay
[d] Instituto de Estudos Avançados, Universidade de São Paulo, C.P. 72012, 05508-970, São Paulo, SP, Brazil
[e] Departamento de Física Matemática, Instituto de Física, Universidade de São Paulo, C.P. 66318, 05314-970, São Paulo, SP, Brazil
[f] Departamento de Física, Instituto Tecnológico de Aeronáutica, DCTA 12.228-900, São José dos Campos, SP, Brazil

ARTICLE INFO

Article history:
Accepted 3 August 2015
Available online 10 August 2015
editor: M. Ramsey-Musolf

Keywords:
Quantum tunneling
Nuclear fusion
Nuclear breakup
Weakly bound nuclei
Neutron–proton-rich nuclei
Unstable beams

ABSTRACT

In this Report we give a balanced account of the experimental and theoretical advances acquired over the last decade in the field of near-barrier fusion reactions induced by weakly bound stable and unstable nuclei. The elastic scattering and breakup reactions of these systems are also extensively reviewed as they play an important role in the fusion process. We review several theoretical tools used in the description of the data. The concepts of Complete Fusion (CF), Incomplete Fusion (ICF) and Total Fusion (TF), which is the sum of CF and ICF, are discussed and recent work on the calculation of these quantities is reviewed. The Continuum Discretized Coupled Channels (CDCC) method and its semiclassical version are described in detail and their limitations are pointed out. More importantly, we describe the salient features of the conclusions reached from the more than 40 measurements made, over a decade, of near-barrier fusion, elastic scattering and breakup reactions, and confront these data with the CDCC or other methods appropriate for these processes at the energy regime in question.

Contents

☆ Work supported in part by the CNPq, CAPES, FAPERJ, FAPESP and PRONEX (Brazil), and by the PENDECIBA and ANII (Uruguay).
* Corresponding author at: Instituto de Estudos Avançados, Universidade de São Paulo, C.P. 72012, 05508-970, São Paulo, SP, Brazil.
E-mail address: hussein@if.usp.br (M.S. Hussein).

http://dx.doi.org/10.1016/j.physrep.2015.08.001
0370-1573/

1. Introduction

The reactions of weakly bound stable and unstable nuclei have been extensively investigated for several decades. Special attention has been devoted to the reactions induced by radioactive halo nuclei which are composed of a tightly bound core plus one or two nucleons orbiting far around the core. At low energies, close to the Coulomb barrier, these reactions are primarily dominated by fusion, where a compound nucleus is formed, and direct reactions in which non-elastic scattering occurs.

The major aim of fusion reaction studies involving tightly bound nuclei over the last four decades has been to produce superheavy elements and to understand the mechanism of quantum tunneling in complex many-body systems. Further, the analysis of fusion data supplies very useful information about the nuclear interaction at distances corresponding to the outer side of the Coulomb barrier. During the last three decades the production of beams of radioactive nuclei has intensified fusion research. The special features of nuclei such as ^{11}Li and ^{6}He (two-neutron halo nuclei), ^{11}Be (one-neutron halo nucleus), and ^{8}B (one-proton halo nucleus), with more diffused density and high probability of breakup, has created much interest. Questions as basic as whether fusion in the Coulomb barrier energy region is enhanced owing to the large extent of the nuclear matter distribution which makes the effective size of, say, ^{11}Li comparable to that of ^{208}Pb, or hindered due the ease with which such nuclei break into two or more fragments owing to the very low threshold of the breakup channel, are addressed by these fusion studies.

Of course fusion, elastic scattering, and other reactions of weakly and tightly bound stable nuclei have been extensively studied and discussed in the literature for many more years. A distinct example is the deuteron nucleus, where one finds a vast literature dating back to the 1940's. In fact, the theoretical description of fusion reactions has benefited greatly from the theory of deuteron induced reactions, developed as a three-body problem (taking the target as structureless) and using the Continuum Discretized Coupled Channels (CDCC) method, which is a two-body coupled channels theory that, through discretizing the two fragment continuum, mocks the salient features of the Faddeev three-body method. The rather small binding energy of the deuteron (2.2 MeV) makes its breakup into a proton and a neutron a dominant channel which influences all other processes, such as fusion, one nucleon transfer, and elastic scattering.

The three-body description of the fusion of a two-cluster projectile is, in principle, more adequate than the CDCC. However, the presence of the long-range Coulomb interaction makes the calculations quite difficult, especially for the case involving nuclei heavier than the deuteron. As mentioned, some calculations of the fusion of weakly bound projectile nuclei

are performed using the CDCC. As in the deuteron case, this method of calculating the different types of reactions relies on a convenient discretization of the continuum states of the fragments forming the weakly bound projectile.

Fusion, elastic scattering, inelastic scattering and elastic breakup (with the target left in its ground state) are calculated by solving a set of coupled channels equations, with both bound and unbound (breakup) intrinsic projectile states. One shortcoming of the present versions of the CDCC is their inability to calculate incomplete fusion which involves the target capturing one of the charged fragments. The data on fusion reactions are usually presented as complete fusion (all the charge of the projectile is captured) and total fusion (complete fusion plus incomplete fusion). Of special interest is the complete fusion, since through its analysis one may learn the overall effect of the extended density of the weakly bound projectile and its breakup. The lack of a fully quantum mechanical theory which supplies the incomplete fusion cross section hinders the advancement of the field. Currently, a significant amount of effort is dedicated to find ways to calculate this important reaction mechanism. Recent semiclassical calculations of the complete and incomplete fusion processes is one of such attempts.

From the experimental side, several experiments have been performed, both with stable and radioactive weakly bound nuclei, using different experimental methods. In several of those experiments, only total fusion cross sections could be measured, since the evaporation residues from complete and incomplete fusion cannot be separated, especially for light nuclei. However, there are also reported data, especially in recent years, on complete and incomplete fusion processes, measured separately. There are also several recent measurements of elastic scattering, quasi-elastic scattering, transfer and breakup reactions in collisions of weakly bound nuclei.

Some reviews have been published on the subject of fusion reactions induced by weakly bound nuclei [1,2]. A review on elastic scattering of weakly bound nuclei has also been published [3]. Very recently, two reviews were published on fusion reactions, one theoretical on sub-barrier fusion [4] and a more general one on fusion [5]. In 2006, our group published an extensive review of the subject which also included an account of the fusion of strongly bound nuclei, a subject of great interest on its own merit [6]. The many more refined experimental measurements and the accompanying theoretical developments in the intervening years certainly call for a new review of the section on "fusion and direct reactions of weakly bound nuclei at low energies" of the Rare Ion Beams Physics (RIB) program which is an important field of current nuclear physics research, considered a priority program in Japan, the European Union, the USA, and many other countries around the world.

The current review starts, in Section 2, with a summary of the scattering theory needed to describe the reactions induced by weakly bound stable and unstable projectile nuclei. This section is meant to guide the data analyzer and the newcomer to the field through the necessary definitions, concepts and calculational instructions, as well as to set the stage for the theoretical developments in fusion theory, elastic scattering, and breakup reactions, described in the other sections, and to facilitate the comprehension of the recent theoretical works briefly described in those sections. In it we review the single channel and coupled channels descriptions of elastic scattering and fusion, and in particular the CDCC and its extensions, as well as the potentials employed in those calculations. The dynamic polarization potential, which simulates the effect of the breakup channel coupling, is discussed within a single channel approach to elastic scattering and fusion. The energy dependences of the imaginary and real parts of the dynamic polarization potential obtained from the experimental data analyses are discussed and are found to be constrained by the dispersion relation, $\mathrm{Re}\{V_{\mathrm{pol}}(E)\} = -(1/\pi)\,\mathcal{P}\int dz\,\mathrm{Im}\{V_{\mathrm{pol}}(z)\}\,[E-z]^{-1}$, as required by the general principle of causality. The strongest energy dependence of the polarization potentials occurs when the energy is lowered to the Coulomb barrier and lower. Then, the barrier acts as a natural "threshold" for processes involving the action of the nuclear force. The causality constraints alluded to above are commonly referred to as the Threshold Anomaly (TA) for strongly bound nuclei such as ^{16}O, and Breakup Threshold Anomaly (BTA) for weakly bound nuclei, such as ^{6}He. We give a detailed account of the TA and BTA as exhibited by analyses of data for several systems.

In the following Section 3 we consider the elastic and the quasi-elastic (QE) processes. The latter is the sum of the elastic and the direct non-elastic scattering contributions. We briefly review the barrier distributions both for QE and fusion. We also present in this section recent experimental results on elastic and QE scattering, as well as measurements of elastic scattering which allow to investigate the presence of the BTA for weakly bound systems. Finally, a recent method using backangle QE scattering data to derive fusion and total reaction cross sections is presented.

Section 4 discusses breakup reactions. In it, the theory of elastic breakup and inclusive non-elastic breakup and incomplete fusion are described in detail. We also discuss recent results and calculations of direct breakup, as well as of sequential breakup (breakup following transfer).

Section 5 deals with theories of fusion reactions. In it we present and discuss fusion barriers calculated microscopically or from different bare potentials. The fusion of weakly bound nuclei is then described, in the light of the developments presented in the previous sections. We briefly describe other quantum mechanical approaches to the calculation of fusion cross sections and barrier distributions. Here is also discussed the present status of the origin of the observed hindrance of fusion at deep sub-barrier energies.

Section 6 presents a rather extensive account of the recent experimental data on fusion reactions, including the recent search for a systematic behavior of the complete fusion suppression at energies slightly above the Coulomb barrier. It presents also a brief discussion of some consequences of transfer reactions on fusion measurements. Finally, in Section 7 we present our conclusions and outlook for the future of the field.

2. A summary of scattering theory

2.1. The single channel approach

Single channel calculations are the simplest quantum mechanical way to evaluate the elastic and the reaction cross sections. In this approach, the total potential,

$$V(r) = V_{\rm N}(r) + U_{\rm C}(r), \tag{1}$$

with $V_{\rm N}(r)$ and $U_{\rm C}(r)$ standing respectively for its nuclear and Coulomb parts, does not depend on any intrinsic degree of freedom.

To calculate the cross sections, the nuclear scattering amplitude, $f_{\rm N}(\theta)$, is expanded in partial-waves,

$$f_{\rm N}(\theta) = \frac{1}{2ik}\sum_l (2l+1)\ P_l(\cos\theta)\, e^{2i\sigma_l}\ \left(S_{{\rm N},l} - 1\right), \tag{2}$$

where P_l is the Legendre polynomial, σ_l is the Coulomb phase shift (known analytically) and $S_{{\rm N},l}$ is the nuclear S-matrix. The elastic cross section is given by the expression

$$\frac{d\sigma(\theta)}{d\Omega} = \left|f_{\rm N}(\theta) + f_{\rm C}(\theta)\right|^2, \tag{3}$$

where $f_{\rm C}(\theta)$ is the well known Coulomb amplitude.

Usually, fusion and direct reactions have strong influence on the elastic cross section and this fact cannot be ignored. The incident wave in the elastic channel is attenuated as other channels are populated. Thus, a single channel approach obeying the continuity equation would be unrealistic. It is then necessary to add an imaginary part to the nuclear potential, to account for the loss of flux. That is, one writes

$$V_{\rm N}(r) = U_{\rm N}(r) - i\,W(r), \tag{4}$$

where $U_{\rm N}(r) = {\rm Re}\,\{V_{\rm N}(r)\}$ and $W(r)$ is a short ranged function of r.

An immediate consequence of the complex potential is that the resulting Hamiltonian is non-Hermitian and the S-matrix loses its unitary property. Thus, the modulus of the S-matrix at the partial-waves influenced by $W(r)$ is less than one.

The absorption cross section is given by the difference between the incident flux and the emergent flux. In principle, it corresponds to the sum of all processes simulated by the imaginary potential. Thus, it is the total reaction cross section. One can easily show that this cross section is given by (see, *e.g.* Ref. [7]),

$$\sigma_{\rm R} = \frac{\pi}{k^2}\sum_l (2l+1)\ \mathcal{T}_l^{\rm R}(E), \tag{5}$$

which is obtained from the asymptotic form of the radial wave functions, $u_l(k, r)$. Above,[1]

$$\mathcal{T}_l^{\rm R}(E) = 1 - \left|S_{{\rm N},l}\right|^2 \tag{6}$$

is the reaction probability at the angular momentum l in a collision with energy E.

However, the above expression presents serious problems at very low collision energies. In this case, the distance of closest approach is much larger than the range of the imaginary potential. From the quantum mechanical point of view, this means that the incident wave is almost completely reflected outside the range of $W(r)$. This makes $|S_{{\rm N},l}|$ very close to one and $\mathcal{T}_l^{\rm R}(E)$ becomes very small. It is then necessary to determine $|S_{{\rm N},l}|$ with great accuracy. Below some limiting energy, $\mathcal{T}_l^{\rm R}(E)$ is smaller than the rounding errors of the calculations and Eq. (6) becomes useless. It is then necessary to resort to the expression [7],

$$\mathcal{T}_l^{\rm R}(E) = \frac{1}{|A|^2}\,\frac{4k}{E}\int dr\, W(r)\,|u_l(k, r)|^2\,, \tag{7}$$

where A is the normalization function of the radial wave function. This expression is accurate at all collision energies.

Eq. (7) has an additional advantage over Eq. (6). In some situations the imaginary potential is the sum of two or more terms and each one is associated with a particular reaction mechanism. As an example, we consider the situation where $W(r)$ can be put in the form,

$$W(r) = W^{\rm F}(r) + W^{\rm D}(r), \tag{8}$$

[1] Note that the absorption cross section vanishes for Hermitian Hamiltonians, where the S-matrix is unitary. In typical nuclear reactions, the projectile–target interaction excites intrinsic degrees of freedom. In this way, the incident current emerges both in the elastic and in all non-elastic channels. Accordingly, one has to include all the corresponding channels in the description of the reaction process. The multi-channel S-matrix is still Hermitian. However, if one uses a reduced description that includes only the elastic channel, the other channels are implicitly taken into account through the use of an absorptive complex potential (the optical potential), which results in a sub-unitary reduced S-matrix.

where $W^{\rm F}(r)$ is a short-range volumetric term associated with fusion, and $W^{\rm D}(r)$ is an imaginary potential with a longer range, arising from couplings with direct reaction channels. Usually the latter is peaked at grazing distances. One can then use Eq. (7) for each piece of the imaginary potential. This leads to the fusion and to the direct reaction probabilities, given by

$$\mathcal{T}^{\rm F}(l,E) \;=\; \frac{1}{|A|^2}\,\frac{4k}{E}\int dr\, W^{\rm F}(r)\;|u_l(k,r)|^2\,, \tag{9}$$

$$\mathcal{T}^{\rm D}(l,E) \;=\; \frac{1}{|A|^2}\,\frac{4k}{E}\int dr\, W^{\rm D}(r)\;|u_l(k,r)|^2\,. \tag{10}$$

Inserting these coefficients into Eq. (5), one gets the corresponding fusion and direct reaction cross sections,

$$\sigma_{\rm F}(E) \;=\; \frac{\pi}{k^2}\sum_l (2l+1)\;\mathcal{T}^{\rm F}(l,E), \tag{11}$$

$$\sigma_{\rm D}(E) \;=\; \frac{\pi}{k^2}\sum_l (2l+1)\;\mathcal{T}^{\rm D}(l,E). \tag{12}$$

2.2. The coupled channel approach

The coupled channel (CC) method is the most powerful tool to study multi-channel scattering. It allows explicit consideration of the projectile–target separation vector, $\mathbf{r}$, and also the intrinsic coordinates of the collision partners, labeled by ξ. The system Hamiltonian is[2]

$$\mathbb{H} = H + h + \mathbb{V}, \tag{13}$$

where H acts only on the collision degrees of freedom, h is the intrinsic Hamiltonian, acting on the ξ-space, and $\mathbb{V} \equiv \mathbb{V}(\mathbf{r},\xi)$ is the interaction coupling the collision and the intrinsic degrees of freedom.

To derive the coupled channel equations, one first performs the channel expansion of the full scattering state,

$$\Psi^{(+)}(\mathbf{k}_0;\mathbf{r}) = \sum_\alpha \psi_\alpha^{(+)}(\mathbf{k}_0;\mathbf{r})\,|\varphi_\alpha)\,, \tag{14}$$

where $\psi_\alpha^{(+)}(\mathbf{k}_0;\mathbf{r})$ is the scattering wave projected onto channel α and $|\varphi_\alpha)$ is the intrinsic bound state of the system with eigenvalue ε_α. These states satisfy the equations,

$$h\;|\varphi_\alpha) = \varepsilon_\alpha\;|\varphi_\alpha) \quad \text{and} \quad (\varphi_\alpha\,|\,\varphi_{\alpha'}) = \delta_{\alpha\alpha'}. \tag{15}$$

Inserting the channel expansion of Eq. (14) into the Schrödinger equation for the scattering system, one gets the coupled channel equations,

$$\left[E_\alpha - H_\alpha\right]\psi_\alpha^{(+)}(\mathbf{k}_0;\mathbf{r}) = \sum_{\alpha'} V_{\alpha\alpha'}(\mathbf{r})\,\psi_{\alpha'}^{(+)}(\mathbf{k}_0;\mathbf{r}), \quad \alpha,\alpha' = 0,1,\ldots. \tag{16}$$

Above, $E_\alpha = E - \varepsilon_\alpha$ and H_α and $V_{\alpha\alpha'}$ are the matrix-elements

$$H_\alpha = (\varphi_\alpha|\;H\;|\varphi_\alpha) \quad \text{and} \quad V_{\alpha\alpha'} = (\varphi_\alpha|\;\mathbb{V}\;\left|\varphi'_\alpha\right). \tag{17}$$

The channel projected wave functions corresponding to a wave incident in the elastic channel with wave vector $\mathbf{k}_0$, $\psi_\alpha^{(+)}(\mathbf{k}_0;\mathbf{r})$, should have the asymptotic form

$$\psi_\alpha^{(+)}(\mathbf{k}_0;\mathbf{r}) \;\to\; A\left[\phi_c\,(\mathbf{k}_0;\mathbf{r})\;\delta_{\alpha 0} + f_{{\rm N},\alpha}(\mathbf{k}_\alpha,\mathbf{k}_0)\,\frac{e^{i\Theta_\alpha(r)}}{r}\right], \tag{18}$$

where A is the normalization factor, usually equal to $(2\pi)^{-3/2}$, and $\phi_{\rm C}\,(\mathbf{k}_0;\mathbf{r})$ is the wave function for Coulomb scattering in the entrance channel. Above, $f_{{\rm N},\alpha}(\mathbf{k}_\alpha,\mathbf{k}_0)$ is the nuclear scattering amplitude in channel α for the final wave vector $\mathbf{k}_\alpha$, and

$$\Theta_\alpha\,(r) = k_\alpha r - \eta_\alpha\,\ln(2k_\alpha r) \tag{19}$$

is the phase of the Coulomb distorted spherical wave, scattered by the nuclear potential. In Eq. (19), $k_\alpha = \sqrt{2\mu E_\alpha}/\hbar$ and η_α is the corresponding Sommerfeld parameter.

The cross sections are then given by

$$\frac{d\sigma_\alpha(\mathbf{k}_\alpha,\mathbf{k}_0)}{d\Omega} = \frac{k_\alpha}{k_0}\left|f_{\rm C}(\mathbf{k}_\alpha,\mathbf{k}_0)\;\delta_{\alpha 0} + f_{{\rm N},\alpha}(\mathbf{k}_\alpha,\mathbf{k}_0)\right|^2. \tag{20}$$

[2] We use different fonts to distinguish operators acting on the full space (*e.g.*, $\mathbb{H}$) from the ones acting only on $\mathbf{r}$ or on ξ (*e.g.*, H and h).

Above, f_C is the point charge Coulomb amplitude, which contributes only to elastic scattering. The remaining amplitude is usually expanded in partial-waves as[3]

$$f_{N,\alpha}(\mathbf{k}_\alpha, \mathbf{k}_0) = \frac{1}{2i\sqrt{k_\alpha k_0}} \sum_{lm} 4\pi\, Y^*_{lm}(\hat{\mathbf{k}}_0)\, Y_{lm}(\hat{\mathbf{k}}_\alpha)\, e^{i(\sigma_{0l}+\sigma_{\alpha l})} \left[S_{N,\alpha l} - \delta_{\alpha 0}\right], \tag{21}$$

where $Y_{lm}(\hat{\mathbf{k}})$ is the spherical harmonic for angular momentum l and z-projection m taken at the orientation $\hat{\mathbf{k}}$, and σ_{0l} and $\sigma_{\alpha l}$ are respectively the Coulomb phase-shifts for this angular momentum in the entrance and exit channels. To evaluate the S-matrix elements, $S_{N,\alpha l}$, it is necessary to solve the partial-wave projected coupled channel equations and look at the asymptotic forms of the radial wave functions.

In a coupled channel calculation the absorption cross section is given by a straightforward generalization of its single channel expression. Assuming that all relevant direct reaction channels are explicitly included in the CC equations, absorption arises exclusively from fusion and the corresponding cross section is [7],

$$\sigma_F = \frac{1}{|A|^2}\,\frac{k_0}{E} \sum_{\alpha\alpha'} \left\langle \psi^{(+)}_\alpha(\mathbf{k}_0) \left| W_{\alpha\alpha'} \right| \psi^{(+)}_{\alpha'}(\mathbf{k}_0) \right\rangle. \tag{22}$$

If one assumes that the channel-coupling interaction is real, as many authors do, the fusion cross section can be written as a sum of contributions from the channels involved in the CC calculation. That is,

$$\sigma_F = \sum_\alpha \sigma_F^{(\alpha)}, \tag{23}$$

where

$$\sigma_F^{(\alpha)} = \frac{1}{|A|^2}\,\frac{k_0}{E} \left\langle \psi^{(+)}_\alpha(\mathbf{k}_0) \right| W_\alpha \left| \psi^{(+)}_{\alpha'}(\mathbf{k}_0) \right\rangle. \tag{24}$$

Above, we used a simplified notation for the diagonal matrix-elements of the imaginary potential, $W_{\alpha\alpha} \equiv W_\alpha$. Eq. (24) is very important in collisions of weakly bound nuclei. The assumption of a diagonal imaginary potential in channel space allows the calculation of individual cross sections for complete fusion and incomplete fusion [10].

The reaction cross section is obtained summing the fusion cross section with the cross section for non-elastic channels integrated over angles. Calling,

$$\sigma_\alpha = \int \frac{d\sigma_\alpha}{d\Omega}\, d\Omega, \tag{25}$$

we can write

$$\sigma_R = \sigma_F + \sum_{\alpha\neq 0} \sigma_\alpha. \tag{26}$$

2.2.1. Couplings with continuum states

In collisions of typical strongly bound nuclei the relevant channels in the coupled channel treatment are all bound. However, in collisions of weakly bound nuclei the breakup process is very important and couplings with intrinsic states in the continuum must also be considered. Then, the coupled channel approach becomes very complicated. It is necessary to take into account the intrinsic bound states of the weakly bound nucleus, $|\varphi_\alpha\rangle$, and also the ones in the continuum,[4] $|\varphi_\varepsilon\rangle$. The channel expansion then becomes

$$\left|\Psi^{(+)}(\mathbf{k_0})\right\rangle = \sum_\alpha \left|\psi^{(+)}_\alpha(\mathbf{k}_0)\right\rangle \otimes |\varphi_\alpha\rangle + \int d\varepsilon \left|\psi^{(+)}_\varepsilon(\mathbf{k}_0)\right\rangle \otimes |\varphi_\varepsilon\rangle\,. \tag{27}$$

The integration variable in the above integral, ε, represents the energy of the "excited" continuum. Following the same procedures as in the case of tightly bound nuclei, one obtains the corresponding coupled channel equations

$$\left[E_\alpha - H_\alpha\right] \psi^{(+)}_\alpha(\mathbf{k}_0;\mathbf{r}) = \sum_{\alpha'} V_{\alpha\alpha'}(\mathbf{r})\, \psi^{(+)}_{\alpha'}(\mathbf{k}_0;\mathbf{r}) + \int d\varepsilon'\, V_{\alpha\varepsilon'}(\mathbf{r})\, \psi^{(+)}_{\varepsilon'}(\mathbf{k}_0;\mathbf{r}), \tag{28}$$

[3] To keep the notation simple, we ignore channel spins and mass transfer. If spins are taken into account, the expressions become more complicated, involving vector coupling coefficients, and the S-matrix may have off-diagonal matrix-elements in the l-space. For details, see, *e.g.*, Refs. [7–9].

[4] For simplicity, we label the continuum states only by their energy. Usually other quantum numbers are needed to specify the state. In this case, Eq. (27) should include also a summation over these quantum numbers.

for the components of the scattering wave function in the space of intrinsic bound states, and

$$\left[E_\varepsilon - H_\varepsilon\right] \psi_\varepsilon^{(+)}(\mathbf{k}_0;\mathbf{r}) = \sum_{\alpha'} V_{\varepsilon\alpha'}(\mathbf{r})\, \psi_{\alpha'}^{(+)}(\mathbf{k}_0;\mathbf{r}) + \int d\varepsilon'\, V_{\varepsilon\varepsilon'}(\mathbf{r})\, \psi_{\varepsilon'}^{(+)}(\mathbf{k}_0;\mathbf{r}), \tag{29}$$

for the component associated with the continuum intrinsic states.

A successful approach to handle this situation is the Continuum Discretized Coupled Channel (CDCC) method [11,12]. It consists of approximating the continuum by a finite set of states. There are different ways to achieve the discretization [13]. The most frequently used methods are the discretization by bins, in the k- or the E-space, and the pseudostate method.

In the bin discretization in the energy space, one replaces the basis of intrinsic continuum states $\{\varphi_\varepsilon(x)\}$, where x is the relative coordinate of the fragments within the weakly bound nucleus, by the finite set,

$$\phi_n(x) = \int d\varepsilon\; \Gamma(\varepsilon - \varepsilon_n)\, \varphi_\varepsilon(x), \quad n = 1, 2, \ldots. \tag{30}$$

Above, $\Gamma(\varepsilon - \varepsilon_n)$ is a function of ε peaked at $\varepsilon = \varepsilon_n$, with width Δ. In this way, the continuum quantum number ε is replaced by the discrete label n and the expansion is truncated. The problem is then reduced to a conventional coupled channel problem, involving only a finite number of bound channels.

In the pseudostate method the states are approximated by the eigenstates of the Hamiltonian expanded in a truncated basis of square integrable functions. The expansion coefficients are then obtained by the diagonalization of the Hamiltonian in the truncated space. The eigenstates with negative energy correspond to the bound states of the projectile whereas the eigenstates with positive energy, called pseudostates, are a finite set approximation to the continuum.

The CDCC has been put to test over and over again in the case of deuteron-nucleus scattering [12] and more recently in heavy ion reactions [14], both with stable and unstable projectiles, as well as in atomic and molecular scattering [15–17].

2.3. Bare and polarization potentials

Frequently, one is interested in a detailed description of a group of channels. This group is a subspace of the whole channel space and it is characterized by an operator P, which projects onto it.[5] However, the remaining channels cannot be completely ignored because they have influence on the dynamics in the P space. It is then convenient to transform the coupled equations into a reduced set of equations involving only the channels in the P space, but containing an effective potential that simulates the effects of the remaining channels. An elegant procedure to derive the effective potential was developed by Feshbach [18], using projector techniques. This procedure is briefly described below.

Let us consider the situation where the P space is spanned by the channels corresponding to the N intrinsic states, $|\varphi_0\rangle, |\varphi_1\rangle, \ldots, |\varphi_{N-1}\rangle$. One then introduces the operator P, that projects onto the selected channels, and the complementary operator Q, that projects onto the remaining part of the channel space. They are given by

$$P = \sum_{\alpha=0}^{N-1} |\varphi_\alpha)\,(\varphi_\alpha|\,; \qquad Q = \sum_{\beta=N}^{\infty} \left|\varphi_\beta\right)\left(\varphi_\beta\right|. \tag{31}$$

In the simple situation of potential scattering, P projects onto the elastic channel and Q projects on all non-elastic ones.

Applying these projectors on the scattering state, one gets its components in the two subspaces,

$$\left|\Psi_{\mathrm{P}}^{(+)}\right\rangle \equiv P\left|\Psi^{(+)}\right\rangle = \sum_{\alpha=0}^{N-1} \left|\psi_\alpha^{(+)}\right\rangle \otimes |\varphi_\alpha) \quad \text{and} \quad \left|\Psi_{\mathrm{Q}}\right\rangle \equiv Q\left|\Psi^{(+)}\right\rangle = \sum_{\beta=N}^{\infty} \left|\psi_\beta^{(+)}\right\rangle \otimes \left|\varphi_\beta\right). \tag{32}$$

The projected wave functions satisfy a system of coupled equations, which arises from the Schrödinger equation for the full many-body wave function. This set can be reduced to a single equation in the P space,

$$\left[E - \mathbb{H}_{\mathrm{eff}}\right] \left|\Psi_{\mathrm{P}}^{(+)}\right\rangle = 0, \tag{33}$$

where $\mathbb{H}_{\mathrm{eff}}$ is the effective Hamiltonian

$$\mathbb{H}_{\mathrm{eff}} = \mathbb{H}_{\mathrm{PP}} + \mathbb{V}_{\mathrm{PQ}}\, \mathbb{G}_{\mathrm{Q}}^{(+)}(E)\, \mathbb{V}_{\mathrm{QP}}. \tag{34}$$

Above, $\mathbb{H}_{\mathrm{PP}} = P\mathbb{H}P$, $\mathbb{H}_{\mathrm{QQ}} = Q\mathbb{H}Q$, $\mathbb{V}_{\mathrm{PQ}} = P\mathbb{V}Q$, $\mathbb{V}_{\mathrm{QP}} = Q\mathbb{H}P$, and $\mathbb{G}_{\mathrm{Q}}^{(+)}(E)$ is the Green's operator in the Q space,

$$\mathbb{G}_{\mathrm{Q}}^{(+)}(E) = \frac{1}{E - \mathbb{H}_{\mathrm{QQ}} + i\epsilon}. \tag{35}$$

[5] Although the subspace and its projector are different objects, we will call P both the subspace and the operator that projects onto it.

The first term of the effective Hamiltonian,

$$\mathbb{H}_{PP} = K + h + \mathbb{V}_{PP}, \tag{36}$$

is the system's Hamiltonian with the couplings between the P and the Q spaces switched off. Using the explicit form of the projector P (Eq. (31)) in Eq. (33), one obtains the coupled equations of Section 2.2 (Eq. (16)). However, now the coupled equations are restricted to the P space.

The diagonal matrix elements[6] of $\mathbb{H}_{PP}$,

$$H_\alpha = \varepsilon_\alpha + K + V_\alpha, \tag{37}$$

are the components of the Hamiltonian in channel α and the potential V_α is called the *bare potential* in channel α. It is real, so that we can write

$$V_\alpha \equiv U_\alpha. \tag{38}$$

The off-diagonal matrix-elements of $\mathbb{H}_{PP}$, namely $V_{\alpha\alpha'}$ with $\alpha \neq \alpha'$, couple the channels within the P space among themselves.

The second term of the effective Hamiltonian, which arises from couplings with the Q space,

$$\mathbb{V}_{pol} = \mathbb{V}_{PQ}\, \mathbb{G}_Q^{(+)}(E)\, \mathbb{V}_{QP}, \tag{39}$$

is called *the polarization potential* [9]. If there are open channels in the Q space, the $i\epsilon$ in G_Q (see Eq. (35)) leads to the complex polarization potential operator,

$$\mathbb{V}_{pol} = \mathbb{U}_{pol} - i\,\mathbb{W}_{pol}. \tag{40}$$

The exact calculation of $\mathbb{V}_{pol}$ is extremely difficult. However, approximate calculations of this potential are feasible and may be very useful. In Section 4.4 we derive the polarization potential associated with breakup couplings and show some applications.

In coupled channel calculations that include the main direct reaction channels, $\mathbb{U}_{pol}$ is a small correction to the bare potential, which is the interaction in the P-projected Schrödinger equation in the limit $\mathbb{V}_{PQ} = \mathbb{V}_{QP} = 0$. On the other hand, $\mathbb{W}_{pol}$ is very important, except at energies much below the Coulomb barrier. It takes into account the coupling with the fusion channel, which cannot be explicitly included in the coupled equations. For practical purposes, the real part of the effective potential (the bare potential plus a small correction $\mathbb{U}_{pol}$) is approximated by some model (double-folding, proximity etc.) and its imaginary part, $\mathbb{W}_{pol}$, is parametrized by a simple function. The resulting interaction is called the *optical potential*. Typically, the optical potential changes slowly with the system's mass and charge.

In most collisions, it is convenient to split the P space into two subspaces, P_1 and P_2, with P_1 containing the elastic channel plus several important inelastic channels which couple strongly to the elastic channel, and P_2 containing the other direct channels. This latter set of channels is treated by the polarization potential method. In this way, the dimension of the coupled-channel calculations can be considerably reduced and the numerical calculations become much simpler. For example: in a collision of a weakly bound projectile, it is convenient to include the elastic and the inelastic channels in the P_1 space and the breakup channel in the P_2 space. The couplings within P_1 are then taken into account through the coupled channels equations, whereas the effects of the breakup channel are expressed by polarization potentials included in these equations. In contrast with the optical potential, this polarization potential has a strong dependence on the nuclear structure properties of the collision partners. Thus, they must be evaluated by some reliable approximation, like the one proposed by Thompson et al. [19].

2.3.1. The dispersion relation and threshold anomalies

The general mathematical property [20]

$$\lim_{\epsilon\to 0}\left\{\frac{1}{x \pm i\epsilon}\right\} = \mathcal{P}\left\{\frac{1}{x}\right\} \mp i\pi\,\delta(x), \tag{41}$$

where $\mathcal{P}$ stands for Cauchy's principal value, leads to a dispersion relation connecting the real and imaginary parts of the polarization potential.

The first step to derive the dispersion relation is to use the spectral representation of $\mathbb{G}_Q^{(+)}(E)$. In general, the Hamiltonian $\mathbb{H}_{QQ}$ has bound and unbound eigenvalues, satisfying the equations,

$$\mathbb{H}_{QQ}\,|\phi_n\rangle = E_n\,|\phi_n\rangle \quad \text{and} \quad \mathbb{H}_{QQ}\left|\phi_{E,\alpha}\right\rangle = E\left|\phi_{E,\alpha}\right\rangle, \tag{42}$$

[6] In Eq. (37) and throughout this section, we adopt the short-hand notations, $H_{\alpha\alpha} = H_\alpha$ and $V_{\alpha\alpha} = V_\alpha$.

where α represents any additional quantum numbers needed to specify unbound eigenstates. Then, the completeness relation has the form

$$\sum_n |\phi_n\rangle \langle\phi_n| + \sum_\alpha \int dE' \, |\phi_{E',\alpha}\rangle\langle\phi_{E',\alpha}| = \mathbb{I}, \tag{43}$$

where $\mathbb{I}$ is the identity operator.

Let us make the simplifying assumption that $\mathbb{H}_{QQ}$ has no bound states, or the bound states are not relevant for the calculation of the polarization potential. In this case, the spectral representation of $\mathbb{G}_Q^{(+)}(E)$ reduces to

$$\mathbb{G}_Q^{(+)}(E) = \sum_\alpha \int dE' \, \frac{|\phi_{E',\alpha}\rangle\langle\phi_{E',\alpha}|}{E - E' + i\epsilon}. \tag{44}$$

Now we use Eq. (41) and write

$$\frac{1}{E - E' \pm i\epsilon} = \mathcal{P}\left\{\frac{1}{E - E'}\right\} \mp i\pi \, \delta(E - E'). \tag{45}$$

The above Green's function then takes the form

$$\mathbb{G}_Q^{(+)}(E) = \sum_\alpha \mathcal{P} \int dE' \, \frac{|\phi_{E',\alpha}\rangle\langle\phi_{E',\alpha}|}{E - E'} - i\pi \sum_\alpha |\phi_{E,\alpha}\rangle\langle\phi_{E,\alpha}|. \tag{46}$$

Using this representation of the Green's function in Eq. (39) and writing separately the real and imaginary parts of the polarization potential, one gets,

$$\mathrm{Re}\left\{\mathbb{V}_{\mathrm{pol}}(E)\right\} = \sum_\alpha \mathcal{P}\left\{\int dE' \, \frac{\mathbb{V}_{PQ}|\phi_{E',\alpha}\rangle\langle\phi_{E',\alpha}|\mathbb{V}_{QP}}{E - E'}\right\} \tag{47}$$

and

$$\mathrm{Im}\left\{\mathbb{V}_{\mathrm{pol}}(E)\right\} = -\pi \sum_\alpha \mathbb{V}_{PQ}|\phi_{E,\alpha}\rangle\langle\phi_{E,\alpha}|\mathbb{V}_{QP}. \tag{48}$$

Inspecting the above two equations, one immediately gets the dispersion relation,

$$\mathrm{Re}\left\{\mathbb{V}_{\mathrm{pol}}(E)\right\} = -\frac{1}{\pi}\mathcal{P}\left\{\int dE' \, \frac{\mathrm{Im}\left\{\mathbb{V}_{\mathrm{pol}}(E')\right\}}{E - E'}\right\}. \tag{49}$$

One can also derive the similar expression [21],

$$\mathrm{Im}\left\{\mathbb{V}_{\mathrm{pol}}(E)\right\} = \frac{1}{\pi}\mathcal{P}\left\{\int dE' \, \frac{\mathrm{Re}\left\{\mathbb{V}_{\mathrm{pol}}(E')\right\}}{E - E'}\right\}, \tag{50}$$

where the real and imaginary parts of the potential exchange places. It corresponds to the Hilbert transform [22] of Eq. (49).

The above equation involves several approximations. The form factors operators $\mathbb{V}_{PQ}$ and $\mathbb{V}_{QP}$ are taken as real, energy-independent and local in the coordinate space. Frequently, the subspace P contains only the elastic channel, that is $P = |0)\,(0|$, and it is calculated in the coordinate representation. Assuming that the form factors are local, Eq. (39) leads to the expression

$$V_{\mathrm{pol}}(E; \mathbf{r}, \mathbf{r}') = \langle \mathbf{r}; 0|\mathbb{V}_{PQ}\,\mathbb{G}_Q^{(+)}(E)\,\mathbb{V}_{QP}|0; \mathbf{r}'\rangle. \tag{51}$$

One should realize that in typical situations the bare potential is assumed to be local,[7] whereas the polarization potential is intrinsically non-local, owing to the non-locality of the Green's function. Thus, including the polarization potential in the Schrödinger equation, one has to deal with an integro-differential equation. However, several assumptions are invoked to reduce $V_{\mathrm{pol}}(E; \mathbf{r}, \mathbf{r}')$ to a local potential. Some local approximations for the polarization potential, like that of Thompson et al. [19] were shown to give very good approximations to results of full coupled channel calculations [23].

In some situations the channel Hamiltonian $\mathbb{H}_{QQ}$, appearing in the Green's function $G_Q^{(+)}$, is not Hermitian, owing to the presence of other channels besides the ones of the Q space (compound nucleus). Nevertheless, detailed coupled channels calculations of the polarization potential [21], have shown that the resulting potential does obey the dispersion relation.

[7] The locality of the bare potential is conditioned to the neglect of exchange terms, or to the use of some local approximation for them.

The usual application of the dispersion relation is to verify experimental findings about the energy dependence of the optical potential extracted from elastic scattering. This analysis supplies information about the total polarization potential. The dispersion relation comes into the picture by taking the imaginary potential as given through analysis of elastic data. Since this imaginary part is expected to become very small as the energy is lowered below the Coulomb barrier, which acts as a natural threshold for non-elastic couplings, the general behavior of the energy dependence of the total imaginary potential is taken as roughly constant (or very slow energy dependent) above the barrier, followed by a rather sharp drop to zero as the energy is lowered below the barrier energy. The dispersion relation will supply the energy dependence of the real part. This procedure has become part of the analyses of reactions induced by stable strongly bound nuclei [24,25].

Recently, an extension of the application of the dispersion relation to cases where breakup channels are important, such as the case of reactions induced by weakly bound nuclei, has been made [26]. In such systems, the energy dependence of the imaginary part is significantly different from the case of strongly bound nuclei, as, even when the energy is lowered below the Coulomb barrier, the absorption continues to be strong since the threshold of the breakup coupling is quite small. Accordingly, there is an increase in the imaginary part followed by the drop to zero as the energy is further lowered. This has the consequence that the real part will show an energy dependence in marked difference to the case of strongly bound nuclei. In fact the experimental data seem to show this difference: whereas in the case of strongly bound nuclei the real part shows an increase in attraction as the energy is lowered below the Coulomb barrier, the scattering of weakly bound nuclei shows a reduction of attraction (effective repulsion). These different behaviors became known as the Threshold Anomaly (TA) [24], and the Breakup Threshold Anomaly (BTA) [26], respectively.

2.4. Recent extensions of the CDCC

The usual method of solving the CDCC equations is to consider the projectile as a two-cluster nucleus and take for the projectile–target interaction the sum of the optical potentials of each cluster with the target. Standard CDCC calculation involve only bound and unbound states of the relative two-cluster motion. However, intrinsic excitations of the clusters may play an important role in elastic scattering and breakup reactions. Summers, Nunes and Thompson [27,28] developed an extended version of the CDCC method (XCDCC), in which core excitations can be taken into account. Recently, de Diego et al. [29] used the XCDCC method to study the influence of core excitation in the breakup of ^{11}Be projectiles on several targets.

In many cases the optical potentials of the breakup fragments and the target are not so well known. In such cases, one of the practices is to use known optical potentials for projectiles very close in mass number to the fragments and to change the radius as $r_0 A^{1/3}$. In developing the CDCC further, a more refined treatment based on the use of the nucleon-target optical potentials is invoked. This enables one to reduce the degree of uncertainty of the calculation and gives more reliable results. Recent calculations of the elastic scattering of weakly bound nuclei using this "microscopic CDCC" has proven to be quite promising [30,31].

An additional complication is that many important weakly bound nuclei, such as ^{6}He and ^{11}Li, dissociate into three fragments. Then, the description of the continuum becomes much more complicated and the states are labeled by a larger number of quantum numbers. However, the generalization of the CDCC to three-body dissociation is straightforward, despite the larger computational effort required [32–35]. In such cases, the continuum states are usually discretized by the pseudostates method, described in Section 2.2.1.

The four-body CDCC approach is well suited to perform a more reliable calculation of the fusion cross section of three-cluster nuclei, such as ^{9}Be, treated as $\alpha + \alpha + n$. A calculation along these lines has been recently carried out [36]. The method has been used to evaluate elastic scattering, breakup and total fusion cross sections in the $^{9}\mathrm{Be} + {}^{208}\mathrm{Pb}$ collision, and the results were compared to data. This unified and consistent treatment significantly enhances the reliability of the model, since no parameter is fitted, and since the theory can be tested on well-known elastic-scattering data. The overall agreement of their theoretical results with experiment was rather good. The elastic and fusion cross sections of this calculation will be discussed in Sections 3 and 5, respectively.

3. Elastic and quasi-elastic scattering

The elastic scattering of the heavy-ion system is of paramount importance as it furnishes information about the interaction potential at distances corresponding to the exit branch of the Coulomb barrier. This is so since elastic scattering, specially at low energy, measures the reflection of the flux as it reaches the region of the interaction. The same holds for the quasi-elastic cross section, which is the incoherent sum of the elastic plus the peripheral non-elastic cross sections. At angles close to 180°, the elastic and quasi-elastic cross sections supply information about the potential at the shortest distances where reflection could occur. The interaction potential obtained from a careful analysis of the elastic scattering data contains the bare potential and the dynamic polarization potential. This latter satisfies the dispersion relation discussed in the previous section. Both the TA and the BTA (see Section 3.4) were found through such analysis. In this section we give a brief account of the theory of the elastic scattering of heavy ions with special emphasis on the case of weakly bound projectiles, where the breakup coupling is expected to be important. We also discuss the elastic and quasi-elastic cross sections at back angles and the information they supply about the potential, and, in particular the quasi-elastic barrier

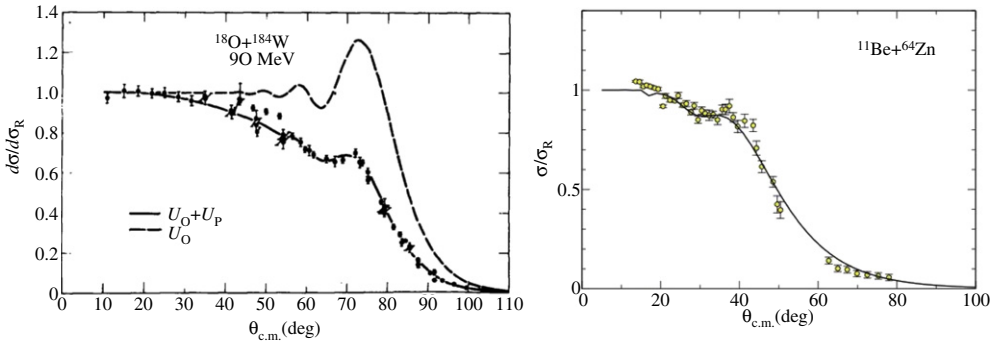

Fig. 1. (Color online) Left panel: The angular distribution for the $^{18}O + {}^{184}W$ system in comparison of a single-channel calculation with a standard optical potential (dashed line) and with a calculation that includes also the long-range dynamical polarization potential (solid line). Right panel: Elastic angular distribution for the $^{11}Be + {}^{64}Zn$ system at $E_{c.m.} = 24.5$ MeV, normalized with respect to the Rutherford cross section [40]. The solid line is the result of an optical model analysis.
Source: The figure is from Ref. [38] and the data from Ref. [39].

distribution and its connection with the fusion barrier distribution. The section concludes with a review of the present status of the BTA effect found for these weakly bound systems.

3.1. Basic theory and recent measurements

We start our discussion with the basic form of the nuclear part of elastic scattering amplitude, given in Eq. (3) of Section 2.1. The cross section is then given by $|f_N(\theta) + f_C(\theta)|^2$. This procedure of evaluating the cross section is employed in numerical calculations, as it avoids the Coulomb singularity. For the purpose of qualitative analysis, one usually employs the partial-wave expansion of the full amplitude $f(\theta) = f_N(\theta) + f_C(\theta)$ which is simply,

$$f(\theta) = \frac{1}{2ik} \sum_l (2l+1)\ P_l(\cos\theta)\ \left(e^{2i\sigma_l}\, S_{N,l} - 1\right). \tag{52}$$

The qualitative properties of the above form of the amplitude, Eq. (52), for the elastic scattering of heavy ions, where the Coulomb effects are important, has been exhaustively discussed in the literature. We will not repeat this discussion in this Report, and refer the reader to the appropriate literature (see *e.g.* Refs. [7–9]). We shall, however, emphasize the salient features of the amplitude at the near-barrier energies considered both for strongly and weakly bound nuclei.

As it is well known, at these low energies Coulomb scattering is dominant and the amplitude is predominantly near-sided. In general, the near-side amplitude is characterized by conspicuous Fresnel diffraction (or Coulomb rainbow). The ratio of the cross section to that of point charge Coulomb cross section exhibits a value close to unity at small angles followed by increasing oscillations, and a rather large bump, and then a gradual drop to small values at back angles. This behavior is a signature of Fresnel diffraction, and it can be observed in most of the available data.

In cases where besides the Coulomb potential, another long-range potential operates, one finds a damped Fresnel diffraction, with the big bump alluded to above reduced considerably. Further, the region where the ratio σ/σ_{Ruth} is close to one is then restricted to very forward angles. A study of this effect in collisions of tightly bound and halo projectiles has recently been published [37].

A classical example of this situation is the collision of a heavy projectile with a highly deformed target. In this case, the Coulomb quadrupole coupling has a long range, so that it produces Coulomb excitation even in distant collisions which lead to small scattering angles. In collisions of halo nuclei, there is a similar effect. The coupling interaction has a long range, owing both to the Coulomb dipole term and to the extended nuclear form factor resulting from the halo. Correspondingly, the couplings with the breakup channel leads to a long-range complex polarization potential, which changes the Fresnel diffraction pattern as in the case of Coulomb excitation. The analogy of the two situations is illustrated in Fig. 1. The left panel shows the angular distribution for the collision of ^{18}O projectiles with the highly deformed ^{184}W target, normalized with respect to the Rutherford cross section. The dashed line corresponds to an optical model calculation with a standard heavy ion potential and the solid line was obtained including the dynamical polarization potential of Love, Terasawa and Satchler [38], which accounts for the quadrupole excitation of the rotational band of ^{184}W. One observes the damping of the rainbow maximum at $\theta_{c.m.} \sim 75^\circ$. The right panel shows the elastic angular distribution for the collision of the neutron-halo ^{11}Be projectile on ^{64}Zn. On sees clearly that the rainbow maximum at $\theta_{c.m.} \sim 40^\circ$ is strongly damped and the ratio σ/σ_R remains below one all the way down to $\sim 20^\circ$. The two panels exhibit the same qualitative behavior, resulting from the absorption due to a long-range imaginary potential. Recently these effects have been observed for several unstable projectiles, mainly neutron-halo nuclei. In the last few years, several experiments to determine angular distributions of halo nuclei have been performed. Examples are: (i) ^{11}Be on ^{209}Bi [41] and ^{64}Zn [40,42]; (ii) ^{6}He on ^{9}Be [43], ^{27}Al [44], ^{58}Ni [45],

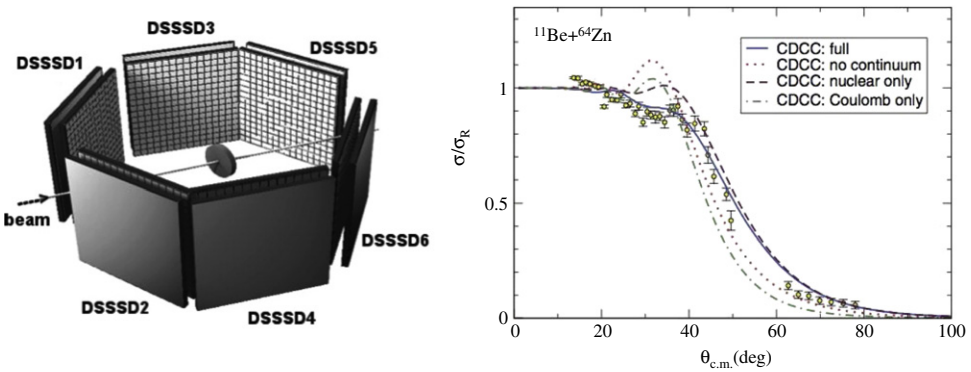

Fig. 2. (Color online) Left panel: The experimental set up used in Ref. [40]; Right panel: Experimental angular distribution for the ^{11}Be + ^{64}Zn system, in comparison with the calculations described in the legend.
Source: The figure was taken from Ref. [40].

^{120}Sn [46], ^{206}Pb [47] and ^{208}Pb [48–50]; (iii) ^{8}He on ^{65}Cu [51]. We discuss below some results showing the damping of the rainbow maximum for these systems.

Let us first consider angular distributions in collisions of the one-neutron halo nucleus ^{11}Be. Mazzocco et al. [41] measured the angular distribution of ^{11}Be projectiles on a ^{209}Bi target, at the beam energy of 40 MeV. The experiment was performed at the RIPS fragment separator in RIKEN. More recently, Di Pietro et al. [40,42] measured elastic, quasi-elastic and transfer/breakup cross sections for the ^{11}Be + ^{64}Zn system. The experiment was performed at the REX-ISOLDE facility of CERN. As the average intensity of the ^{11}Be beam was too low, of the order of 10^4 pps, it was necessary to use a large detection system, covering a wide solid angle. The experimental set-up is represented schematically on the left panel of Fig. 2. It used an array of six Silicon detector telescopes of double-sided silicon strip detectors (DSSSD), with a total of 1536 pixels. The right panel of Fig. 2 shows the elastic angular distribution of Ref. [40], in comparison with results of several calculations. The red dotted line corresponds to a calculation that does not include breakup couplings. It exhibits the typical Fresnel pattern of heavy-ion scattering at near-barrier energies. Clearly, this cross section is very different from the data. When the full breakup couplings[8] are taken into account in a CDCC calculation (blue solid line), the experimental angular distribution is reproduced accurately. On the other hand, if it includes only the Coulomb or the nuclear couplings, the agreement between theory and experiment becomes much poorer, mainly in the region of the rainbow maximum. This point was emphasized in a recent paper by Diaz-Torres and Moro [52]. The important role of the nuclear component of the breakup couplings has also been pointed out in the CDCC calculations of Keeley et al. [53]. In this connection, we mention also de *R*-matrix based CDCC calculations of Druet and Descouvemont [54], which reproduce the data equally well and present a detailed discussion of the interactions and other aspects involved in the work. We should mention that the data was also compared with results of a single channel calculation with the bare potential plus the dynamic breakup polarization potential of Andres, Gomez-Camacho and Nagarajan [55] (not included in the figure). The resulting angular distribution was in qualitative agreement with the data. Considering that this polarization potential is derived through a simple procedure that considers only the Coulomb dipole coupling, this agreement is quite reasonable.

Now we discuss some angular distributions in collisions of the two-neutron halo nuclei. We begin with ^{6}He. Several experiments have been performed to study elastic scattering of ^{6}He beams on different targets. Morcelle et al. [45] measured angular distributions for the ^{6}He + ^{58}Ni system, at the beam energies $E_{\rm lab}$ = 12.2, 16.5 and 21.7 MeV. Their experiments were performed at the RIBRAS facility, of the University of São Paulo. The left panel of Fig. 3 shows their data in comparison with results of a calculation that neglects couplings with the breakup channel (dotted line), and with 3-body (dashed lines) and 4-body (red solid lines) CDCC calculations. First, one notices that the experimental rainbow maximum is damped, in comparison with the calculation that neglects breakup effects (dotted line), although this effect is not very pronounced. One notices also that this calculation underestimates the data at large angles, mainly for $E_{\rm lab}$ = 16.5 MeV. The results of the 3-body CDCC calculations (blue and green dashed lines) are slightly better but the discrepancies at large angles remain. On the other hand, the cross section obtained with the 4-body CDCC calculation is very close to the data, over the whole angular range and for the three collision energies. This damping was also observed for the elastic scattering of the proton-halo ^{8}B nucleus on the same target ^{58}Ni, at near barrier energies [56,57].

Kakuee et al. [48] measured angular distributions for the ^{6}He + ^{208}Pb system at the collision energies $E_{\rm lab}$ = 14, 16, 18 and 22 MeV, over the angular range of 6°–72°. Their experiments were performed at the CRC facility at Louvain-la-Neuve. Five years later, Sánchez-Benítez et al. [49] extended this study to the higher energy $E_{\rm lab}$ = 27 MeV. The experiment was performed in the same facility and in this case it covered a broader angular interval, in the forward (5°–65°) and backward (135°–170°) regions. The results of these two experiments [48,49] were analyzed by Fernández-García et al. [58], with

[8] There are two types of couplings: the long-range Coulomb couplings, associated with the Coulomb field, and the short-range nuclear couplings, arising from nuclear forces.

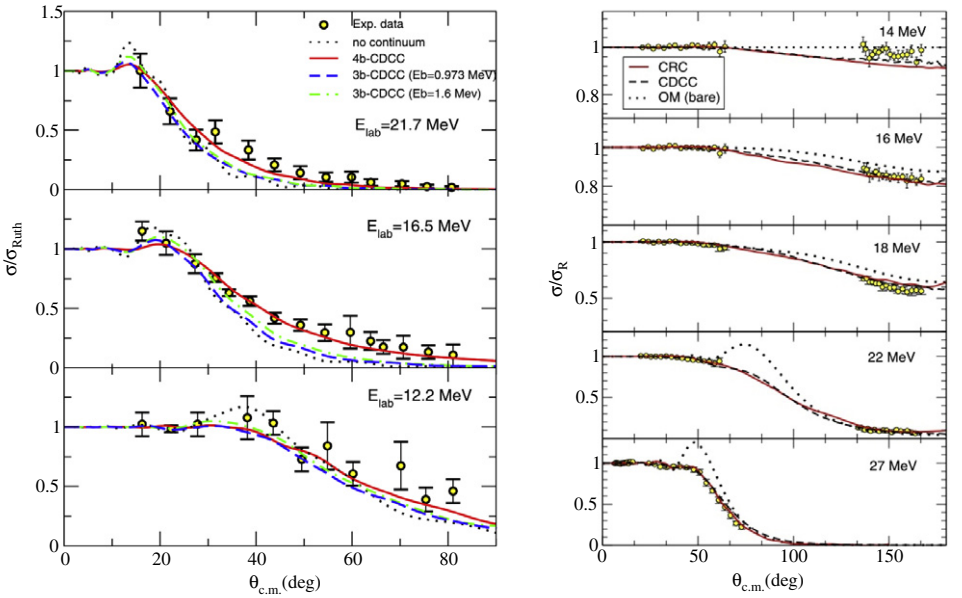

Fig. 3. (Color online) Left panel: Angular distributions for the ^{6}He + ^{58} Ni system, measured at the beam energies of 12.2, 16.5 and 21.7 MeV [45], in comparison with the different calculations described in the legend; Right panel: Theoretical analysis of elastic angular distribution for the ^{6}He + ^{208}Pb system at several collision energies [58] and the calculations are indicated in the legend and discussed in the text. (For interpretation of the references to color in this figure legend, the reader is referred to the web version of this article.)
Source: The data are from Refs. [48,49].

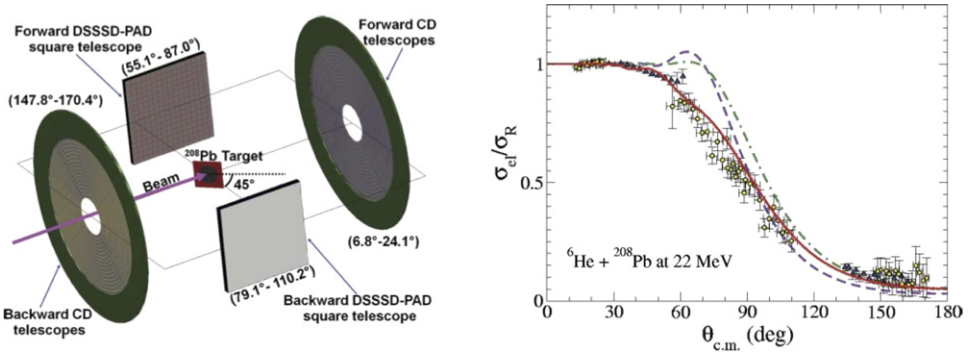

Fig. 4. (Color online) Left panel: Schematic representation of the experimental set-up of Ref. [50]. The range of scattering angles (in the laboratory frame) covered by each telescope is indicated; Right panel: The experimental angular distribution for the ^{6}He +^{208} Pb system at $E_{\rm lab}$ = 22 MeV, in comparison with results of three calculations. The purple dashed curve corresponds to a calculation in which couplings with the continuum are totally neglected. The green dot-dashed curve are results of a CDCC calculation with continuum couplings but neglecting the dipole term of the interaction. The red solid curve are results of a CDCC calculation with full couplings.
Source: The figure was taken from Ref. [50].

3-body CDCC and CRC calculations. The latter was used to describe the stripping of two neutrons, which leads to the production of alpha-particles. The results are shown on the right panel of Fig. 3. One observes that the data are equally well described by the 3-body CDCC (dashed lines) and the CRC (red solid lines) calculations. The large bump of the Fresnel pattern, predicted by the single-channel calculation with the bare potential (dotted line), is strongly damped in the CDCC and CRC calculations, in agreement with the data. The experimental cross sections at large angles are also well reproduced by these calculations, except for the lowest collision energy, $E_{\rm lab}$ = 14 MeV. A favorable point for the CRC calculation is that it also reproduces the measured alpha-particle production.

More recently, Acosta et al. [50] used a sophisticated experimental set up to perform a new measurement of the ^{6}He + ^{208} Pb angular distribution at $E_{\rm lab}$ = 22 MeV. Their experiment was performed also in Louvain-la-Neuve, but with a ^{6}He beam with improved intensity ($\sim 10^{6}$ pps). The detection system was the DINEX silicon detector array, shown on the left panel of Fig. 4. They used two groups of telescopes, each one with a silicon strip ΔE and a PAD E detector, with the shape of compact disk (CD). In addition, they had two square telescopes with DSSSD ΔE detectors and a PAD E detector. The measured angular distribution is shown on the right panel of Fig. 4. As in the previously discussed experiments with the same system, the rainbow maximum is strongly damped and the 3-body CDCC calculations with full couplings with the

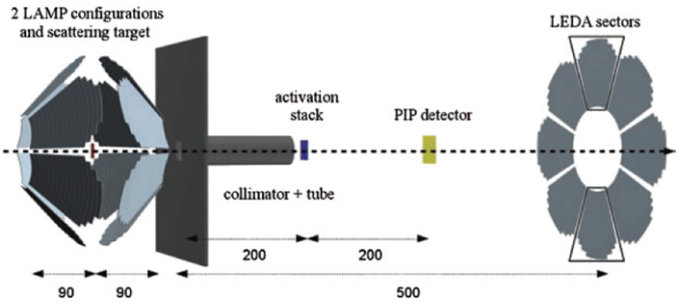

Fig. 5. (Color online) Schematic representation of the experimental set-up of Ref. [47].

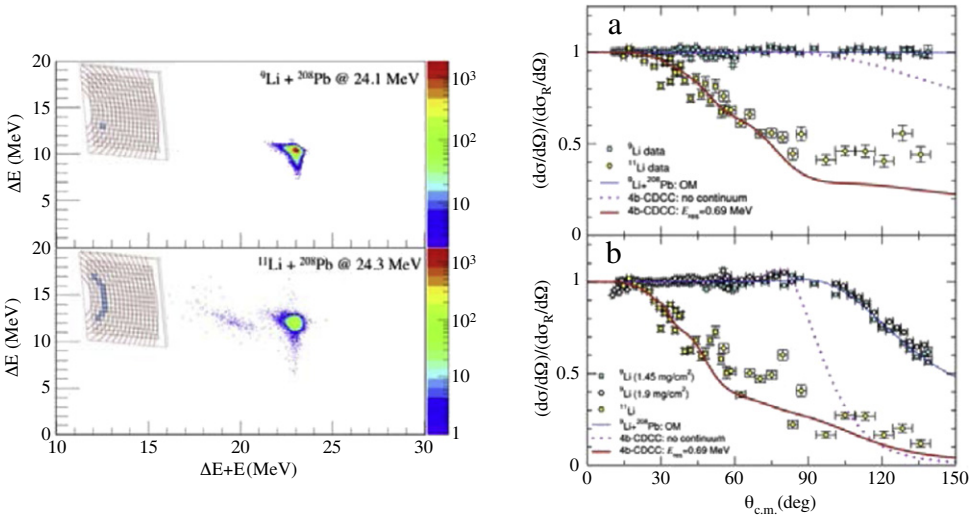

Fig. 6. (Color online) Left panel: Two dimensional plot of $\Delta E \times (\Delta E + E)$ at a forward telescope [59]. The pixels are illustrated on the left part. The ^{9}Li scattering data are shown on the upper part of the figure and that for ^{11}Li at the bottom. The events from ^{9}Li and ^{11}Li scattering are separated; Right panel: Elastic angular distributions for ^{9}Li and ^{11}Li on ^{208}Pb [59]. The collision energies are $E_{\text{c.m.}} = 23.1$ MeV (panel (a)) and 28.3 MeV (panel (b)). Further details of the experiment and of the 4-body CDCC calculations can be found in Ref. [59].

breakup channel are in good agreement with the data. On the other hand the agreement between the experimental angular distribution and the CDCC calculation without dipole coupling is much poorer. This indicates that this part of the couplings is very important, as the easily polarizable projectile exhibits an appreciable dipole excitation. This is known as the Pygmy Dipole Resonance, which is the coherent vibration of the excess neutrons against the tightly bound core (dipole mode).

Another recent experiment on ^{6}He elastic scattering on lead was performed in Louvain-la-Neuve by Standyło et al. [47]. In this case they used a high intensity ^{6}He beam (1.6×10^{7} pps) and the target was ^{206}Pb. Owing to the high beam intensity, it was possible to use a target thinner than in other experiments involving this projectile. The experimental setup is shown in Fig. 5. The detection system consisted of two LEDA (Louvain Edinburgh Detector Array) of five sectors each arranged in a six-sided cone (LAMP) configuration covering angles from 25° to 70° and from 105° to 165°. Each sector consisted of 16 strips. To monitor the incident flux, two other LEDA sectors in annular configuration were placed downstream of the activation stack, normal to the beam direction. Their experimental angular distribution is similar to the ones for the ^{208}Pb targets in the same energy range. They compared the data with the results of CDCC and CRC calculations and concluded that the one- and two-neutron transfer channels are very important.

In a recent experiment, Cubero et al. [59] determined elastic angular distributions for the ^{11}Li + ^{208}Pb system. They measured both ^{11}Li and ^{9}Li elastic scattering at two collision energies, one slightly above the barrier and one slightly below The experiment was performed in the ISAC-II line at TRIUMF, Vancouver. The average intensity of the ^{11}Li beam was only 4×10^{3} pps. The experimental setup consisted of four telescopes, two at forward directions and two at backward directions. Each telescope consisted of a windowless thin DSSSD ΔE detector and a Si PAD E detector. The segmentation of the detector system has 256 pixels per telescope, and the configuration allowed high angular resolution with large angular coverage, from 10° to 140°. Clear identification of the elastic peaks and fragments of ^{9}Li and ^{11}Li could be achieved, as can be seen on the left panel of Fig. 6. The results are shown on the right panel of the same figure. Comparing the cross section for the two Li isotopes, one observes that the one for ^{11}Li is drastically suppressed, even at very small scattering angles and at $E_{\text{c.m.}} = 23.1$ MeV, which is below the Coulomb barrier. The theoretical predictions of a 4-body CDCC calculation are in very good agreement with the data.

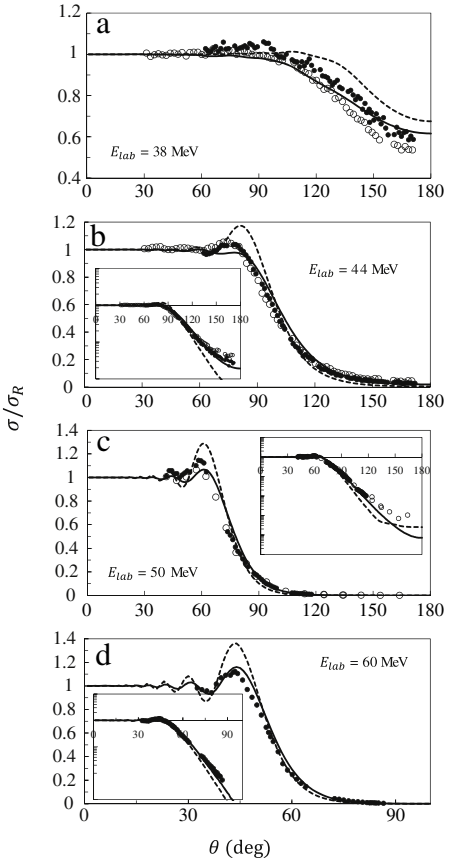

Fig. 7. Elastic angular distributions in ^{9}Be + ^{208}Pb scattering at several bombarding energies, normalized with respect to the Rutherford cross sections. The dashed lines are results of single-channel calculations (limited to the g.s. of ^{9}Be) and the solid lines correspond to four-body CDCC calculations [36] (full circles) and [61] (open circles). The insets show the results on a logarithmic scale.
Source: The data are from Refs. [60].

It is interesting that the elastic scattering of ^{6}He on ^{208}Pb can be well reproduced by three-body CDCC calculations, whereas that of ^{6}He on the lighter ^{58}Ni target cannot. In the latter case, as Ref. [45] points out, a good description of the data requires a four-body CDCC calculation. This situation is not surprising. In Coulomb breakup of ^{6}He, dominated by the dipole term, the coupling depends on the distance between the center of mass of the alpha cluster and that of the neutron pair. Thus, it is not sensitive to the individual coordinates of the neutrons. In this way, the four-body CDCC calculation, where the projectile is modeled as a 3-cluster system (^{4}He + n + n), and the three-body CDCC calculation, where the two neutrons are approximated by a single cluster, the di-neutron, should lead to similar results. In contrast, nuclear breakup depends on the individual coordinates of the alpha cluster and of each of the two neutrons. In this way, a four-body CDCC description of nuclear breakup is expected to be more successful than the three-body one. Therefore, one expects that collisions with light targets, dominated by nuclear breakup, would require the four-body CDCC, whereas collisions with heavy targets, where Coulomb breakup is more important, could be well described by the three-body CDCC.

In a very recent paper, Descouvemont et al. [36] performed four-body CDCC calculations of elastic cross sections in ^{9}Be + ^{208}Pb scattering. The ^{9}Be projectile was treated as a $\alpha + \alpha + n$ three-cluster nucleus. The projectile–target interaction was written as the sum of standard $\alpha - ^{208}$Pb and $n - ^{208}$Pb optical potentials available in the literature. Fig. 7 shows angular distributions for four energies in the 38–60 MeV range. The calculated cross sections are compared to the available data. One sees that the CDCC cross sections agree very well with the data, whereas the agreement of the single channel calculations with the data is much poorer.

3.2. The quasi-elastic cross section at backward angles

For the purpose of obtaining insight into the quasi-elastic cross section[9] we consider the excitation of collective states in the target in the sudden approximation, and ignore the spins of these states. If we designate by x the parameter that

[9] Note that the concept of quasi-elastic scattering may have a different meaning in other scattering problems. This is the case, for example, in electron scattering from nuclei, where quasi-elastic scattering refers to a process where a single nucleon knockout is dominant.

represents the collective degrees of freedom (phase of the oscillator in the case of vibrations, orientation angle of the deformed target in the case of rotations), then for a fixed value of this parameter, the "elastic" $S_{N,l}$ elements become $S_{N,l}(x)$, and the scattering amplitude becomes a function of x, $f(\theta, x)$. Correspondingly, the cross section becomes $d\sigma(\theta, x)/d\Omega$. Of course, this cross section has to be averaged over all values of x, which is done by calculating the ground state $|0\rangle$ expectation value before actually comparing with data. One may define two cross sections,

$$\left\langle \frac{d\sigma(\theta, x)}{d\Omega} \right\rangle = \langle 0| \ |f(\theta, x)|^2 \ |0\rangle, \tag{53}$$

and another cross section, the genuine elastic cross section, which is calculated from the x-averaged amplitude,

$$\frac{d\sigma(\theta)}{d\Omega} = \left|\langle 0|f(\theta, x)|0\rangle\right|^2. \tag{54}$$

It is easy to show that the cross section defined in Eq. (53) contains the elastic one, Eq. (54), plus all the inelastic cross sections. This can be clearly seen by writing,

$$\langle 0| \ |f(\theta, x)|^2 \ |0\rangle = \sum_n \langle 0 \, |f(\theta, x)| \, n\rangle \ \langle n|f^*(\theta, x)|0\rangle = \sum_n |f_{0n}(\theta)|^2 .$$

Thus, in the sudden limit, we identify Eq. (53) with the quasi-elastic cross section.

Of interest here is the cross section at $\theta = \pi$. As we mentioned in the beginning of Section 3, the cross sections in this angular region supply information about the nuclear potential. It is evident from the discussion above, and the fact that the amplitude at near-barrier energies is predominantly near-sided, that a semiclassical evaluation of $f(\theta, x)$ involves a single stationary point in the phase of $S_{N,l}$. Furthermore, its modulus, $|S_{N,l}|$, near $\theta = \pi$ is a slowly varying function of the angular momentum. Under these conditions we may write,

$$f(\theta, x) = f_C(\pi) \, S_{N,\lambda_C}(x), \tag{55}$$

where $\lambda = l + 1/2$, and λ_C is related to the scattering angle through the usual formula, $\eta/\lambda_C = \tan(\theta/2)$. Accordingly, the quasi-elastic cross section is given by,

$$\left\langle 0 \left| \frac{\sigma(\pi, x)}{\sigma_{\rm Ruth}(\pi)} \right| 0 \right\rangle = \left\langle 0 \left| \left|S_{N,\lambda_C}(x)\right|^2 \right| 0 \right\rangle = 1 - \langle 0|T_0(E, x)|0\rangle, \tag{56}$$

where $\sigma_{\rm Ruth}$ is the Rutherford cross section and $T_0(E, x)$ is the $l = 0$ transmission coefficient as a function of energy and the parameter x.

Recently it has been shown that quasi elastic scattering at backward angles can also be employed to derive fusion and reaction cross sections [62–67]. As quasi-elastic processes are much simpler to be measured than fusion, this is a very useful tool to, at least, estimate fusion cross sections. This simple method is based on the conservation of reaction flux. We define the quasi-elastic scattering probability, for a center of mass energy E and total angular momentum J as

$$P_{\rm qe}(E, J) = P_{\rm el}(E, J) + P_{\rm in}(E, J) + P_{\rm tr}(E, J), \tag{57}$$

where $P_{\rm el}$, $P_{\rm in}$, and $P_{\rm tr}$ stand for the elastic scattering, inelastic and transfer probabilities, respectively. The total reaction probability may be written as

$$P_{\rm R}(E, J) = P_{\rm in}(E, J) + P_{\rm tr}(E, J) + P_{\rm cap}(E, J) + P_{\rm BU}(E, J), \tag{58}$$

where $P_{\rm R}$ refers to the non-elastic reaction channel probability, $P_{\rm cap}$ is the capture probability (sum of fusion and quasi-fission probabilities), and $P_{\rm BU}$ is the breakup probability. From the conservation of the total reaction flux one can write the expression

$$P_{\rm el}(E, J) + P_{\rm R}(E, J) = 1, \tag{59}$$

or

$$P_{\rm qe}(E, J) + P_{\rm cap}(E, J) + P_{\rm BU}(E, J) = 1. \tag{60}$$

Since the quasi-elastic probability for angular momentum $J = 0$ is given by the ratio of the quasi-elastic differential cross section and the Rutherford differential cross section at 180°, $\sigma_{\rm qe}(E, \pi)$ and $\sigma_{\rm Ruth}(E, \pi)$, respectively, neglecting for the moment $P_{\rm BU}(E, J)$, one can extract the capture probability $P_{\rm cap}$ at $J = 0$ from the experimental quasi-elastic probability as:

$$P_{\rm cap}(E, 0) = 1 - P_{\rm qe}(E, 0) = 1 - \frac{\sigma_{\rm qe}(E, \pi)}{\sigma_{\rm Ruth}(E, \pi)}. \tag{61}$$

Furthermore, one can approximate $P_{\rm cap}(E,J)$ by its $J=0$ value[10] at the shifted energy [68],

$$\varepsilon_J = E - \frac{\hbar^2 J(J+1)}{2\mu R_{\rm B}^2},$$

where μ is the reduced mass of the colliding system. One then gets,

$$P_{\rm cap}(E,J) \approx P_{\rm cap}(\varepsilon_J,0) = 1 - P_{\rm qe}(\varepsilon_J,0). \tag{62}$$

The barrier radius of the effective J-dependent potential is assumed to be independent of J, having the value $R_{\rm B}$. The total capture cross section is then given by

$$\sigma_{\rm cap}(E) = \sum_{J=0}^{J_{\rm cr}} \sigma_{\rm cap}(E,J) = \pi\,\frac{\hbar^2}{2\mu E}\,\sum_{J=0}^{J_{\rm cr}} (2J+1)\left[1 - P_{\rm qe}\left(\varepsilon_J\right)\right], \tag{63}$$

where $J_{\rm cr}$ is the critical angular momentum at which the potential pocket in the nucleus–nucleus interaction potential vanishes. Above, we used the compact notation, $P_{\rm qe}\left(\varepsilon_J\right) = P_{\rm qe}\left(\varepsilon_J,0\right)$.

Taking into account lowest order corrections to the J-dependent barrier radius and barrier height [68], Sargsyan et al. [62] converted the sum over J into an integral over $\varepsilon_J \equiv \varepsilon$ and obtained the expression,

$$\sigma_{\rm cap}(E) = \frac{\pi R_{\rm B}^2}{E}\int_{\varepsilon_{\rm cr}}^{E} d\varepsilon \left[1 - \frac{\sigma_{\rm qe}(\varepsilon,\pi)}{\sigma_{\rm Ruth}(\varepsilon,\pi)}\right]\left(1 - \frac{4(E-\varepsilon)}{\mu\omega^2 R_{\rm B}^2}\right), \tag{64}$$

where $\hbar\omega$ is the curvature of the Coulomb barrier and

$$\varepsilon_{\rm cr} = E - \frac{\hbar^2 J_{\rm cr}\,(J_{\rm cr}+1)}{2\mu R_{\rm B}^2}.$$

This equation relates the capture cross section with the backward quasi-elastic excitation function. At energies above the barrier, good agreement was found between the capture (fusion) cross sections obtained by this method and direct fusion cross section data for several tightly bound systems [62]. In collisions of weakly bound nuclei, the breakup process must be taken into account. This can be done easily, replacing in Eq. (64): $\sigma_{\rm qe}(\varepsilon,\pi) \to \sigma_{\rm qe}(\varepsilon,\pi) + \sigma_{\rm BU}(\varepsilon,\pi)$. That is,

$$\sigma_{\rm cap}(E) = \frac{\pi R_{\rm B}^2}{E}\int_{\varepsilon_{\rm cr}}^{E} d\varepsilon \left[1 - \frac{\sigma_{\rm qe}(\varepsilon,\pi) + \sigma_{\rm BU}(\varepsilon,\pi)}{\sigma_{\rm Ruth}(\varepsilon,\pi)}\right]\left(1 - \frac{4(E-\varepsilon)}{\mu\omega^2 R_{\rm B}^2}\right). \tag{65}$$

The left panel of Fig. 8 compares the absorption cross sections for the ^{6}Li + ^{208}Pb system obtained by this method (red solid line) with the absorption cross section measured directly [69] (full square). Note that for this system absorption corresponds to fusion. For the indirect determination of $\sigma_{\rm cap}$, through Eq. (64), Sargsyan et al. [62] used the quasi-elastic and breakup data of Lin et al. [70]. The agreement is good at near-barrier energies.

The extension of the above procedure to determine the reaction cross section is straightforward. One has just to replace in Eq. (64) the quasi-elastic cross section by the elastic one [63]. That is

$$\sigma_{\rm R}(E) = \frac{\pi R_{\rm B}^2}{E}\int_{\varepsilon_{\rm cr}}^{E} d\varepsilon \left[1 - \frac{\sigma_{\rm el}(\varepsilon,\pi)}{\sigma_{\rm Ruth}(\varepsilon,\pi)}\right]\left(1 - \frac{4(E-\varepsilon)}{\mu\omega^2 R_{\rm B}^2}\right). \tag{66}$$

The right panel of Fig. 8 shows the reaction cross section for the ^{6}Li + ^{64}Zn system obtained from the above equation (red solid line), in comparison with the cross section determined from elastic scattering angular distributions (full circles). The two cross sections are in very good agreement. The figure shows also the fusion (absorption) cross section obtained from backward quasi-elastic and breakup data through Eq. (65) (dashed line), together with experimental results obtained by direct measurements [71–74]. The cross section derived through Eq. (65) agrees quite well with the direct measurements, except for the data of Refs. [73,74], which are represented by squares. However, it has already been pointed out that these data are underestimated, owing to experimental problems [75].

This method to estimate reaction cross sections is very simple and it seems to work very well. It has been used in other very recent works [76]. It has also been extended to derive breakup probabilities [77]. Recently, it has been shown [78] that the predictions of this method are in agreement with coupled channel calculations.

[10] This is based on the assumption that the angular momentum dependence of the barrier radius is negligible, which is a good approximation in heavy ion collisions. To illustrate this point, we consider ^{16}O + ^{144}Sm scattering and adopt the Akyüz–Winther potential for the nuclear interaction. In this case, the barrier radii for all partial-waves contributing to fusion lie in the range 9.5–10.5 fm.

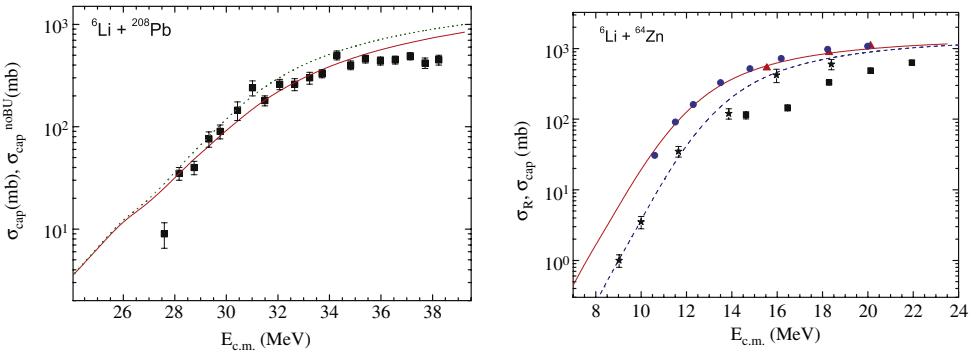

Fig. 8. (Color online) Left panel: Absorption cross sections for the ^{6}Li + ^{208}Pb system. The red solid line represents results obtained by Sargsyan et al. [62] through Eq. (65), using the backward quasi-elastic and breakup data of Ref. [70]. The full squares correspond to the fusion cross section measured directly [70]; Right panel: Reaction and fusion cross sections for the ^{6}Li + ^{64}Zn system. The solid line was obtained by Sargsyan et al. [63] through Eq. (66), using backward elastic scattering data [71,72]. The full circles are experimental results obtained from elastic scattering angular distributions [71,72]. The dashed line is the absorption cross section derived from Eq. (65) [63], using the backward quasi-elastic and breakup data of Refs. [71,72], whereas the full stars [71,72] and squares [73,74] are fusion data measured by standard procedures.

3.3. Quasi-elastic and fusion barrier distributions

An interesting consequence of Eq. (56) is its derivative with respect to energy, as it supplies us with the barrier distribution,

$$D_{\rm qel} = -\frac{d}{dE}\left[\frac{\sigma(\pi, x)}{\sigma_{\rm R}(\pi)}\right] = \frac{d\langle 0|T_0(E,x)|0\rangle}{dE} = \frac{dT_0(E)}{dE}. \tag{67}$$

This quantity is very sensitive to channel coupling effects. Thus, comparisons of theoretical and experimental barrier distributions lead to relevant information about the nuclear structure of the collision partners. Performing the same type of calculation on the genuine elastic cross section obtained from the amplitude $\langle 0|f(\theta, x)|0\rangle$, one gets

$$-\frac{d}{dE}\left[\frac{\sigma_{el}(\pi)}{\sigma_R(\pi)}\right] = -\frac{d\left(|\langle 0|S_l(E,x)|0\rangle|^2\right)}{dE} = \frac{dT_0^{(\rm R)}(E)}{dE}, \tag{68}$$

where $T_0^{(\rm R)}(E)$ is the genuine elastic $l = 0$ transmission coefficient. The difference between $T_0(E)$ and $T_0^{(\rm R)}(E)$ is that the former pertains to fusion whereas the latter to the total reaction cross section. It is thus fortunate that the fusion barrier distribution can be studied using the back angle quasi-elastic data, whose measurement is more easily attainable. Of course, in actual applications to data, the back-angle behavior of the quasi-elastic cross section is measured and its derivative with respect to energy is constructed giving the barrier distribution which, in principle, coincides with the distribution obtained from fusion measurements. This distribution has been used to learn about the collective channels that affect most the fusion cross section. More recently, the barrier distribution has been used to assess the importance of non-collective channels. We return to this issue in the following sections.

To show why Eq. (68) is in fact the barrier distribution, we recognize first that, in the case of a single barrier, the transmission coefficient $T_0(E)$ is, close to the barrier, given to a very good approximation by the Hill–Wheeler (HW) expression

$$T_0(E) = \frac{1}{1 + \exp\left[2\pi\left(E - V_{\rm B}\right)/\hbar\omega\right]}.$$

Here $\hbar\omega$ is directly related to the curvature of the inverted parabola form assumed for the barrier in the HW approximation. Accordingly, the derivative with respect to energy is

$$-\frac{dT_0(E)}{dE} = \frac{2\pi}{\hbar\omega}\,\frac{\exp[2\pi(E - V_{\rm B})/\hbar\omega]}{\left\{1 + \exp[2\pi(E - V_{\rm B})/\hbar\omega]\right\}^2}, \tag{69}$$

which peaks at $E = V_{\rm B}$ and has a width given precisely by the barrier curvature parameter $\hbar\omega$. Accordingly, the use of Eq. (68) would supply a complete determination of the fusion barrier. We should, however, emphasize that the HW approximation employed in $T_0(E)$ is valid only at energies in the vicinity of the barrier height, $V_{\rm B}$, and in general one has to assume a more general form of the $l = 0$ transmission coefficient. Further, coupled channels effects render the barrier multi-valued which results in a more diffuse barrier distribution with some structure.

In actual applications to data analysis, a full CC calculation is performed and the quasi-elastic cross section and its derivative with respect to energy are calculated. These are, in turn, compared to the corresponding experimental quantities. For more details we refer the reader to the original literature [79,80]. The measurement and analysis of the quasi-elastic

cross section at very back angles has been shown to be quite valuable in furnishing information about the fusion barrier distribution, which complements that obtained from the analysis of the fusion excitation function.

The barrier distribution extracted from the fusion excitation function is best discussed from the definition of the cross section [81–83],

$$\sigma_{\rm F}(E) = \frac{\pi}{k^2}\sum_{l=0}^{\infty}(2l+1)\,T_l(E). \tag{70}$$

The dependence of T_l on angular momentum is, within the HW approximation, of the form of a shifted energy, $E_l = E - \hbar^2\, l(l+1)/2\mu R_{\rm B}^2$, and thus $T_l(E) = T_0(E_l)$. We may replace the sum over l, by an integral over E_l, and write,

$$E\,\sigma_{\rm F}(E) = \pi R_{\rm B}^2\int_{-\infty}^{E} dE'\,T_0(E'). \tag{71}$$

Accordingly, $d(E\sigma_{\rm F}(E))/dE = \pi R_{\rm B}^2\,T_0(E)$, and thus,

$$D_{\rm F} = \frac{1}{\pi R_{\rm B}^2}\frac{d^2(E\,\sigma_{\rm F}(E))}{dE^2} = \frac{dT_0}{dE}. \tag{72}$$

Comparing Eq. (67) with Eq. (72), we reach the important equality,

$$D_{\rm F} = D_{\rm qel}. \tag{73}$$

This equality shows that one can obtain detailed information about coupling effects on the fusion process by the precise measurement of backward quasi-elastic scattering and the consequent derivation of the quasi-elastic barrier distribution. Since usually it is much simpler to measure backward quasi-elastic scattering than fusion and it is also much simpler to derive the barrier distribution from the first derivative of excitation function than from the second derivative, the equality of Eq. (73) is indeed very useful.

In Fig. 9 we show barrier distributions for tightly bound systems. We consider both quasi-elastic and fusion barrier distributions in collisions of ^{16}O with ^{92}Zr, ^{144}Sm, ^{154}Sm and ^{186}W targets. We see clearly that the equality Eq. (73) is nicely satisfied by the data. Application of the above analysis has been mostly made for the case of strongly bound nuclei. In recent years, this type of analysis has been extended to weakly bound nuclei as well. As we will show later in this section, the equality of Eq. (73) is not fully satisfied in this case.

The total reaction cross section extracted from the elastic scattering cross section is given by

$$\sigma_{\rm R}(E) = \frac{\pi}{k^2}\sum_{l=0}^{\infty}(2l+1)\,T_l^{\rm (R)}(E). \tag{74}$$

If transfer channels can be neglected, the reaction cross section corresponds to the sum of the fusion cross section and the cross sections for all inelastic channels integrated over angles. To see this, one analyzes the fusion transmission coefficient $T_0(E) = 1 - \langle 0||S_l(E,x)|^2|0\rangle$. Using a complete set of states representing the target, the transmission can be written as $T_{0l}(E) = T_l^{\rm (R)}(E) - \sum_{n\neq 0}|\langle n|S(E,x)|0\rangle|^2$. Accordingly,

$$\sigma_{\rm R}(E) = \sigma_{\rm F}(E) + \sigma_{\rm in}(E). \tag{75}$$

Since the inelastic transitions are peripheral, so that its contribution at back angles is not very important, one would expect that barrier distribution analysis can also be performed using the elastic cross section. In cases where some inelastic channels contribute at back angles, we expect the barrier distribution extracted from the elastic cross section to be a bit wider than the one obtained from the quasi-elastic or fusion cross sections.

3.3.1. *Barrier distributions for weakly bound systems*

In collisions of weakly bound nuclei there are different fusion processes. The first is the complete fusion (CF), which is analogous to the fusion of tightly bound nuclei. In this case, the whole projectile fuses with the target, forming a compound nucleus with $A_{\rm P} + A_{\rm T}$ nucleons. There are also other fusion processes following the projectile's breakup. One of them is the incomplete fusion (ICF), defined as the fusion of part of the projectile's mass with the target. In the simplest case, where the projectile dissociates into two fragments, one of the fragments fuses with the target whereas the other is scattered out of the interaction region. There is also the possibility that the two fragments are sequentially absorbed by the target. This is called sequential complete fusion (SCF). From the experimental point of view, this process cannot be distinguished from the direct CF, which is not preceded by breakup. Although some experiments determine the CF cross section, most experiments determine only the sum of all fusion processes, which is called total fusion (TF). A detailed discussion of this subject will be presented in Sections 5.2 and 6. There is also the possibility that the projectile breaks up and none of the fragments is captured by the target. This process is called non-capture breakup (NCBU).

When one is dealing with weakly bound systems, the equality between the backscattered quasi-elastic barrier distribution (QEBD) and the fusion barrier distribution (FBD) is no longer valid, as first pointed out by Zagrebaev [85].

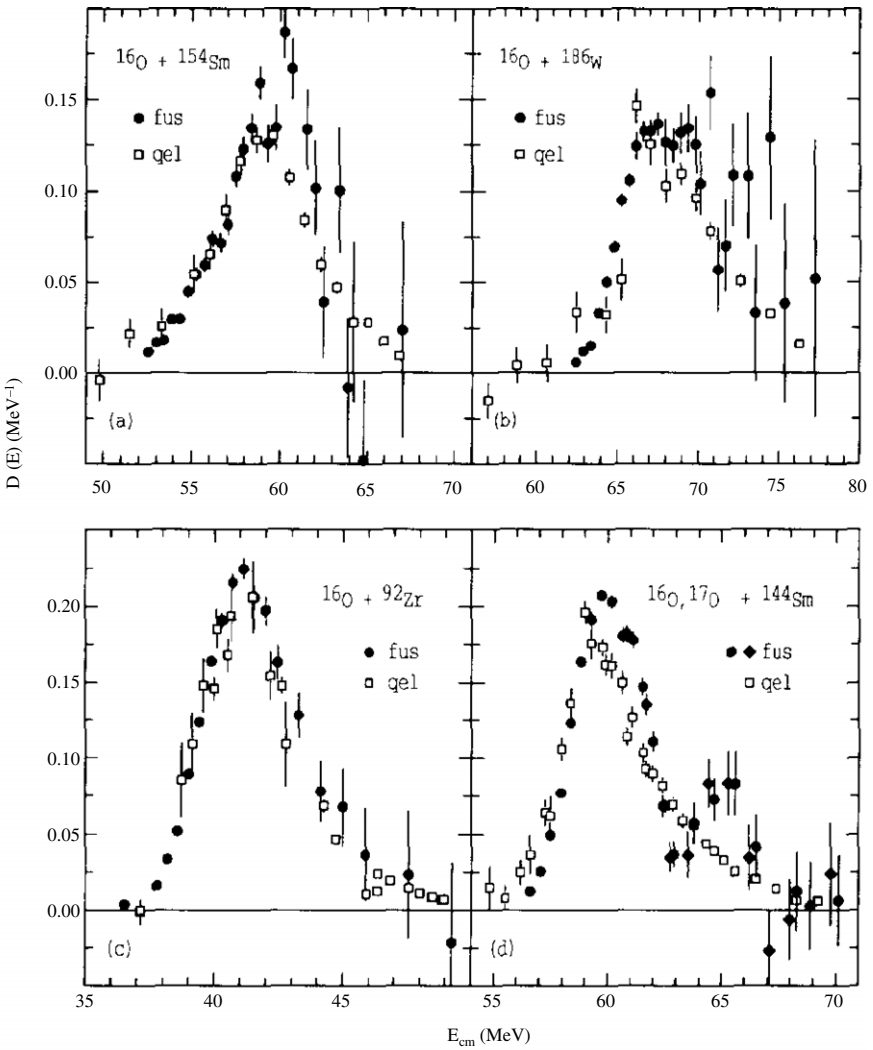

Fig. 9. Comparison between quasi-elastic and fusion barrier distributions for several tightly bound systems [84].

When very heavy nuclei are involved, the deep inelastic process may be an important reaction channel and when weakly bound nuclei are involved, breakup needs to be included. So, Zagrebaev interpreted that the quasi-elastic barrier distribution corresponds to the reaction threshold distribution, instead of the fusion barrier distribution. Furthermore, Lubian et al. [86] pointed out that different fusion data are associated with different barrier distributions. The use of CF or TF leads with different quasi-elastic barrier distributions. Owing to the breakup process, the incident wave is attenuated before it reaches the fusion barrier and thus the sum of the transmission and reflection coefficients is less than one. One may write

$$T + R = 1 - P_{\mathrm{BU}}, \tag{76}$$

where T and R are respectively the transmission and reflection coefficients and P_{BU} is the probability that the projectile breaks up.

The quasi-elastic barrier distribution associated with the CF fusion barrier distribution should then include all processes following breakup. On the other hand, if TF is the measured quantity, breakup also contributes to fusion. If the projectile dissociates into two fragments, the breakup probability can be split as

$$P_{\mathrm{BU}} = P_{\mathrm{ICF}_1} + P_{\mathrm{ICF}_2} + P_{\mathrm{SCF}} + P_{\mathrm{NCBU}}, \tag{77}$$

where ICF_1 and ICF_2 denote ICF of fragments 1 and 2, respectively. Therefore, the complementary cross section should include only the remaining one, *i.e.* σ_{NCBU}. The quasi-elastic barrier distribution associated with TF should then include NCBU but not ICF and SCF.

If one wants to compare the QEBD with the FBD, all relevant reaction channels which must be considered in the QE process should be measured, but this is not the usual case. Keeley [87] also showed that the neutron stripping transfer has

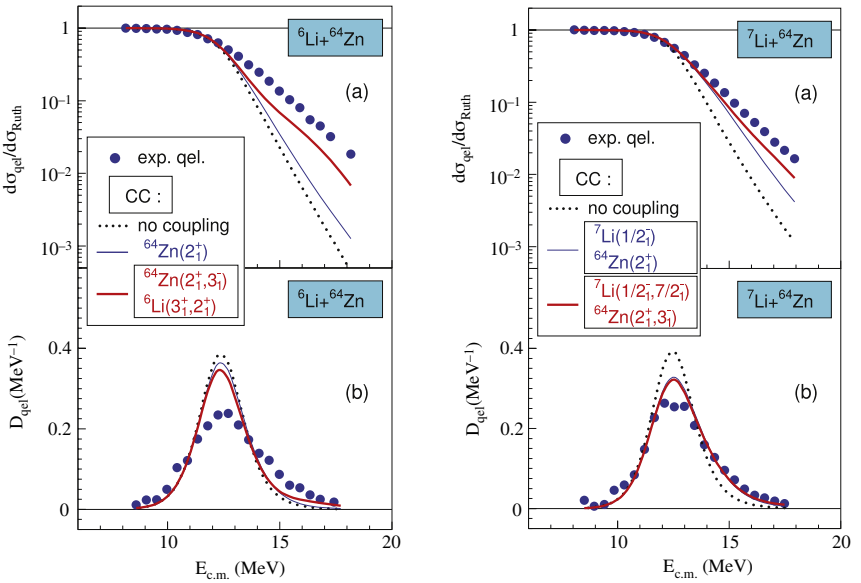

Fig. 10. (Color online) Left panel: quasi-elastic backscattering excitation function (top) and barrier distribution (bottom) for the ^{6}Li + ^{64}Zn system; Right panel: same as left panel but for the ^{7}Li + ^{64}Zn system.
Source: The results in both panels are from Ref. [93].

a very important effect on the calculated barrier distribution of neutron-rich radioactive nuclei such as ^{6}He and ^{8}He, what should make QEBD and FBD quite different for reactions involving those nuclei.

The first reported experiment on QEBD of weakly bound systems was made by Signorini et al. [88], in 1999, for the ^{9}Be + ^{209}Bi system. They found that the QEBD was much broader than the FBD for the same system. The first reported QEBD experiment involving the ^{6,7}Li isotopes was performed by Lin et al. [70]. More recently, new experiments with ^{6,7}Li projectiles were reported. They measured the QEBD in collisions with the ^{28}Si [89,90], ^{58}Ni [91], ^{64}Ni [92], ^{64}Zn [93], ^{116,120}Sn [91], ^{144}Sm [94,95], ^{197}Au [96], ^{208}Pb [91], ^{209}Bi [97] and ^{232}Th [98] targets.

Jia et al. [99] reported new measurements for the ^{9}Be + ^{208}Pb system. All these works compare the experimental QEBD with theoretical predictions of CC calculations that do, and others that do not take into account specific channels. By doing so, it was possible to verify the importance of different reaction couplings, such as inelastic excitations, breakup, or the first resonance of ^{6}Li, among others. It is remarkable how sensitive is the analysis of the effect of couplings on the QEBD at near barrier energies. Because of this feature, such analyses become a powerful tool for probing the optical potential at sub-barrier energies, where the usual angular distribution measurements are not too sensitive to the details of the nuclear potential.

We remind the reader that quasi-elastic barrier distributions are very sensitive to channel coupling effects, and supply an important tool to investigate nuclear properties. The effect of the breakup of ^{6}Li projectiles was found to be larger than that of ^{7}Li, in experiments using the same target. The discrepancies between CC calculations and the QEBD extracted from the data are attributed to important channels not included in the calculations, such as transfer and breakup triggered by transfer.

Lubian et al. [86] performed CDCC calculations for the ^{8}B + ^{58}Ni system and showed that the breakup coupling shifts the QEBD centroid to a higher energy. More recently, Palshetkar et al. [96] found the same effect for the ^{6,7}Li + ^{197}Au systems. Figs. 10 and 11 show some examples of QEBD analyses for weakly bound systems. Fig. 10 shows the quasi-elastic angular distributions (top) and QEBD analysis (bottom) for the ^{6}Li + ^{64}Zn (left panel) and ^{7}Li + ^{64}Zn (right panel) systems, reported by Zadro et al. [93]. The discrepancies between theoretical predictions and experimental data are attributed to the breakup, breakup following transfer and direct transfer channels not included in the coupling scheme. A detailed derivation of this equation can be found in appendix A of Ref. [100].

Fig. 11 illustrates the difference between quasi-elastic and complete fusion barrier distributions in collisions of weakly bound nuclei. Panel (a) shows the QEBD for the ^{6}Li + ^{144}Sm system, measured by Monteiro et al. [95]. Panel (b) shows the CFBD obtained by Rath et al. [101] for the same system. These distributions are clearly different. The difference can be seen more clearly in the work of Palshetkar et al. [96], where the QEBD and the CFBD are plotted together. The barrier distributions for the ^{6}Li + ^{197}Au system are shown on panel (c), together with the results of CCFULL calculations with (solid lines) and without (dotted lines) channel couplings. A similar plot for the ^{7}Li isotope is shown on panel (d). In this case, the CFBD is not available. Note that the QEBD is determined including (red open circles) and not including (green solid circles) α particles. One notices that the centroid of the QEBD is around 3 MeV lower than the one for CFBD. This is consistent with the conclusions of Ref. [86], for the ^{8}B + ^{58}Ni system. It is interesting to notice that when the measured alpha particles, most of them associated with the breakup of the projectile, are added to the quasi-elastic events, the QEBD shifts to higher

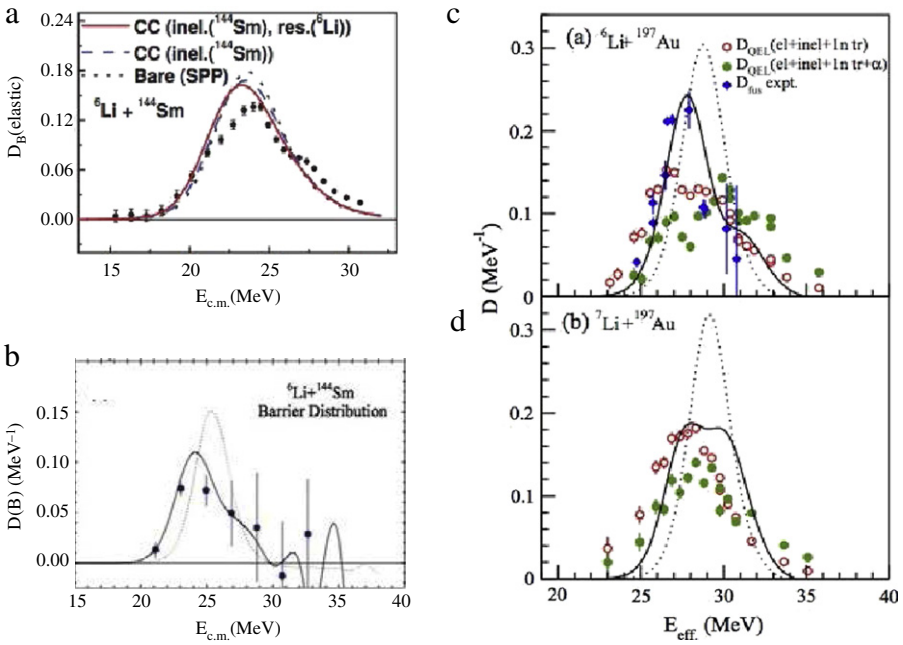

Fig. 11. (a) QEBD for the ^{6}Li + ^{144}Sm system [95]. The curves are results of different calculations; (b) Experimental CFBD for the ^{6}Li + ^{144}Sm system [101]. The dotted and the solid lines are respectively the results CCFULL calculations with and without channel couplings; (c) QE and CF barrier distributions for the ^{6}Li + ^{197}Au system. The green solid circles and the red open circles are the QEBD including and not including α particles and the blue solid circles with large error bar is the CFBD. The solid and the dotted lines are results of CCFULL calculations with and without channel couplings; (d) QE barrier distribution for the ^{7}Li + ^{197}Au system [96]. The notation is the same as in (c). (For interpretation of the references to color in this figure legend, the reader is referred to the web version of this article.)

energies, in agreement with our previous discussion. Jia et al. [99] investigated QEBD and CFBD for the ^{9}Be + ^{197}Au system, and observed that the QEBD centroid is shifted towards lower energies with respect to the CFBD, as it is also the case for Li projectiles. Comparing the CFBD obtained in calculations with (solid lines) and without (dotted lines) couplings, one concludes that the effects of channel coupling are very strong.

3.4. Threshold anomalies

Several recent papers have studied the energy dependence of the optical potential in the elastic scattering of weakly bound systems. In many cases of collisions involving weakly bound nuclei, the imaginary potential increases or remains constant as the bombarding energy decreases towards the Coulomb barrier, contrariwise to what happens with tightly bound systems, when the imaginary potential always decreases in that situation. Most of the data are on the scattering of the stable weakly bound projectiles, ^{6}Li, ^{7}Li and ^{9}Be, but there are also data for the radioactive neutron-halo ^{6}He, proton-halo ^{8}B and no-halo ^{7}Be nuclei. In the following, we summarize the main conclusions reached for each of these weakly bound projectiles. The analyses of the elastic scattering data performed in several of those papers employed different optical potentials, such as double folding or Woods–Saxon shapes, but the results were similar for all of the potentials considered.

For ^{6}Li projectiles, there are several experiments using a wide range of targets: ^{27}Al [102], ^{28}Si [103], ^{58}Ni [104], ^{59}Co [105], ^{64}Ni [104], ^{64}Zn [106], ^{80}Se [107], ^{90}Zr [108], ^{116}Sn [109], ^{138}Ba [110,111], ^{144}Sm [112], ^{208}Pb [113], ^{209}Bi [114] and ^{232}Th [115]. For all these systems it is observed the presence of the BTA, since the imaginary potential increases as the bombarding energy decreases towards the Coulomb barrier. Only when there are not data at energies sufficiently below the barrier, as for the ^{59}Co system [105], the increase of the imaginary potential cannot be observed. For a few systems it was possible to see a decrease of the imaginary potential, which is expected to vanish at very low energies. The extrapolation of the imaginary potential to energies below the measured data points suggests that it would vanish at $\sim$0.85 V_B, where all reaction channels are closed. However, in most cases, the data at the lowest energies are still in a region where the imaginary potential is increasing as the energy decreases. Thus, an extrapolation to the region where the imaginary potential goes to zero would be meaningless. Fig. 12 shows the energy dependence of the optical potential for ^{6}Li projectiles in collisions with the ^{80}Se (left panel) and ^{144}Sm targets. In these cases there are data at sufficiently low energies to show the increase of the imaginary potential followed by a decrease.

For the ^{7}Li projectile, the situation is not so clear because ^{7}Li has one excited bound state and a higher breakup threshold energy. Thus, there is a competition between the repulsive polarization potential due to the breakup and the attractive polarization potential due to the inelastic excitation. This point is discussed in detail in Section 4.4. The net result is that the imaginary potential remains almost constant with energy. This behavior is also a signature of the BTA, although not

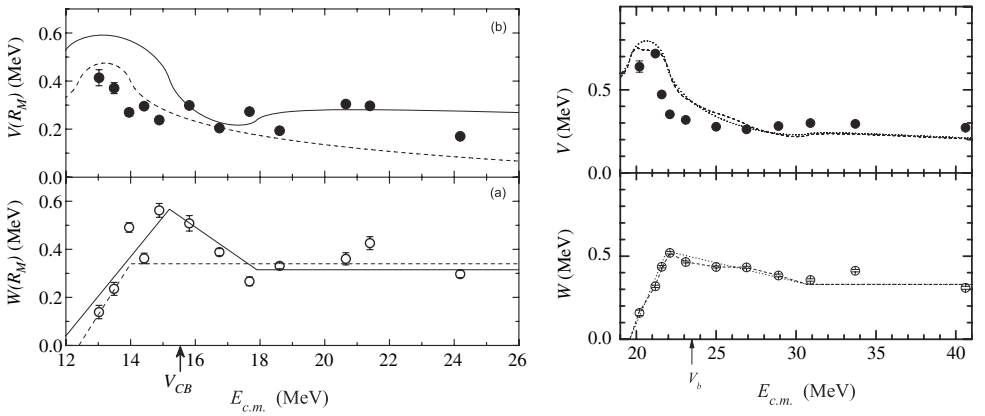

Fig. 12. Left panel: The strengths of the real (b) and imaginary (a) parts of the optical potential at the distance of maximal absorption, R_M, in collisions of ^{6}Li projectiles with the ^{80}Se target [107]; Right panel: the same as in the left panel but for a ^{144}Sm target [112].
Source: For detail, see the original papers [107,112].

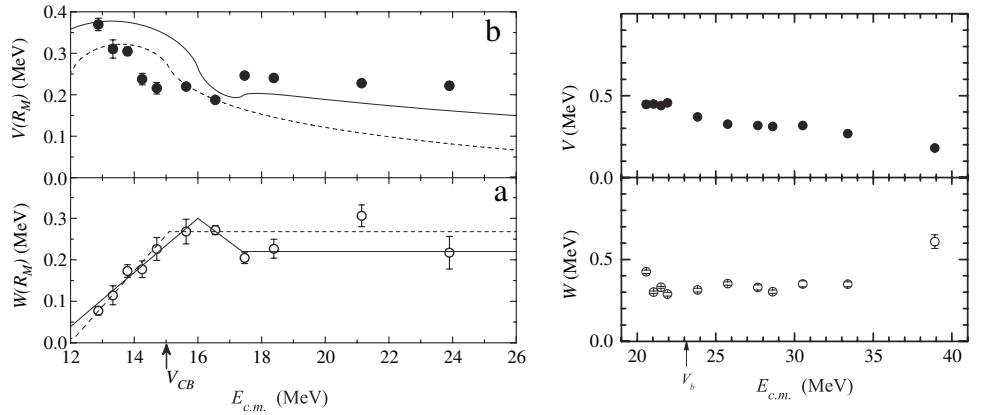

Fig. 13. Left panel: Analogous to the previous figure but now the projectile is ^{7}Li. The targets are ^{80}Se (left panel) and ^{144}Sm (right panel). For details, see Refs. [107,112].

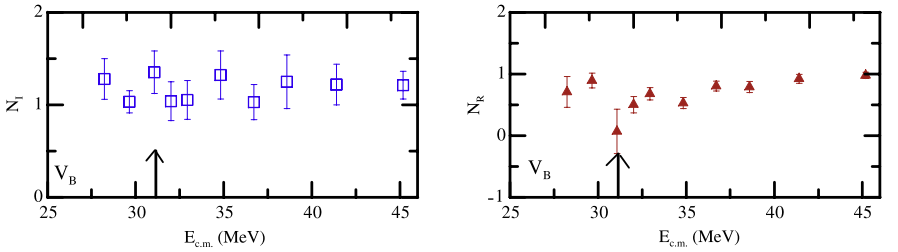

Fig. 14. (Color online) Energy dependence of the imaginary (left panel) and real (right panel) parts of the optical potential for the ^{9}Be + ^{144}Sm system [120]. The arrows indicate the Coulomb barrier.

so clear as when the imaginary potential increases when the energy decreases. There are also several works on the elastic scattering of ^{7}Li with different targets, with the aim of investigating the energy dependence of the optical potential at near barrier energies: ^{27}Al [116], ^{28}Si [103], ^{59}Co [105], ^{80}Se [107], ^{116}Sn [117], ^{138}Ba [110,118], ^{144}Sm [112], ^{208}Pb [113,119] and ^{232}Th [115]. In Fig. 13 we illustrate the energy dependence of the real and imaginary parts of the optical potential, in collisions of ^{7}Li with the same targets as in the previous figure.

For ^{9}Be the situation is even less clear than for ^{7}Li, since in some cases the real and imaginary potentials which fit the elastic scattering data do not obey the dispersion relation [121,122,60]. For this projectile there are not too many systems investigated: ^{12}C [121], ^{27}Al [123], ^{89}Y [124], ^{144}Sm [120], ^{208}Pb [122,60], ^{209}Bi [122]. The situation is illustrated in Fig. 14. In this case the real and imaginary parts of the optical potential are given by the double-folding São Paulo potential [125,126], multiplied respectively by the renormalization factors N_R and N_I. Fig. 14 shows the energy dependence of these factors.

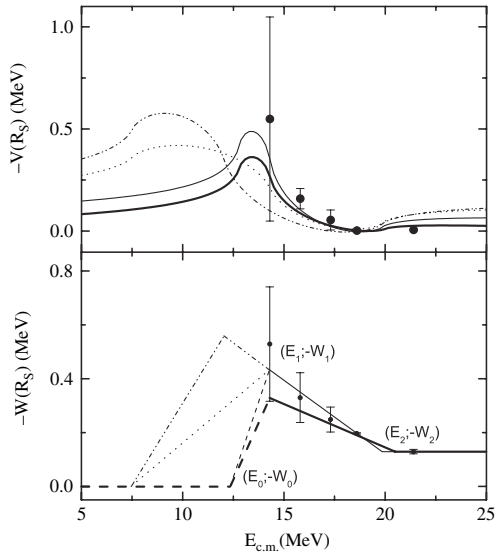

Fig. 15. Energy dependence of the real (upper panel) and imaginary (lower panel) parts of the optical potential for the ^{6}He + ^{209}Bi system evaluated at the sensitivity radius [127] (see text for details).
Source: The data are from Ref. [129].

For radioactive projectiles, there are few investigations. An increase of the imaginary potential was found for the ^{6}He + ^{209}Bi [127,119] and for the ^{6}He + ^{208}Pb [49,128] systems. The studies of Refs. [127] and [128] were based on the data of Refs. [129] and [49], respectively. This behavior can be observed in Fig. 15, which shows the energy dependence of the real (upper panel) and imaginary (lower panel) parts of the optical potential for the ^{6}He + ^{209}Bi system, calculated at the sensitivity radius [127]. For ^{7}Be on ^{58}Ni [130], with data from [57], the same behavior as for ^{6}Li was observed. This was to be expected because ^{7}Be and ^{6}Li have similar breakup thresholds. For ^{8}B on ^{58}Ni [130], with data from [57], the imaginary potential is almost energy independent.

Another approach to investigate the role of breakup on the energy dependence of the optical potential is the simultaneous fit of elastic scattering angular distributions and fusion excitation functions. This approach consists in dividing the optical potential into two parts. A short range potential $V_F + i\,W_F$ is responsible for fusion, and a superficial potential $V_{DR} + i\,W_{DR}$ for direct reactions. Gómez-Camacho et al. [120,131–138] and So et al. [139–145] have used this approach to investigate several weakly bound systems (^{6,7}Li + ^{28}Si, ^{8}B + ^{58}Ni, ^{9}Be + ^{27}Al, ^{28}Si, ^{64}Zn, ^{144}Sm, ^{208,209}Pb). They found, for all systems studied, that the fusion imaginary potential W_F presents the usual TA, whereas the direct reaction imaginary potential W_{DR} shows a BTA behavior. Both potentials satisfy the dispersion relation. In Fig. 16 we show some results for the ^{8}B + ^{58}Ni and ^{9}Be + ^{144}Sm systems.

3.5. The reaction cross section extracted from elastic scattering

Elastic scattering data can be used to extract information about other channels. The classical example is the total reaction cross section, σ_R, which is the main subject in this sub-section. Since this cross section is defined as the sum of the cross sections for all non-elastic channels, it is associated with the total flux diverted from the elastic channel. Therefore, the reaction cross section is equal to the absorption cross section in a single-channel optical model analysis. In this way, one can determine the optical potential fitting elastic scattering data at several angles, and with this potential evaluate the nuclear S-matrix elements, $S_{N,l}$. The reaction cross section can then be evaluated through Eqs. (5) and (6). This indirect determination of the reaction cross section has been used for decades and it is still a very important tool to investigate reaction mechanisms in collisions of different nuclei, tightly or weakly bound. From the experimental point of view, this method is much simpler than the alternative procedure of measuring the cross section for each relevant non-elastic process and summing them. This task is particularly hard for weakly bound systems. Thus, it has been accomplished in very few situations. The main examples are the experiments on collisions of ^{6}He projectiles on ^{209}Bi, performed in Notre Dame [129,146–148], and collisions of the same projectile on ^{65}Cu and on ^{197}Au targets [51,149] and on ^{9}Be [150].

The reaction cross section is given by the sum

$$\sigma_R = \sigma_F + \sigma_D, \tag{78}$$

where σ_F is the fusion cross section and σ_D is the cross section for all direct reactions. In some situations, like collisions of ^{6}He at sub-barrier energies, σ_D is responsible for most of the reaction cross section. In other situations, like most heavy-ion collisions at above-barrier energies, σ_F is the dominant contribution to σ_R. When one determines σ_R from elastic scattering data and measures one of these contributions, that is σ_F or σ_D, the remaining one can be determined taking the difference

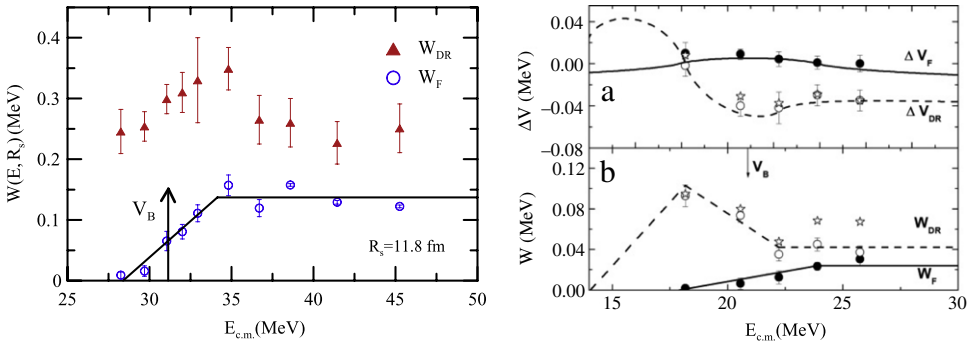

Fig. 16. (Color online) Left panel: Volume (open circles) and surface (full triangles) parts of the polarization potential for the ^{9}Be + ^{144}Sm system, evaluated at the strong absorption radius. Right panel: Energy dependence of the real (top) and imaginary (bottom) parts of the polarization potential for the ^{8}B + ^{58}Ni system. The volumetric (solid lines) and surface (dashed lines) parts of the polarization potential are plotted separately.
Source: Left panel: The figure was taken from Ref. [120]. Right panel: The figure was taken from Ref. [131].

in Eq. (78). This procedure has been used by several authors. Examples where fusion cross sections were estimated through difference between σ_R (determined from elastic or quasi-elastic data) and the cross sections for transfer or alpha yields can be found in Refs. [151–156]. On the other hand, Eq. (78) has been used to determine the cross section for the transfer + breakup processes. In this case the reaction cross section has been determined from scattering data and the fusion and inelastic cross sections have been measured directly. Then, σ_D was determined from σ_R and σ_F through Eq. (78), and the cross section for transfer+breakup is determined subtracting the inelastic cross section from σ_D. This procedure has been used, for example, in Refs. [120,74,72,157].

An important issue in studies of reaction cross sections for weakly bound systems is whether one can identify a signature of the low breakup threshold in the data. The same question was raised about the fusion cross sections and a detailed discussion about this topic, in the case of fusion, is presented in Section 6.4. Here we discuss this issue in the case of reaction cross sections. Direct comparisons of reaction cross sections for different systems do not lead to reliable conclusions about the role of the low breakup threshold. The reason is that there are trivial differences, like the charges and masses of the system, that make the cross sections very different, regardless of the system's binding energy. It is then necessary to compare reduced data, instead of comparing the reaction cross sections directly. However, the reduction procedure is not unique. Presently, there are two reduction methods widely used in literature. The first was proposed by Gomes et al. [158], in 2005, and the second by Shorto et al. [159], in 2009. The latter transforms the reaction cross section into a *reaction function*. This is an extension of the 'fusion function' method proposed by Canto et al. [160,161], to reduce fusion cross sections (see Section 6.4). In the following we will briefly discuss comparisons of reaction cross sections reduced according to these two prescriptions, pointing out that they may lead to different conclusions. Gomes' method was used to compare total reaction cross sections of tens of systems [44,158,162–166]. Starting in 2009, Shorto's method was used in Refs. [159,167–171]. One also finds works where both methods were used [46,172,173]. Yang et al. [170] carried out a comprehensive investigation by analyzing a large number of systems with Shorto's method. In the remaining part of this sub-section we show some reduced reaction cross sections for halo nuclei, for non-halo weakly bound and for tightly bound nuclei, using both reduction methods.

We start with the Gomes' method. The left panel of Fig. 17 shows reduced reaction cross sections for several projectiles on the same ^{27}Al target [159]. The results for all weakly bound projectiles are similar, being much larger than the ones for the tightly bound ^{16}O projectile. The right panel of Fig. 17 shows a similar plot, but including targets with different mass. The cross sections for the heavier and tightly bound ^{16}O projectiles are still smaller than those for the weakly bound ones. However, one observes that the cross sections for halo projectiles are systematically larger than those for non-halo ones. The same trend is observed on the left panel of Fig. 18, where the reduced reaction cross section for ^{6}He + ^{120}Sn is compared with cross sections for other similar systems. The data can be grouped into 3 curves. A curve with higher cross sections for the halo systems, an intermediate curve for stable weakly bound systems and one for tightly bound systems, which have the lowest cross sections. Another comparative study of reduced total reaction cross sections following the method of Ref. [158] is presented on the right panel of Fig. 18. It shows results for the tightly bound ^{4}He and for the neutron-halo ^{6}He projectiles in collisions with targets in different mass ranges. One sees that results for the two projectiles show very different trends, following two different curves. The results for the tightly bound ^{4}He projectile are systematically lower than those for ^{6}He.

Now we discuss applications of the reduction method proposed by Shorto et al. [159]. As it will be clear below, the conclusions may be very different. The left panel of Fig. 19 shows reduced cross sections for the same systems on the left part of Fig. 17, but using the procedure of Ref. [159]. Now the results for the tightly bound ^{16}O lies roughly on the same curve as those for the weakly bound projectiles. The curve is the benchmark UFF, to be introduced in Section 6.4. The central panel of Fig. 17 shows reduced reaction cross sections for medium mass targets. Now the results for ^{16}O are not smaller than the ones for weakly bound projectiles (in fact they are even a bit larger). The right panel of the same figure shows reaction

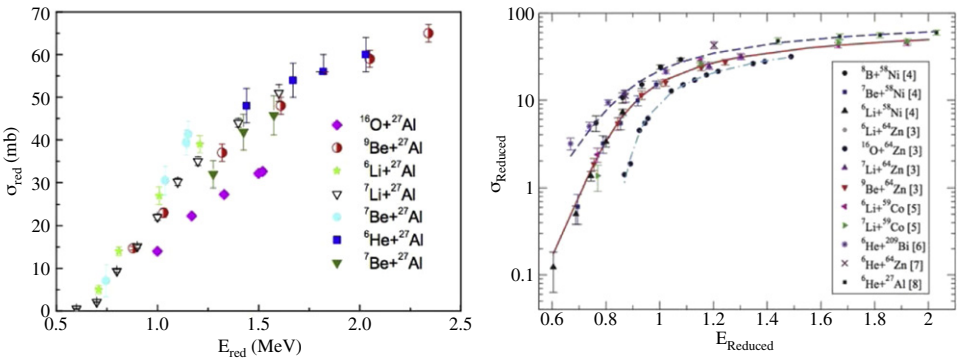

Fig. 17. (Color online) Left panel: Reduced reaction cross sections for several projectiles on ^{27}Al. The reduction is performed according to the method of Gomes et al. [158]. Right panel: Reduced reaction cross sections for different tightly and weakly bound projectiles on targets in different mass ranges. The reduction is made according to the procedure of Ref. [158].
Source: Left panel: The figure is from Ref. [173]. Right panel: The figure is taken from the work of Kolata and Aguilera [162].

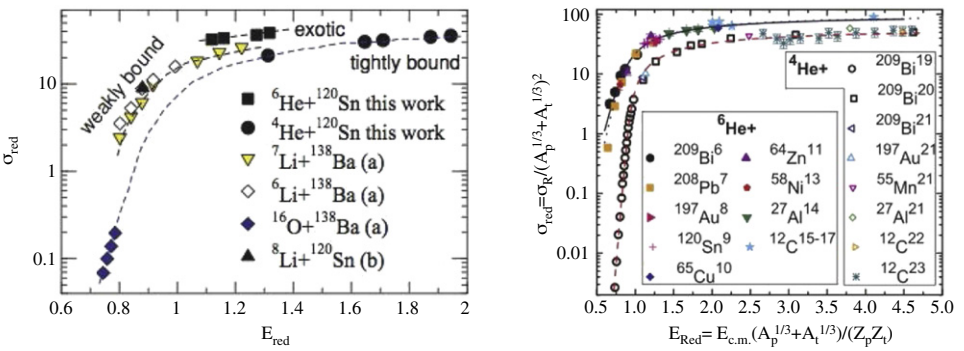

Fig. 18. (Color online) More data reduced by the method of Ref. [158]. Left panel: reduced cross section for the ^{6}He + ^{120}Sn system, compared with cross sections for other similar systems [46]; Right panel: Reduced reaction cross sections for ^{4}He and ^{6}He projectiles on several targets in different mass ranges [166].

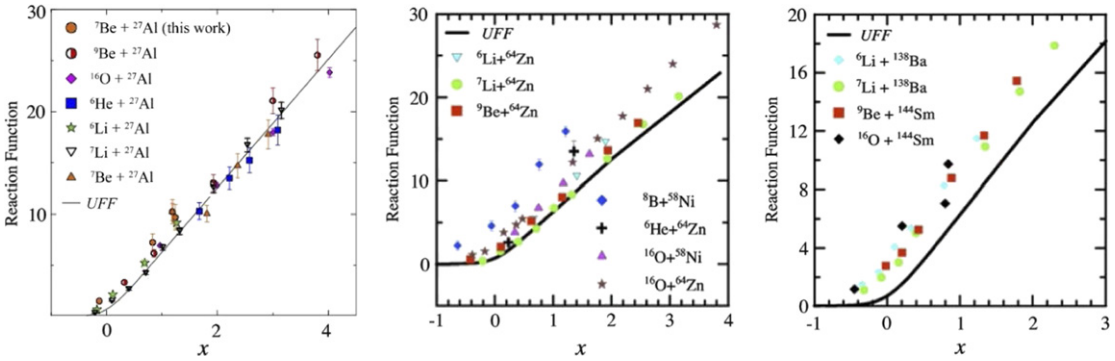

Fig. 19. (Color online) Reaction cross sections reduced by the method of Ref. [159]. Left panel: reaction functions for weakly bound projectiles on ^{27}Al [173]. For comparison, results for the ^{16}O projectile and the Universal Fusion function (UFF) of Section 6.4 are also shown; Central panel: A similar plot for the medium-light ^{58}Ni and ^{64}Zn targets. Right panel: A similar plot but for heavier targets [159].
Source: The figure is from Ref. [159].

functions for heavier targets. Again, the results for the tightly bound ^{16}O projectile follow the same trend as the stable weakly bound projectiles. In this case, all reaction functions are above the UFF. This expresses the fact that the reaction cross section is larger than the fusion cross section, owing to the contribution from direct reaction channels.

The above discussion suggests that finding a satisfactory procedure to reduce total reaction cross sections is a hard task. It is much harder than in the case of fusion, which is basically a tunneling phenomenon. The reaction cross section is more complicated because it has also a substantial contribution from direct reactions which have a very different nature. As a consequence, different choices of the reduction procedure may lead to conflicting conclusions about the trends of the reduced data for weakly bound or tightly bound systems. This has recently been pointed out in a paper by Morcelle

et al. [173]. When one is dealing with fusion reactions, the fusion cross section reduced by the fusion function method [160,161] and renormalized as to eliminate the influence of bound channels allows a clear-cut separation of above-barrier results for weakly bound and tightly bound systems (see Section 6.4). This works because, to a first approximation σ_F is given by tunneling through a parabolic barrier, as assumed in Wong's formula [174]. The method of Canto et al. [160,161] does not work very well for the reaction cross section due to the surface absorption associated with direct reactions. For the time being, neither of the two reduction methods discussed above is fully satisfactory, as recently demonstrated [175]. This is an interesting and complex issue that requires further investigation.

4. Breakup reactions

One of the most important features of the scattering of weakly bound nuclei is the coupling of the elastic channel to the breakup of one of both collision partners. One reason for the interest in this channel is that coupling to breakup may produce strong effects on fusion and elastic scattering.

The study of the breakup process has been an ongoing research for several decades. The simplest description was provided by Serber [176], back in 1947, who postulated that at high energies the inclusive breakup cross section is given by the product of a kinematical factor and the modulus square of the Fourier transform of the ground state wave function of the fragmenting nucleus. The application of this model to deuteron breakup has shown the adequacy of the physics behind the model. No distortion of the fragments was included in this description. Further work on breakup relying on the Distorted Wave Born Approximation (DWBA) and on three-body descriptions of the process was performed by Hussein and McVoy [177]. In the case of collisions involving heavy ions, the Coulomb interaction becomes important. Baur and Bertulani [178] developed a comprehensive theory of Coulomb excitation, including the continuum states (breakup). In their approach they relied on the theory of Winther and Alder [179]. In this section we give a short account of the breakup reaction theory and discuss the main experiments performed recently.

4.1. Quantum theory of elastic and inclusive non-elastic breakup

We follow the developments of Austern et al. [12] and Hussein and McVoy [177]. These authors use a three-body model to derive the cross section which is found to be composed of elastic breakup and inclusive non-elastic breakup. This latter was also derived in Ref. [177] within the DWBA. We treat the problem within the spectator model. Here the observed fragment is taken as a spectator with only optical distortion in the field of the target. Let us call the two fragments of the projectile F_1 and F_2, and consider F_1 as the spectator. The target is represented by A and K_1 and K_2 are the kinetic energy operators of the two fragments. The exact Hamiltonian of the system then is,

$$H = H_A + K_1 + K_2 + U_1 + V_{F_2A} + V_{12}, \tag{79}$$

where H_A is the full Hamiltonian of the target, treated as a many-body system, U_1 is the optical potential of fragment 1, V_{F_2A} is the interaction between F_2 and the target and V_{12} is the interaction between the two fragments. The exact amplitude is then given by,

$$T = \left\langle \chi_1^{(-)}(\mathbf{k}_1, \mathbf{r}_1)\, \Phi^{\alpha}_{F_2A} \right| V_{12} \left| \Xi^{(+)}(\mathbf{r}_1, \mathbf{r}_2, A) \right\rangle, \tag{80}$$

where $\mathbf{r}_1$ and $\mathbf{r}_2$ are respectively the position vectors of fragments 1 (the spectator) and 2, and $\left|\Xi^{(+)}(\mathbf{r}_1, \mathbf{r}_2, A)\right\rangle$ is the exact scattering wave function, describing the collision of the incident projectile, treated as a bound two-cluster nucleus, with the target A. Above, the wave function $\left|\chi^{(+)}(\mathbf{k}_1, \mathbf{r}_1)\right\rangle$ is the distorted wave of fragment F_1 and, finally, $\Phi^{\alpha}_{F_2A}$ is the exact wave function describing the dynamics of the participant fragment F_2 and the target nucleus. The spectrum of this subsystem (including bound and continuum states) is labeled by α.

The cross section for observing fragment F_1 is then given by,

$$\frac{d^2\sigma_{F_1}}{dE_1\, d\Omega_1} = \frac{2\pi}{\hbar v_P}\, \rho(E_1) \sum_{\alpha} \left| \left\langle \chi_1^{(-)}(\mathbf{k}_1, \mathbf{r}_1)\, \Phi^{\alpha}_{F_2A} \right| V_{12} \left| \Xi^{(+)}(\mathbf{r}_1, \mathbf{r}_2, A) \right\rangle \right|^2 \delta(E - E_1 - E_\alpha), \tag{81}$$

where v_P is the projectile's velocity. The density of states, given by Ref. [177], is $\rho(E_1) = Mk_1/(2\pi)^3\,\hbar^2$.

Next, one writes the exact wave function in the form of a product, $\left|\Xi^{(+)}(\mathbf{r}_1, \mathbf{r}_2, A)\right\rangle = \left|\Psi^{(+)}(\mathbf{r}_1, \mathbf{r}_2)\right\rangle |\Phi_A\rangle$, where $\left|\Psi^{(+)}(\mathbf{r}_1, \mathbf{r}_2)\right\rangle$ is the exact three-body scattering wave function of the three nuclei, F_1, F_2 and A. Using the usual procedure of replacing the delta function by the imaginary part of a Green's function which contains the energy of the $F_2 + A$ system, allowing thus the use of closure involving $\Phi^{\alpha}_{F_2A}$, and going through some algebra [177], the inclusive breakup cross section is found to be composed of two distinct terms, the elastic breakup, EB, and the inclusive non-elastic breakup, INEB. In the former, the target remains in its ground state, whereas in the latter it does not. That is, the target is excited or it captures F_2. Thus, we can write,

$$\frac{d^2\sigma_{F_1}}{dE_1\, d\Omega_1} = \frac{d^2\sigma^{EB}_{F_1}}{dE_1\, d\Omega_1} + \frac{d^2\sigma^{INEB}_{F_1}}{dE_1\, d\Omega_1}. \tag{82}$$

The first term corresponds to the situation where the projectile breaks up and the two fragments scape from the interaction region, leaving the target in its initial intrinsic state. It is given by,

$$\frac{d^2\sigma_{\mathrm{F}_1}^{\mathrm{EB}}}{dE_1\,d\Omega_1} = \frac{2\pi\,\rho(E_1)}{\hbar v_{\mathrm{P}}} \sum_{\mathbf{k}_2} \left| \left\langle \chi_2^{(-)}(\mathbf{k}_2,\mathbf{r}_2)\,\chi_1^{(-)}(\mathbf{k}_1,\mathbf{r}_1) \mid V_{12} \mid \Psi^{(+)}(\mathbf{r}_1,\mathbf{r}_2) \right\rangle \right|^2 \delta(E-E_1-E_2), \tag{83}$$

where $\left|\Psi^{(+)}(\mathbf{r}_1,\mathbf{r}_2)\right\rangle$ is the exact scattering state. The second term can be obtained with some further manipulations, as made in Ref. [12], and the result is,

$$\frac{d^2\sigma_{\mathrm{F}_1}^{\mathrm{INEB}}}{dE_1\,d\Omega_1} = \frac{2\rho(E_1)}{\hbar v_{\mathrm{P}}} \left\langle \hat{\rho}^{(+)}(\mathbf{r}_2) \middle| W_2 \middle| \hat{\rho}^{(+)}(\mathbf{r}_2) \right\rangle. \tag{84}$$

Above, $\hat{\rho}^{(+)}(\mathbf{r}_2)$ is the source wave function: $\hat{\rho}^{(+)}(\mathbf{r}_2) = -\left\langle \chi_1^{(-)}(\mathbf{r}_1) \middle| \Psi^{(+)}(\mathbf{r}_1,\mathbf{r}_2) \right\rangle$, where W_2 is the imaginary part of the potential V_{F_2A}. Thus, simplifying the notation,

$$\sigma_{\mathrm{INEB}} = \frac{2\rho(E_1)}{\hbar v_{\mathrm{P}}} \left\langle \hat{\rho}^{(+)} \middle|\, W_2 \,\middle| \hat{\rho}^{(+)} \right\rangle. \tag{85}$$

The imaginary potential of fragment F_2 is further decomposed into a direct part, W_2^{D}, and a fusion part, W_2^{F}. Accordingly, the total inclusive non-elastic breakup cross section, can be written as a sum of two terms. The first, associated with W_2^{D} absorption, corresponds to Inclusive Direct Non-Elastic Breakup (IDNEB). In this process, the target is excited, while fragments F1 and F2 emerge from the interaction region. The second is associated with the absorption of the fragment F_2 by W_2^{F}. Therefore it corresponds to incomplete fusion of F_2 (ICF_2). Thus, we can write

$$\sigma_{\mathrm{INEB}} = \sigma_{\mathrm{IDNEB}} + \sigma_{\mathrm{ICF}_2}, \tag{86}$$

where,

$$\sigma_{\mathrm{IDNEB}} = \frac{2\rho(E_1)}{\hbar v_{\mathrm{P}}} \left\langle \hat{\rho}^{(+)} \middle|\, W_2^{\mathrm{D}} \middle| \hat{\rho}^{(+)} \right\rangle \tag{87}$$

and

$$\sigma_{\mathrm{ICF}_2} = \frac{2\rho(E_1)}{\hbar v_{\mathrm{P}}} \left\langle \hat{\rho}^{(+)} \middle|\, W_2^{\mathrm{F}} \middle| \hat{\rho}^{(+)} \right\rangle. \tag{88}$$

Most theoretical studies of fusion of weakly bound systems can only determine the TF cross section (see Section 3.3.1). So far, only classical [180–182,100,183] and semiclassical [184] theories give CF and ICF cross sections individually. This can also be achieved in full quantum mechanical calculations, using the CDCC method, in the particular case where one of the fragments is much heavier than the others [10]. A detailed discussion of this subject is presented in Section 5.2. The spectator model, described in the beginning of the present section, can be used to make predictions of the ICF cross section. However, it cannot be used for CF, where the weakly bound nucleus is treated as a single particle, instead of two fragments. Therefore, there can be no spectator fragment.

It has been customary to define the No-Capture Breakup as the sum of Elastic Breakup (EB) plus Direct Inclusive Non-Elastic Breakup (DINEB), $\sigma_{\mathrm{NCBU}} = \sigma_{\mathrm{EB}} + \sigma_{\mathrm{DINEB}}$, which for all practical purposes is the measured one. Accordingly we can finally write,

$$\sigma_{\mathrm{BU}} = \sigma_{\mathrm{NCBU}} + \sigma_{\mathrm{ICF}}. \tag{89}$$

The source function $\hat{\rho}^{(+)}(\mathbf{r}_2)$ is an overlap of the distorted wave of the outgoing fragment (the spectator) with the exact three-body wave function of the system. In Ref. [177] a DWBA approximation is employed for the latter wave function, $\left|\Psi^{(+)}(\mathbf{r}_1,\mathbf{r}_2)\right\rangle = \left|\chi_1^{(+)}(\mathbf{r}_1)\,\chi_2^{(+)}(\mathbf{r}_2)\right\rangle$. The resulting DINEB cross section is then amenable to a DWBA calculation. The above formalism was used to calculate the spectra of outgoing fragments at intermediate energies. The structure of Eq. (85), is easy to understand. The source wave function represents the negative energy wave function of fragment F_2 as it is carried by the projectile. The matrix element $\left\langle \hat{\rho}^{(+)} | W_2^{\mathrm{F}} | \hat{\rho}^{(+)} \right\rangle$ is then the "fusion cross section" of this fragment. As such, the cross section represents the process where F_2 is captured by the target, while the EB cross section, Eq. (83), represents the breakup process where both F_1 and F_2 scatter elastically. In the formalism above there is no feedback from the breakup channel on the elastic one.

4.2. Elastic breakup—classical and semiclassical treatments

One of the first fully classical treatments of breakup was that of Hagino, Dasgupta and Hinde [181]. In this work the system is assumed to be composed of three bodies: the two-cluster projectile, and the target. The classical equations of motion for the three bodies interacting with suitably chosen potentials are solved, with appropriate initial conditions and some restrictions. One of these restrictions is that the collision takes place in a plane, which helps reduce the number of degrees of freedom that need to be considered. The other initial conditions are the distance r_0 between the CM of the two clusters that compose the projectile, and the orientation θ of the line that joins those Centers of Mass with respect to the direction of the initial asymptotic velocity of the projectile. The initial velocities of these two clusters with respect to the CM of the projectile are restricted to be along this line and with values that are related, by energy conservation, to the breakup Q-value and the interaction potential between the two clusters. The internal orbital angular momentum of the motion of the two clusters around the projectile CM was therefore not considered. Furthermore, no attempt was made to account for Quantum effects, in particular barrier penetration and the zero-point motion in the description of the initial state of the two-cluster projectile.

For each impact parameter b, the calculation of the breakup probability requires to perform a Monte Carlo average over the values of the parameters r_0 and θ. In fact, the calculation yields not only this elastic breakup probably, but, with more emphasis, the contributions to the different fusion processes. For this reason more details on these calculations are given in Section 5.2.1.

Many of the assumptions and restrictions of this work were eliminated in the also fully classical description of the breakup process of Diaz-Torres and colaborators [182,100]. Namely, the calculation is fully three-dimensional, the clusters in the projectile have an initial zero-point motion, and also orbital angular momentum, so their initial velocity is not restricted to the line that joins them. Their computer code is available in Ref. [183]. The calculation has all the ingredients to calculate the breakup probability directly from the trajectories of the projectile clusters, as in Ref. [181], and it would be interesting to see its predictions. However the breakup probability along the trajectory is an input to the calculation. Therefore this is not a stand-alone calculation of the breakup process. The main purpose of model is to study the different fusion process in collisions of weakly bound nuclei. Thus, we postpone a detailed discussion of this model to Section 5.2.1.

The reason for this approach is that, while CDCC calculations were shown to give an accurate description of breakup, they have intrinsic limitations in their ability to properly account for the complete fusion process. Essentially, anticipating what will be discussed in Section 5.2.2, this is because CDCC calculations cannot disentangle the incomplete fusion process from the contribution to the complete fusion process that arise from the sequential fusion of all of the breakup fragments. Clearly the classical calculations described above do not suffer from this deficiency, as it is clearly pointed out in Refs. [181,182,100].

An alternative procedure is to consider a semiclassical description of the collision, in which the orbital relative motion of projectile and target is treated classically, while internal degrees of freedom of the fragmenting projectile are described in quantum mechanical terms. This method was proposed in Ref. [185] and extended in Ref. [186], and briefly reviewed below.

The projectile is described in the two-cluster model as being composed of two fragments, F_1, F_2. The scattering process is described in terms of the vector joining the centers of the projectile and the target, $\mathbf{R}$, and the intrinsic vector, $\mathbf{r}$, joining the centers of F_1 and F_2. The initial ground state of the projectile is coupled to its excited bound states, if any, and to the continuum of $F_1 + F_2$. For a given impact parameter b the projectile–target relative motion is given by a classical trajectory $\mathbf{R}(t)$, and the intrinsic dynamics is treated as a time-dependent quantum mechanics problem.

For the semiclassical calculation, the interaction is split into an 'optical potential', V_0, and a coupling interaction, $U(\mathbf{R}, \mathbf{r})$, which leads to breakup.

The time-dependent wave function describing the $F_1 - F_2$ relative motion in the projectile-frame is expanded as

$$\Psi(b,t) = \sum_i c_i(b,t)\,\psi_i\,e^{-i\varepsilon_i t/\hbar} + \Psi_C(b,t), \tag{90}$$

where the ψ_i represent the bound states and $\Psi_C(b,t)$ are the components of $\Psi(b,t)$ in the continuum,

$$\Psi_C(b,t) = \sum_{l_\alpha J_\alpha J_\alpha M_\alpha} \int d\varepsilon_\alpha\; c_\alpha(b,t)\,e^{-i\varepsilon_\alpha t/\hbar}\;\Psi_\alpha. \tag{91}$$

The amplitudes $c_i(b,t)$ and $c_\alpha(b,t)$ are functions of time. Their time evolution is obtained from the time-dependent Schrödinger equation,

$$i\hbar\,\frac{\partial\Psi(t)}{\partial t} = [h + U(t,\mathbf{r})]\,\Psi(t), \tag{92}$$

with the Hamiltonian $h + U(t,\mathbf{r})$, where h is the Hamiltonian operator associated with the $F_1 - F_2$ relative motion, and $U(t,\mathbf{r}) \equiv U(\mathbf{R}(t),\mathbf{r})$. This leads to a set of semiclassical coupled-channel equations for the amplitudes $c_i(b,t)$ and $c_\alpha(b,t)$, from which the final values of the amplitudes are determined. These final values determine the observables in a

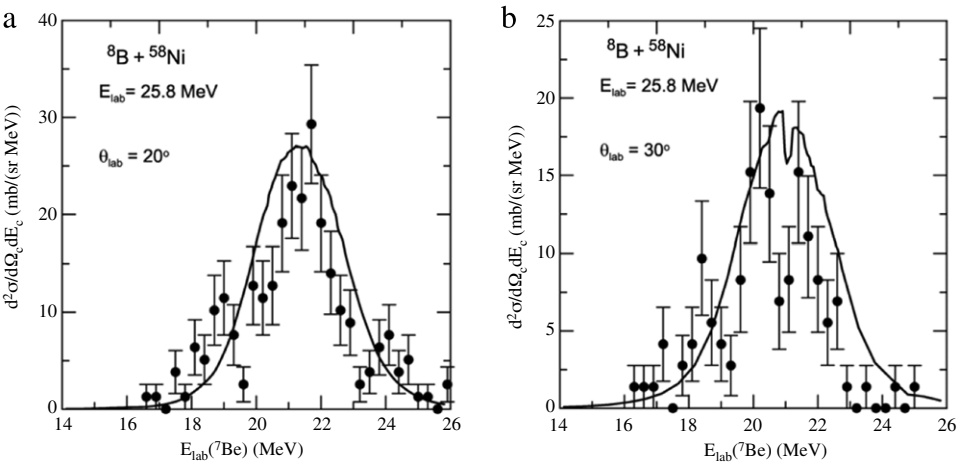

Fig. 20. Inclusive energy distribution of the ^{7}Be fragment detected at the laboratory angles: (a) 20° and (b) 30°, with respect to the incident beam direction. The energy of the incident ^{8}B projectiles is $E_{\rm lab} = 25.8$ MeV. The solid circles are the experimental data of Ref. [187] and the solid lines are the results of the semiclassical calculations of Ref. [186].

breakup process: angular distributions of the fragments, and their momentum and energy distributions. As it will be seen in Section 5.2.1, intermediate values of these breakup amplitudes serve also as an input to the calculation of the different fusion processes that can take place in a collision involving weakly bound nuclei.

As an example of these calculations, we present in Fig. 20 the energy distribution of the ^{7}Be fragments produced in the ^{8}B breakup when these projectiles collide with ^{58}Ni. Those results show that the description of the experimental data by means of semiclassical approximations can be quite satisfactory.

4.3. Elastic breakup within CDCC

The three-body Continuum Discretized Coupled Channels method, replaces the three-body problem by a two-body one with continuum. The continuum is discretized and the usual CC method of calculation is employed. This method is particularly suited for heavy-ion reactions at low energies. Here we only mention that besides allowing the calculation of the elastic scattering cross section, fully affected by the breakup channel coupling, the CDCC also allows the calculation of the elastic breakup cross section. This cross section is the inclusive"inelastic" cross section, where"inelastic" here refers to transition to the continuum. Further, complete fusion, to be discussed in the next section, can also be calculated. Since the CDCC is a two-body scattering theory, it cannot calculate the inclusive breakup cross section.

The elastic breakup cross section calculated within the CDCC contains both the nuclear and the Coulomb contributions. The Coulomb one is particularly important for an unambiguous extraction of nuclear structure information of the dissociating collision partner, such as the dipole response. The Coulomb and the nuclear breakup amplitudes interfere, so that the breakup cross section can be written as,

$$\sigma_{\rm bu} = \sigma_{\rm bu}^{\rm N} + \sigma_{\rm bu}^{\rm C} + \sigma_{\rm bu}^{\rm int}, \tag{93}$$

where $\sigma_{\rm bu}^{\rm N}$ and $\sigma_{\rm bu}^{\rm C}$ are respectively the Coulomb and the nuclear contributions, and $\sigma_{\rm bu}^{\rm int}$ is the interference term. In analyzing data, practitioners assume the interference term to be small. Accordingly, to extract the Coulomb breakup, which is easy to relate to the structure of the breaking up projectile, one usually subtracts from the cross section the nuclear contribution $\sigma_{\rm bu}^{\rm N}$. To be in close touch with the data, the usual procedure followed in this subtraction is the so-called scaling method. There, one measures the elastic breakup on a light target, such as ^{12}C, where the Coulomb contribution is quite small, and assumes that the nuclear cross section has a linear dependence on the radius of the target.[11]

Thus,

$$\sigma_{\rm bu}^{\rm N} = P_1 + \sigma_{\rm bu}(^{12}{\rm C})\left[\frac{A_{\rm T}^{1/3}}{12^{1/3}}\right] \equiv P_1 + P_2\, A_{\rm T}^{1/3} \tag{94}$$

where P_1, P_2, do not depend on the target mass (they do depend on the structure of the projectile and on the center of mass energy). The above scaling relation is applied for a given projectile and value of the center of mass energy. With the above,

[11] Since nuclear breakup occurs in peripheral collisions, the cross section should be proportional to the area of a ring with average radius $R = R_{\rm P} + R_{\rm T}$, and a width $\Delta_{\rm R}$, related to the surface thickness. Thus, the nuclear breakup cross section is expected to be proportional to R.

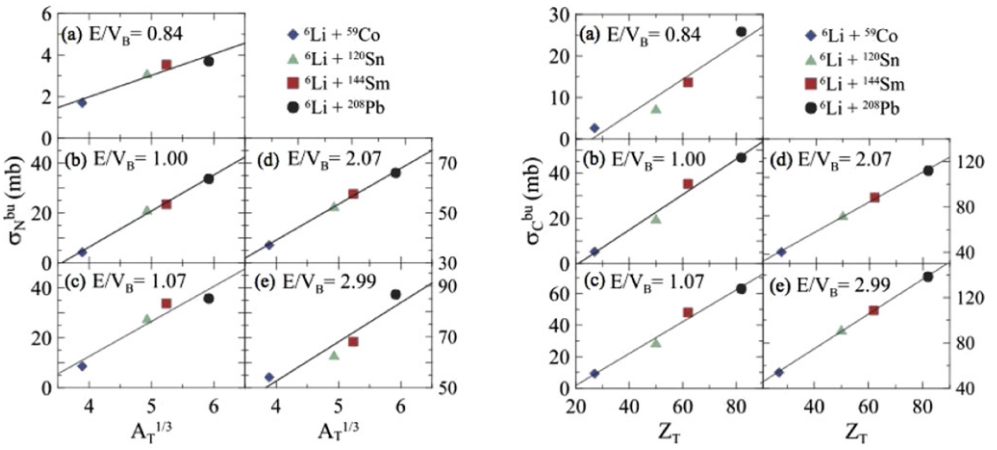

Fig. 21. (Color online) Nuclear (left panel) and Coulomb (right panel) scaling laws. On the left panel the nuclear breakup cross sections for several systems with equal values of E/V_B are plotted as a function of A_T. On the right panel the Coulomb breakup cross sections for the same systems and collision energies are plotted against Z_T.
Source: The figures on both panels were taken from Ref. [188].

one then extrapolates the ^{12}C measurement to heavier targets and uses the subtraction procedure to obtain the Coulomb breakup. At low energies, relevant to our discussion of near-barrier fusion, the scaling formula above is modified to account for the threshold effect of the barrier. The quantity to maintain fixed is E/V_B, where V_B is the height of the Coulomb barrier. It was found in Ref. [188] that the Coulomb breakup cross section also scales but with the target charge Z_T, for a fixed value of E/V_B.

With the above scaling law one has a handle on the relative importance of both nuclear and Coulomb breakup cross sections at near barrier energies. This in turn should be useful in the study of fusion of weakly bound nuclei as the scaling law supplies a mean to assess the feasibility of performing a given experiment which aims to discern the influence of elastic breakup on fusion. An illustration of the working of the scaling laws at low energies is shown in Fig. 21. The Nuclear and the Coulomb breakup cross sections were obtained with CDCC calculations [188,189].

Recent CDCC calculations by Kucuk and Moro [190] for the exclusive breakup of ^{17}F in collisions with ^{58}Ni and ^{208}Pb at 10 AMeV have shown the need for the inclusion of high multipoles, up to $\lambda = 5$, in order to achieve full convergence. This need for high multipoles makes it difficult to disentangle structure and reaction effects from low-energy data. Therefore, for the purpose of extracting this kind of information, it is better to consider higher incident energies, where the process is largely dominated by E1 couplings. Another relevant result of these calculations is the complicated interplay between the breakup induced by the Coulomb and nuclear interactions. This can be seen in figure 6 of Ref. [190], which is reproduced here as Fig. 22. In the case of ^{58}Ni, as observed in previous calculations for other targets, the interference between the Coulomb and nuclear couplings is destructive at small angles and constructive at larger ones, especially in the region where the breakup cross section reaches its maximum. For ^{208}Pb targets at small angles the breakup process is dominated by the Coulomb interaction, but beyond the grazing angle the Coulomb breakup is almost completely suppressed by absorption effects.

An interesting comparison between full few body Faddeev-type calculations and three-body CDCC calculations was performed in Ref. [191]. Those calculations show a fairly good agreement between the Faddeev and CDCC calculations, better than in a previous work [192], because of an improvement in the speed of the convergence in the most recent ones. As shown in Fig. 23, the results are very sensitive to the choice of the potential employed, making it clear one needs to use realistic potentials. Furthermore, the agreement with data is reasonable at low energies, in the region around the 1.275 MeV resonance shown in the upper panels, although at some angles it underestimates data by about 40%. The discrepancy is even larger in the non-resonant region at higher energies, illustrated in the lower panels, where the calculations fail to reproduce the data. The reason for this discrepancy is not well understood, making necessary further work on this problem.

Mukeru, Lekala and Denikin [193] investigated the influence of diagonal (between the same bin states) and off-diagonal (between different bin states) continuum matrix-elements on the breakup cross section. They studied collisions of ^{8}B and ^{19}C projectiles with ^{58}Ni and ^{208}Pb targets. For this purpose, they performed CDCC calculations switching on and off either the diagonal or the off-diagonal matrix-elements. They found that the diagonal couplings have strong influence on the angular distribution at back-angles, leading to a reduction of the cross section. On the other hand, the off-diagonal couplings are more important at forward angles. When they are included, the breakup cross sections are dominated by the Coulomb couplings, whereas without them the nuclear interaction is more important. The same group studied the effects of nuclear and Coulomb interactions in the breakup of ^{19}C on ^{208}Pb [194]. They found the predominance of Coulomb breakup over the nuclear one, and the destructive interference between them. The dipole component was the dominant multipole in the Coulomb breakup while the d-waves were leading for the nuclear breakup.

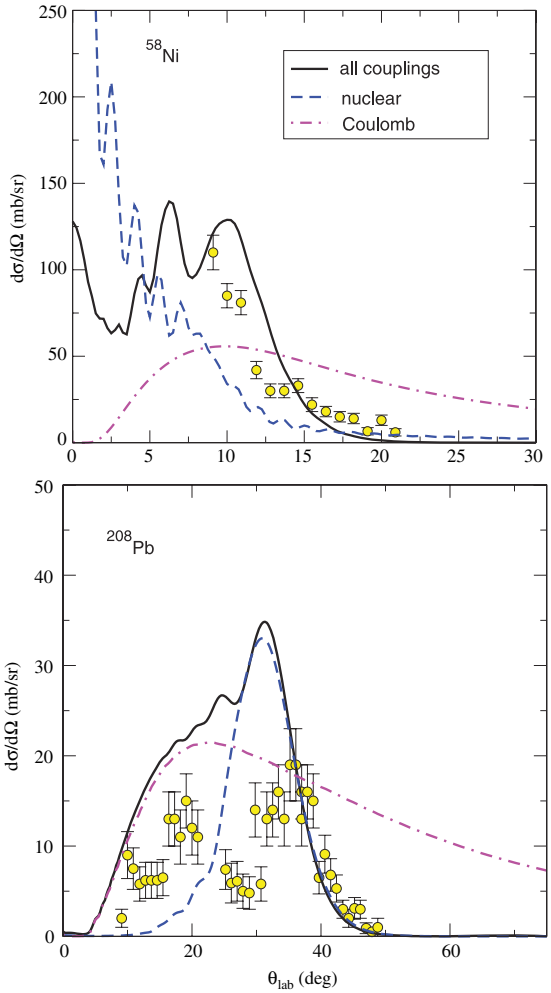

Fig. 22. (Color online) Nuclear (dashed lines) and Coulomb (dot-dashed lines) contributions to the ^{17}F exclusive breakup cross section. The figures show angular distributions of the center of mass of the $p + {}^{16}$O breakup fragments vs. the angle in the laboratory frame. The collision energy is 10 MeV/nucleon. The solid line is the full CDCC calculation, including both nuclear and Coulomb couplings.
Source: The figure was taken from Ref. [190].

4.4. The breakup dynamic polarization potential

Dynamical polarization potentials have been traditionally introduced as a correction to the bare potential, to reduce the coupled channel equations to a single-channel problem. These potentials were introduced in Section 2.3 and, using projection operator techniques, the following equation was derived (Eq. (51) of Section 2.3),[12]

$$V_{\rm pol}(\mathbf{r}, \mathbf{r}') = \left\langle \mathbf{r}; 0 \left| \mathbb{V}_{\rm PQ}\, \mathbb{G}_{\rm Q}^{(+)}\, \mathbb{V}_{\rm QP} \right| 0; \mathbf{r}' \right\rangle, \tag{95}$$

where $\mathbb{G}_{\rm Q}^{(+)}$ is the Green's function in the Q-space, given by Eq. (35). The above equation is very general, valid for any situation, but it is not useful for practical purposes. The function $\mathbb{G}_{\rm Q}^{(+)}$ is not easy to evaluate and the exact polarization potential is non-local and energy-dependent. Furthermore, when angular momentum projection is carried out, it becomes also angular momentum-dependent. Thus, it is necessary to develop approximate polarization potentials.

The use of approximate polarization potentials is a common practice in heavy ion collisions. The approximations used for this purpose can be tested by comparing the resulting cross sections with the ones obtained in the corresponding coupled channel calculations (or CDCC calculations, in the case of breakup polarization potentials). The simplest approximations for the polarization potential lead to very qualitative results. However, the cross sections obtained through more realistic approximations [19] can be quite accurate [19,23] (see right panel of Fig. 24).

[12] To simplify the notation, we are dropping the E in the arguments of the polarization potential and the Green's function.

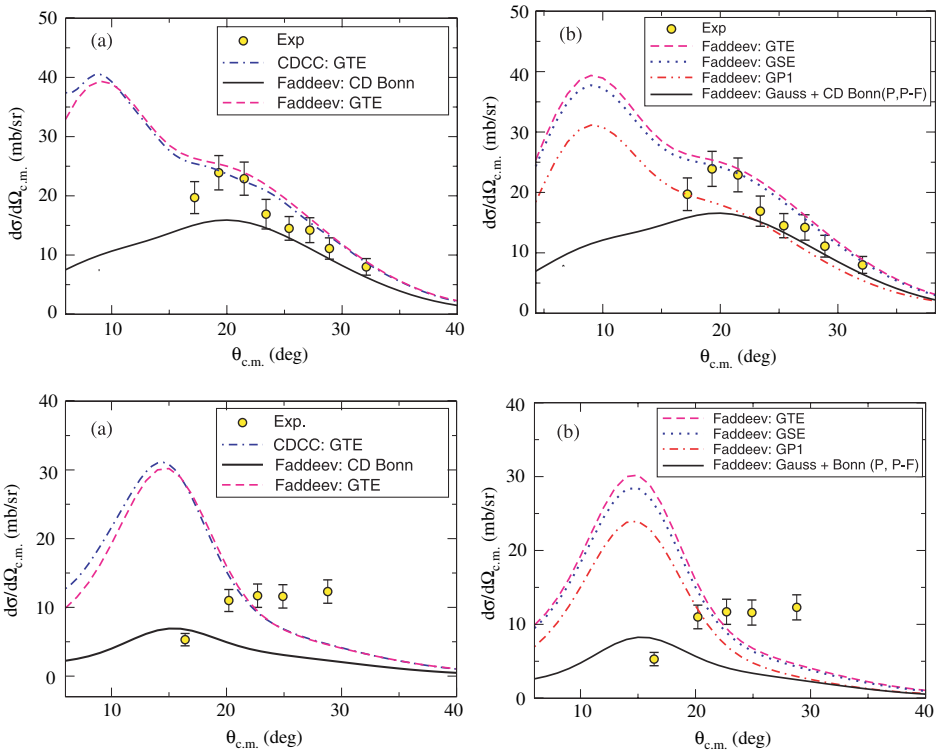

Fig. 23. (Color online) Angular distribution for the breakup $p(^{11}\mathrm{Be}, p)^{10}\mathrm{Be} + n$ at 63.7 MeV/u integrated over the energy range $E_{\mathrm{rel}} = 0 - 2.5$ MeV (upper part) and integrated over the energy range $E_{\mathrm{rel}} = 2.5$–5.0 MeV (lower part).
Source: The figure was taken from Ref. [191].

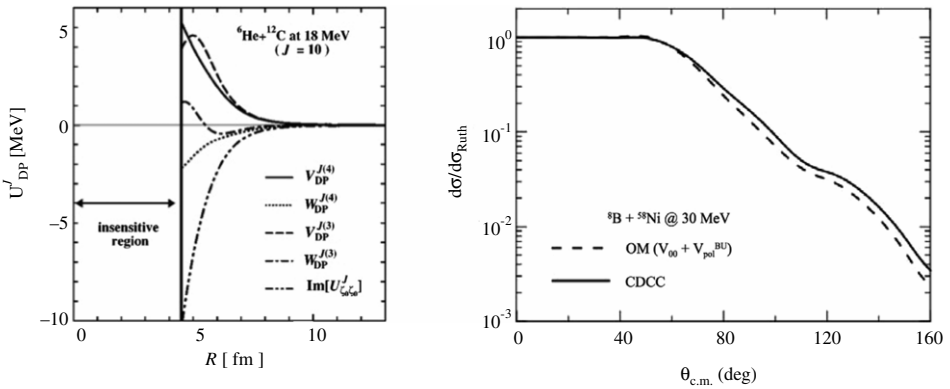

Fig. 24. Left panel: Real (V_{DP}) and imaginary (W_{DP}) parts of the polarization potentials for $J = 10$ evaluated using three- and four-body CDCC calculations [35]. For comparison, the imaginary part of the optical potential, $\mathrm{Im}[U^{J}_{\zeta_0\zeta_0}]$, is also shown; Right panel: Angular distributions obtained with a CDCC calculation (solid line) and with an optical model calculation including the dynamical breakup polarization potential, calculated by the method of Thompson et al. [19]. For details see the text.

The earliest approximations for V_{pol} were developed to take into account the effects of inelastic couplings. They replaced $\mathbb{G}_{\mathrm{Q}}^{(+)}$ by the non-interacting Green's function [38], or by the Coulomb Green's function [195], and made additional simplifying assumptions. The non-locality was then eliminated replacing the potential by its trivially equivalent local version. The first calculations of breakup polarization potentials considered only the nuclear [196,197] or the Coulomb [55,198,199] part of the coupling. In Refs. [196,197,199,200], $\mathbb{G}_{\mathrm{Q}}^{(+)}$ was approximated by the Coulomb Green's function, as in Ref. [195], and angular momentum dependent potentials were determined. These works calculated the imaginary part of the polarization potential and then evaluated its real part using the dispersion relation. On the other hand, Refs. [55,198] obtained an angular momentum independent potential from semiclassical amplitudes. Despite its qualitative nature, the semiclassical

polarization potential of Ref. [55] was used to calculate the elastic cross section in ^{11}Be–^{64}Zn scattering [40], and the results were in reasonable agreement with the data.

Kakuee et al. [48] adopted a phenomenological approach to investigate the breakup polarization potential in ^{6}He–^{208}Pb scattering, at the collision energy $E_{\rm lab} = 27$ MeV. They made an optical model analysis using the optical potential that reproduces the elastic scattering of the stable ^{6}Li projectile on the same target, and added the Coulomb dipole polarization potential derived by the semiclassical procedure of Andrés, Gomez-Camacho and Nagarajan [55,201]. The results of the calculation were compared with the data. They found that the rainbow maximum was damped in comparison with its behavior in the absence of the polarization potential. However it was not enough to describe the data. The diffusivity of the imaginary part of the optical potential was then treated as an adjustable parameter. To reproduce the damping of the experimental rainbow maximum it was necessary to use a very large diffusivity: 3 fm. This indicates that the contributions from nuclear couplings and/or higher Coulomb multipoles give an important contribution to the breakup polarization potential.

Mackintosh and Keeley [202] used a different approach to evaluate the breakup polarization potential for the same system and the same collision energy. They performed a CDCC calculation to determine the components of the elastic S-matrix, and obtained a phase-shift equivalent local polarization potential using a S-matrix inversion procedure.

Instead of evaluating the polarization potential using projector techniques, as in Section 2.3, one can find an expression for a local polarization potential directly from its definition. The starting point is the radial equation for the elastic wave function in a coupled channel problem. For simplicity, we discuss the particular situation of spin zero, where the orbital angular momentum of the projectile–target motion, L, is the only angular momentum involved in the equation. In this case, it is a constant of motion. This equation is,[13]

$$\left[T_L + V_0\,(R) - E\right] u_{0L}(R) = -\sum_{\alpha\neq 0} V_{0,\alpha}\,(R)\,u_{\alpha L}(R), \tag{96}$$

where $E = E_{\alpha=0}$ is the relative energy in the elastic channel and $V_{0,\alpha}$ are the matrix-elements of the interaction between the elastic channel and channel α. In principle, $V_0\,(R)$ should correspond to the diagonal matrix-element $V_{0,0}(R)$. However, it is usually replaced by a complex optical potential. The polarization potential, $V^{(L)}_{\rm pol}(R)$, is defined by the condition,

$$\left[T_L + V_0\,(R) + V^{(L)}_{\rm pol}\,(R) - E_\alpha\right] u_{0L}(R) = 0. \tag{97}$$

That is, adding the polarization potential to the left hand side of Eq. (96) and dropping the coupling terms on its right hand side, one should get the same radial wave function. Comparing Eqs. (96) and (97), one concludes that the above definition of the polarization potential is equivalent to the equation,

$$V^{(L)}_{\rm pol}\,(R) = \frac{1}{u_{0L}(R)}\sum_{\alpha\neq 0} V_{0,\alpha}\,(R)\,u_{\alpha L}(R). \tag{98}$$

The above potential has the disadvantages of being L-dependent and having poles at the zeroes of the radial wave function. However, for high enough angular momentum at near-barrier energies, the poles tend to be located at large distances. We remark that in the case of breakup polarization potentials, which is the subject of this sub-section, the spin-zero simplification cannot be used. The radial wave function then carries other quantum numbers and so does the polarization potential. In this case the total angular momentum, J, is conserved but L and the intrinsic angular momenta are not. However, handling this technical problem is straightforward and we are not going into the details here.

Matsumoto at al. [35] used this approach to investigate the breakup polarization potential for ^{6}He–^{12}C scattering at the beam energy of 18 MeV. For this purpose, they performed three- and four-body CDCC calculations, where the optical potential was evaluated by the folding model. They multiplied the folding potential by the complex factor $N_{\rm R} + i\,N_{\rm I}$, taking $N_{\rm R} = 1$ and using $N_{\rm I}$ as an adjustable parameter. The radial wave functions were then used to derive the polarization potential, through the spin-dependent version of Eq. (98) (see Ref. [35]). The potentials for the total angular momentum $J = 10$ are shown on the left panel of Fig. 24. One observes that the polarization potentials obtained with the three-body and four-body CDCC calculations are both repulsive (positive valued). This behavior has an important consequence for the calculation of the fusion cross section. The barrier for the effective potential becomes higher, which leads to a reduction of the fusion probability.

Nowadays, realistic L-independent approximations for the dynamical polarization potentials are available. We discuss below the polarization potential of Thompson et al. [19], which has been widely used in recent years. The idea behind this method is very simple and we outline its derivation here, for the simplified case of spin-zero. It consists of making an appropriate angular momentum average of the L-dependent polarization potential of Eq. (98), so that one gets rid of poles and eliminates the angular momentum dependence. The polarization potential of Thompson et al. is given by the expression

$$V_{\rm pol}(R) = \frac{\sum_L \omega_L(R)\,V^{(L)}_{\rm pol}(R)}{\sum_L \omega_L(R)}, \tag{99}$$

[13] Note that we are using a different notation for the projectile–target separation vector. We are denoting it by **R**, so that R stands for the radial coordinate.

where $\omega_L(R)$ is the weight function

$$\omega_L(R) = \left(2L+1\right)\left[1-|S_{\alpha L}|^2\right]\left|u_{0L}(R)\right|^2. \tag{100}$$

One can easily check that the weight function cancels the poles of the L-dependent polarization potential, at the zeroes of the elastic radial wave function. However, to use this method to evaluate breakup polarization potentials, it is necessary to generalize the above equations as to include the angular momentum associated with the relative motion of the fragments inside the target, and also their spins. This generalization is straightforward but it is not carried out here. It can be found in Ref. [23].

Before we discuss some applications of this method, it is necessary to understand clearly how breakup polarization potentials should be used. Clearly, they cannot be meant as a method to calculate the no-capture breakup cross section. One could be tempted to associate this cross section with the absorption due to the imaginary part of $V_{\rm pol}$. However, if the original CDCC calculation uses complex potentials in the discretized continuum, the breakup cross section evaluated in this way is overestimated. Although the absorbed flux goes into the breakup channel, it does not necessarily contribute to the breakup cross section. The reason is that the breakup process may be followed by the capture of one or both fragments. These processes, which are not described in the single channel approach, contribute to the incomplete and to the complete fusion cross sections, respectively. On the other hand, this is irrelevant for elastic scattering. Therefore, the breakup polarization potential can be very useful to calculate the elastic cross section. It is also useful to handle situations where one wants to evaluate inelastic or transfer cross sections in collisions where the breakup channel plays an important role. In this case, one can eliminate breakup couplings including the breakup polarization potential in the CC equations involving the elastic and the relevant inelastic channels.

Several authors have used the methods discussed above to calculate breakup polarization potentials and apply them to obtain cross sections. Keeley, Kemper and Rusek [203] used the breakup polarization potential to evaluate the fusion cross section for the ^{6,7}Li + ^{16}O systems. First, they performed a CDCC calculation and derived the breakup polarization potential using the method of Thompson et al. [19]. The real part of this potential was then summed to the bare potential and the fusion cross section was evaluated as a tunneling problem, through the modified barrier.

Keeley, Kemper and Rusek [204] made a comparative study of the breakup polarization potentials for collisions of the ^{11}Li, ^{6}He and ^{6}Li projectiles on ^{208}Pb. They used the method to derive trivially equivalent l-dependent local potentials in Refs. [205,195]. They found that the polarization potentials for ^{11}Li and ^{6}He have a long-range attractive and absorptive tail, characteristic of the Coulomb dipole coupling, which is not present in the potential for ^{6}Li. This is explained by the fact that the Coulomb dipole coupling vanishes in the $\alpha + d$ cluster model for ^{6}Li.

Lubian and Nunes [23] used the method of Thompson et al. [19] to calculate the breakup polarization potential for the ^{8}B + ^{58}Ni system, $V_{\rm pol}^{\rm (BU)}(R)$. The elastic angular distribution was then evaluated through a single channel calculation adding $V_{\rm pol}^{\rm (BU)}(R)$ to the optical potential. The results are represented by a dashed line on the right panel of Fig. 24. To check the validity of the polarization potential, this angular distribution was compared with the one obtained through the direct solution of the CDCC equations, shown as a solid line in the same figure. One observes that the two curves are quite close, which means that the polarization potential obtained in this way can be used to simplify the scattering problem considerably.

Other authors used the method of Thompson et al. to evaluate breakup polarization potentials for different systems [114,206,207]. Santra et al. [114] calculated the dynamic polarization potential due to direct breakup of ^{6}Li, in the ^{6}Li–^{209}Bi collision at near-barrier energies. They found that the real part of the polarization potential is repulsive, leading to a higher fusion barrier, and the imaginary part is absorptive and has a long-range.

Parkar et al. [206] studied the effects of breakup and 1n transfer in the elastic scattering of ^{9}Be on ^{28}Si, ^{64}Zn and ^{144}Sm. First, they performed three-body CDCC–CRC calculations, using the ^{5}He + α cluster model to represent ^{9}Be breakup. The real part of $V_{\rm pol}^{\rm (BU)}$ was found to be repulsive, both below and above the Coulomb barrier. Then, they used the ^{8}Be + n cluster model to represent ^{9}Be breakup. In this case, they found that the real part of the polarization potentials for the ^{64}Zn and ^{144}Sm targets are attractive, both below and above the Coulomb barrier. On the other hand, for the lighter ^{28}Si target, it is attractive below the barrier and repulsive above. When they calculated the 1n transfer polarization potential (found repulsive) for the ^{9}Be + ^{64}Zn and ^{9}Be + ^{144}Sm systems and added it to $V_{\rm pol}^{\rm (BU)}$, they got an overall repulsive polarization potential at long distances. It would be interesting to check whether the polarization potentials obtained with more realistic four-body CDCC calculations confirm this trend. Other calculations for the ^{9}Be + ^{144}Sm system using an approach that makes no assumption about the specific structure of the ^{9}Be projectile leads to a repulsive polarization potential [208].

Keeley et al. [207] performed similar calculations of the polarization potential for the ^{9}Be + ^{208}Pb system using the ^{5}He+α cluster model. They evaluated the overall polarization potential, summing the contributions from breakup and one-neutron stripping couplings. The resulting polarization potential was found to be repulsive, showing in the surface region the same characteristics of breakup polarization potentials alone. They have also shown that the dynamic polarization potential has a strong influence on the elastic angular distribution. The rainbow maximum is strongly damped, as shown on the left panel of Fig. 25. The damping can be traced back to the long-range imaginary part of the breakup polarization potential. When the effects of one-neutron stripping are included, the damping increases, due to the extra absorption produced by these couplings.

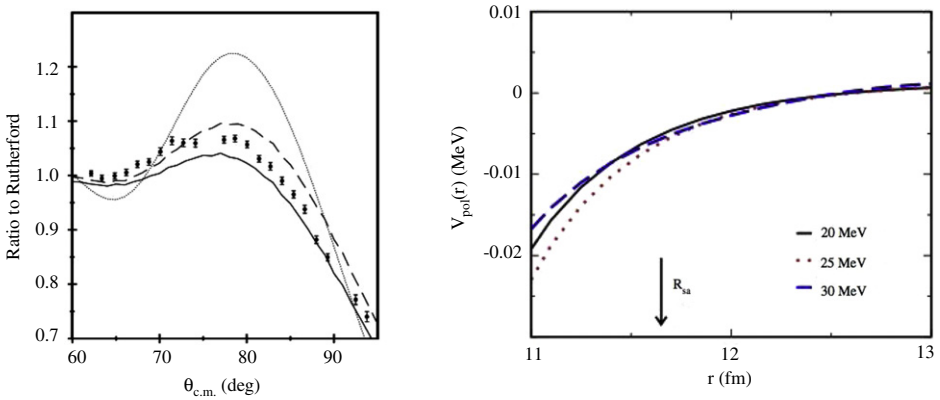

Fig. 25. (Color online) Left panel: Angular distributions in the Coulomb rainbow regions in ^{9}Be–^{208}Pb scattering at the collision energy $E_{lab} = 44$ MeV [207]. The dotted, the dashed and the solid lines correspond respectively to no-coupling calculations, couplings with breakup only and couplings to both breakup and one-neutron stripping. For details, see Ref. [207]; Right panel: Real part of the dynamic polarization potential around the strong absorption radius for ^{7}Li + ^{144}Sm at laboratory energies above (30 MeV), below (20 MeV) and close to the barrier (25 MeV) for breakup of ^{6}Li into $\alpha + d$ following the one-neutron stripping of ^{7}Li.
Source: This figure was taken from Ref. [209].

Recently So et al. [210] studied the elastic scattering angular distributions of the ^{6}He +^{208} Pb and ^{11}Li + ^{208}Pb systems, at near-barrier energies. They have shown that the Coulomb dipole polarization is not strong enough to explain the damping of their elastic angular distributions at forward angles. To describe the data, they introduced a phenomenological nuclear dynamic polarization potential, parametrized by a Woods–Saxon shape, and fitted their parameters. They found parameters corresponding to larger than usual radii and diffuseness, indicating that these potentials have a long range. The real part of the polarization potential was also found to be repulsive.

The breakup polarization potentials discussed above lead to some interesting conclusions, that are summarized below.

1. The imaginary part of the breakup polarization potential has a long tail, producing long-range absorption. Thus, it damps strongly the Coulomb rainbow maximum and suppresses the cross section at forward angles.
2. In most cases, the real part of the breakup polarization potential is repulsive, above and below the Coulomb barrier. The exceptions are collisions of ^{9}Be, when the ^{8}Be + n breakup model is adopted. In this case it is attractive for the ^{64}Zn and the ^{144}Sm targets, at energies above and below the barrier. In the case of the lighter ^{28}Si target, it is repulsive above the barrier and attractive below.

We remark that the repulsive trend of the breakup polarization potential in collisions of weakly bound systems does not seem to be consistent with the enhancement of the cross section for these systems at sub-barrier energies. It suggests an attractive polarization potential in this energy region. Thus, it should not be associated with the non-capture breakup considered above. Recently, Otomar et al. [209,211] performed CCBA calculations for the ^{7}Li + ^{144}Sm system to investigate the importance of one-neutron stripping of ^{7}Li followed by ^{6}Li breakup. In this case, the polarization potential associated with transfer followed by breakup becomes attractive, as shown on the right panel of Fig. 25. The authors then conclude, in agreement with the experimental evidences [212–222], that at energies below the Coulomb barrier the one-neutron transfer followed by breakup must be the leading mechanism, whereas the non-capture breakup must be the prevailing mechanism at above-barrier energies.

Gómes Camacho et al. [223] investigated the effects of ^{6}Li resonances on near-barrier scattering of this nucleus from ^{28}Si and ^{58}Ni targets. For this purpose, they switched on and off the couplings with the $l = 2, J^{\pi} = 3^{+}, 2^{+}$ and 1^{+} resonances in CDCC calculations of angular distributions. For both targets, they found that these effects are very small. They found also that the real part of the polarization potential is repulsive.

4.5. Recent measurements of breakup cross sections

Several measurements of breakup cross sections have been reported. In most cases, inclusive breakup cross sections are determined through measurements of total alpha yields. However, a few papers report experimental results for the NCBU cross section, obtained through exclusive coincidence measurements of two light particles. Experiments to study the breakup of ^{7}Li, ^{9}Be, ^{6}He and mainly ^{6}Li projectiles, in collisions with several targets, have been reported [46,124,154,156,217, 224–233]. More recently, the breakup of ^{11}Li has also been investigated [234]. In all cases, large alpha yields were observed. This is because the detected alpha particles may be originated in several different processes, such as fusion-evaporation, direct transfer, breakup (resonant, non-resonant), and ICF. From the angular distributions and kinematics considerations one tries to disentangle the origins of these alpha particles, or at least to estimate the contribution of each process to the alpha production. A very important feature of the breakup process is its influence on fusion. However, we will not address it

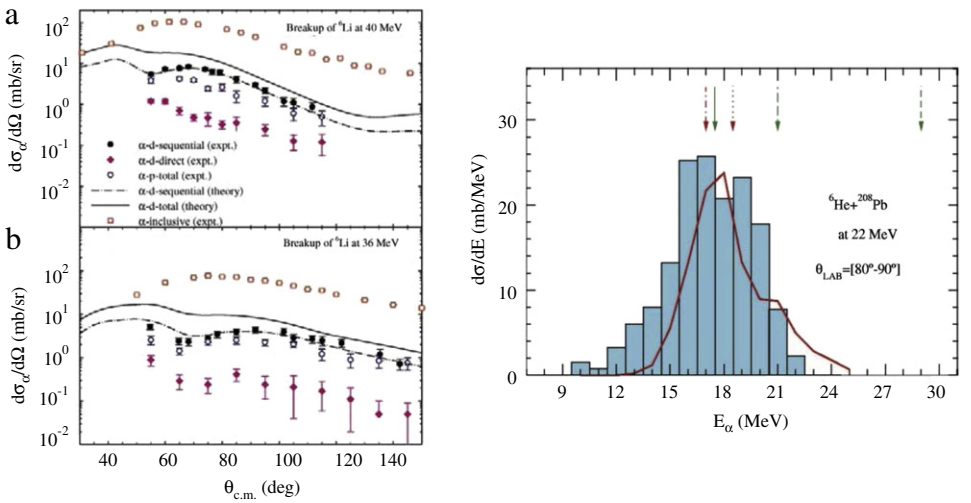

Fig. 26. (Color online) Left panel: α-production cross section at two collision energies (open squares) and exclusive breakup cross section ($^6\text{Li} \rightarrow \alpha + d$ and $^6\text{Li} \rightarrow p + {}^5\text{He}$). See Ref. [217] for detail; Right panel: Experimental energy distribution of the α-particle production in collisions of ^{6}Li projectiles on ^{208}Pb in the angular range $80^\circ < \theta_{\text{lab}} < 90^\circ$ (bars), compared with a DWBA calculation where transfer to the continuum is considered (solid line). The arrows indicate the expected energy of the scattered α-particle at $\theta_{\text{lab}} = 85^\circ$, assuming (i) 1n-transfer for Q_{gg} (dotted line) and $Q = 0$ (dot-dashed line); (ii) 2n-transfer for Q_{gg} (dashed line), for $Q = 0$ (long dashed line) and $Q = -4$ MeV (solid line).

here. This topic will be discussed extensively in Sections 5 and 6. In the following we discuss a few exclusive measurements of breakup cross sections.

Santra et al. [217] performed exclusive measurements of ^{6}Li breakup on a ^{209}Bi target. Their data are shown on the left panel of Fig. 26 for two collision energies, in comparison with results of CDCC calculations. They found that the sequential breakup via the 3^+ resonant state (solid squares) predominates in the $\alpha + d$ fragmentation, and that the data are very well described by the corresponding CDCC calculations (dashed lines). One can also observe that inclusive alpha particles yields (open squares) are much larger than the predictions of the CDCC calculation with full continuum couplings (resonant and non-resonant).

Kumawat et al. [156] measured inclusive α-particle production in the $^6\text{Li} - {}^{90}\text{Zr}$ collision. After subtracting from the yields the theoretical prediction for the α-particles originated from fusion-evaporation, they obtained the yield corresponding to the breakup plus transfer processes. This yield turned out to be much larger than the one resulting from fusion. From DWBA calculations they concluded that most of the alpha particles from direct reactions come from transfer processes, and that this behavior is almost target independent.

Similar conclusions were reached by Acosta et al. [50,232] measuring inclusive α-particle production in the $^6\text{He} - {}^{208}\text{Pb}$ collision. They compared the data with CDCC and DWBA calculations and found that most of the α-particles are generated by transfer to the continuum. Experimental and theoretical α-particle energy distributions are shown in Fig. 26. One sees that the agreement is quite reasonable. However, Fernández-García et al. [58,130] analyzed the same system and the CRC and CDCC calculations were not able to explain the measured α-particle yields.

Presently, there is no coupled channel code capable of including transfer and continuum discretization (breakup) in a single calculation. The reason is that such a calculation would require a prohibitively large amount of memory and/or computer time. Therefore, the present theoretical framework cannot handle collisions when both breakup and particle transfer couplings are very strong. The CRC handles transfer but not breakup, whereas the CDCC handles breakup but not particle transfer.

4.5.1. Prompt breakup, delayed breakup and time-scales

Recent investigations of the influence of breakup on fusion have lead to dramatic improvements in breakup experiments. To determine this influence, it is necessary to distinguish prompt breakup from delayed breakup. In the former, the breakup process occurs when the weakly bound projectile approaches the target, reaching the range of the coupling interaction. The latter takes place in two steps. First, the projectile is excited to a long-lived resonance above the breakup threshold, as it traverses the interaction region. Then, the resonance decays into the breakup channel, when the projectile is following the outgoing branch of the trajectory. Only prompt breakup, which occurs in a time scale of 10^{-22} s, may affect fusion. In delayed breakup the resonance life-time is much longer than the collision time. Thus, the projectile breaks up when the collision is over and hence it cannot affect the fusion cross section.

Recently, de Diego et al. [29] studied the effect of core excitation on the resonant breakup of ^{11}Be on a proton target, using the XCDCC approach of Summers, Nunes and Thompson [27,28] (see Section 2.4). The energy of the ^{11}Be beam was 67.2 MeV/nucleon. The calculation takes into account the excitation of the 2^+ rotational state of ^{10}Be. They calculated the

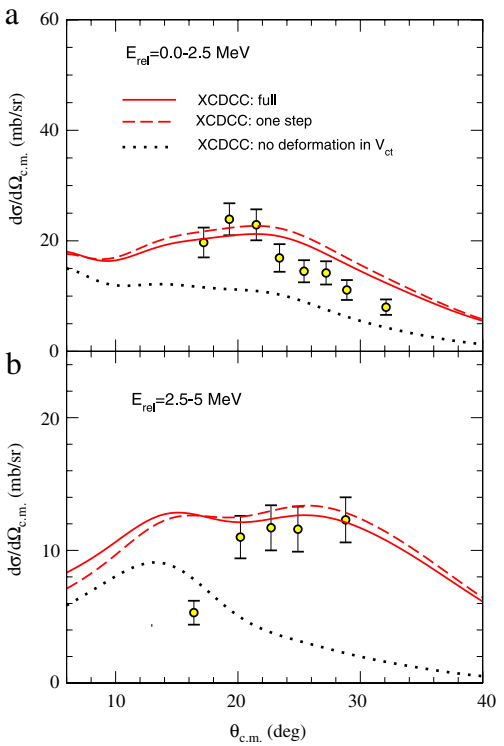

Fig. 27. (Color online) Angular distribution of the center of mass of the ^{10}Be $-$ n fragments, in the breakup of ^{11}Be on a proton target. The two panels show results for different ranges of the kinetic energy of the relative motion of the fragments. The dotted lines correspond to CDCC calculations neglecting core excitations, while the dashed and solid lines represent results of calculations including core excitations. For further details see the Ref. [29].
Source: The data are from Ref. [235].

angular distribution of the excited ^{11}Be projectile, and compared it with the experimental distribution of the center of mass of the ^{10}Be $-$ n fragments. The results are shown in Fig. 27. One concludes that the predictions of the full XCDCC calculation are in very good agreement with the data, whereas the results of the CDCC calculations without core excitation are much poorer.

Usually breakup experiments measure the breakup cross section, which is the sum of contributions from prompt and delayed processes. However, very recently, the Australian National University group developed ingenious experimental set-ups to distinguish prompt breakup from delayed breakup [212–214]. Their experiments allowed the determination of the time scale of the breakup events in collisions of the weakly bound ^{6,7}Li and ^{9}Be projectiles on different targets. In the following, we mention some previous works and give some details of the new ANU experiments.

Early in 2002, Hinde et al. [215] performed coincidence experiments to determine time scales in the breakup of ^{9}Be, in collisions with a ^{208}Pb target at sub-barrier energies. They were able do disentangle prompt ^{9}Be breakup from the delayed breakup of ^{8}Be, triggered by a one-neutron stripping process. In the latter case, the transfer reaction produces the unstable ^{8}Be nucleus, which has the half-life $t_{1/2} \sim 10^{-16}$ s. Thus, it is several orders of magnitude longer than the collision time ($t_c \sim 10^{-22}$ s). The time scales involved in the breakup process will be discussed in detail in connection with Fig. 30.

In 2006, Shrivastava et al. [216] made exclusive measurements of ^{7}Li breakup, in collisions with ^{65}Cu. The experiment was performed at the BARC-Mumbai and the measurements were made at a single collision energy above the barrier. They found that the yield of coincidences between an α-particle and a deuteron was much larger than that for coincidences between an α-particles and a tritium. This was a surprise, since the widely used two-cluster model for ^{7}Li (^{4}He $+$ ^{3}H) would predict yields of α and tritium fragments, and not of deuterons. Analysis of angular distributions using Born approximation provided clear evidence that the $\alpha - d$ events arise from a two-step process: direct one-neutron stripping, leaving the projectile in the 2.186 MeV (3^+) resonance of ^{6}Li ($t_{1/2} = 2.7 \times 10^{-20}$ s), above the $\alpha - d$ threshold, followed by its decay into an α-particle plus a deuteron. They concluded that the cross section for the two-step breakup process was larger than that for the direct breakup. In their paper they present a very interesting discussion about the need of exclusive coincidence measurements to establish the origin of the large α-particle yields in experiments involving light weakly bound nuclei. We point out that similar conclusions were reached in the work of Santra et al. [217], discussed in the previous section, based on experiments performed in the same laboratory. They found that the cross section for breakup following the excitation of the 3^+ resonance of ^{6}Li was much larger than that for direct breakup. Furthermore, they observed an important cross section for the breakup of ^{5}Li, produced after the stripping of one neutron from ^{6}Li. They also found huge alpha yields in inclusive measurements.

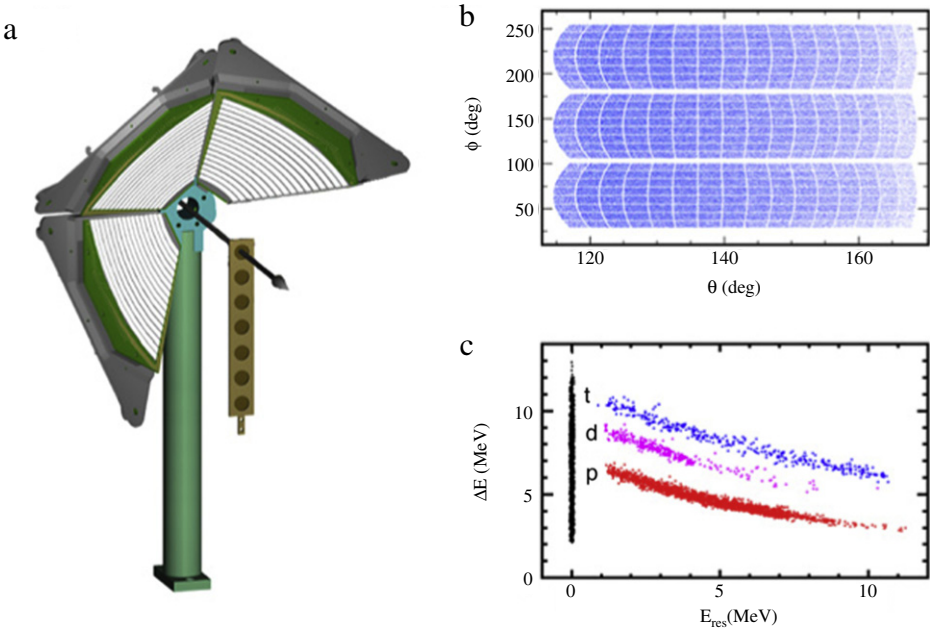

Fig. 28. (Color online) (a) Arrangement of the detector array used at ANU [212–214]. The Arrow corresponds to the beam direction; (b) Pixel separation of the detectors and scattering angle and azimuthal angle ranges; (c) Typical bi-parametric spectrum, separating protons, deuterons and tritons.

A new generation of experiments at the ANU allowed the complete characterization of the breakup process [212–214]. The results of the first experiments were presented at the Nucleus–Nucleus Conference in 2009 [236]. They used four large area double-sided silicon strip detectors (DSSDs), with 128 pixels each, placed at the backward hemisphere, as shown in part (a) of Fig. 28. The experiments were performed at sub-barrier energies, to minimize the probability of incomplete fusion of the charged breakup fragments. This array made possible the reconstruction of the coincident particle properties. The position of the detector array at backward angles minimizes the background from elastically scattered beam particles and forward focused products from reactions with target contaminants. It has also the important advantage of allowing the study of trajectories associated with low angular momenta, which dominate the fusion cross section. For each breakup fragment, one determines the kinetic energy and scattering and azimuthal angles. Then, assuming a three body kinematics, the following equation can be derived:

$$Q = E_1 + E_2 + E_{\rm rec} - E_{\rm lab}, \tag{101}$$

where E_1 and E_2 are the kinetic energies of the fragments, $E_{\rm rec}$ is the recoiling target-like nucleus energy and $E_{\rm lab}$ is the incident energy after the correction by the energy loss in the target. E_1, E_2 and $E_{\rm lab}$ are measured, whereas $E_{\rm rec}$ is determined by momentum conservation. Then, the Q-value can be determined. Some experimental results for the breakup of ^{6}Li (top) and ^{7}Li (bottom) in collisions with ^{208}Pb are shown on the left side of Fig. 29. For the ^{6}Li induced reaction, the most intense peak corresponds to the breakup of excited states of the projectile into $\alpha + d$. However, there are five peaks of $\alpha + p$ (the lowest energy states of ^{209}Pb). After the detector efficiency correction, it was found that ^{5}Li breakup, following the stripping of one-neutron, is more probable than the direct breakup. Note that $\alpha + \alpha$ coincidences were also detected (green structure above 6 MeV). They correspond to ^{8}Be breakup, after the pickup of one proton and a neutron. For the ^{7}Li induced reaction, the $\alpha + t$ peak is the most intense, but events corresponding to $\alpha + d$, $\alpha + p$ and $\alpha + \alpha$ were also observed. The $\alpha + \alpha$ coincidences are originated from ^{8}Be breakup, following the pick-up of a proton. More recently, similar experiments have been performed with the same projectiles but on other targets [214]. Some of their results are shown on the right panel of Fig. 29. A similar study has been performed for ^{9}Be projectiles in collisions with several targets [212]. In this case, the breakup reactions where characterized by coincident events of two alpha particles.

To study the influence of the breakup process on the fusion cross section, it is necessary to determine the time-scale of the breakup events. This can be done if one uses a classical picture for the Coulomb field associated with the target. The following expression can be derived [212–214]:

$$E_{\rm rel} = \frac{m_2 E_1 + m_1 E_2 - 2\,\cos\theta_{12}\sqrt{m_1 m_2 E_1 E_2}}{m_1 + m_2}, \tag{102}$$

where m_1 and m_2 are the masses of the fragments and θ_{12} is the angular separation between the final velocities of the two fragments. As all quantities on the right hand side of Eq. (102) are known, or can be determined experimentally, the relative energy can be derived from the data. A schematic view of the breakup time scale is shown in Fig. 30, where R_0 and T_0 are

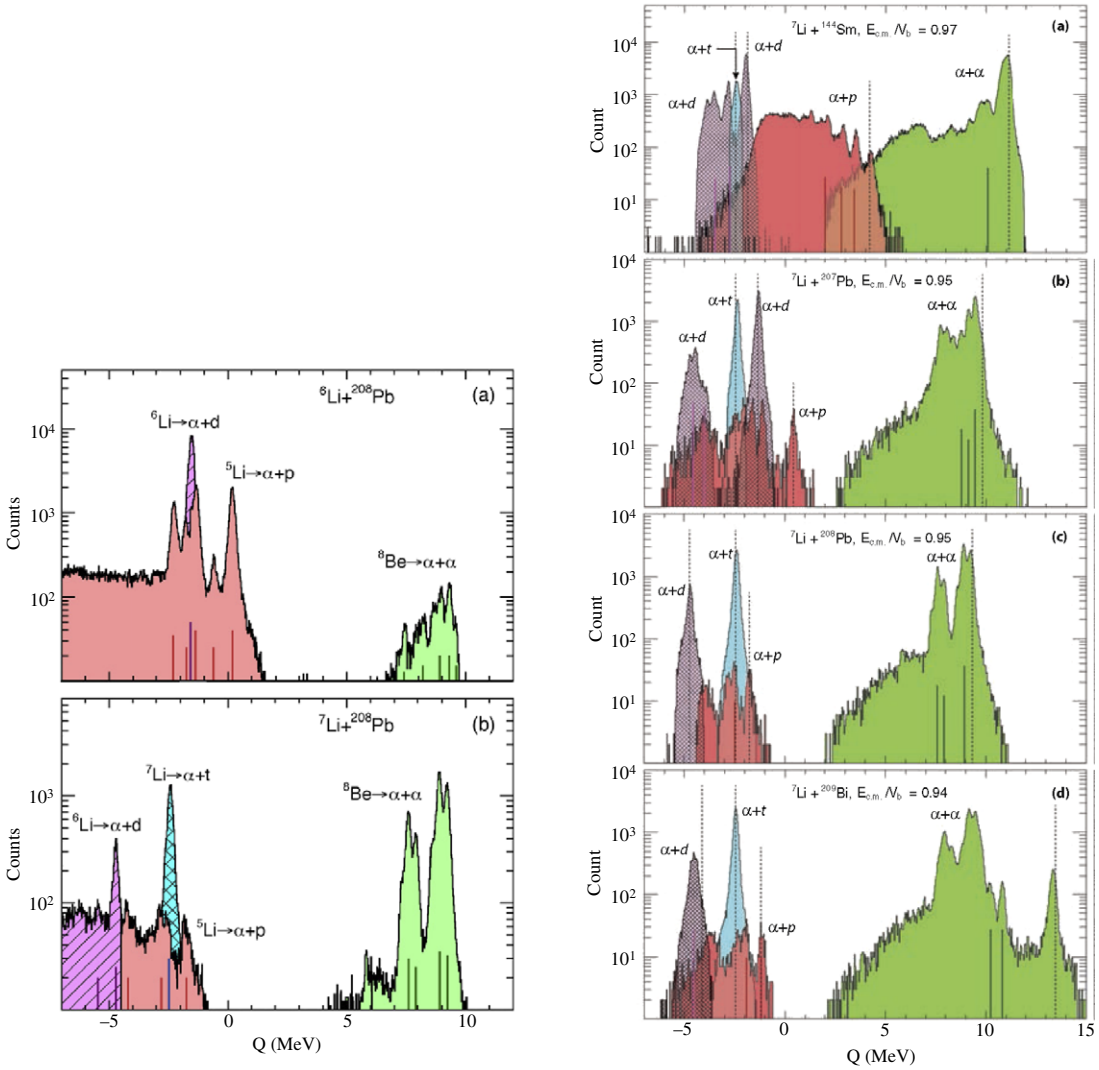

Fig. 29. (Color online) Measured Q-spectra and identified breakup modes for different systems. Left panel: ^{6}Li + ^{208}Pb (top) and ^{7}Li + ^{208}Pb (bottom). One can observe that a large number of events correspond to breakup following transfer; Right panel: similar spectra, for ^{7}Li on different targets.
Source: Left panel: From Ref. [213]. Right panel: The figure was taken from Ref. [214].

the radius and time when the distance of closest approach is reached. The spread of the curved pink band represent the relative kinetic energy of the fragments. In the case of direct breakup, the projectile dissociates as it gets into the range of the coupling interaction and, after that, the fragments interact individually with the target. In this way, they follow different trajectories and emerge at very different angles, as represented in the inset at the lower part of Fig. 30. Thus, the relative angle, θ_{12}, is large and, according to Eq. (102), the relative energy is large. On the other hand, in the case of delayed breakup, the dissociation takes place after the collision, when the projectile–target interaction is less effective. The fragments then emerge with a small relative angle, as represented in the inset at the upper part of the figure. In this case, the relative energy is small. Therefore, the nature of the breakup process can be determined through the analysis of relative energy spectra. Prompt breakup is associated with large relative energies whereas delayed breakup correspond to small relative energies.

Fig. 31 shows relative energy spectra for collisions of ^{6}Li (left panel) and ^{7}Li (right panel) projectiles with ^{208}Pb. The narrow peaks at low relative energies correspond to delayed breakup. The peaks are located at $E_{\rm rel} = E^* + Q_{\rm bu}$, where $Q_{\rm bu}$ is the breakup threshold and E^* is the excitation energy of the resonance, which decays through the breakup channel. The broad distribution at higher relative energies corresponds to prompt breakup, which is the process that can affect the fusion cross section. In the case of ^{6}Li, it is the sum of the tail of the $\alpha - d$ direct breakup with the broad peak of $\alpha - p$ coincidences, which dominates. The latter corresponds to ^{5}Li breakup, following the stripping of one neutron. The right panel of Fig. 31 shows a similar plot for ^{7}Li projectiles. Now, there are sharp peaks at low energies for $\alpha - \alpha$ and $\alpha - d$ coincidences. They correspond to delayed breakup following the pick-up of one proton and the striping of one neutron, respectively. The prompt breakup part of the spectrum is the sum of the broad peaks of the $\alpha - t$ and the $\alpha - \alpha$ coincidences. They correspond

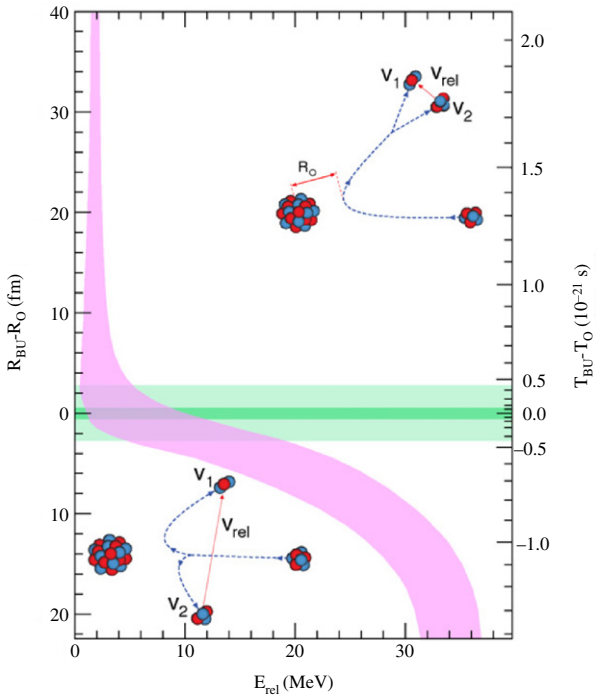

Fig. 30. Schematic representation of prompt (below) and delayed breakup (above) events [213]. The pink band represents the classical spread of the relative energy versus the nuclear separation or time at which breakup occurs, relative to the point of closest approach (R_0, T_0). For details, we refer to the original work [213]. (For interpretation of the references to color in this figure legend, the reader is referred to the web version of this article.)

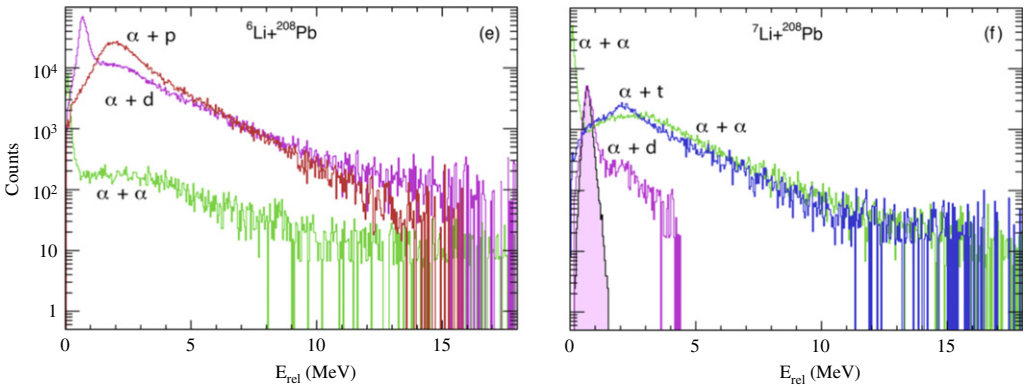

Fig. 31. (Color online) Relative energy spectra of the breakup fragments of ^{6}Li (left panel) and of ^{7}Li (right panel), in collisions with ^{208}Pb. The peaks at small E_{rel} correspond to delayed resonant breakup, which cannot influence fusion. The broad distributions at high relative energies correspond to prompt breakup, that may affect fusion. One can notice the important contribution of breakup following transfer in the case of delayed breakup.
Source: The figure is taken from Ref. [213].

respectively to ^{7}Li direct breakup and ^{8}Be breakup following the pick-up of one proton. Similar results were obtained for other targets [214]. In the case of ^{7}Li breakup in collisions with ^{144}Sm, the stripping of two neutrons followed by the breakup of ^{5}Li was found to be a very important prompt breakup mechanism. For the breakup of ^{9}Be in collisions with several heavy targets [212], most of the $\alpha - \alpha$ coincident events were related to the delayed ^{8}Be ground state breakup. Among the prompt breakup events, the ^{8}Be breakup following one-neutron transfer from ^{9}Be was found to be ten times larger than the breakup following inelastic excitation of the ^{9}Be.

Souza et al. [218] performed exclusive experiments to determine the kinematic of the $\alpha - d$ coincidences in the breakup of ^{6}Li. They studied the ^{6}Li $-$ ^{59}Co collision at $E_{lab} = 29.6$ MeV, which corresponds roughly to twice the Coulomb barrier energy. The experiments were performed in São Paulo, using 11 triple telescopes placed at the forward hemisphere. They used a semiclassical approach to analyze the collision dynamics, in order to determine time-scale of the breakup process. They concluded that breakup events populating the low-lying states in the continuum correspond to delayed processes whereas those going to higher energies could be associated with direct breakup.

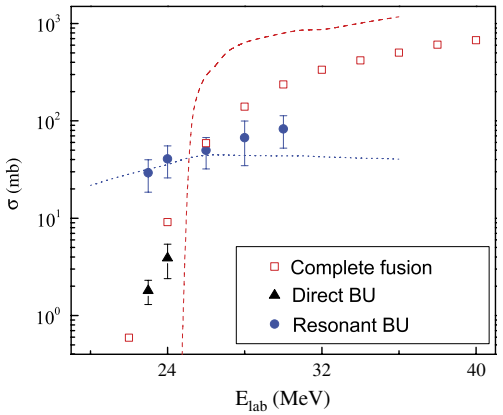

Fig. 32. (Color online) Total cross sections for resonant and non-resonant breakup of ^{6}Li, in collisions with ^{144}Sm. The CF cross section is also shown. The curves are predictions of the model of Refs. [182,100] for the CF (dashed red line) and NCBU (dotted blue line) cross sections.
Source: The figure was taken from Ref. [220].

Capurro et al. [220,225] studied ^{6}Li breakup in ^{6}Li + ^{144}Sm collisions. Their experiments were performed at the Tandar laboratory, in Buenos Aires. First, they made inclusive experiments at energies above and below the Coulomb barrier, with a detector at backward angles [225]. Analyzing the large alpha yields, they suggested that some of the alpha particles could have been produced by ^{5}Li breakup, following the transfer of one-neutron from ^{6}Li. Very recently, the same group performed exclusive measurements for the same system, using two telescopes [220]. They also measured relative energy distributions, like in Ref. [213]. They concluded that the resonant breakup through the 3^{+} state of ^{6}Li (delayed breakup) predominates over the non-resonant breakup.

The Argentinian group [220] developed a code called SUPERKIN [221,222], based on classical kinematics considering three body exit channel, to derive differential cross sections for their data [220]. Fig. 32 shows the direct (filled black triangles) and the resonant (filled blue circles) components of the breakup cross section, together with the CF data (open red squares). The dotted blue curve and the dashed red curve correspond respectively to the theoretical predictions of the classical model of Diaz-Torres [182,100,183] (see Section 5.2.1) for the NCBU (resonant + non-resonant) and CF cross sections. One can observe that the resonant breakup cross section is of the same order as the CF cross section at near-barrier energies, but it is much larger at energies below the Coulomb barrier. In this energy range the CF cross section drops rapidly, whereas the resonant breakup cross section decreases slowly with the collision energy.

The final step of this kind of investigation is to relate the prompt breakup events with the suppression of CF at energies above the barrier. This has been done [212–214] using a tri-dimensional classical dynamical model [182], through numerical calculations performed by the PLATYPUS code [183]. This model relates the suppression of CF above the barrier with the ICF of prompt breakup fragment. As the breakup events that may affect fusion are triggered by transfer, one may conclude that the effect of the breakup on fusion depends both on the properties of the projectile and target nuclei.

From the above discussion one learns that the breakup of weakly bound nuclei is much more complex than the simple picture of the direct dissociation of the projectile. Furthermore, it suggests that the influence of the breakup process on fusion cross sections is strongly dependent on its time scale. In this way, the recent experimental development described above is a new ingredient to shed light on the reaction mechanisms involved in collisions of weakly bound nuclei.

5. Fusion reactions: theoretical approaches

The general problem of fusion reaction of heavy ions has been under experimental and theoretical scrutiny over the last eight decades, since the seminal work of Gamow on the tunneling process and alpha radioactivity. Owing to the existence of the Coulomb barrier between charged particles, the very low energy tunneling probability or fusion is basically determined by the well known WKB expression for the transmission/tunneling through a real barrier,

$$\mathcal{T}(l,E) = \exp\left[-\frac{2}{\hbar}\int_{r_1}^{r_2} dr\,\sqrt{2\mu\,(V_l(r)-E)}\right] = \exp\big[-2\,\Phi(l,E)\,\big]. \tag{103}$$

Above, μ is the reduced mass of the projectile–target system and r_1 and r_2 are the inner and outer turning points. These points are determined from the condition $V_l(r) = E$, where E is the collision energy in the center of mass frame and $V_l(r)$ is the real interaction (Coulomb + nuclear + centrifugal terms), representing the barrier. Notice that the factor Φ is large at very low energies. For energies close to the top of the barrier, Φ becomes small, and in this case the expression for $\mathcal{T}(l,E)$ was derived by Kemble [237] and is given by,

$$\mathcal{T}(l,E) = \frac{1}{1+\exp\left[\,2\Phi(l,E)\right]}. \tag{104}$$

The fusion cross section is then evaluated using the above transmission coefficient in the partial-wave expansion,

$$\sigma_{\rm F}(E) = \frac{\pi}{k^2} \sum_{l=0}^{\infty} (2l+1)\, \mathcal{T}(l,E). \tag{105}$$

Notice that the Kemble formula fails at energies above the barrier of the $V_l(r)$ potential, denoted by B_l. Since there are no real classical turning points in this energy region,[14] Kemble's transmission factor has the constant value $\mathcal{T}(l,E) = 1/2$. This result disagrees with Quantum Mechanics, according to which the transmission coefficient tends to 1 as the collision energy increases beyond B_l. This shortcoming can be remedied by using the parabolic approximation for the barrier,

$$V_l(r) = B_l - \frac{1}{2}\,\mu\omega_l\,(r-R_l)^2\,,$$

where R_l is the radius of the barrier at the lth-partial wave and $\hbar\omega_l$ is the corresponding barrier curvature. Kemble used this approximation to correct his WKB expression above the Coulomb barrier. Hill and Wheeler [238] went further, using the parabolic approximation above and below the barrier. In this way, they got the closed expression,

$$\mathcal{T}(l,E) = \frac{1}{1+\exp\left[2\pi\,(E-B_l)\,/\hbar\omega_l\right]}. \tag{106}$$

Finally, Wong [174] managed to perform the l-sum in the fusion formula analytically. Using the Hill–Wheeler form of the tunneling probability and approximating:

$$\omega_l \simeq \omega_0 \equiv \omega, \qquad R_l \simeq R_0 \equiv R_{\rm B} \quad \text{and} \quad B_l \simeq V_{\rm B} + \frac{\hbar^2}{2\mu R_{\rm B}^2}\,(l+1/2)^2\,,$$

he obtained the now widely used Wong formula for fusion

$$\sigma_{\rm F}^{\rm (W)} = R_{\rm B}^2\,\frac{\hbar\omega}{2E}\,\ln\left[1+\exp\left\{\frac{2\pi\,(E-V_{\rm B})}{\hbar\omega}\right\}\right]. \tag{107}$$

Wong's formula is accurate for collision energies around the Coulomb barrier, where the parabolic expansion works. At lower energies, it becomes progressively different from the fusion cross section obtained by exact calculation of the probabilities of tunneling through the barrier of the bare potential.

On the other hand, the fusion cross section at sub-barrier energies is influenced by couplings with non-elastic channels, which lead to lower effective barriers. This effect is particularly strong for systems like ^{16}O + ^{154}Sm, where the rotational states of the highly deformed samarium isotope are easily excited. This entails modifying the fusion cross section predicted by the *naïve* barrier penetration model discussed [239–241]. A more formal demonstration that coupling to other degrees of freedom besides the radial separation enhances tunneling was given by Ref. [83] and more recently by Ref. [242].

Nowadays, powerful computer codes based on full Quantum Mechanics, like FRESCO [243], are available. They solve large sets of couple channel equations, including inelastic and transfer channels, or the breakup channel, within the CDCC approximation [12] (see Section 2.2.1).

5.1. Fusion barriers

Nuclear fusion is associated with the transmission of the incident wave through a potential barrier, resulting from nuclear attraction plus Coulomb repulsion. However the meaning of the fusion barrier depends on the description of the collision. Coupled channel calculations involve static barriers, corresponding to frozen densities of the projectile and the target. Changes in the intrinsic densities during the collision are taken into account through the population of non-elastic channels. However, in some time-dependent approaches, the densities change as the collision develops. One can then derive dynamic potential barriers in this way. In this section we consider some aspects of static and dynamic barriers.

5.1.1. Static fusion barriers

In the coupled channel description of nuclear collisions, the Hamiltonian contains a complex potential. Its imaginary part accounts for the flux lost to channels which are not explicitly included in the calculation. If all relevant channels are included, it represents exclusively fusion absorption. In most cases, the imaginary part of the potential is diagonal in channel space. In this way, the channel projected imaginary potential gives the probability of fusion through the corresponding channel. These potentials are very strong, have short-range and a small diffusivity, so that they absorb completely the current transmitted through the potential barrier.[15] As such, their effects are analogous to those of a black disk in the scattering of light.

[14] In fact, Kemble's formula can be extended to above-barrier energies if one considers complex turning points [237].

[15] According to Eq. (24), the fusion cross section depends strongly on the intensity of the channel wave functions at small distances, where the imaginary potential is strong. These wave functions are influenced by the real part of the bare potential but also by the channel coupling. Thus, fusion can be considered a tunneling problem but the tunneling is through effective barriers, rather then through the barriers of the bare potential [240,241].

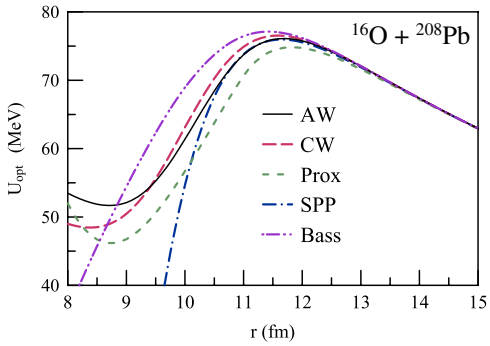

Fig. 33. (Color online) Potential barriers for the $^{16}O + ^{208}Pb$ according to different models for the bare potential available in the literature. *Source:* Figure taken from Ref. [7].

Frequently, one investigates the influence of some particular channels on fusion, comparing the predictions of coupled channel (CC) calculations with experimental data. For this purpose it is necessary to have a bare potential that gives a reasonable description of the fusion process when all couplings are weak.[16] Further, this potential should be valid for systems over a wide range of the periodic table. Unfortunately, there are several models for bare potentials and these models may lead to very different results. To illustrate this point, we compare the $^{16}O + ^{208}Pb$ barriers predicted by several models. We consider the potentials of Akyüz–Winther [244], Christensen–Winther [245], proximity [246], São Paulo (SPP) [125,126] and Bass [247]. The results are shown in Fig. 33, which was taken from Ref. [7]. The barriers may differ by a few MeV and this difference leads to very different cross sections, specially at sub-barrier energies.

Most of the recent studies of fusion, specially of weakly bound systems, use the Akyüz–Winther or the São Paulo approach to evaluate the bare potential. These approaches are based on the double-folding model [248], with the M3Y nucleon–nucleon interaction [249,250]. This interaction is appropriate for collisions at near-barrier energies, although it must be modified when the folding model is used in other situations, like in the study of deep sub-barrier fusion [251,252] or in large angle scattering at energies well above the barrier [253]. The São Paulo potential has the advantage of using realistic densities for the projectile and the target, and of including some effects of the Pauli Principle.[17] On the other hand, to evaluate this potential it is necessary to have a computer code to carry out the double-folding integration numerically. The Akyüz–Winther potential is much simpler. In this case, the double-folding integral is approximated so that the potential is given by a simple Woods–Saxon shape, with parameters given by smooth functions of the masses and charges of the collision partners. For this reason, this potential is adopted by many authors.

In most cases, the fusion barriers obtained with the São Paulo and the Akyüz–Winther potentials are very similar. Typically, the barrier heights agree within a few hundred keV and the radii agree within 0.5 fm. However, for systems having unusual densities, like halo nuclei, the agreement may be poorer. In such cases, it is safer to use the São Paulo potential. As an example, we show the fusion cross sections obtained in single-channel calculations using these potentials. In these calculations, fusion corresponds to absorption by a deep short-range imaginary potential. The results are shown on panels (a) (linear scale) and (b) (logarithmic scale) of Fig. 34. The cross sections below the Coulomb barrier ($E < V_B \sim 21$ MeV), where they change rapidly with E, are not close. On the other hand, at several MeV above the barrier the predictions of the two potentials agree within ∼20%. However, this is about the order of magnitude of the suppression of complete fusion in collisions of weakly bound nuclei.

The potential barriers in the coupled channel approach to fusion do not have the same meaning as in a realistic single-channel calculation. In the latter, the barrier is given by the sum of the bare potential in the elastic channel with the polarization potential arising from the channel-coupling interactions, as discussed in Section 2.3. To calculate the fusion cross section one evaluates the transmission factor through the barrier associated to the l-dependent effective potential,

$$V_l(r) = V^{\rm opt}(r) + V^{\rm pol}(r) + \frac{\hbar^2}{2\mu}\,\frac{l(l+1)}{r^2}. \tag{108}$$

Above, $V^{\rm opt} = U^{\rm bare} - iW^{\rm F}$ is the optical potential. Its real part is the bare potential and its imaginary part produces short range absorption, corresponding to fusion. The other term, $V^{\rm pol} = U^{\rm pol} - iW^{\rm pol}$, is the complex polarization potential. Its imaginary part takes into account the flux diverted from the elastic channel into inelastic, transfer and breakup channels. The fusion cross section is then given by the partial-wave series of Eq. (11), with the transmission factors, $\mathcal{T}^{\rm F}(l,E)$, given by Eq. (9). Since fusion absorption acts only within the barrier associated with the real part of the total potential, the fusion probability can be approximated by the corresponding transmission factor. A calculation along this line was performed by Keeley, Kemper and Rusek [203] to evaluate fusion cross sections in the $^{6,7}Li + ^{209}Bi$ collisions.

16 The coupling is weak if its inclusion in a coupled channel calculation leads to small changes in the cross sections, which can be neglected or treated by perturbative approximations.

17 These effects are not very important at near-barrier energies.

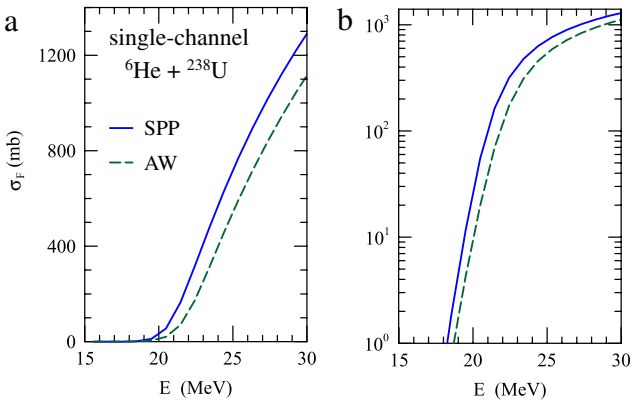

Fig. 34. (Color online) Fusion cross sections obtained in single-channel calculations using the Akyüz–Winther (dashed line) and the São Paulo potentials (solid lines) [254]. The results are shown in linear (panel (a)) and in logarithmic (panel (b)) scales.

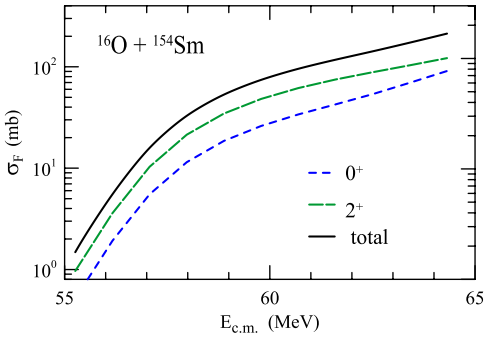

Fig. 35. (Color online) Contributions from the 0^+, and 2^+ channels to the fusion of the $^{16}O + ^{154}Sm$, in comparison with the total fusion cross section. The results were obtained in a coupled channel calculation including only the elastic and the first excited state in the rotational band of ^{154}Sm. For details, see the text.

Evaluations of the fusion cross section based on polarization potentials have some important limitations. First, one should make sure that the approximations involved in the derivation of the polarization potential are sufficiently accurate. An example of a realistic polarization potential, which is frequently used in the literature, is the one proposed by Thompson et al. [19]. The second limitation is the neglect of fusion through non-elastic channels. In realistic coupled channel calculations, the fusion cross section is given by a double sum over channels (Eq. (22)). Assuming that the coupling interaction is real, as it is frequently done, the cross section reduces to a sum of contributions from the elastic and the non-elastic channels (see Eqs. (23) and (24)).

In an idealized situation, where the polarization potential is calculated exactly, the single channel calculation including this potential reproduces the elastic wave function of the coupled channel equations. Consequently, its contribution to the fusion cross section, namely the $\alpha = 0$ term of Eq. (23), is reproduced exactly. However, the contributions from the non-elastic channels will be missing. This would not be a serious problem if these contributions were negligible. It could be the case of the CF cross section in collisions of weakly bound nuclei, if the couplings are dominated by the breakup channel. In this case, the breakup channel can only contribute to CF if all fragments are absorbed sequentially. This is a process of higher order, which tends to be less important that direct CF (this point will be discussed in detail in Section 5.2). On the other hand, in typical situations the contributions from non-elastic channels to the fusion cross section may be very important.

We illustrate this point with a simple coupled channel calculation. We consider the $^{16}O + ^{154}Sm$ collision, which is strongly influenced by the rotational band of the highly deformed ^{154}Sm nucleus. For simplicity, our CC calculation includes just the 0^+ and the 2^+ channels. In Fig. 35 we show the contributions from the 0^+ (short-dashed line) and from the 2^+ (long-dashed line) channels and also the total fusion cross section (solid line), which is the sum of the two contributions. It is clear that the contribution from the elastic channel is less important than that of the excited 2^+ channel. At energies around the barrier ($V_B = 60.4$ MeV) it is less than 30% of the total fusion cross section. The small contribution of the elastic channel results from the attenuation of the incident current, as the 2^+ channel is populated. In terms of the single channel approach, this reduction arises from the imaginary part of the polarization potential. We remark that this reduction will not occur in calculations that evaluate the fusion cross section using WKB tunneling probabilities. In this case, the attenuation of the incident current is neglected.

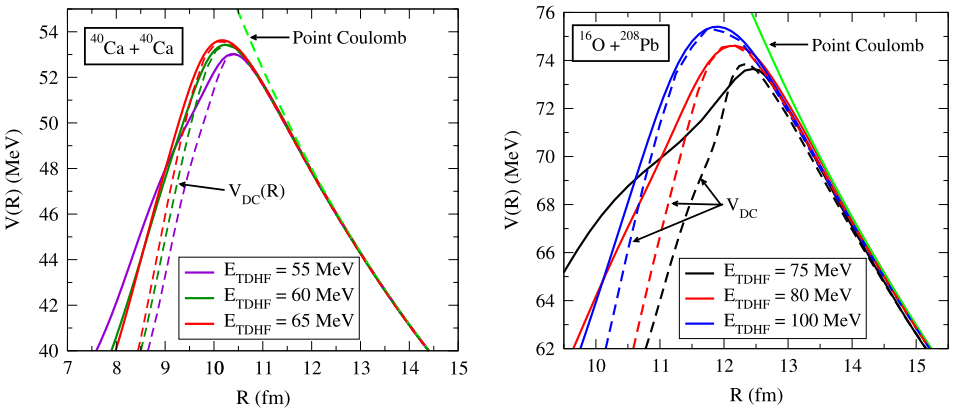

Fig. 36. (Color online) The dynamical barriers obtained by TDHF calculations for the ^{40}Ca + ^{40}Ca (left panel) and ^{16}O + ^{208}Pb (right panel) systems [256]. The solid lines and the dashed lines correspond respectively to dynamical barriers for coordinate-dependent and coordinate-independent mass parameters. Further details can be found in the original paper.

5.1.2. Time-dependent Hartree–Fock and Hartree–Fock approaches to dynamic fusion barriers

A microscopic approach to the calculation of the fusion barriers is certainly desired. This has been done by several authors using the TDHF method. Of course this theory cannot calculate the tunneling probability itself, as it is "classical" in the sense that the density matrix evolves in time and in the space of determinants in a classical way. Nevertheless, the method supplies a powerful mean to obtain the interaction potential between the two ions at distances allowed by the its limitations. The idea is to determine the densities through the equation,

$$i\hbar\frac{d\rho}{dt} = [h(\rho), \rho], \tag{109}$$

where $h(\rho)$ is the density-dependent Hamiltonian density. The Skyrme interaction is used for the potential part of $h(\rho)$. Currently there are available codes for three dimensional TDHF and HF calculations, which are used to solve the above equation. The HF equation is simply obtained by setting the time derivative equal to zero. That is,

$$[h(\rho), \rho] = 0. \tag{110}$$

In Refs. [255,256] the TDHF was employed for the calculation of the fusion barriers of the ^{A_1}Ca + ^{A_2}Ca, and ^{16}O + ^{208}Pb systems, while in Ref. [257] the calculations were based on the HF theory. Further, in the latter the TDHF was used to account for the excitation of collective states in the symmetric systems ^{40}Ca + ^{40}Ca and ^{56}Ni + ^{56}Ni. Both the TDHF and the HF calculations supply the energy of the combined system $E_{A_1+A_2}$, and the ion–ion interaction is calculated as [258],

$$V(R) = E(A_1 + A_2, R(t)) - E_1 - E_2, \tag{111}$$

where E_i is the binding energy of nucleus i, calculated within HF using the same Skyrme effective interaction. In these works, the fusion cross section and the barrier distributions are calculated a posteriori using a Schrödinger equation with an incoming wave boundary condition.

In Fig. 36 we show the barriers obtained in the TDHF calculations of Umar, Simenel and Oberacker [256] for the ^{40}Ca + ^{40}Ca (left panel) and ^{16}O + ^{208}Pb (right panel) systems (solid lines). The energies $E_{\rm TDHF}$ indicated in these figures correspond to the center of mass energies. It is clear from these calculations that the fusion barrier does depend on the energy as it is a dynamical quantity. This energy dependence is found to be more pronounced in the highly asymmetrical system, ^{16}O + ^{208}Pb. The dashed lines are the scaled potentials obtained through a coordinate transformation that eliminates the coordinate dependence of the mass [255]. The calculated TDHF barriers were shown to be particularly good in accounting for the deep sub-barrier fusion. Simenel et al. [257] used the potential obtained from the HF calculation to perform a CC calculation of fusion using the code CCFUS. The calculations included the channels corresponding to excitations of states with small amplitude obtained with the TDHF. They compared the resulting barrier distributions with data. The results of these microscopic calculations are quite encouraging and certainly should be pursued further. They supply fusion barriers which are free from the inherent uncertainties in the phenomenological ones.

5.2. Fusion of weakly bound systems

As we have discussed in Section 3.3.1, there are different fusion processes in collisions of weakly bound nuclei: complete fusion, which is the sum of the direct and the sequential contributions, and incomplete fusion. The sum of complete and incomplete fusion is called total fusion. In this section, we discuss the theoretical approaches to describe these processes. We begin with the earliest works, in which some of the relevant aspects of the problem were taken into account in a schematic way, going to the most recent treatments using powerful coupled channel calculations involving the continuum.

Fusion reactions with weakly bound nuclei are influenced by several factors. These factors are listed below.

1. *Static enhancement effect:* weakly bound nuclei have one or more nucleons with small binding energy. This leads to nuclear densities with tails spreading out further than those of tightly bound nuclei, giving rise to lower fusion barriers. An immediate consequence is that the resulting fusion cross section is larger than it would be if all nucleons were tightly bound.
2. *Dynamical suppression of* CF: Owing to the low breakup threshold, the couplings with the breakup channel are much stronger than for tightly bound systems. This leads to an attenuation of the incident current, with large population of channels in the continuum. Since the latter cannot produce direct complete fusion, the main part of the CF cross section, this dynamic effect hinders the CF cross section, specially at above-barrier energies. This behavior can be identified in the data, as we will shown in Section 6.4.
3. *Dynamical enhancement of sub-barrier fusion*: Similarly to the case of tightly bound system, the couplings among bound channels lead to lower eigen-barriers. This effect brings about large enhancements of the fusion cross section at sub-barrier energies.

The first theoretical studies of fusion reactions with weakly bound nuclei, in the early nineties, considered these effects only partially. Takigawa and Sagawa [259] studied the correlation between the breakup threshold energy and the barrier height and made estimates of the static enhancement of fusion in collisions of the ^{11}Li halo nucleus. The dynamic hindrance of ^{11}Li fusion reactions was investigated by Hussein et al. [260] and Takigawa, Kuratani and Sagawa [261]. In these papers the effects of couplings with the breakup channel were taken into account through the inclusion of an imaginary polarization potential in the elastic channel. In these works, the couplings with bound channels were treated very schematically, through a shift of the collision energy. These couplings were better treated in the work of Dasso and Vitturi [262], who showed that the fusion cross section below the Coulomb barrier was strongly enhanced. The different conclusions of these works resulted from the fact that they were very schematic calculations which did not consider properly the different effects listed above. These works investigated the CF cross section but did not make any estimate of the IFC cross section.

5.2.1. Classical and semiclassical approaches to CF and ICF

The first calculations of separate cross sections for the CF and ICF processes were performed by Hagino, Dasgupta and Hinde [180,181], treating the reaction as a three-body problem in two dimensions and using classical physics. Their model is briefly described below (for details see Ref. [181]). The three-body system consisting of the target (T) and the two projectile's fragments (1 and 2) is represented by the position vectors $\mathbf{R}(t)$, $\mathbf{r}_1(t)$ and $\mathbf{r}_2(t)$. The motion is kept on the x-y plane, with x being the direction of the incident beam. The classical dynamics is determined by the Hamiltonian

$$H = \frac{P_{\rm T}^2}{2m_{\rm T}} + \frac{p_1^2}{2m_1} + \frac{p_2^2}{2m_2} + V_{\rm T1}\left(\mathbf{R}-\mathbf{r}_1\right) + V_{\rm T2}\left(\mathbf{R}-\mathbf{r}_2\right) + V_{12}\left(\mathbf{r}_1-\mathbf{r}_2\right). \tag{112}$$

The calculation begins at $t = 0$, with the target at rest at the origin of the laboratory frame. The projectile (P) has the initial coordinates $X_P(0) = R_{\rm max}$ and $Y_P(0) = b$, where $R_{\rm max}$ is some large distance and b is the impact parameter, and it approaches the target with an initial velocity parallel to the x-axis. The modulus of this velocity is determined by the collision energy in the laboratory frame and the potentials $V_{\rm T1}$ and $V_{\rm T2}$ taken at the initial positions of the fragments $r_1(0)$ and $r_2(0)$. These positions are given in terms of the projectile's coordinates and the initial relative vector $\mathbf{r}(0)$, which is chosen randomly, but constrained to the classically allowed region. The initial velocities are treated similarly.

Classical approximations are widely used in heavy ion collisions at near-barrier energies. In this case, the de Broglie wave-lengths are small in comparison with typical lengths of the system, so that classical concepts may be used [263–266]. Hagino, Dasgupta and Hinde [180,181] employed the classical equations of motion derived from the Hamiltonian of Eq. (112) to study the time-evolution of the three-body system. These dynamical equations are run with a selection of initial conditions that sample the available phase-space. Fusion of a single fragment (ICF) or both (CF) takes place if the barrier of the target is transposed. Further, the model can distinguish DCF from SCF. The former takes place when the two-fragments remain bound when they fuse with the target and the latter occur otherwise. Finally, if the two fragments become unbound during the collision but neither fuse with the target, the final state corresponds to NCBU.

The model described above was used to calculate TF and CF cross sections for the ^{6,7}Li + ^{209}Bi systems [180] and the results were compared to the data. They are shown in Fig. 37, which was taken from Ref. [180]. The comparisons indicate that despite its classical nature, the classical trajectory three-body model leads to quite reasonable results, except at low collision energies, near and below the fusion barrier. Since this region is strongly influenced by tunneling effects, absent in a classical model, this discrepancy should be expected.

Diaz-Torres et al. [182,100,183] developed an improved version of the classical model, extending it to three dimensions and treating the breakup of the projectile as a stochastic process. An R-dependent breakup probability can be inferred from experimental breakup cross sections or from CDCC calculations [182]. In a collision with energy E_0 and angular momentum L_0, the breakup probability depends exponentially on the distance of closest approach, $R_{\rm ca} \equiv R_{\rm ca}(E_0, L_0)$, and one can write [182,100,183],

$$P_{\rm BU}(R_{\rm ca}) \equiv 2\int_{R_{\rm ca}}^{\infty} \mathcal{P}_{\rm BU}^{\rm L}(R)\, dR = A\, e^{-\alpha R_{\rm ca}}. \tag{113}$$

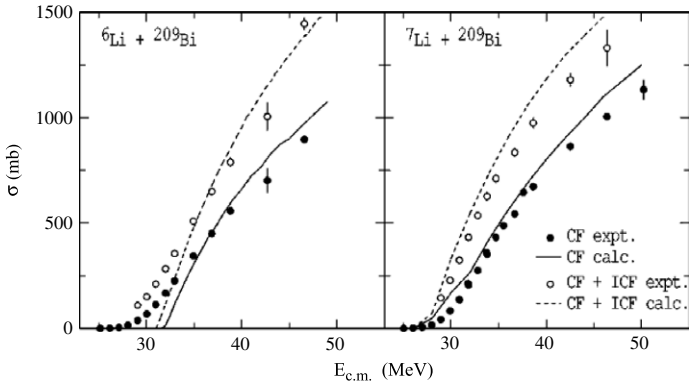

Fig. 37. CF and TF cross sections in the ^{6,7}Li + ^{209}Bi collisions. The solid line and the dashed line correspond respectively to the CF and TF cross sections calculated by the three-body classical trajectory model.
Source: The calculations and the data are from the work of Dasgupta et al. [180].

Above, $\mathcal{P}^{\rm L}_{\rm BU}(R)$ is the probability density for breakup during the motion from R to $R+dR$. A detailed derivation of this equation can be found in appendix A of Ref. [100]. The values of the constants A and α can be extracted from breakup cross sections, either by fitting data or results of CDCC calculations, and then $\mathcal{P}^{\rm L}_{\rm BU}(R)$ can be determined. The classical calculations of NCBU, CF, and ICF in this model are similar to those of Refs. [180,181]. However, the classical motion is in three dimensions and the trajectory calculation changes instantaneously from a two-body system (P and T) to a three-body one (fragment-1, fragment-2 and T) at the moment of breakup.

This model was used to evaluate the CF and ICF cross section for the ^{9}Be + ^{208}Pb system, and the results compared with the data [182]. The complication of the three-fragment ^{9}Be projectile ($\alpha + \alpha + n$) was avoided replacing it by a pseudo two-fragment ^{8}Be projectile ($\alpha + \alpha$). The theoretical results, which were shown to depend strongly on the choice of $\mathcal{P}^{\rm L}_{\rm bu}(R)$, were in qualitative agreement with the data.

Very recently, Marta, Canto and Donangelo [184] developed a method to include tunneling effects in a calculation of individual CF and ICF cross sections. Although there are several quantum mechanical calculations of fusion in collisions of weakly bound nuclei, they cannot separate the CF and ICF components of the TF cross section, except for some particular systems (see Section 5.2.2). They used a semiclassical method, where the projectile–target relative motion is described by classical mechanics, whereas the intrinsic dynamics of the collision partners is treated by time-dependent quantum mechanics [263]. This method has been widely used in nucleus–nucleus collisions [266,267]. When the breakup channel is taken into account [186,268,265], it is necessary to discretize the continuum using the same procedures as in the CDCC method (see Section 2.2.1).

With the classical treatment, the projectile–target separation vector becomes a known function of the time, $\mathbf{R}(t)$, and so do the interactions of the target with the fragments. The relative wave function of the fragments in a collision with impact parameter b, $\psi_b(\mathbf{r}; t)$, is the solution of the equation,

$$\left[h + V_{\rm T1}(\mathbf{r}, t) + V_{\rm T2}(\mathbf{r}, t)\right] \psi_b(\mathbf{r}, t) = i\hbar \frac{d}{dt}\, \psi_b(\mathbf{r}, t). \tag{114}$$

To solve this equation, the wave function is expanded in terms of the bound, $\varphi_i(\mathbf{r})$, and unbound, $\varphi_\varepsilon(\mathbf{r})$ eigenfunctions of the intrinsic Hamiltonian, h, as

$$\psi_b(\mathbf{r}, t) = \sum_i c_i(b, t)\, e^{-i\varepsilon_i t/\hbar}\, \varphi_i(\mathbf{r}) + \int d\varepsilon\, c_\varepsilon(b, t)\, e^{-i\varepsilon t/\hbar}\, \varphi_\varepsilon(\mathbf{r}). \tag{115}$$

Using this expansion in Eq. (114), one obtains an infinite set of coupled first order differential equations for the amplitudes, which is reduced to a finite set through the CDCC procedure. These equations are then solved starting from a point where the projectile–target distance is large enough for the coupling interaction to be negligible, with the projectile in its ground state ($\varphi_0(\mathbf{r})$). One then sets the initial conditions: $c_i = \delta_{i0}$, $c_\varepsilon = 0$.

The collision evolves until the projectile reaches the distance of closest approach or goes inside the potential barrier. From the values of the amplitudes at this instant one gets the breakup probability, $P_L^{\rm bup}$, and the momentum distribution of the continuum component of the wave function. The DCF cross section is then evaluated by the expression,

$$\sigma_{\rm DCF} = \frac{\pi}{K^2} \sum_L (2L+1) \left(1 - P_L^{\rm bup}\right) T_L^{(\rm P)}, \tag{116}$$

where K is the incident wave number and $T_L^{(\rm P)}$ the tunneling probability, which is approximated by the Hill–Wheeler formula [238]. The expressions for the ICF cross sections of the two fragments and that for SCF are more complicated, since

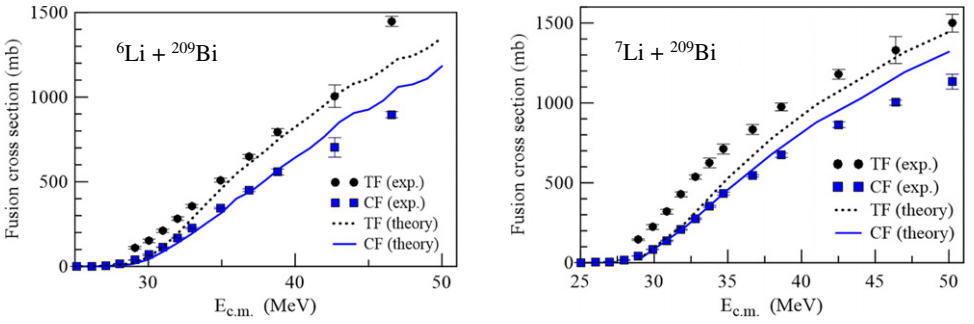

Fig. 38. (Color online) Left panel: Semiclassical CF (solid line) and TF (dotted line) cross sections for the ^{6}Li + ^{209}Bi system [184], in comparison with the corresponding experimental results. Right panel: same as left panel but for the ^{7}Li + ^{209}Bi system.
Source: The data are from Ref. [269].

they are given by integrations over the momentum distribution of the relative wave function in the continuum multiplied by the corresponding fusion probabilities, P_{F_1}, P_{F_2} and P_{SCF}. These probabilities are calculated by the equations

$$P_{F_1} = T^{(1)}\left[1 - T^{(2)}\right], \qquad P_{F_2} = T^{(2)}\left[1 - T^{(1)}\right] \quad \text{and} \quad P_{SCF} = T^{(1)}\,T^{(2)}, \tag{117}$$

where $T^{(1)}$ and $T^{(2)}$ are transmission coefficients for the two fragments, also calculated within the Hill–Wheeler approximation.

This method was used to study CF and TF in the ^{6,7}Li + ^{209}Bi collisions, and the theoretical cross sections were compared to the data of Dasgupta et al. [180,269]. The results are shown in Fig. 38. In the case of ^{6}Li, the theoretical CF is in very good agreement with the data and the agreement for the TF cross sections is also good. In the case of ^{7}Li, the agreement for CF remains good, specially below 40 MeV, but the agreement for TF is considerably poorer. It has been suggested [184] that the discrepancy may arise from important channels that have not been taken into account in the theory. First, the nuclei produced by ICF can also be produced by cluster transfer, which is an entirely different mechanism. Cluster transfer corresponds to a single step process whereas ICF requires two steps. The second factor, is that there are strong experimental evidences [214,216] that nucleon transfer plays a very important role in the ^{7}Li − ^{209}Bi collision and these channels are not considered in the theory. A final remark on the calculations of Ref. [184] is that the contribution from the SCF to the CF cross section is quite relevant, reaching 30%–40% of that from DCF. The importance of the SCF contribution to the CF cross section has also been emphasized in the very recent work of Boselli and Diaz-Torres [270], where they studied the different fusion mechanisms with a schematic quantum model.

The study of Ref. [184] suggests that semiclassical calculations may be able to describe the fusion processes involved in collisions of weakly bound nuclei. These calculations are simpler, and, as they involve classical trajectories, more easy to visualize than the full quantum mechanical calculations of CDCC.

5.2.2. Quantum mechanical CDCC calculations of fusion cross sections

The most powerful theoretical tool to calculate fusion cross sections in collisions of weakly bound systems is the CDCC method, introduced in Section 2.2.1. Calculations along this line were performed by several authors [10,203,271–273]. In these calculations, the fusion cross sections are given by the absorption arising from short-range imaginary potentials with small diffusivity parameters, which depend on the projectile–target distance, or on the relative coordinates of the target with respect to the fragments. For a detailed discussion of this point we refer to the work of Thompson and Diaz-Torres [274].

Most of CDCC calculations of fusion adopt complex potentials for the interaction between the target and each fragment. Diaz-Torres, Thompson and Beck [272] used this procedure and identified the TF cross section with the absorption due to the imaginary part of the sum of the fragment–target potentials. They applied this method to the ^{6,7}Li + ^{59}Co and ^{6,7}Li + ^{209}Bi systems and compared the available data with the results of calculations with and without breakup couplings. They concluded that the breakup channel does not lead to appreciable changes in the cross section well above the barrier but enhances the cross section near and below the barrier. This effect is more pronounced in the case of ^{6}Li projectiles, which has a lower breakup threshold.

A few years later, Beck, Keeley and Diaz-Torres [275] used the same approach to calculate the TF cross section for ^{6}He projectiles on a ^{59}Co target, at near-barrier energies. In their calculations, they approximated the two-neutron halo structure of ^{6}He by a di-neutron. Comparing the results with the corresponding experimental cross sections for the stable ^{6}Li and ^{4}He projectiles on the same target, they found that the ^{6}He cross section is much larger than those for ^{6}Li and ^{4}He over the whole energy range.

In a very recent paper Jha, Parkar and Kailas [273] performed similar CDCC calculations to obtain TF, transfer and breakup cross sections in collisions of ^{9}Be projectiles with targets in different mass ranges. They performed a CDCC–CRC calculation that takes into account transfer and breakup couplings [206]. They make the simplifying assumption that ^{9}Be is formed by two fragments: a ^{8}Be core and a neutron. This greatly simplifies the calculations. On the other hand, it leaves no room

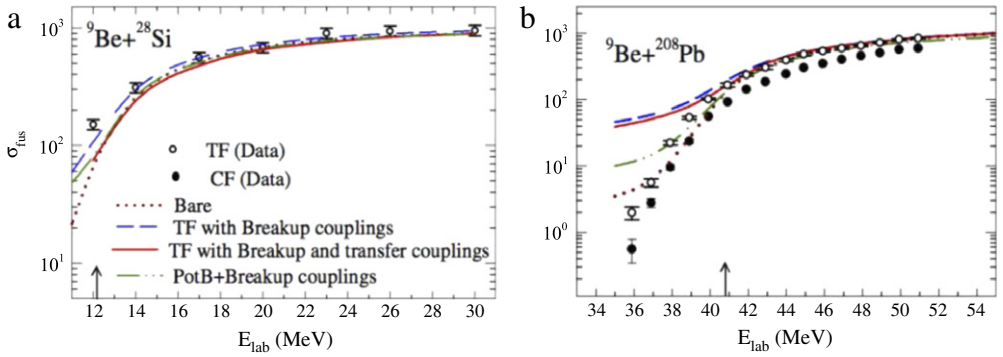

Fig. 39. (Color online) CDCC calculations of the TF cross sections in collisions of ^{9}Be projectiles with ^{28}Si (panel (a)) and ^{208}Pb (panel (b)) targets [273]. For details, see Ref. [273].
Source: The data for the ^{28}Si and the ^{208}Pb targets are respectively from Refs. [276] and [269].

for a quantitative description of ICF, where an α-particle produced in the breakup of ^{9}Be fuses with the target. As in Refs. [272,275], the projectile–target interaction is given by the sum of two complex potentials, $V_{^{8}\mathrm{Be}-\mathrm{T}}$ and $V_{n-\mathrm{T}}$. These potentials contain short-range imaginary terms ($r_0 = 0.9$ fm and $a = 0.25$ fm) that account for the absorption of the fragments by the target. The fusion cross section is evaluated by the expression,

$$\sigma_{\mathrm{F}} = \sigma_{\mathrm{R}} - \sum_{\alpha\neq 0} \sigma_{\alpha}. \tag{118}$$

Above, σ_{R} is the total reaction cross section and σ_{α} is the cross sections for excitation of channel α. The elastic channel, represented by $\alpha = 0$, is excluded from the summation. The absorption cross section is calculated in terms of the modulus of the l-components of the elastic S-matrix, through the expression

$$\sigma_{\mathrm{R}} = \frac{\pi}{k^2} \sum_{l} (2l+1)\left[1 - |S_{0l}|^2\right]. \tag{119}$$

Fig. 39 shows results for two of the systems studied in Ref. [273]: ^{9}Be + ^{28}Si (panel (a)) and ^{9}Be + ^{208}Pb (panel (b)). The experimental TF and CF (when available) cross sections are compared with the results of several calculations, as indicated in the legend of panel (a). Some calculations include transfer couplings and others do not. The fusion cross sections obtained by single-channel calculations with only the bare potential are also shown. The results labeled as PotB, are obtained neglecting the absorption of the neutron. The overall agreement with the data is reasonable, specially above the barrier. In the case of the ^{208}Pb target, the theoretical cross sections overestimate the data, specially when it includes neutron absorption which, from the experimental point of view, does not correspond to fusion of any kind.

An important shortcoming in the above papers is that they do not consider what happens to the remaining fragments when a particular one fuses with the target. Thus, it only gives the total fusion cross section, being unable to predict the CF and ICF contributions, separately. This problem does not occur in the CDCC calculations of Hagino et al. [271] and Diaz-Torres and Thompson [10]. These authors adopt a single imaginary potential, representing the absorption of the whole projectile by the target. Thus, it is a function of the vector joining the centers of mass of the collision partners, **R**, whereas it is independent of the intrinsic coordinates of the projectile, **r**. In this way, the imaginary potential is diagonal in channel-space. The use of a diagonal imaginary potential is justified as the non-diagonal terms are quite small due to the fact that they represent absorption and excitation at the same time (multistep process).

The general expression of the fusion cross section (Eq. (22)) then becomes much simpler. It reduces to a sum of contributions from the channels involved in the calculation (Eqs. (23) and (24)), bound and unbound. It is then possible to associate the contributions from bound channels with CF.

The meaning of contributions from unbound channels is not so clear. In this case, the distance between the fragments, $|\mathbf{r}|$, tends to be very large, so that the center of mass of the projectile is far from both fragments. However, if the mass of one fragment, say F_1, is much larger than that of F_2, the center of mass of the projectile is close to that of F_1. Thus, when the center of the projectile lies within the range of the imaginary potential the same tends to happen with the heavy fragment. On the other hand, in this situation the lighter fragment is frequently outside the range of absorption. It is then reasonable to assume that the contributions from unbound channels to fusion correspond to ICF. In the case of the ^{11}Be + ^{208}Pb system, studied in Refs. [10,271], the ^{11}Be projectile dissociates into a ^{10}Be fragment and a neutron. The above condition is then clearly satisfied. The absorption in the unbound channels is then attributed to ICF.

The calculations of Diaz-Torres and Thompson [10] are similar to the earlier work of Hagino et al. [271]. However, they are improved in two ways. First, they extend the discretized basis of the continuum to higher energies and larger angular momenta, to achieve proper convergence of the calculations. The second modification is that they take into account the continuum–continuum couplings (CCC), which were left out in Ref. [271]. Both calculations lead to the same qualitative

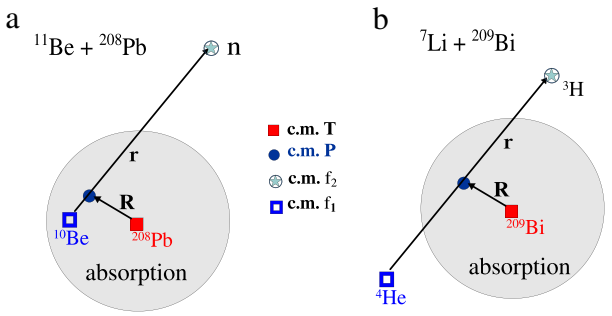

Fig. 40. (Color online) Absorption from an unbound channel in two situations. Panel (a) represents the breakup of ^{11}Be in ^{11}Be + ^{208}Pb collisions, with the projectile's center lying within the imaginary potential (gray region). In this case it is likely that the heavy fragment is within the range of absorption whereas the light fragment is not. Panel (b) corresponds to the breakup of ^{7}Li in a ^{7}Li + ^{209}Bi collision. Now the two fragments have similar masses. In this case, the c.m. of the projectile may be within the imaginary potential with both fragments lying outside.

conclusion: when the CF cross section is compared with predictions of one-dimensional barrier penetration models, it is enhanced at low enough energies and is hindered at high enough energies. However, the energy where the transition from enhancement to hindrance takes place is quite different in each calculation. The inclusion of CCC reduces considerably the CF cross section at all energies. Consequently, the CF cross section of Diaz-Torres and Thompson is hindered at energies around and above the Coulomb barrier. Only at energies a few MeV below the Coulomb barrier their CF cross section exceeds the prediction of one-dimension barrier penetration models. For a more quantitative comparison of these calculations, we refer to Ref. [6].

However, when the two fragments have comparable masses, the approach of Refs. [10,271] cannot be used. In this case, unbound states of the projectile correspond to a situation where both fragments are far from the projectile's center of mass. Thus, the center of the projectile being within the range of the imaginary potential does not imply the absorption of any fragment. Fig. 40 illustrates continuum states of two systems: ^{11}Be + ^{208}Pb (panel (a)) and ^{7}Li + ^{209}Bi (panel (b)). In the former the CDCC method can be applied to calculate separately the CF and ICF cross sections, whereas in the latter it cannot.

Keeley, Kemper and Rusek [203] used the CDCC approach in an indirect investigation of the ^{6,7}Li + ^{16}O fusion reactions. Their calculations were developed in two steps. First, they performed CDCC calculations to derive the dynamic breakup polarization potentials for the ^{6,7}Li + ^{16}O systems, adopting the prescription of Thompson et al. [19] (see Section 4.4), as it has been done in a previous work of the group [277]. The projectile–target interaction was given by the sum of the fragment–target optical potentials. That is, the interactions of the target with ^{2}H and ^{4}He, for ^{6}Li, and with ^{3}H and ^{4}He, for ^{7}Li. The CDCC calculations took into account the bound states of the projectile and both its resonant and non-resonant breakup. Next, they evaluated the fusion probability at each partial wave as the transmission factor through the one-dimension barrier determined by the sum of the real parts of the optical and the breakup polarization potentials. Their theoretical cross sections were shown to be in reasonable agreement with the data.

Similar calculations were performed by Keeley, Kemper and Rusek to study ^{7}Li + ^{208}Pb and ^{7}Be + ^{208}Pb fusion [278], and the same approach was used to investigate the influence of the breakup channel on ^{6}Li + ^{209}Bi and ^{6}He + ^{208}Pb fusion reactions [279,280]. They have shown that the CF of ^{6}Li + ^{209}Bi is mainly influenced by nuclear breakup, whereas in the CF of ^{6}He + ^{208}Pb Coulomb breakup dominates.

We remark that this approach may have two shortcomings. First, it does not take into account the imaginary part of the polarization potential, which would attenuate the incident current. This attenuation would reduce the CF cross section. The importance of this effect depends on the strength of the imaginary part of the polarization potential. Rusek et al. [280] have shown that this strength is related with the choice of the imaginary part of the fragment–target interactions. If one considers fragment–target optical potentials with short-range absorption, then the imaginary part of the polarization potential is important. On the other hand, if the optical potentials still contribute significantly to the absorption in the Coulomb barrier region, then the imaginary part of the polarization potential is much smaller. The second shortcoming is that the single channel description of the collision (including the breakup polarization potential) cannot account for fusion through non-elastic channels. The contribution from the breakup channel to CF could only take place through the sequential absorption of the fragments by the target. This process would not be expected to be important, since it is of third order. That is, breakup followed by the absorption of fragment 1 followed by the absorption of fragment 2. However, classical [180,181] and semiclassical [184] estimates indicate that they may correspond to 30%–40% of the CF cross section.

More recently, the polarization potential approach was used to investigate the influence of continuum–continuum couplings (CCC) on the CF cross section [281]. Diaz-Torres and Thompson have clearly shown that the inclusion of CCC leads to a strong suppression of the CF. The nature of this effect can be qualitatively understood in terms of the breakup polarization potential. The situation is schematically represented in panel (a) of Fig. 41, for the ^{8}B + ^{58}Ni system. It shows the incident ($j_{\rm in}$), reflected ($j_{\rm R}$) and transmitted ($j_{\rm T}$) currents around the barrier of the total (optical + polarization + centrifugal) potential. In this approach, the fusion process corresponds to the total absorption of $j_{\rm T}$, as it reaches the strong imaginary potential inside the barrier. As the projectile approaches the target, the incident current is attenuated by the imaginary part

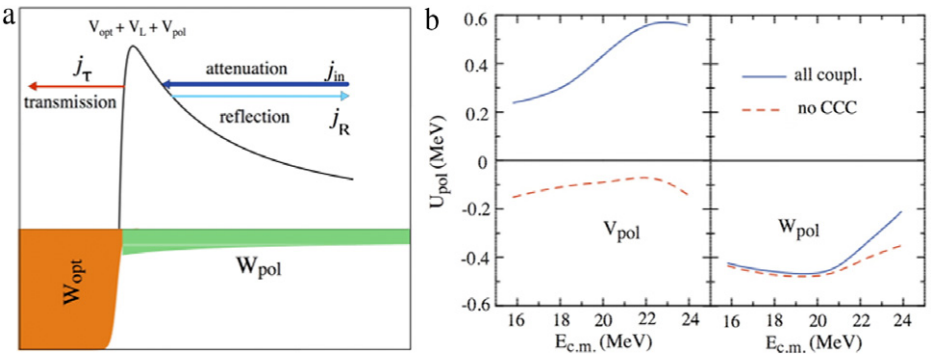

Fig. 41. (Color online) (a): Schematic representation of the incident, reflected and transmitted currents in the neighborhood of the barrier (for details see the text). (b): Real (left panel) and imaginary (right panel) parts of the polarization potential for the $^{8}B + {}^{58}Ni$ system. Polarization potentials based on CDCC calculations including and not including CCC are represented respectively by solid and dashed lines.
Source: The figures on both panels were taken from Ref. [281].

of the polarization potential and at the classical turning point the current is partly reflected and partly transmitted. Thus, a reduction of the transmitted current, and hence the CF cross section, can be caused both by a higher barrier, due to the real part of the polarization potential, or an increase of the long-range absorption, arising from the imaginary part of the polarization potential. These possibilities were checked in Ref. [281]. The authors used the method of Thompson et al. [19] to evaluate the breakup polarization potential in the CDCC description of the $^{8}B + {}^{58}Ni$ collision. The real and the imaginary parts of the polarization potential were evaluated at the barrier radius, as a function of the collision energy. The calculations were performed without (dashed lines) and with CCC (solid lines). The results are shown in panel (b) of Fig. 41. One observes that the inclusion of the CCC does not lead to appreciable changes in the imaginary part of the polarization potential. On the other hand, it has a strong influence on its real part. Without the CCC the polarization potential gives an attractive correction to the barrier. The inclusion of the CCC changes completely the situation, changing the sign of the correction. In this case, it makes the barrier higher. This leads to a strong suppression of CF, as found in the CDCC calculations of Diaz-Torres and Thompson [10].

Hashimoto et al. [282] proposed an interesting way to determine individual CF and ICF cross sections in CDCC calculations. They considered collisions of a deuteron beam with a ^{7}Li target. In this case, the projectile dissociates into two particles: a proton (position vector $\mathbf{r}_1$ with respect to the target) and a neutron (position vector $\mathbf{r}_2$). In their approach, the projectile–target interaction is given by a sum of complex potentials representing the interaction of each projectile's particle with the target, $V_1(\mathbf{r}_1) + V_2(\mathbf{r}_2)$. Thus, the imaginary part of each potential accounts for the absorption of the corresponding particle (the proton or the neutron). In this way, CF corresponds to the situation where both particles are absorbed, whereas in ICF one particle is absorbed while the other is not. The new idea of Ref. [282] is to associate the CF and ICF cross sections to contributions with different regions of the $\{\mathbf{r}_1, \mathbf{r}_2\}$-space, as shown on the left panel of Fig. 42. If the modulus of $\mathbf{r}_i$ $(i = 1, 2)$ in the integrand is kept inside the range of absorption, fragment i fuses. Complete fusion is obtained imposing this restriction on the coordinates of both fragments, whereas ICF is obtained keeping the coordinates of one of the fragments inside the absorption range and those of the other outside it. The first step to implement this procedure is to perform a change of variables: $\{\mathbf{R}, \mathbf{r}\} \rightarrow \{\mathbf{r}_1, \mathbf{r}_2\}$, leading to the transformation

$$|\Psi(\mathbf{r}, \mathbf{R})|^2 \; d^3\mathbf{r}\, d^3\mathbf{R} \rightarrow |\Phi(\mathbf{r}_1, \mathbf{r}_2)|^2 \; d^3\mathbf{r}_1\, d^3\mathbf{r}_2.$$

One then calculates the cross sections through integrals of the total imaginary potential, $\mathrm{Im}\{V(\mathbf{r}_1, \mathbf{r}_2)\} \equiv \mathrm{Im}\{V_1(\mathbf{r}_1) + V_2(\mathbf{r}_2)\}$, over selected regions of the $\{\mathbf{r}_1, \mathbf{r}_2\}$-space, as follows

$$\sigma_{CF} = \int_{|\mathbf{r}_1|<\mathbf{r}_{abs};\ |\mathbf{r}_2|<\mathbf{r}_{abs}} F(\mathbf{r}_1, \mathbf{r}_2)\, d^3\mathbf{r}_1\, d^3\mathbf{r}_2, \tag{120}$$

$$\sigma_{ICF_1} = \int_{|\mathbf{r}_1|(\mathbf{r}_{abs};\ |\mathbf{r}_2|)\mathbf{r}_{abs}} F(\mathbf{r}_1, \mathbf{r}_2)\, d^3\mathbf{r}_1\, d^3\mathbf{r}_2, \tag{121}$$

$$\sigma_{ICF_2} = \int_{|\mathbf{r}_1|>\mathbf{r}_{abs};\ |\mathbf{r}_2|<\mathbf{r}_{abs}} F(\mathbf{r}_1, \mathbf{r}_2)\, d^3\mathbf{r}_1\, d^3\mathbf{r}_2. \tag{122}$$

Above, we used the short-hand notation,

$$F(\mathbf{r}_1, \mathbf{r}_2) = \frac{1}{|A|^2}\,\frac{k}{E}\;\; |\Phi(\mathbf{r}_1, \mathbf{r}_2)|^2 \;\mathrm{Im}\{-V(\mathbf{r}_1, \mathbf{r}_2)\}\,. \tag{123}$$

Using this method Hashimoto et al. [282] calculated the TF and the CF cross sections for the $^{2}H + {}^{7}Li$ system. The results are shown on the right panel of Fig. 42 as functions of the collision energy, E_d^{L}. Cross sections for the ICF of the neutron and the proton and also for NCBU are also shown. They are denoted by $\sigma_{IF}^{(n)}$, $\sigma_{IF}^{(p)}$ and σ_{EB}, respectively.

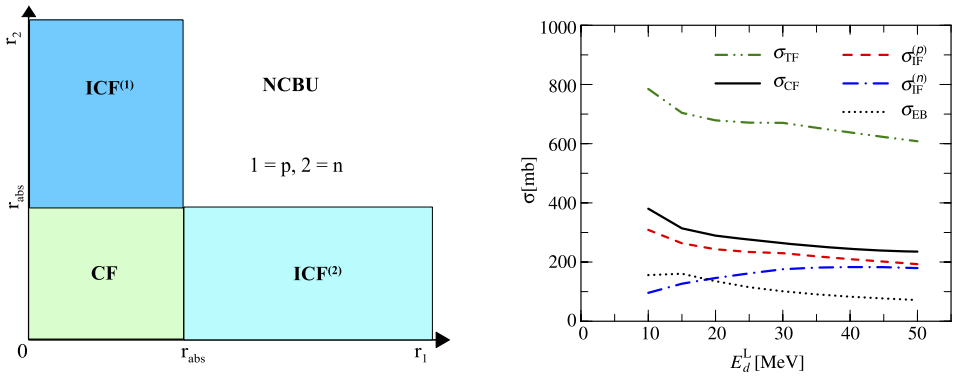

Fig. 42. (Color online) Left panel: Integration regions used in Ref. [282]; Right panel: cross sections for the different processes discussed in the text. *Source:* Left panel: Figure taken from Ref. [283]. Right panel: Figure was taken from Ref. [282].

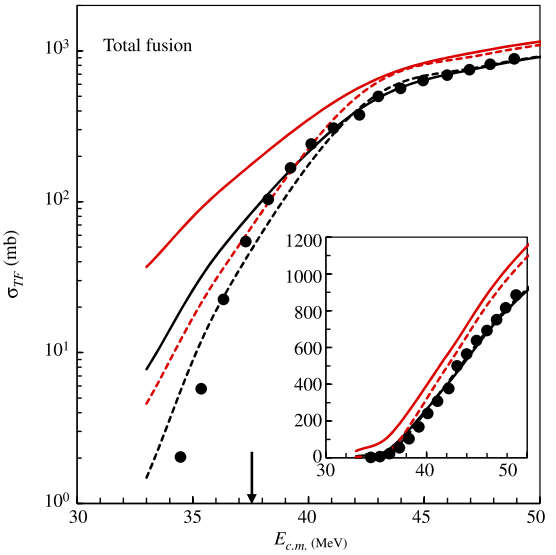

Fig. 43. Theoretical TF cross sections for the ^{9}Be + ^{208}Pb system compared to the data of Dasgupta et al. [284]. The dashed and the solid lines correspond respectively to results of the single-channel and the CDCC calculations. The red curves include the absorption of the neutron whereas the black curves considers only the absorption of the charged fragments. The vertical arrow indicates the height of the Coulomb barrier. (For interpretation of the references to color in this figure legend, the reader is referred to the web version of this article.)

Recently, Descouvemont et al. [36] performed a four-body CDCC calculation of the TF cross section for the ^{9}Be + ^{208}Pb system. In this work, the weakly bound ^{9}Be nucleus was treated as a $\alpha + \alpha + n$ three-body cluster and the projectile–target interaction was written as the sum of standard optical potentials between each cluster and the target.

The results are shown in Fig. 43, on logarithmic and linear (inset) scales. The dashed and the solid lines correspond respectively to the single-channel and the CDCC calculations. The fusion cross sections were evaluated by integrations of the wave functions with the imaginary parts of the cluster–target potentials, as indicated in Eq. (22). In the case of the CDCC calculations, the sums run on both bound channels and pseudo-channels. The red lines were obtained summing the absorption of the alpha-particles and of the neutron, whereas the black lines do not include neutron absorption. Since the experiment measures only absorption of charge, the data should be compared with the black lines. The comparison indicates that the predictions of the CDCC calculations are in good agreement with the data, except for the lowest energy data points, where they overestimate the experimental cross section.

5.2.3. Other quantum mechanical approaches

(a) *Time-dependent three-body model*

Yabana, Nakatsukasa and Ito [285–287] developed a time-dependent quantum mechanical approach to describe fusion and other nuclear processes involving weakly bound nuclei. They use a three-body model, consisting of the target and a projectile formed by the core and a weakly bound nucleon, interacting with each other and with the target. Fusion corresponds to the absorption by an imaginary potential between the core and the target. The dynamics of the system is determined by the solution of the time-dependent Schrödinger equation for the three-body system. Initially, the projectile–target state is

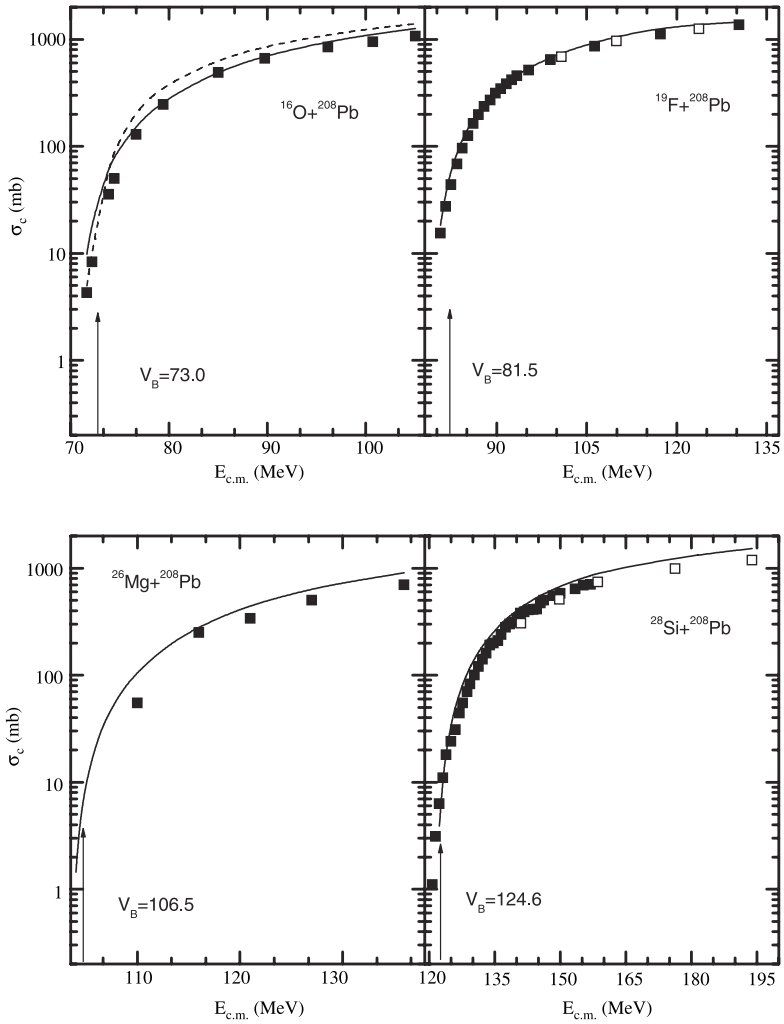

Fig. 44. Comparison of capture cross sections predicted by the quantum diffusion model [288] (solid lines) with experimental data. The dashed line is a prediction of Wong's formula [174].
Source: The data for ^{16}O are from Ref. [289], for ^{19}F are from Refs. [290,291], for ^{26}Mg are from Ref. [292] and for ^{28}Si are from Refs. [291,293].

given by a spatially localized Gaussian wave packet, multiplied by an incoming wave for the projectile–target motion, and the cluster–nucleon state is the weakly bound orbital given by the internal Hamiltonian of the projectile. The time evolution of the system is then given by the Schrödinger equation. This method was used to evaluate the TF cross section for the ^{10,11}Be + ^{209}Bi systems. Their results were shown to be in good agreement with the data.

(b) *Dissipation–Fluctuation models*

The fusion process involves dissipation of energy as the system reaches the interaction region. This is accompanied by fluctuations of the radial variable. Accordingly, it is possible that the system has a chance to "see" a lower or higher barrier, resulting in an enhanced or hindered tunneling. This idea was tested back in 1989, using an oscillator model [294]. Recently, the same idea was invoked by Kanokov et al. [295] and by Sargsyan et al. [288,296–298] in a more elaborate model of diffusion. This results in a master equation which is solved for the case of a damped oscillator treated in the sudden approximation. These authors discuss the fusion of several systems and obtain very good results. In a nutshell the model gives a tunneling probability which contains the fusion barrier, plus another parameter that represents the effect of dissipation. The other processes that accompany fusion, such as quasi-elastic scattering, breakup etc., are obtained using simple unitarity relations. One particular application which is worth noting is the deep sub-barrier fusion hindrance, where the authors discuss the effect of nuclear deformations and neutron transfer. They reach the conclusion that both effects are very important for the hindrance of the tunneling at sub-barrier energies. An illustration of the results obtained by this method is presented in Fig. 44.

(c) *Coupled channels treatment with Random Matrix Theory*

The usual application of the coupled channels method involves the inclusion of several collective states of the target and/or the projectile. The resulting fusion cross section and quasi-elastic cross section are invariably pretty good

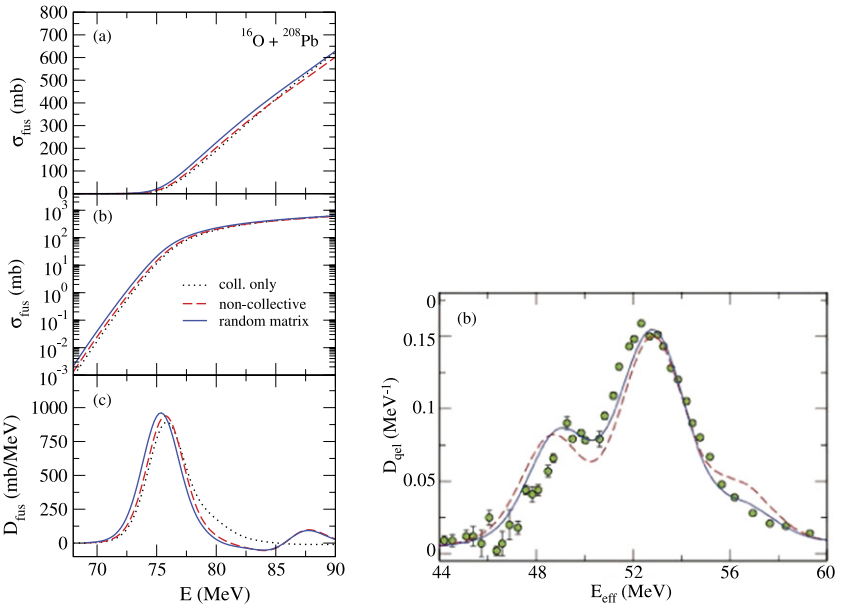

Fig. 45. (Color online) Left panel: Calculated fusion cross section and the barrier distribution of the $^{16}O + ^{208}Pb$ system [299]. The full curve corresponds to RMT prediction, the dashed curve corresponds to the calculation including the experimental deformation parameters of the non-collective states in ^{208}Pb and the dotted curve represents the result without the non-collective excitations (only the collective states in ^{208}Pb are taken into account); Right panel: The quasi-elastic barrier distribution for the $^{20}Ne + ^{90}Zr$ system calculated with (solid line) and without (dashed line) the inclusion of non collective excitations [300], in comparison with the data of Piasecki et al. [301].

representation of the data of fusion and barrier distribution. In several cases it was realized that besides the collective channels, one is required to include several non-collective states in the target/projectile system [302]. Typical cases recently studied are the $^{20}Ne + ^{90,92}Zr$ systems, where it was found that the barrier distribution of $^{20}Ne + ^{92}Zr$ is more smeared compared to that of $^{20}Ne + ^{90}Zr$ [301]. Usual CC calculations involving only low lying collective states in the deformed Neon projectile give similar barrier distributions for the two systems. Piasecki et al. [301] suggested that the inclusion of non-collective states in the Zirconium target may resolve the problem. Explicit inclusion of non-collective channels using the experimentally known spectra of the $^{16}O + ^{208}Pb$ system was made in the calculation of Yusa, Hagino and Rowley [303], and they found a significant change in the barrier distribution. Similar results were obtained for the Ne + Zr system. It was also realized that an alternative way to account for the many non-collective states is to use Random Matrix Theory (RMT) method. Such ideas were originally developed for the treatment of deep inelastic collisions by Agassi, Ko, and Weidenmüller [304–307]. In the current context, Yusa, Hagino and Rowley [299] employed the RMT model to solve the coupled channels equations containing both collective and statistical channels. The RMT involves the use of the Gaussian distribution of the matrix elements of the statistical states in the sense

$$\overline{V_{nn'}} = 0 \tag{124}$$

and

$$\overline{V_{n_1n_2}V_{n_3n_4}} = [\delta_{n_1n_3}\delta_{n_2n_4} + \delta_{n_1n_4}\delta_{n_2n_3}]\,\overline{V^2}. \tag{125}$$

The important point to mention here is the implicit appearance of the density of states in the strength of the coupling, $(\overline{V^2})^{1/2}$. The CC equations are then solved and the result was found to be quite accurate when compared to the one obtained from conventional CC calculations [303]. The significance of these developments resides in the fact that in many cases complete experimental information about the non-collective states (usually obtained from proton inelastic scattering) are not available, and RMT could then come to the rescue in assessing their importance in fusion and quasi-elastic cross sections at near-barrier energies. An example of a calculation using the RMT [299] is given on the left panel of Fig. 45. The same authors used the RMT description in the calculation of the quasi-elastic cross sections and the corresponding barrier distributions for the system $^{20}Ne + ^{90,92}Zr$ [300]. An illustration of these applications is presented on the right panel of Fig. 45.

(d) *The empirical coupled-channel (ECC) approach*

As it is in general difficult to include nucleon transfer channels in coupled-channels calculations, Zagrebaev [308] proposed to treat them within an empirical way. In the ECC, the transfer probabilities are estimated using a semiclassical approximation. The fusion probabilities are then obtained summing the contributions from the elastic and transfer channels, with the transfer probabilities used to evaluate the weights.

This method was recently applied to the case of sub-barrier fusion of weakly bound nuclei [309]. The role of the neutron binding energy in the sub-barrier fusion enhancement was observed to depend on the mass of the donor nucleus. In the

case of light donor nuclei, there is a strong dependence of the enhancement with the binding energy, and this dependence becomes much less marked in the case of heavy donors.

The explanation for this surprising behavior lies in the different shapes of the nuclear potentials in the light and heavy donor cases. In the case of light donor nuclei, the Coulomb barrier lies lower but it is wider than in the heavy donor case. Therefore, the classical turning point lies at a larger distance between nuclear surfaces than in the heavy donor case, due to the strength of the Coulomb interaction. This difference increases with the decrease of the collision energy. As a consequence, the neutron transfer probability decreases much more rapidly with an increase in the binding energy in the case of the light donor nuclei.

The ECC can also be employed to study the effects of deformation and vibrations on the fusion probability of weakly bound systems at sub-barrier energies, using the same idea of performing averages over the tunneling probabilities for the different barriers. On this subject, there is a recent work showing that, for systems for which the change in deformation due to transfer is small, the transfer of the two neutrons in ^{6}He enhances the fusion cross section, while if the change in deformation is appreciable, there could appear either a suppression, if the deformation decreases, or enhancement, if it increases as a result of the transfer [310].

5.3. Hindrance of fusion at deep sub-barrier energies

Recently, the Argonne group [311] has shown that the fusion of some medium mass systems is hindered at deep sub-barrier energies. This has been observed for ^{58}Ni + ^{58}Ni, ^{90}Zr + ^{92}Zr and ^{60}Ni + ^{89}Y, and more recently similar results have been obtained for several other systems [312–316]. Before we discuss the physics involved in this phenomenon, one should understand clearly what one means by *hindrance*. The words enhancement and hindrance are based on a comparison with some standard cross section. Thus, the choice of the standard should be very clear. In the present case, the standard is the cross section predicted by coupled channels calculations that reproduce the data at near barrier energies, where the cross section is of the order of milibarns. At lower energies, where the cross section drops to micro barns or below, the experimental data fall well below the coupled channels cross section. This is the hindrance phenomenon considered here. It should be stressed that, although the data fall below the coupled channels cross section in this energy region, they may remain much larger than the fusion cross section predicted by the one-dimensional barrier penetration model.

Since the above mentioned phenomenon has not been observed for weakly bound systems, it goes beyond the scope of the present review. However, we present in this section a very brief discussion of this topic. A detailed discussion of the problem can be found in the recent review article of Back et al. [5].

The deep sub-barrier hindrance phenomenon brought into focus the question of the uncertainty inherent in the nuclear interaction employed in the analysis. One possible cause of this hindrance is the existence of a shallow pocket [317] in the potential due to short distance repulsion [251,252,318,319]. In this way, these works obtained reasonable agreement with the data. A different approach to the problem was proposed in Refs. [320–322]. These works assumed that there is a transition from a two-body regime to a one-body regime in the way to fusion. This transition would take place at the point where the summed densities of the two tails reached the value of the central density of the nuclei. In the two-body regime the collision could be handled by the coupled channel method. However, within the one-body regime the system would evolve adiabatically. This transition would lead to a damping of the quantum vibration [322], reducing the fusion cross section. This model also leads to good agreement between theory and experiment.

In all these studies the general characteristics of the compound nucleus formed in the fusion process is completely overlooked. The reason being that at the energies involved the compound nucleus is formed at high enough excitation energy that many overlapping resonances are involved, and therefore there is no hindrance since the colliding nuclei see a continuum of states in the compound nucleus. At very low energies the compound nucleus characteristics may become important in the fusion process as was recently found in the system ^{12}C + ^{12}C by C.L. Jiang et al., Phys. Rev. Lett. 110, 072701 (2013).

6. Fusion of weakly bound systems: recent measurements

Since 2006, around forty experimental papers on fusion reactions with weakly bound projectiles have been published.[18] They report measurements of fusion cross sections in collision of stable and radioactive weakly bound beams with targets in different regions of the periodic table, from light to very heavy ones, at energies ranging from a few MeV below the Coulomb barrier to two or three times the barrier height, although measurements around the barrier energy are more frequent. Usually, the experiments determine only the TF cross section. However, in several cases it is possible to measure the CF cross section.

Most experiments were performed using the gamma ray spectroscopy method (on-line and/or off-line), with a variable number of detectors, ranging from a single Ge detector to large gamma detector arrays. Several other measurements were performed by detecting alpha particles emitted in the decay of residual nuclei, or delayed X-rays emitted in the decay of

[18] For a discussion of earlier experimental papers, we refer to previous review articles [2,6].

Table 1
Experimental studies of fusion cross sections of stable weakly bound systems.

Projectile	Target	Reference	$E_{c.m.}$ (MeV)	V_B (MeV)	Measured
^{7}Li	^{24}Mg	Ray et al. [324]	4.6–23.2	5.9	TF
	^{28}Si	Sinha et al. [325]	5.6–9.2	6.8	TF
		Sinha et al. [326]	9.2–20.8		TF
	^{64}Zn	Di Pietro et al. [72]	10.1–28.3	13.1	TF
	^{144}Sm	Rath et al. [327]	19.1–38.1	24.0	CF
	^{152}Sm	Rath et al. [327]	19.1–38.2	23.7	CF
	^{159}Tb	Mukherjee et al. [328]	26.8–41.2	24.7	CF
	^{197}Au	Palshetkar et al. [96]	22.3–42.7	28.9	CF, ICF
	^{238}U	Raabe et al. [329]	31.3–35.9	32.5	CF
^{6}Li	^{24}Mg	Ray et al. [324]	4.8–24.0	6.1	TF
	^{28}Si	Sinha et al. [330]	5.8–19.8	7.0	TF
	^{64}Ni	Shaikh et al. [331]	10.0–25.6	12.4	TF
	^{64}Zn	Di Pietro et al. [72]	10.1–28.3	13.4	TF
	^{90}Zr	Kumawat et al. [332]	12.2–28.1	16.9	CF
	^{96}Zr	Hu et al. [333]	15.0–26.3	16.4	CF, ICF
	^{144}Sm	Rath et al. [101]	19.2–38.4	24.4	CF
	^{152}Sm	Rath et al. [334]	19.2–38.5	24.1	CF
	^{159}Tb	Pradhan et al. [335]	22.2–37.6	25.0	CF, ICF
	^{197}Au	Palshetkar et al. [96]	22.3–42.7	29.3	CF, ICF
	^{198}Pt	Shrivastava et al. [336]	19.4–34.0	28.9	CF
^{9}Be	^{89}Y	Palshetkar et al. [337]	17.7–28.9	21.4	CF
	^{124}Sn	Parkar et al. [338]	23.3–34.7	26.0	CF
	^{144}Sm	Gomes et al. [339]	28.2–41.4	31.7	CF, ICF
	^{169}Tm	Fang et al. [340]	30.5–45.6	33.6	CF, ICF
	^{181}Ta	Zhang et al. [341]	33.6–47.9	35.2	CF, ICF
	^{186}W	Fang et al. [342]	39.1–50.5	36.1	CF, ICF
	^{187}Re	Fang et al. [340]	32.6–46.8	35.9	CF, ICF
	^{209}Bi	Dasgupta et al. [343]	42.1–67.0	39.7	CF, ICF
	^{238}U	Raabe et al. [329]	46.5–54.0	42.9	CF
^{10}B	^{159}Tb	Mukherjee et al. [328]	35.8–67.7	40.7	CF
	^{209}Bi	Gasques et al. [344]	52.3–71.4	49.6	CF

residual nuclei by electron capture. For a few heavy systems, fission is the main decay mode of the compound nucleus and in such cases the fusion cross section is determined through the detection of fission fragments. As those experimental methods were extensively described in a previous review article [6], we are not repeating the description here. Thus, we will concentrate in the discussion of a few special experimental setups.

Only a few papers derive fusion barrier distributions. Some experiments study other reaction processes, like direct transfer and breakup. Usually the experiments detect single fragments, although a few experiments perform coincidence measurements. In most experimental papers the measured fusion cross sections are compared with predictions of coupled channel calculations. These calculations involve the main inelastic collective states and, in some cases, also transfer channels. They are performed using the CCFULL [323] and/or the FRESCO [243] codes. In general, the comparisons of measured CF cross section with theory lead to the conclusions that CF data is suppressed at energies above the barrier, and it is slightly enhanced at sub-barrier energies. A list of recent fusion measurements is presented in Tables 1 (stable weakly bound systems) and 2 (unstable weakly bound systems).

In the following, we give a few details of some works listed in the tables, describing a few special experimental setups and pointing out some important results. The experiments with stable weakly bound projectiles (^{6}Li, ^{7}Li, ^{9}Be, ^{10}B) and the ones with radioactive nuclei (neutron halo (^{6}He, ^{8}He, ^{11}Be, ^{11}Li), proton-halo (^{8}B, ^{17}F) and non-halo (^{8}Li, ^{7}B)) are discussed in the next two sub-sections. In these sections, the results of the experiments will be considered individually. A systematic study of the CF and TF cross sections for weakly bound projectiles and targets all over the periodic table is presented afterwards, in a separate section.

6.1. Fusion of stable weakly bound nuclei

The effects of the breakup channel on fusion reactions with radioactive nuclei is a subject of great interest. Owing to their very low breakup threshold, the breakup channel is expected to be very important. However, the low intensity of radioactive beams, several orders of magnitude lower than those of stable beams, reduces drastically the accuracy of the data. On the other hand, despite some particular characteristics of unstable nuclei, like the halo structure, the reaction mechanisms involved in collisions of stable and unstable weakly bound nuclei should be similar. In this way, understanding fusion reactions with the former should shed light on fusion reactions with the latter. For this reason, and also for its intrinsic interest, several measurements of fusion cross sections in collisions of stable weakly bound nuclei have been performed over

Table 2
Same as the previous table but for radioactive weakly bound projectiles.

Projectile	Target	Reference	$E_{c.m.}$ (MeV)	V_B (MeV)	Measured
neutron-halo					
^{6}He	^{64}Zn	Scuderi et al. [345]	13.7–16.4	8.7	TF
	^{197}Au	Penionzhkevich et al. [346]	14.5–58.5	19.2	TF
	^{206}Pb	Penionzhkevich et al. [346]	9.7–25.3	19.8	TF
		Lukyanov, et al. [347]	16.5–26.2		TF
		Wolski et al. [348]	14.4–17.5		TF
^{8}He	^{65}Cu	Lemasson et al. [51]	17.7–27.2	8.1	CF
	^{197}Au	Lemasson et al. [149]	15.5–28.0	18.7	CF
^{11}Li	^{208}Pb	Vinodkumar et al. [349]	27.1–37.9	28.5	TF
^{11}Be	^{209}Bi	Hinde [350]	37.3–52.0	39.0	TF
proton-halo					
^{8}B	^{28}Si	Pakou et al. [351]	15.5–27.2	11.6	TF
	^{58}Ni	Aguilera et al. [352]	15.2–23.2	21.1	TF
no-halo					
^{8}Li	^{208}Pb	Aguilera et al. [353]	32.1–37.5	29.4	CF
^{7}Be	^{238}U	Raabe et al. [329]	38.8–54.4	43.8	CF
	^{58}Ni	Martinez-Quiroz et al. [354]	13.9–19.0	16.6	TF

the last decade. Some experiments measure only TF whereas in other experiments separate measurements of CF and ICF plus cluster transfer are carried out. In a few situations, only the CF cross section can be measured.

Several papers were published on fusion reactions induced by ^{6,7}Li beams, colliding with different targets. Most of the experiments were performed at BARC-Mumbai, using on-line and/or off-line gamma ray detection. Sinha et al. [325,326] measured TF for the ^{7}Li + ^{28}Si system, at energies below and above the barrier. The experiments were performed at BARC–TIFR-Mumbai and Bhubaneswar. They compared the data with CC calculations. They found a slight enhancement at sub-barrier energies and no effect at energies just above the barrier. However, for energies more than twice the barrier, the TF cross sections showed some suppression compared with the barrier penetration model. Ray et al. [324] measured TF of the ^{6,7}Li + ^{24}Mg systems at BARC-Mumbai, with the gamma ray method. They compared their results with the total reaction cross section, obtained by optical model analysis, and with the theoretical TF cross section obtained with a coupled channel calculation. At energies below and around the Coulomb barrier, they found that the experimental TF cross section is close to that for total reaction (TR). However, at higher energies the latter exceeds the former. On the other hand, the experimental TF cross section is in reasonable agreement with the results of the CCFULL calculations in the whole energy range.

Kumawat et al. [332] measured the CF cross section for the ^{6}Li + ^{90}Zr system at energies above the Coulomb barrier. The experiment was performed at BARC-Mumbai, using the gamma ray method. Comparing their CF data with predictions of coupled channel calculations, they found that the data was suppressed by 34%. However, Hu et al. [333] measured the CF cross section for ^{6}Li + ^{96}Zr, a similar system, at above-barrier energies and found a suppression of only 25%. Their experiment was performed at the CIAE-Beijing, using the on-line gamma ray method.

Shaikh et al. [331] measured TF of ^{6}Li + ^{64}Ni at Mumbai, using also the on-line gamma ray method. They found that the TF cross section was in good agreement with predictions of coupled-channel calculations. On the other hand, their experimental CF cross section, based on statistical model assumptions, was suppressed by only 13%.

Rath et al. [101,327,334] measured CF and TF of the ^{6,7}Li + ^{144,152}Sm systems, at energies below and above the Coulomb barrier. The experiments were carried out at the BARC laboratory, using the gamma ray method. They compared their experimental CF cross sections with predictions of coupled channel calculations involving inelastic channels, using the CCFULL code [323]. They also performed calculations involving both inelastic and transfer channels, using the FRESCO code [243]. In this way, the importance of transfer channels could be assessed. Their results are reproduced in Fig. 46. The comparisons indicate a suppression of the experimental CF cross section of the order of 30% for all systems. They indicated also that the suppression is more important for fusion induced by ^{6}Li than by ^{7}Li. The comparison of the coupled channel calculations including only inelastic couplings with the ones including also transfer, showed that the influence of inelastic channels on fusion is much stronger.

Pradhan et al. [335] measured the CF and ICF cross sections for the ^{6}Li + ^{159}Tb systems, at energies above the Coulomb barrier. The experiments were performed at BARC-Mumbai, using the gamma ray method. Comparing their CF data with results of coupled channel calculations, they found that the experimental CF cross section for ^{6}Li + ^{159}Tb is suppressed by more than 30%. Mukherjee et al. [328] performed a similar experiment in the same laboratory for the ^{7}Li + ^{159}Tb system. They found a suppression of 26%.

Palshetkar et al. [96] measured CF, ICF and transfer cross sections for the ^{6,7}Li + ^{197}Au systems, at energies below and above the barrier. The experiments were made at the BARC laboratory, using the INGA gamma array. The measured CF cross sections were compared with results of no-couplings and CC calculations involving inelastic channels. Their results are shown on the left panel of Fig. 47, in (a) logarithmic and (b) linear scales. The comparison between experiments and CC calculations indicated that the CF data for the ^{6}Li and ^{7}Li projectiles were suppressed by 35% and 15% respectively. The

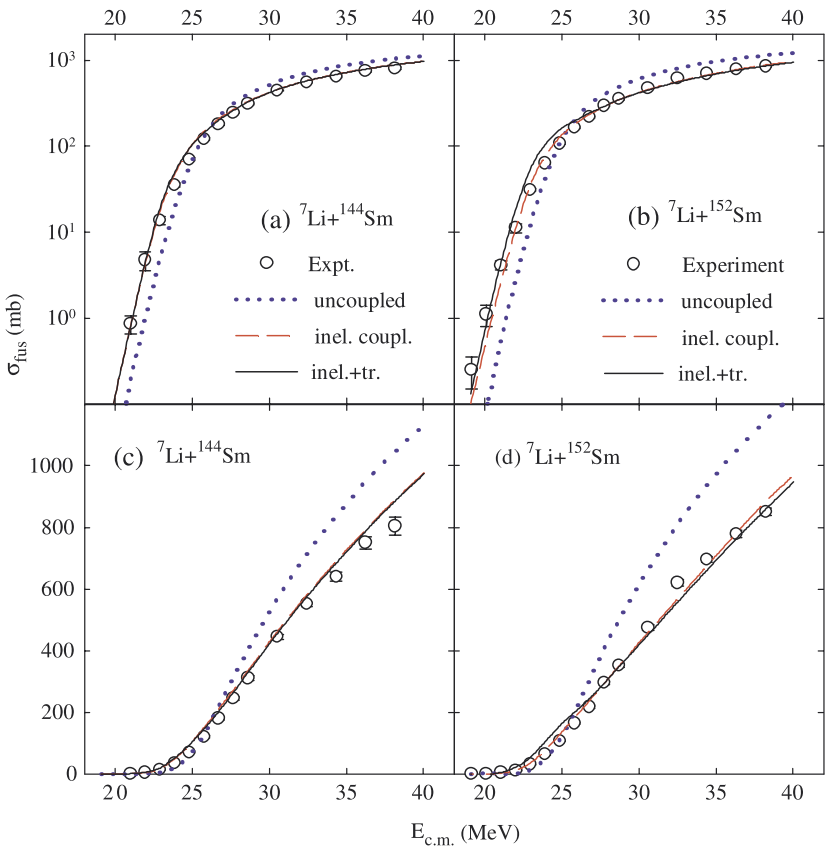

Fig. 46. (Color online) Comparison of the experimental CF cross section of Ref. [327] with theoretical predictions. The dotted, dashed and solid lines correspond respectively to the single channel calculation, the CC calculation restricted to inelastic couplings and the CC calculation involving both inelastic and transfer channels. For details, Ref. [327].

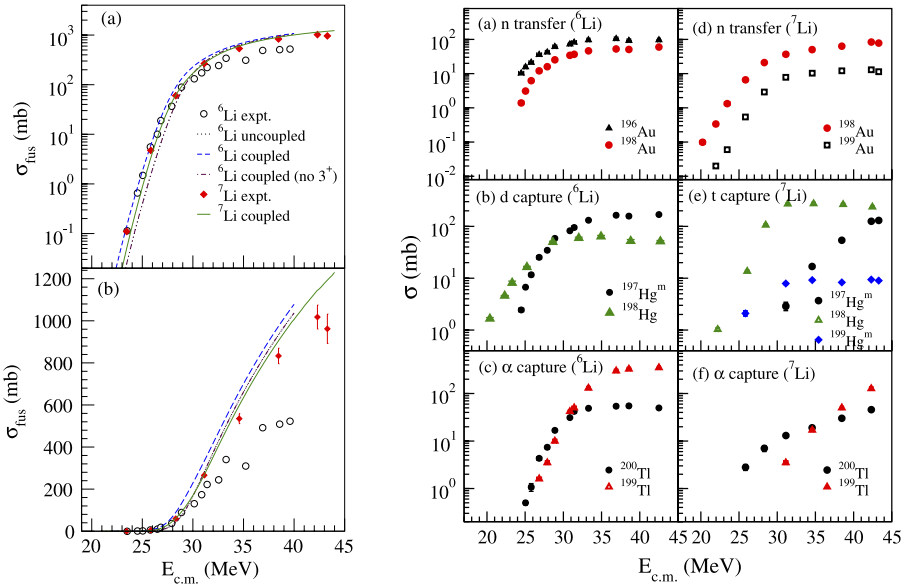

Fig. 47. (Color online) Left panel: Experimental and theoretical CF cross section for the ^{6,7}Li + ^{197}Au systems [96]. The solid lines correspond to CC calculations involving inelastic channels, and for the dashed lines all couplings were switched off. The results are presented both in (a) logarithmic and (b) linear scales; Right panel: Experimental cross sections for neutron-transfer and for captures of a ^{2}H, a ^{3}H or an alpha-particle in the same collision [96].

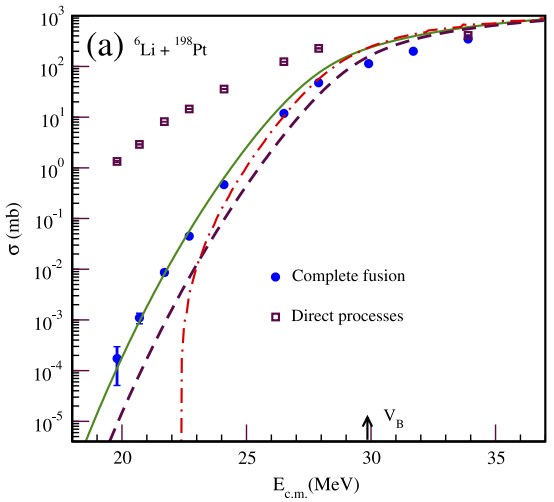

Fig. 48. (Color online) Complete fusion and direct reaction cross sections for the ^{6}Li + ^{198}Pt system. The solid line corresponds to a CC calculation involving the main inelastic channels, whereas the dashed and the dot-dashed lines are results of single-channel calculations with different bare potentials. The arrow indicates the value of the Coulomb barrier, V_B.
Source: The data and the calculations are from Ref. [336].

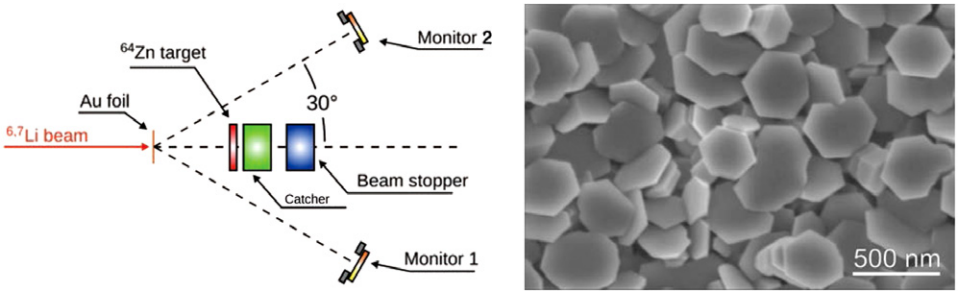

Fig. 49. (Color online) Left panel: The experimental setup used by Di Pietro et al. [72]; Right panel: Electron scanning image of the target in the experiment of Ref. [72].

cross sections for neutron transfer and ICF for the two systems (capture of a ^{2}H, a ^{3}H or an α-particle) are shown on the right panel of Fig. 47. One sees that these cross sections have appreciable values.

Shrivastava et al. [336] measured the CF cross section for the ^{6}Li + ^{198}Pt system. They measured also cross sections for direct processes, including ICF, breakup and transfer. The experiments were performed at BARC-Mumbai, detecting coincidences between gamma and X-rays. They were able to extend the measurements to deep sub-barrier energies, as low as 0.68 V_B. At the lowest energies, the cross sections for direct reactions were shown to be several orders of magnitude larger than that for CF. Their cross sections are shown in Fig. 48, together with results of three calculations. The solid line corresponds to a CC calculation including inelastic channels whereas the dashed and the dot-dashed lines are results with single-channel calculations with different bare potentials. The comparison of the CF data with the CC-calculated cross section is very interesting. The data well below the barrier is very well described by the CC calculation, which is based on a standard bare potential. Thus, there is no hindrance of fusion at deep sub-barrier energies for this system. At energies above the barrier, there is some suppression of the CF cross section.

Di Pietro et al. [72] made very careful measurements of TF and transfer cross sections for the ^{6,7}Li + ^{64}Zn systems, at energies above and below the barrier. They were also able to estimate the contribution of ICF to the TF cross section. The experiments were performed at the LNS-Catania laboratory, using the activation technique method. They measured the X-rays emitted in the decay of the nuclei by electron capture. A schematic view of the experimental setup is shown on the left panel of Fig. 49. The targets were selected by their uniformities, observed by electron scanning microscopy. This is illustrated on the right panel of Fig. 49. Fig. 50 shows the experimental TF excitation functions in the collisions of ^{6}Li (left panel) and ^{7}Li (right panel) with ^{64}Zn. The data of earlier experiments [355,356] are also shown. The experimental cross sections are compared with results of the barrier penetration model (solid lines) and CC calculations (dotted lines). Above the Coulomb barrier, the data of Di Pietro et al. [72] are in good agreement with the theoretical results, contrasting with the data of earlier experiments, which show some suppression. At sub-barrier energies the experimental TF cross section [72] is enhanced with respect to the theoretical predictions and in this region the cross section for ^{6}Li is larger than that for ^{7}Li. This can be seen more clearly in Fig. 51, which shows the ratio of the TF cross sections for the ^{6}Li and ^{7}Li projectiles, in collisions

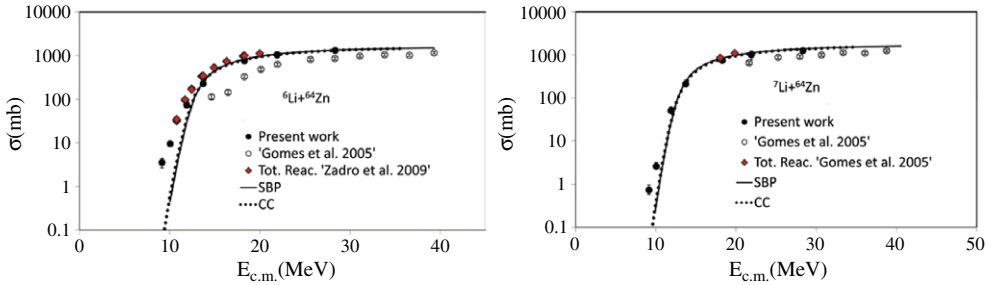

Fig. 50. (Color online) Experimental TF cross sections for the ^{6}Li + ^{64}Zn (left panel) and ^{7}Li +^{64} Zn (right panel) systems [72] in comparison of predictions of the single barrier penetration model (solid lines) and of CC calculations (dotted line). For details, see Ref. [72].

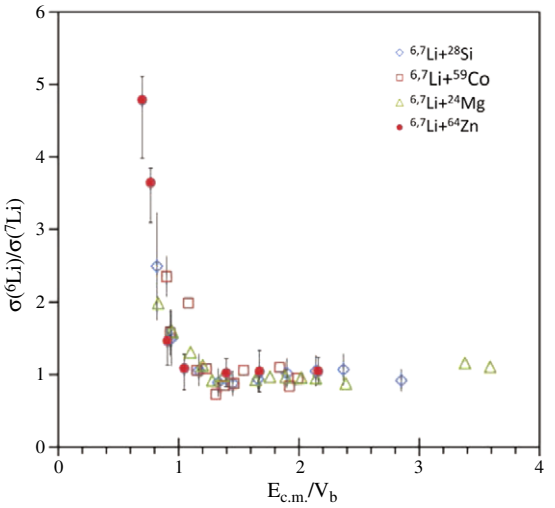

Fig. 51. (Color online) Ratio of the TF cross sections for ^{6}Li to that of ^{7}Li, in collisions of these projectiles with different targets [72]. The ratio is plotted against the collision energy, normalized with respect to the Coulomb barrier.

with ^{64}Zn and other targets. This ratio, shown as a function of the collision energy normalized by the Coulomb barrier, grows as the energy decreases. Using predictions of an statistical code, the authors suggest that the larger cross section of ^{6}Li can be attributed to ICF and/or transfer processes, which are stronger for this projectile. Therefore, all the available experimental TF excitation functions for collisions of ^{6,7}Li with light systems, ranging from ^{12}C to ^{64}Ni [72,324–326,330,357–360,356,151], are in good agreement with predictions of coupled channel calculations.

From 2006 to the present, many authors measured CF cross sections in reactions induced by ^{9}Be beams. They determined cross sections for the ^{89}Y, ^{124}Sn, ^{144}Sm, ^{169}Tm, ^{181}Ta, ^{187}Re and ^{186}W targets [342,337–341,361]. The ^{9}Be + ^{144}Sm fusion was measured at the TANDAR laboratory, Buenos Aires, by the detection of X-rays emitted in the electron capture decay of the residual nuclei [339,361]. All the other systems were measured by the gamma ray method, on-line and/or off-line. The ^{9}Be + ^{89}Y and ^{9}Be + ^{124}Sn systems were measured at the BARC–TIFR in Mumbai [337,338], the ^{9}Be + ^{169}Tm, ^{181}Ta, ^{187}Re systems were measured at Lanzhou [340,341] and the ^{9}Be + ^{186}W system was measured at the CIAE, Beijing [342].

In the above mentioned experiments, the measured CF cross sections were compared with predictions of CC calculations using the CCFULL or the FRESCO codes. In all cases, the data showed some enhancement below the Coulomb barrier. On the other hand, the experimental cross section was systematically suppressed above the barrier. The suppressions found for the ^{89}Y, ^{124}Sn, ^{144}Sm, ^{169}Tm, ^{181}Ta, ^{187}Re and ^{186}W targets were respectively 20%, 28%, 10% (later corrected to 16% [362]), 34%, 34%, 30% and 40%. An earlier measurement of CF for the ^{9}Be + ^{208}Pb system [284,269] found a suppression of 32%. Some of these papers and papers by other authors made systematic investigations of the CF suppression. Studies of this kind will be discussed in detail in Section 6.4.

The situation for the TF cross section is different. The data for the ^{9}Be+^{144}Sm, ^{9}Be+^{208}Pb, ^{9}Be+^{64}Zn [363,73], ^{9}Be+^{169}Tm, ^{9}Be + ^{181}Ta, ^{9}Be + ^{187}Re [341,340] and ^{9}Be + ^{27}Al systems [364] are in agreement with CC calculations. This indicates that, at energies slightly above the barrier, there is no significant influence of the breakup and transfer channels on TF. The situation is illustrated on the left panel of Fig. 52, which shows the cross sections of these systems reduced according to the prescription of Canto el al. [160,161]. When the collision energies and the cross sections are reduced in this way, the influence of the breakup and transfer channels is measured by deviations from the universal curve (see Section 6.4) represented by the solid line in the figure. Clearly, this does not happen. For the ^{9}Be + ^{89}Y and ^{9}Be + ^{124}Sn systems, the ICF cross section could

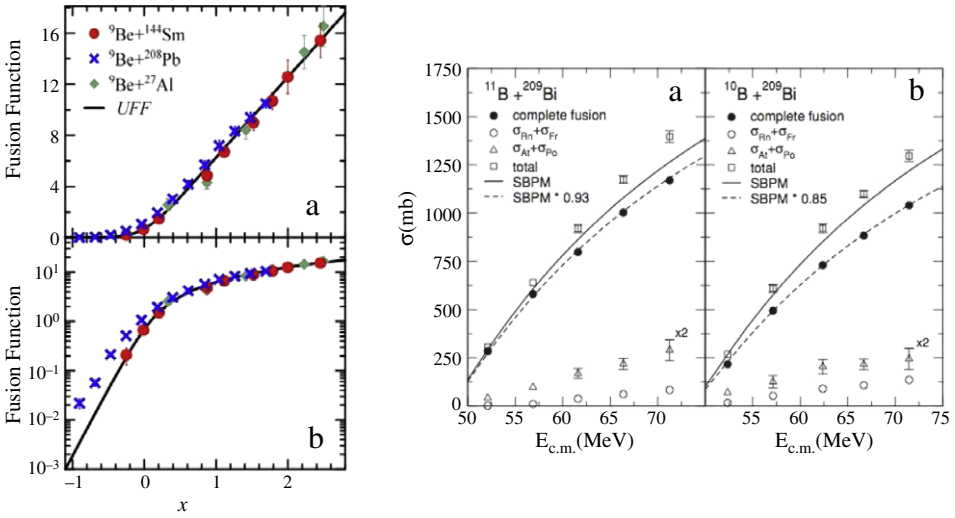

Fig. 52. (Color online) Left panel: Reduced experimental TF cross sections for different systems. The data was reduced by the fusion function method [160, 161] and renormalized to eliminate the influence of couplings with bound channels. The solid line represents the universal fusion function, that corresponds to the situation where there is no breakup coupling; Right panel: Experimental CF cross sections for the ^{10,11}B + ^{209}Bi of Ref. [344], in comparison with predictions of the single barrier penetration model.

not be measured. Therefore, it was not possible to investigate the behavior of TF. Finally, for the ^{9}Be + ^{186}W system [342], a suppression of TF of the order of 25% was found. This behavior, that does not follow the general trend of above barrier TF data (see Section 6.4), deserves further investigation.

The CF cross sections of the not so weakly bound ^{10}B nucleus, with breakup threshold energy of 4.46 MeV, have also been measured. Mukherjee et al. [328] measured CF of the ^{10}B + ^{159}Tb system at BARC-Mumbai, by the gamma ray method. The CF suppression at energies above the barrier, compared with CC calculations, was found to be of the order of 14%, which is not negligible but is smaller than that for more weakly bound nuclei. Gasques et al. [344] measured the CF cross section for the ^{10,11}B + ^{209}Bi systems at the ANU, Canberra. They detected the α-particles emitted by the evaporation residues. They found that the CF cross sections for ^{10}B and for the tightly bound ^{11}B nucleus were suppressed by 15% and 7%, respectively. Their results are shown on the right panel of Fig. 52.

6.2. Fusion of radioactive weakly bound nuclei

Up to the present, the intensities of available radioactive beams are still orders of magnitude lower than those with stable beams. So, fusion cross sections involving radioactive beams have much larger error bars, due to the poorer statistics. To improve this situation, most experiments use very thick targets, which leads to large uncertainties in the value of the average (or effective) incident energy. There are plans for new facilities in the near future, like Spiral2, at GANIL, Fair, in Darmstadt, SPES, at Legnaro, FRIB at the MSU, IMP-HIRFL, in Lanzhou, BRIF at the CIAE-Beijing, RSIP, in Daejong-Korea, and upgrades at RIKEN and VECC-India. In these new laboratories, one expects to obtain radioactive beams with much higher intensities than at the present.

6.2.1. Fusion of neutron-halo nuclei

The pioneer measurements of fusion with radioactive beams were performed in the mid 90's in GANIL, Dubna and Riken [365–367], using ^{11}Be and ^{6}He beams. Later, in 1998, Kolata et al. [146,147] measured the fusion of ^{6}He + ^{209}Bi in Notre Dame. In 2000, Trotta et al. [368] measured fusion of ^{6}He + ^{238}U at Louvain la-Neuve, but a few years later the same group performed an improved experiment with the same system at the same laboratory and reached different conclusions [369]. They realized that most of the cross section attributed to fusion at sub-barrier energies, actually was neutron-transfer cross section. In 2004, Di Pietro et al. [370] measured fusion of the lighter ^{6}He + ^{64}Zn system at Louvain la-Neuve.

In all those works, data of fusion induced by the neutron-halo ^{6}He were compared with fusion induced by the tightly bound isotope ^{4}He (or ^{10}Be in the case of the ^{11}Be projectile) and/or with theoretical predictions of different barrier penetration models or CC calculations. Other important measurements of fusion of neutron-halo nuclei have been reported [88,157,371–374]. Most of them concluded that there is some suppression of the fusion due to breakup effects at energies above the Coulomb barrier and some enhancement at sub-barrier energies. A summary of the conclusions reached in these earlier works may be found in the review papers [1,2,5,6].

Nevertheless, there is an apparent controversy concerning the conclusions of two of the most important papers on fusion of ^{6}He with heavy targets. In their experiment on ^{6}He + ^{238}U fusion, Raabe et al. [369] concluded that the cross section was suppressed at above-barrier energies and showed no enhancement below the Coulomb barrier. On the other hand, Kolata

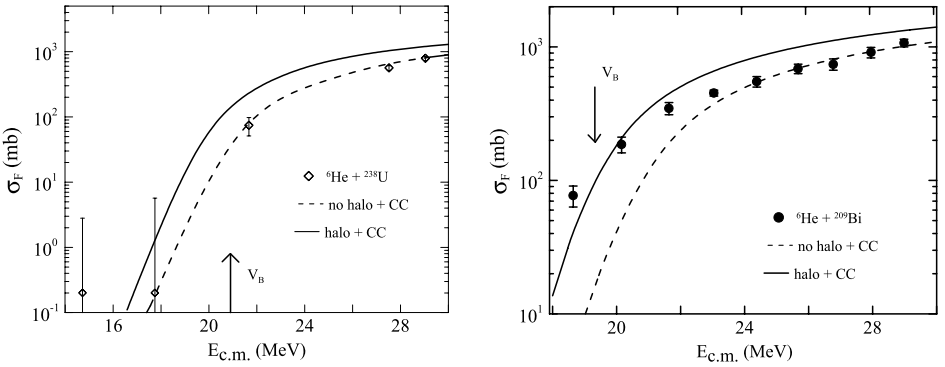

Fig. 53. Experimental fusion cross section for collisions of ^{6}He projectiles on ^{238}U (left panel) and on ^{209}Bi (right panel). The curves are results of CC calculations based on the São Paulo potential evaluated with two ^{6}He densities [375]. One is a realistic density taking into account the two-neutron halo of ^{6}He (solid line) and the other corresponds to a standard density which does not take it into account.

et al. [146,147] measured the fusion of ^{6}He + ^{209}Bi and found different trends. They concluded that the experimental cross section was strongly enhanced below the Coulomb barrier and it exhibited no appreciable effect at above-barrier energies. This led to the suggestion that ^{6}He + ^{209}Bi fusion should be measured again [6].

However, Gomes et al. [375] pointed out that there is no actual controversy between the two sets of data. The different conclusions reached in these works stem from the different benchmark cross sections used in the comparisons. Raabe et al. [369] compared their data with the results of a calculation performed using an effective optical potential that accounts for the breakup of ^{6}He. Kolata et al. [146,147] compared their data with the cross section predicted by a barrier penetration model based on the barrier with parameters fitted to reproduce the data at above-barrier energies. Since the benchmark cross section is built to reproduce the above-barrier data, there can be no fusion suppression in this energy region. Therefore, comparing fusion data with cross sections evaluated by the transmission through an empirical barrier may lead to meaningless conclusions. One should use standard bare potentials obtained by systematic approaches, like the folding model.

To show that the conflicting conclusions of Refs. [146] and [369] do result from the different benchmarks used in each case, Gomes et al. [375] compared the data sets of these works with theoretical cross sections of the same kind. The results for the ^{6}He + ^{238}U and the ^{6}He + ^{209}Bi systems are shown on the left and right panels of Fig. 53, respectively. The data are compared with results of coupled channel calculations using the São Paulo potential [125,126,376] including (solid lines) and not including (dashed lines) the halo in the ^{6}He density. The CC calculations took into account the main inelastic excitation of the targets. Comparing the data with the most realistic calculations (solid lines), one concludes that the two systems exhibit the same behavior: suppression above the barrier and negligible enhancement at sub-barrier energies.

The Catania group, which has previously measured fusion and transfer for the ^{4,6}He + ^{64}Zn system [370], extended the energy range of previous experiment to higher and lower energies [345]. They used a similar experimental set up, where the alpha fragments emitted from direct reactions were detected in arrays of silicon strip detectors (LEDA—Louvain-Edinburgh Detector Array), and the fusion products where measured by the activation method, through the detection of delayed X-rays. The experiments were performed at Louvain-la-Neuve. They also measured alpha particle yields coming from direct one- and two-neutron transfer reactions, from ^{6}He breakup, and from evaporation following fusion. The alpha-particles resulting from direct reactions (neutron-transfer and breakup) were separated from the ones resulting from evaporation through the analysis of their angular distributions. Since the elastic scattering cross sections was also measured, they could evaluate the reaction cross section. They concluded that around 70% of this cross section corresponded to neutron-transfer (1n and 2n) and breakup. Thus, only 30% was left for fusion and inelastic excitations of the target. This contrasts with similar reactions induced by ^{4}He projectiles, where the fusion process is responsible for most of the reaction cross section. The total cross section for emission of α particles in ^{4}He − ^{64}Zn and ^{6}He − ^{64}Zn collisions are compared on the left panel of Fig. 54.

The fusion cross sections measured through the detection of the X-rays emitted by the fusion products are shown on the right panel of Fig. 54. To eliminate trivial differences arising from the geometrical factor, the data is reduced according to the prescription of Ref. [158]. Now the cross sections for the two projectiles are similar, except at the lowest energies, where the cross sections for ^{6}He is appreciably larger. So, the conclusion drawn is that the much larger cross sections for the production of α particles in the case of the neutron-halo ^{6}He beam, as compared with the ^{4}He beam, is indeed due to direct reactions, like transfer or breakup. A similar situation was observed in Ref. [369] for the ^{6}He + ^{238}U system, when they compared their results with those obtained in a previous experiment of the same group [368]. The small enhancement of ^{6}He fusion as compared with ^{4}He fusion at the lowest sub-barrier energy on the right panel of Fig. 54 was attributed by di Pietro et al. to static effects owing to the diffuse radius of ^{6}He.

Fusion cross sections induced by ^{6,8}He radioactive beams have been measured for different heavy targets. The beams were produced by the ISOL method in several laboratories. Experiments to measure cross sections for the ^{6}He + ^{206}Pb [378], ^{6}He + ^{197}Au, ^{206}Pb [346] and ^{4,6}He + ^{206,208}Pb [347] systems were performed at the DRIBs-JINR-Dubna. Measurements

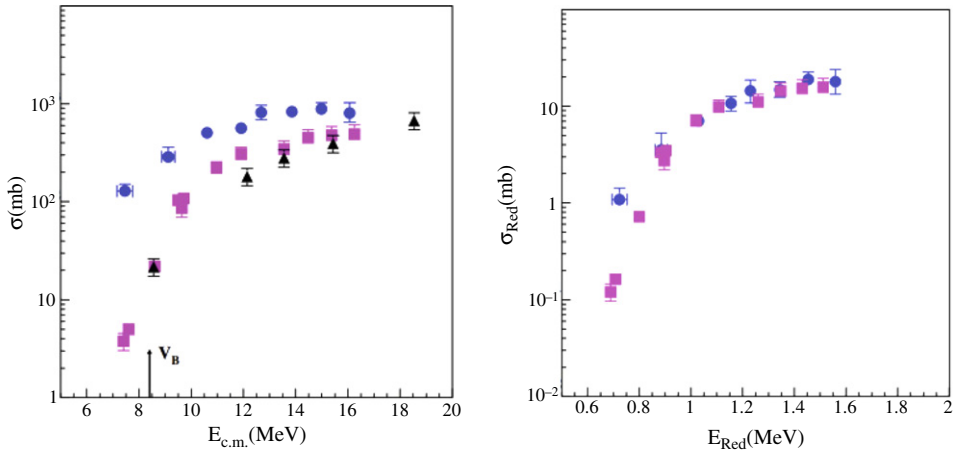

Fig. 54. (Color online) Left panel: Cross section for the emission of heavy fragments in collisions of ^{4}He (squares) and ^{6}He (circles) projectiles colliding with a ^{64}Zn target [345]. The triangles are the ^{6}He + ^{64}Zn data taken from [377]; Right panel: TF cross sections for the same systems.
Source: Both panels were taken from Ref. [345].

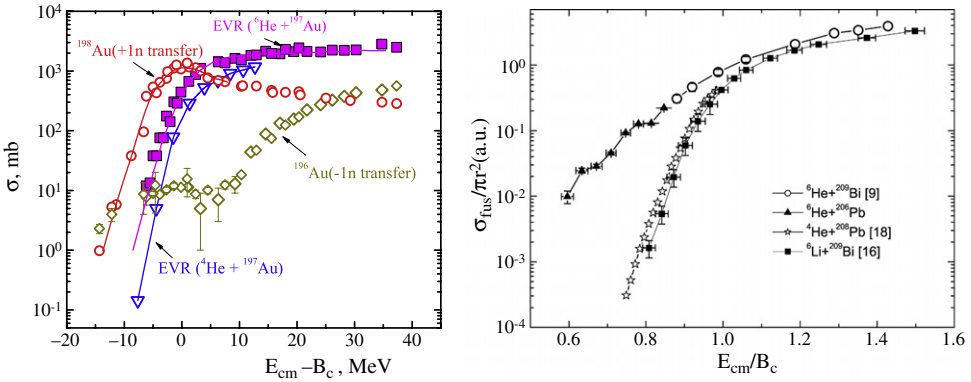

Fig. 55. (Color online) Left panel: Experimental excitation functions for the formation of various nuclei in the ^{6}He − ^{197}Au collision. Right panel: Reduced experimental fusion excitation functions for the ^{6}He + ^{206}Pb, ^{209}Bi, ^{4}He + ^{206}Pb, ^{209}Bi, ^{6}Li + ^{209}Bi systems. The reduction consists of dividing the collision energies by the barrier height and the cross sections by their geometrical values.
Source: Left panel: For detail, see Ref. [346], from which the figure was taken. Right panel: The figure was taken from Ref. [347].

of fusion for the ^{8}He + ^{197}Au system were performed in SPIRAL–GANIL [149], and for the ^{6}He + ^{206}Pb system were performed in Louvain-la-Neuve [348]. To facilitate comparisons among the data of these experiments, we will discuss them simultaneously. The cross sections in the experiments performed in Dubna [346,347,378] were measured using the activation technique and detecting off-line gamma rays and alpha particles produced in the reactions. The measured cross section for the evaporation channels were in agreement with predictions of CN evaporation codes, with the exception of the 2n evaporation channel, where the experimental cross section at sub-barrier energies was strongly enhanced with respect to the theoretical predictions. They also observed very large neutron-transfer cross section, specially 1n stripping in the ^{6}He − ^{197}Au collision. This is shown on the left panel of Fig. 55, which shows the experimental cross sections for several channels. The earlier experiment for the ^{6}He + ^{206}Pb system [346,378] were later repeated in Dubna [347]. They adopted the same experimental method but used a ^{6}He beam with much higher intensity (10^{8} pps) and much smaller energy spread ($\pm$0.5 MeV instead of $\pm$2.5 MeV). The cross section for the 2n evaporation channel which at this energy range corresponds to almost all fusion cross section, was determined. The resulting fusion cross section for this system is shown on the right panel of Fig. 55. One can observe that it follows the trend of the ^{6}He + ^{209}Bi data [146]. At sub-barrier energies, the fusion of ^{6}He with the ^{206,208}Pb targets is strongly enhanced in comparison with the cross sections for the tightly bound ^{4}He or the stable weakly bound ^{6}Li projectiles, with the same targets. The authors of Ref. [347] claim that the experimental results are in agreement with the predictions of the model of Zagrebaev [379], which assumes a sequential transfer of neutrons from ^{6}He to the target, followed by the fusion of the remaining ^{4}He.

However, their results for the fusion of ^{6}He + ^{206}Pb system were questioned by Wolsky et al. [348]. They performed the same experiment at Louvain-la-Neuve. They measured fusion by the activation technique, in the same experiment as they measured elastic and inelastic scattering, in order to determine the fusion cross section with great accuracy due to

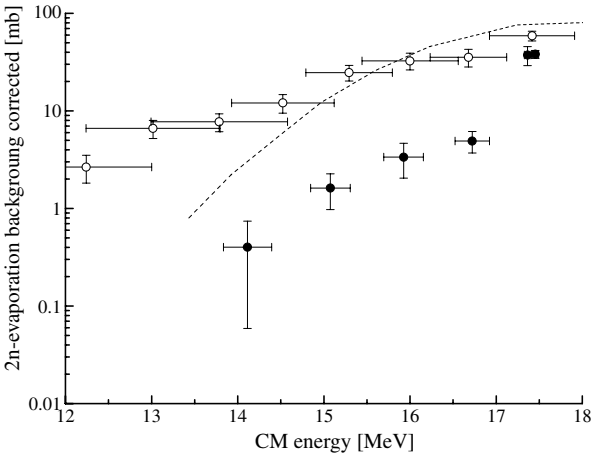

Fig. 56. Cross section for the 2n evaporation channel, which in this energy range corresponds to the fusion cross section. The solid circles are the results from Wolski et al. [348], the open circles are the results of Lukyanov et al. [347] and the dashed line are the predictions of Zagrebaev's model [379].
Source: The figure was taken from Ref. [338].

the normalization of the forward angle elastic scattering. The ^{6}He beam intensity was of the order of 10^{7} pps. Charged particles were detected by the large area silicon multi-detector system LEDA. The alpha activities of the irradiated targets were measured at the University of Huelva, Spain. The cross section of the 2n evaporation channel, corresponding to fusion cross section at this energy range, the product of the total integrated ^{6}He flux at the target and its density were obtained by normalizing the elastic scattering counting rate to the Rutherford scattering. The results obtained are shown in Fig. 56. The solid circles are from Wolski et al. [348], whereas the open circles are from Lukyanov et al. [347]. The dashed curve is prediction from the Zagrebaev's model [379].

Very impressive experimental setups were developed at the SPIRAL facility, in GANIL, to perform simultaneous measurements of several processes involving the radioactive ^{6,8}He nuclei [51,149,157]. Lemasson et al. [149] used beams of ^{8}He with intensities in the $[2-4]\times 10^{5}$ pps range to measure fusion, neutron transfer, direct breakup and elastic scattering cross sections for the ^{8}He + ^{197}Au system. Fig. 57 shows (a) the in-beam experimental setup, (b) the off-beam experimental setup, (c) gamma inclusive and gamma-X ray coincidence spectra, and (d) the activity of one residual nucleus. The gamma and X-rays are emitted in electron capture decays. Different arrays for gamma-X coincidences and maximization of gamma efficiency were made. Some very interesting results of this experiments are displayed in panels (e) and (f) of Fig. 57. Panel (e) shows the experimental neutron transfer (blue triangles) and fusion (red circles) cross sections at energies below and above the barrier (indicated by an up-arrow).

One notices that the neutron transfer cross sections are larger than the fusion cross sections in the whole energy range, specially at the lowest energies, where is larger by about two orders of magnitude. The blue dot-dashed line and the red solid line are predictions of CRC calculations for the neutron-transfer and fusion cross sections, respectively. The calculations were performed using the code FRESCO [243], including neutron-transfer channels. The reasonable agreement between the experimental and the theoretical fusion cross sections shown in this figure indicates that the dynamical effects arising from couplings with the breakup channel are not important for this system. Panel (f) of Fig. 57 shows also the predictions of barrier penetration models based on two different bare potentials. The black dotted and the dashed lines correspond respectively to a parametrized potential ignoring the halo of ^{8}He and to a folding potential, based on a realistic ^{8}He, including the halo. The larger cross section for the folding potential expresses the static effect of the halo of ^{8}He. It is convenient to look at the above fusion cross section from a systematic point of view. This is done on panel (f) of Fig. 57. It shows a comparison of cross sections for ^{4,6,8}He beams in collisions with the same ^{197}Au target. The data for ^{4}He and ^{6}He were taken from Refs. [380] and [346], respectively. One can observe that the fusion excitation function for ^{6}He and ^{8}He are very similar in the whole energy range (below and above the barrier). At sub-barrier energies they are larger than that for ^{4}He, but above the barrier the fusion of the three systems coincide. However, comparing the data reduced by the Fusion Function procedure [160, 161] with the universal fusion function (dotted line in the inset), one observes some suppression for ^{8}He at above-barrier energies.

The same group in GANIL measured fusion, neutron transfer and elastic scattering for the ^{8}He + ^{65}Cu system, at energies above the barrier [51]. Exclusive measurements of gamma rays in coincidence with light charged particles were used to further characterize direct reactions. A schematic view of the experimental setup is shown on the left panel of Fig. 58. Gamma rays from the target-like nuclei were detected by the EXOGAM array. The charged particles were detected by an annular silicon telescope and the neutrons were detected by a neutron wall. Gamma ray inclusive measurements as well as coincidences between charged particles, neutrons and gamma rays were used to identify the characteristic gamma rays. The right panel of Fig. 58 shows various final states that can be formed and detected, following one- and two-neutron transfer. Due to the complexity of the experiment, the cross sections were obtained at only two energies for ^{8}He and three energies

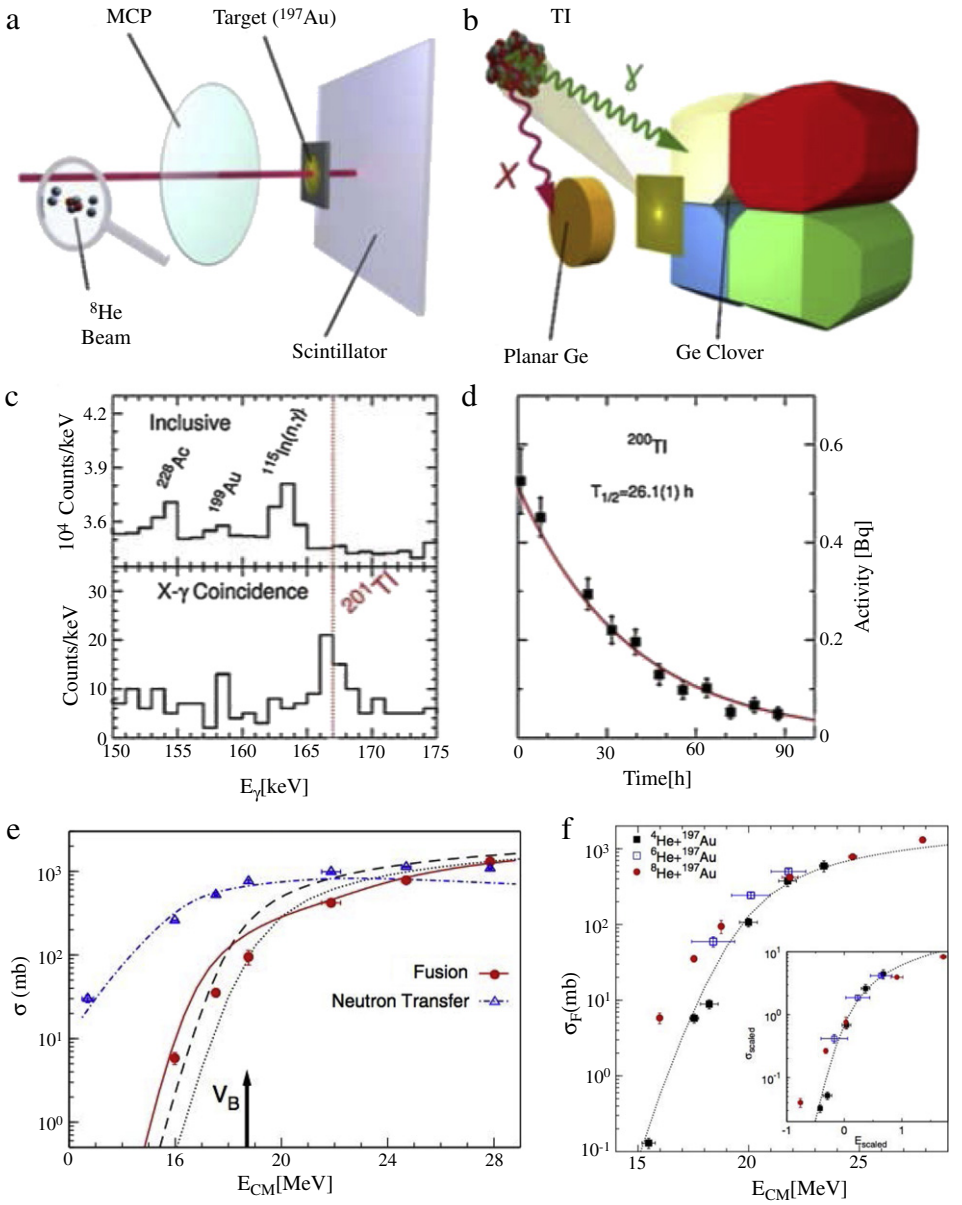

Fig. 57. (a) Schematic views of the in-beam and (b) off-beam setups of the experiments of Ref. [149]; (c) illustration of the sensitivity of the experiment showing inclusive and coincidence gamma-ray spectra; (d) ^{200}Tl activity obtained from the coincidence measurements; (e) Experimental neutron-transfer (blue triangles) and fusion (red circles) excitation functions for the ^{8}He + ^{197}Au system compared with results of the calculations described in the text; (f) Experimental fusion cross sections for the ^{4,6,8}He + ^{197}Au systems, compared with the prediction of the one-dimensional barrier penetration model for ^{4}He + ^{197}Au. For details see the text or the original paper [149], from which the figures were taken. (For interpretation of the references to color in this figure legend, the reader is referred to the web version of this article.)

for ^{6}He. The results are shown in Fig. 59. One can observe that both fusion and neutron transfer reaction cross sections are larger for ^{8}He than for ^{6}He. The data for the ^{6}He + ^{65}Cu system are from Refs. [157,381].

^{11}Li is one of the most investigated neutron-halo nuclei, from the theoretical point of view. On the other hand, it is very difficult to produce ^{11}Li beams at the energies required for studies of near-barrier fusion. So, there was no experimental fusion excitation function for this nucleus available. Very recently, the first preliminary experiment on ^{11}Li fusion has been reported [349]. The experiment was performed by Vinodkumar et al. [349], at the ISAC2 facility at TRIUMF. They measured the TF cross section for the ^{11}Li + ^{208}Pb system, which has been investigated in several theoretical works (for a review see Ref. [6]). The beam intensity was around 10^3 pps, and the cross section was measured at energies above the Coulomb barrier, except for the point with the lowest energy. Off-line alpha particles emitted by the evaporation residues were detected and CF and ICF (fusion of ^{9}Li with the target) channels were identified. The measured TF cross section is shown in Fig. 60, in

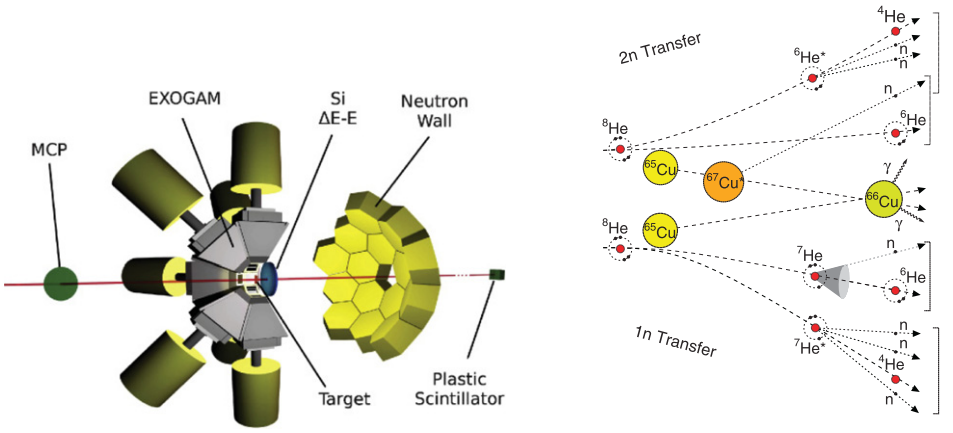

Fig. 58. (Color online) Left panel: Schematic representation of the experimental setup of Ref. [51] showing the EXOGAM array, the $\Delta E - E$ telescope and the Neutron wall; Right panel: Representation of the one- and two-neutron transfer processes in the ^{8}He $-$ ^{65}Cu collision, leading to similar final states.

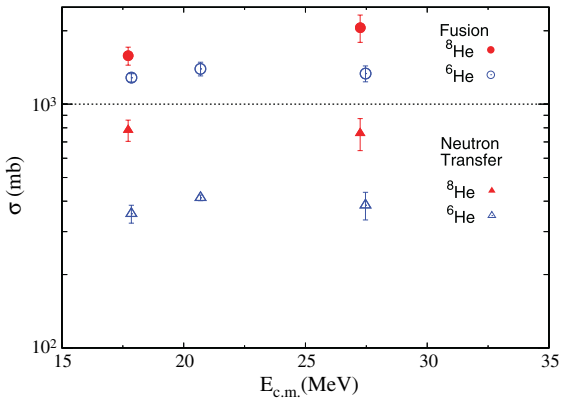

Fig. 59. (Color online) Experimental fusion and transfer excitation functions for the ^{6,8}He $+$ ^{65}Cu system. For detail see the text.
Source: The figure was taken from Ref. [48].

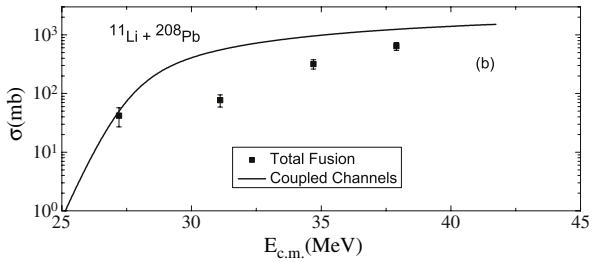

Fig. 60. Comparison between the experimental TF cross section for the ^{11}Li $+$ ^{208}Pb system with the prediction of CC calculations.
Source: The figure was taken from Ref. [349].

comparison with the predictions of coupled channel calculations. The authors claim that they have been able to detect ICF and they found a large amount of those events. An interesting result of this work is that their experimental TF cross section is much smaller than predictions of CC calculations at energies above the Coulomb barrier. It will be very interesting to see, in the near future, results of fusion of ^{11}Li with other targets and, if possible, with an enhanced beam intensity.

There are no recent reports on fusion of ^{11}Be. However, Hinde and Dasgupta [350] have re-analyzed the data obtained at RIKEN, by Yoshida et al. [367] and by Signorini et al. [382]. Fusion cross sections were derived from the measurement of alpha-particles emitted by the decay of residual nuclei. In Ref. [350] there is a long discussion concerning the data and the different ways to analyze them. They point out that these differences may give rise to conflicting conclusions about the effect of breakup on the fusion of ^{9,10,11}Be isotopes. Their suggestion is that new measurements of fusion cross sections should be performed with this very interesting ^{11}Be neutron-halo nucleus.

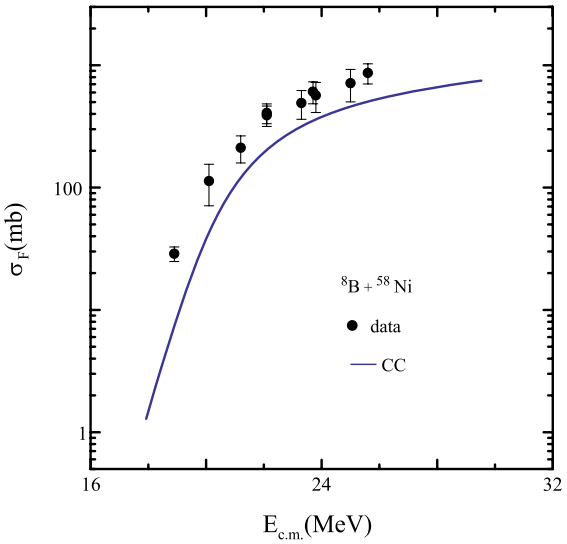

Fig. 61. (Color online) Experimental TF cross section for the $^8B + ^{58}Ni$ system [383], compared with predictions of CC calculations [384]. For detail see the text.
Source: The figure was taken from Ref. [384].

6.2.2. Fusion of proton-halo nuclei

In 1998 Rehm et al. [383] reported the first measurement of fusion involving a proton-drip line nucleus. They measured the TF cross section for the $^{17}F + ^{208}Pb$ system. Comparing their data to predictions of CC calculations, they concluded that there was no suppression at above-barrier energies.

The first fusion experiment involving a proton-halo nucleus in its ground state was performed by Aguilera et al. [352], at Notre Dame University, in 2011. They measured the TF cross section for the $^8B + ^{58}Ni$ system. They detected the protons emitted at backward angles and made the assumption that they were originated exclusively from evaporation of the compound nucleus. Their data were then fitted by Wong's formula [174], with the barrier parameters treated as adjustable variables. This fit lead to unrealistic barrier parameters, as compared with typical values for bare potentials. They found $R_B = 11.1$ fm and $V_B = 20.0$ MeV, whereas the Akyüz–Winther potential [244] predicts 8.9 fm and 21.1 MeV, respectively. The cross section given by Wong's formula with the fitted parameters is much larger than the one obtained with their usual values, over the whole energy range. This was interpreted as an indication that the experimental TF cross section for the $^8B + ^{58}Ni$ system is enhanced below and above the barrier. Rangel et al. [384] reached the same conclusion performing a more conventional analysis of the data. They compared the experimental TF cross section of Ref. [352] with results of CC calculations. Their calculations adopted the SPP[125,126] as the bare potential and included the main inelastic excitations. The results are shown in Fig. 61. Their analysis also indicates an enhancement of TF in the whole energy range.

Similar conclusions were drawn by Gomez-Camacho et al. [132], fitting simultaneously fusion and elastic scattering data for this system. The fit could only be achieved with a very large radius of the optical potential. However, this large enhancement of fusion data below and above the barrier is a very unusual behavior. It has not been observed for any other stable or neutron-halo system. Rangel et al. [384] raised the possibility that the breakup of ^8B could also produced protons at backward angles. In that case, the corresponding yield should be removed from the data analysis and the TF cross section would be lower.

More recently, Pakou et al. [351] measured the TF cross section for the $^8B + ^{28}Si$ system, at Legnaro Laboratory. They detected the α particles emitted at backward angles and made the assumption that they were originated from evaporation of the CN. The conclusions were not the same as in the $^8B + ^{58}Ni$ system. Comparing the data to the prediction of one-dimensional barrier penetration model, they found a small suppression above the barrier, as in the case of neutron-halo systems.

6.2.3. Fusion of non-halo radioactive nuclei

Although the weakly bound ^8Li and ^7Be nuclei are radioactive, their binding energies are closer to those of stable weakly bound nuclei than to those of the neutron-halo nuclei of Section 6.2.1. ^8Li breaks up into $^7Li + n$, with a threshold energy of 2.033 MeV, which stands between those of ^6Li (1.475 MeV) and ^7Li (2.468 MeV). ^7Be is the mirror nucleus of ^7Li and it breaks up into $^4He + t$, with threshold 1.58 MeV, which is close to that of ^6Li. This nucleus has also the interesting property of being the core in the breakup reaction: $^8B \rightarrow ^7Be + p$.

Fusion reactions involving ^8Li and ^7Be are not expected to be very different from those involving $^{6,7}Li$ and ^9Be, for which the beams have much higher intensities. Nevertheless, some studies of fusion involving these nuclei have been reported and in most cases the results are compared with those obtained for similar stable nuclei. Aguilera et al. [353] have measured

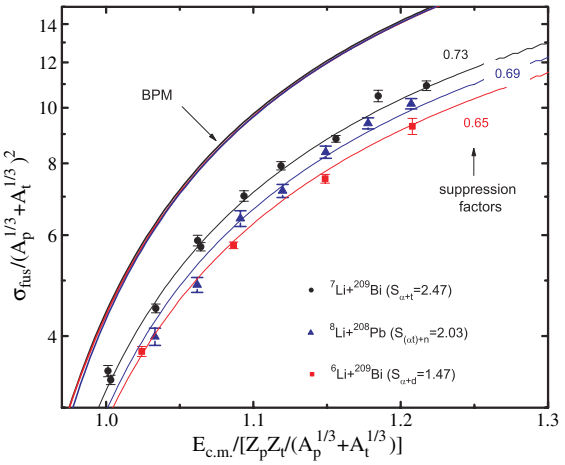

Fig. 62. (Color online) CF cross sections for the ^{8}Li + ^{208}Pb system [353], compared with data for the similar ^{6,7}Li + ^{209}Bi systems [180,269]. The thick solid line is the result of the one-dimensional barrier penetration model.

the CF cross section for the ^{8}Li + ^{208}Pb system. The experiment was performed at Notre Dame University, detecting the α particles emitted by the residual nuclei. The ^{8}Li beam intensity was of the order of 10^5 pps. The results are shown in Fig. 62, in comparison with the fusion excitation functions of the ^{6,7}Li + ^{209}Bi systems [180,269]. Note that this work adopts the experimental definition of CF, that is, the CF data for ^{8}Li include the absorption of its whole mass and also the absorption of ^{7}Li, after ^{8}Li loses one neutron. To compare the different systems, the data was reduced by the method proposed by Gomes et al. [158]. The figure also shows the prediction of the one-dimensional barrier penetration model (thick solid line) and this cross section multiplied by different suppression factors. Taking the solid curve as the reference, one observes that the CF cross section for the three Li isotopes are suppressed at energies above the barrier. The suppression factor for each isotope is directly related with its breakup threshold, so that the cross section for ^{8}Li lies between those for ^{6}Li and ^{7}Li.

Raabe et al. [329] measured CF cross sections in collisions of ^{7,9}Be and ^{7}Li projectiles with ^{238}U targets, at energies around the Coulomb barrier. The experiment was performed at Louvain-la-Neuve and they determined the fusion cross sections measuring the fission fragments [369]. They found that the cross section for ^{7}Be was suppressed and the suppression factor was similar to the one found for ^{6}Li + ^{209}Bi and slightly above that for the ^{7}Li + ^{209}Bi system [180,269]. This is consistent with the assumption that the CF suppression above the barrier is a monotonic function of the breakup threshold energy.

Kalita et al. [385] determined TF fusion cross sections in collisions of ^{7}Be and ^{7}Li projectiles on ^{27}Al, using an indirect procedure. Their experiments were performed at the HIRA-RIB facility at IUCC, New Delhi. First, they measured the quasi-elastic scattering and transfer cross section for these systems, and obtained the total reaction cross section from the scattering data. The fusion cross section was then determined subtracting the cross section for direct processes. They concluded that their TF cross sections for the ^{7}Be and ^{7}Li projectiles were similar.

Recently, Martinez-Quiroz et al. [354] measured the TF cross section for the ^{7}Be + ^{58}Ni system. The experiment was performed at Notre Dame, using the proton multiplicity method. Comparing the experimental cross section with predictions of optical model calculations, they found that the data was enhanced at both sub-barrier and above-barrier energies. These conclusions are similar to the ones they reached for the ^{8}B + ^{58}Ni system, which has already been discussed.

6.3. *Influence of transfer on fusion experiments*

It has been known for decades that transfer channels may have strong influence on the fusion of tightly bound heavy ion, specially at sub-barrier energies [386,387]. In the case of weakly bound heavy ions, couplings to transfer channels may lead to similar effects. In addition, the transfer process may lead to some complications in experimental and theoretical studies of fusion. One example is the ICF cross section in collisions of weakly bound projectiles like ^{6}Li. In this case, the direct transfer of a ^{2}H or a ^{4}He cluster produces the same final states as the ICF of the corresponding fragment, after ^{6}Li breakup. From the experimental point of view, these processes cannot be distinguished. On the other hand, from the theoretical point of view, transfer and ICF are very different processes. The former takes place in a single step whereas the latter is a two-step process (breakup and then partial fusion). Thus, both the transfer channel and the discretized continuum pseudo-channels should be included in CDCC calculations and this is a very hard task.

Transfer reactions are particularly important in collisions of neutron-halo nuclei, like ^{6}He or ^{8}He. In these cases the neutron-stripping cross sections are very large, mainly at sub-barrier energies. This may lead to difficulties to measure the fusion cross section. A classical example is the fusion cross section for the ^{6}He + ^{238}U system. In this case, the fusion process leads to a compound nucleus that decays mainly through the fission channel. Thus, the fusion cross section is measured through the detection of the fission fragments. This cross section was measured in Louvain-la-Neuve in two experiments by the same group.

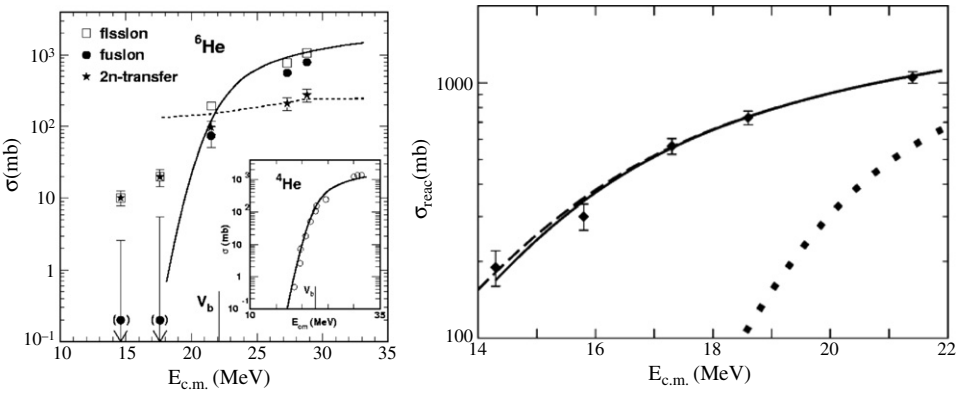

Fig. 63. Left panel: the fusion (solid circles), fission (open squares) and 2n-transfer (solid stars) cross sections for the ^{6}He + ^{238}U system; Right panel: Total reaction cross section obtained summing the angle-integrated ^{4}He yield with the fusion cross section measured in Ref. [146]. The reaction cross section is represented by the points with large cross sections and error bars, whereas the fusion cross sections are represented by the data points with cross sections at least one order of magnitude lower.

The first experiment [368], performed in 2000, found that the fusion cross section at sub-barrier energies was enhanced in comparison to predictions of barrier penetration models.

In 2004, an improved experiment [369] detected triple-coincidence events. The fission of the target-like nucleus produced in the collision could be triggered by fusion but it could be triggered also by inelastic scattering and by neutron transfer. With the triple coincidence, it was possible to disentangle the contributions of these processes to the large α yields obtained in the previous experiment. The fusion cross section obtained by Raabe et al. [369] is shown on the left panel of Fig. 63, together with the cross sections for fission and two-neutron transfer. At the lowest energies, the fission cross section is much larger than the fusion cross section. In this energy region fission is triggered dominantly by two-neutron transfer. After eliminating the large contributions from transfer, the enhancement of the fusion cross section found in their previous experiment disappears. Then, the main reaction process in this energy range was identified as the two-neutron stripping reaction.

Other experiments on collisions of the ^{6}He projectile on a heavy target lead to similar conclusions. In this case the experiments were performed in Notre-Dame, by Aguilera et al. [129,148], and the target was ^{209}Bi. They have shown that neutron transfer and breakup were responsible for most of the reaction cross section at sub-barrier energies. Their results are shown on the right panel of Fig. 63. Later, coincidence experiments between α particles and neutrons were performed in the same laboratory [373,374]. They indicated that more than 50% of the α events were originated from two-neutron stripping. The remaining events resulted from one-neutron stripping and fusion. It is important to mention that in most experiments the α particle yields could not be attributed to processes of a single kind, like neutron-stripping. They result also from transfer + breakup processes. When one measures the characteristic γ- or X-rays of the target-like nucleus (after the absorption of one or two neutrons), the transfer stripping can be identified reliably.

Di Pietro et al. [370] performed experiments on the ^{6}He − ^{64}Zn collision at Louvain-la-Neuve. They found that the breakup plus transfer cross processes were responsible for around 80% of the total reaction cross section at near-barrier energies. Measuring the fusion evaporation channels and using estimates of evaporation codes, they determined the contribution from each evaporation channel. It was then possible to identify an important contribution from the stripping of one-neutron. In a more recent experiment [345], the same group extended the measurements to a wider energy range and obtained similar results. This can be seen on the left panel of Fig. 54, in Section 6.2.1, which shows the cross sections for the emission of heavy fragments in the ^{4,6}He − ^{64}Zn collisions. In the case of ^{4}He, fusion is the only process producing heavy fragments. On the other hand, for ^{6}He they can also be produced by neutron-stripping. The difference between the heavy fragment cross section (blue circles) and the fusion cross section (black triangles) then gives the contribution from neutron-stripping in ^{6}He.

Navin et al. [157] performed coincident experiments at the SPIRAL-ISOL facility in Ganil. They measured coincidences of α particles and γ-rays in the ^{6,8}He − ^{63,65}Cu collisions at near-barrier energies. They concluded that the neutron transfer channels are the dominant processes below the Coulomb barrier. Later, the same group [51] performed similar experiments at energies above the barrier. They found that in this energy region the fusion cross section is larger than that for neutron-transfer (one and two neutrons). This can be seen in Fig. 59 of Section 6.2.1. However, the one- and two-neutron transfer cross sections remain rather large, specially for ^{8}He. In an earlier experiment at GANIL, studying the same ^{6}He − ^{65}Cu collision [381], it was found that the di-neutron configuration of ^{6}He plays a dominant role in the reaction mechanism. The same group in GANIL performed experiments to determine fusion and neutron-transfer cross sections in ^{8}He − ^{197}Au collision [149]. The neutron-transfer cross section was found to be larger than the fusion cross section, both below and above the Coulomb barrier. This can be observed on panel (e) of Fig. 57, in Section 6.2.1.

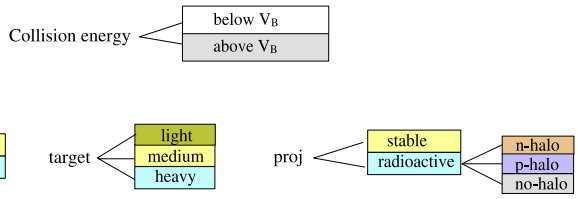

Fig. 64. (Color online) Schematic representation of the different criteria that can be used to classify sets of data with the same trends.

The one-neutron transfer and the fusion cross sections for the ^{6}He + ^{197}Au system were measured by Penionzhkevich et al. [346], in Dubna. The one-neutron transfer cross section below the Coulomb barrier was found to be much larger than the fusion cross section. At above-barrier energies they found the opposite situation, with the one-neutron transfer cross section being much smaller. This is shown on the left panel of Fig. 55, in Section 6.2.1. Below the Coulomb barrier, the stripping of one-neutron (red open circles) is about one order of magnitude larger than fusion (pink solid square). The two cross sections have similar values at the barrier, and at higher energies the fusion cross section is about one order of magnitude larger.

Acosta et al. [232] investigated the ^{6}He − ^{208}Pb collision and concluded that the observed large α particle yield was produced mainly by neutron-stripping reactions. Similar conclusions were reached for collisions of stable weakly bound projectiles, specially at sub-barrier energies. Pakou et al. [151,152,230] have investigated the ^{6,7}Li − ^{28}Si collisions and found large α particles yields, which were attributed mainly to transfer reactions.

Shrivastava et al. [336] measured one-neutron stripping and one-neutron pickup in the ^{6}Li − ^{198}Pt collision. They have shown that the direct reaction cross section is much larger than the fusion cross section at energies below the barrier, as shown in Fig. 48 of Section 6.1. They investigated also the ^{7}Li − ^{198}Pt system [224] and found that the one- and two-neutron stripping and the one-neutron pickup reactions have important cross sections.

Palshetkar et al. [96] investigated ^{6,7}Li − ^{197}Au collisions. They found sizeable transfer cross sections for ^{6}Li (one-neutron stripping and one-neutron pickup) and ^{7}Li (one- and two-neutron stripping) induced reactions, as can be observed on the left panel of Fig. 47, in Section 6.1.

Di Pietro et al. [72] investigated the ^{6,7}Li − ^{64}Zn collision. They concluded that CF is the main process at above-barrier energies whereas transfer and ICF are the dominant processes below the Coulomb barrier. For ^{9}Be induced reactions, one-neutron stripping has been observed in collisions with several targets [215,342,388,389]. For the ^{8}Li − ^{9}Be collision, it was also found [390,391] that one-neutron pickup and one-neutron stripping are important reaction mechanisms and for the ^{8}Li − ^{208}Pb collision, transfer and breakup are the dominant processes at sub-barrier energies [392].

6.4. Systematic trends of the fusion cross sections

One of the main goals of the papers discussed in the previous section is to look for systematic trends in fusion reactions induced by weakly bound projectiles. This could be achieved comparing the cross sections in many different situations, like CF cross sections in collisions of stable weakly bound projectiles on targets in a given mass range, TF in collisions of neutron-halo projectiles on heavy targets, and so on. Furthermore, the trends of the cross section at sub-barrier energies are, in general, quite different from those above the Coulomb barrier. One should then try to identify the trends of the sets of data corresponding to some particular experimental situation. These sets may be classified according to different criteria, like TF vs. CF, stable projectiles vs. radioactive projectiles, etc. These criteria are schematically represented in Fig. 64.

There are important experimental limitations in systematic studies. First, only a few experiments can determine individual cross sections for both CF and TF. In most cases, only the TF cross section is measured and in some experiments only the CF cross section is determined. Frequently, some evaporation channels cannot be measured, owing to their long lifetimes. Their contributions to the fusion cross section have then to be estimated by evaporation codes, like CASCADE [393] or PACE [394], and this adds uncertainties to the experiment. This is not a serious problem if their contribution is only a few percent. However, when they represents about 30%, or more, the 'experimental' cross section is strongly affected by the theoretical predictions of the evaporation code. In such cases, the error bars associated to statistical factors do not represent the real uncertainty of the measurement. Therefore, one should be careful when investigating effects of the order of 5 to 10% in the cross section. Experiments with radioactive beams have still greater uncertainties. First, the beam intensities are several orders of magnitude lower than those of stable weakly bound nuclei. Additional uncertainties in these experiments come from the poorer energy resolution.

6.4.1. Reduction of fusion data

To establish the influence of the low breakup threshold on fusion, one frequently compares experimental excitation functions for different systems. However, the fusion cross section is also influenced by trivial differences among the systems, like their sizes and their charges. One then tries to eliminate this influence through the reduction of the fusion data. There are, however, several procedures to achieve this goal. The basic idea is to perform transformations on the collision energy and on the cross section so that the transformed excitation function looks the same for any system that is not affected by

the intrinsic structure of the collision partners. The simplest idea is the change of variables,

$$E \longrightarrow \varepsilon = \frac{E}{V_B}, \qquad \sigma_F \longrightarrow Y = \frac{\sigma_F}{\pi R_B^2}. \tag{126}$$

The above expression is based on the classical approximation for potential scattering, where $|S_l(E)|$ is equal to 0 or 1, depending on the energy being lower or higher than the barrier of the l-dependent effective potential. In this case the cross section is given by the well known expression,

$$\sigma_F = \pi R_B^2 \left[1 - \frac{V_B}{E}\right]. \tag{127}$$

The transformation of Eq. (126) then leads to the universal function,

$$Y(x) = 1 - \frac{1}{\varepsilon}. \tag{128}$$

Thus, if the fusion cross section can be treated as a potential scattering problem (no influence of intrinsic structure) and the classical approximation for the transmission coefficient holds, the cross sections for all systems coincide. The nuclear structure of the collision partners would then influence the fusion cross section, leading to deviations from this behavior. However, this classical expression for the fusion cross section is inaccurate just above the barrier and is completely wrong at sub-barrier energies. Gomes et al. [158] proposed a reduction method based on the same idea. Instead of dividing the energy by the barrier height and the cross section by its geometrical value, as in Eq. (126), they divide by constants that are proportional to these quantities. Since,

$$R_B = r_0 \left[A_P^{1/3} + A_T^{1/3}\right] \quad \text{and} \quad V_B \simeq \frac{Z_P Z_T e^2}{R_B}, \tag{129}$$

they adopt the transformation

$$E \longrightarrow E_{red} = E \left[\frac{A_P^{1/3} + A_T^{1/3}}{Z_P Z_T e^2}\right], \qquad \sigma_F \longrightarrow \sigma_{red} = \frac{\sigma_F}{\left(A_P^{1/3} + A_T^{1/3}\right)^2}. \tag{130}$$

In this way, the reduction method becomes model independent. It does not require the barrier parameters of the bare potential. Owing to this feature, it has been frequently used in the literature.

However, the above reduction methods have the drawback of being based on a classical expression for the cross section. Thus, they do not work properly just above the Coulomb barrier and break down at sub-harrier energies. This is illustrated in Fig. 65, where we compare the cross sections for four systems in different mass ranges. The dashed line corresponds to the classical cross section of Eq. (128). Although the cross sections go to the same limit at high enough energies, this limit may be reached very slowly, mainly for light projectiles like ^{6}He. Thus, the differences among the reduced cross sections at near-barrier energies cannot be attributed to the intrinsic structure of the collision partners (neglected in the figure).

The problem with the above reduction methods stems from its underlying classical nature. This shortcoming is avoided in the Fusion Function approach of Refs. [160,161]. The authors propose the transformations,

$$E \longrightarrow x = \frac{E - V_B}{\hbar\omega}, \qquad \sigma_F \longrightarrow F(x) = \frac{2E}{\pi R_B^2} \times \sigma_F. \tag{131}$$

This transformation is based on the Wong's approximation [174] for the fusion cross section,

$$\sigma_F^W = \frac{\pi R_B^2}{2E} \ln\left[1 + \exp\left(2\pi \frac{E - V_B}{\hbar\omega}\right)\right]. \tag{132}$$

It can be immediately checked that if the fusion cross section is well approximated by Wong's formula, the fusion function takes the universal form

$$F_0(x) = \left[1 + \exp(2\pi x)\right]. \tag{133}$$

This expression was called the Universal Fusion Function (UFF) in Refs. [160,161]. In Fig. 66, we show the cross sections for the systems of the previous figure but now they are reduced by the fusion function method. The cross sections for the four systems now are almost identical. The goal of the reduction is then achieved: differences in the excitation functions can be attributed to the intrinsic structure of the systems.

Comparisons among experimental cross sections reduced by the fusion function procedure are useful for studies of the influence of excited channels on fusion. However, systematic studies of weakly bound systems require a very exclusive piece of information. One wants to investigate the influence of the breakup channel. Therefore, it is necessary to disentangle it from the influence of couplings with bound channels. This is achieved by the renormalization of the fusion function

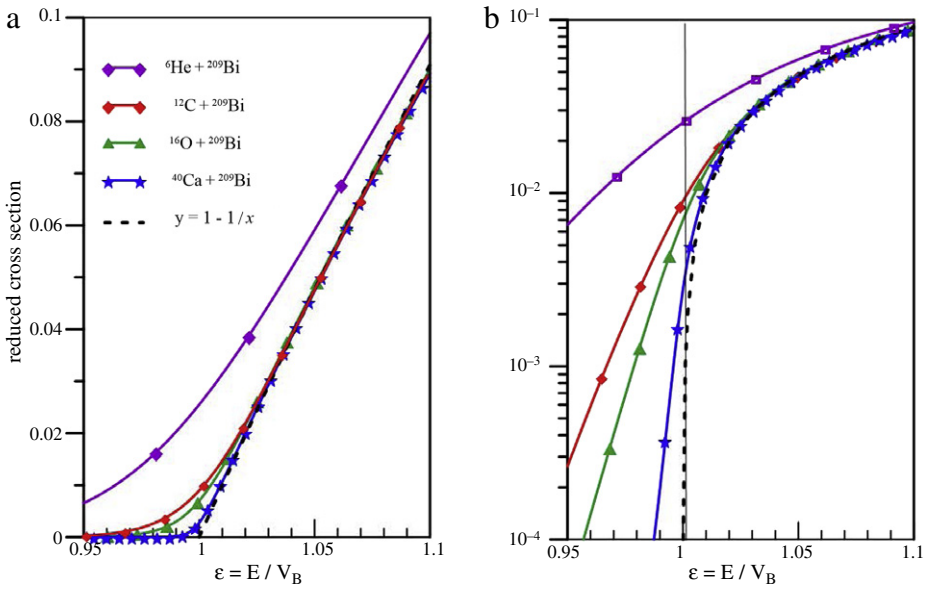

Fig. 65. (Color online) Fusion cross sections for the ^{6}He + ^{209}Bi, ^{12}C + ^{209}Bi, ^{16}O + ^{209}Bi and ^{40}Ca + ^{209}Bi systems reduced by the transformation of Eq. (126). The cross sections were obtained solving the one-dimensional radial equations using the Akyüz–Winther potential [244] and short-range absorption. The dashed line corresponds to the classical expression of Eq. (128). The results are shown in (a) linear and (b) logarithmic scales.

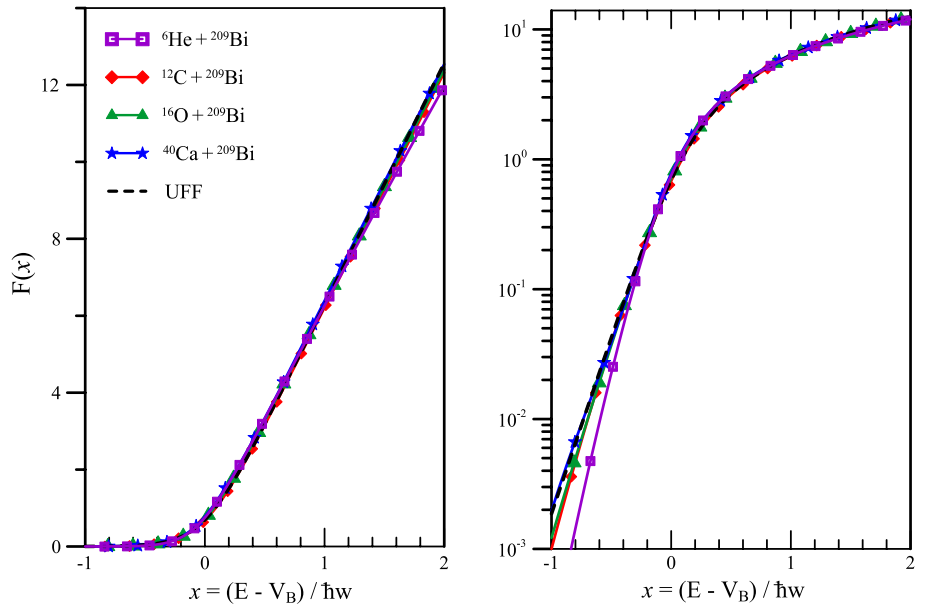

Fig. 66. (Color online) Same as the previous figure but now the excitation function was reduced by the fusion function method of Refs. [160,161].

[160,161], as follows. First, one evaluate the experimental fusion function, $F_{\rm exp}(x)$, through Eq. (131), using the experimental fusion cross section. Then, the renormalized function, $\bar{F}^{\rm exp}(x)$ is obtained by the equation,

$$\bar{F}^{\rm exp}(x) = F^{\rm exp}(x) \times \frac{\sigma_{\rm F}^{\rm W}}{\sigma_{\rm F}^{\rm CC}}, \tag{134}$$

where $\sigma_{\rm F}^{\rm W}$ is Wong's cross section (Eq. (132)) and $\sigma_{\rm F}^{\rm CC}$ is the fusion cross section given by a CC calculation that includes couplings with all relevant bound channels. This procedure has been adopted by several authors [75,96,149,298,327,351, 395–397]. However, in comparisons of data with theoretical cross sections, one should keep in mind that measurements of ICF or TF tend to be more inclusive than the calculations. No experiment can distinguish ICF of a given fragment of the projectile from the direct transfer of the same fragment. Experimentally, these processes are equivalent, but from

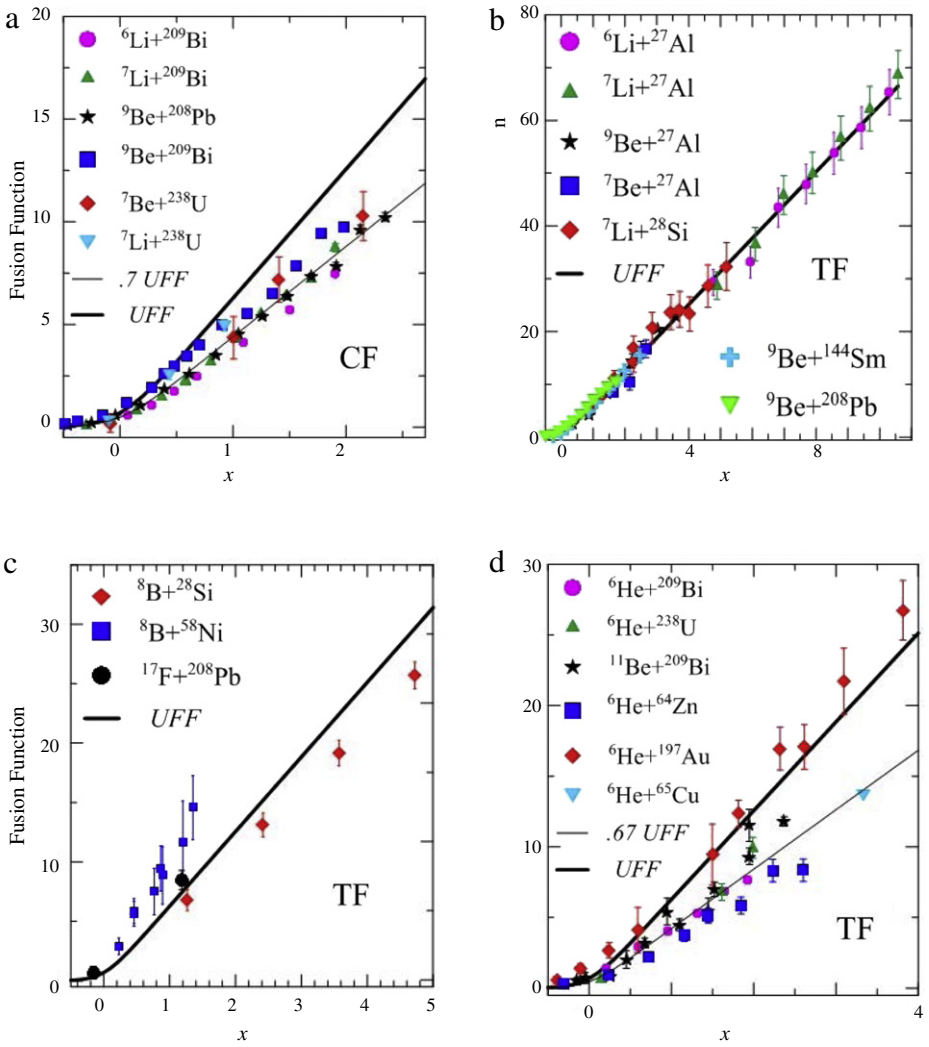

Fig. 67. (Color online) Experimental renormalized fusion functions for several systems: (a) CF of stable weakly bound systems, (b) TF for stable weakly bound systems, (c) TF for proton-halo weakly bound projectiles and (d) TF for neutron-halo projectiles. The origin of the experimental data for each system can be found in Tables 1 and 2 and, in each case, the renormalization of the experimental fusion function was based on CC calculations including all relevant inelastic channels.

the theoretical point of view they are very different. The former is a second order process (breakup followed by fusion) whereas the latter takes place in a single step. In the case of neutron-halo nuclei, the experimental TF cross section may get important contributions from more complicated process, like the transfer of one or two neutrons before fusion. Usually, these processes are not included in the calculations. From the theoretical side, there are calculations using different bare potentials, barrier parameters, coupled channel schemes and they may lead to appreciable differences in the cross sections [254]. Thus, suppression factors obtained from the same data set but using as a benchmark the results of different theoretical models can be drastically different. The conclusion may even change from suppression to enhancement.

Systematic comparisons of renormalized experimental fusion excitation functions are presented in Fig. 67, in the cases of: (a) CF of stable weakly bound nuclei, (b) TF of stable weakly bound nuclei, (c) TF of proton-halo nuclei and (d) TF of neutron halo-nuclei. The results lead to the following general conclusions about fusion cross sections at above-barrier energies:

(a) CF of stable weakly bound systems tend to be suppressed. The suppression factor (ratio between the thin and thick solid lines) is of the order of 70%;

(b) TF of stable weakly bound system is not influenced by the low breakup threshold. The data follow closely the UFF;

(c) TF of proton-rich systems do not show a systematic trend. The data follow the UFF in the case of $^{17}\mathrm{F} + {}^{208}\mathrm{Pb}$, they are suppressed for $^{8}\mathrm{B} + {}^{28}$ Si but they are enhanced for $^{8}\mathrm{B} + {}^{28}\mathrm{Ni}$. In fact there are not data for a sufficient number of systems to clarify the matter. New experiments would be very welcome;

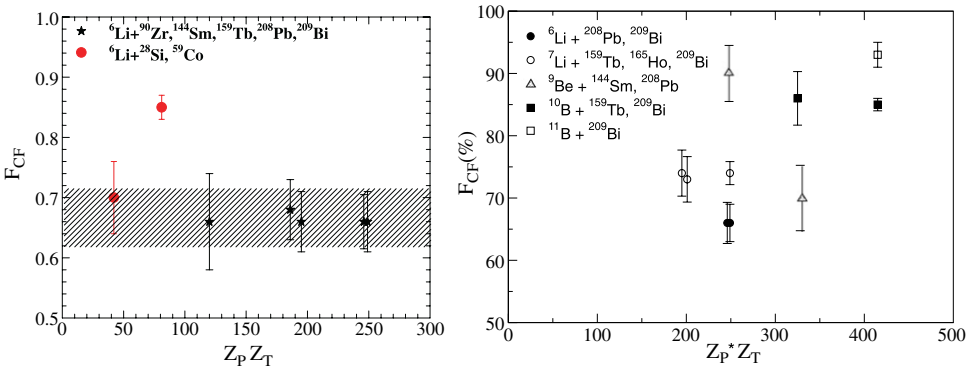

Fig. 68. (Color online) Left panel: CF suppression factors in collisions of ^{6}Li with several targets [332]; Right panel: similar to the left panel but now the suppression factors are given as percentages and several projectiles are considered [344].

(d) TF of radioactive neutron-rich systems tends to be suppressed. The suppression factor is of the same order as for CF of stable weakly bound systems. However, here there is a clear exception: the data of Penionzhkevich et al. [346] for the ^{6}He + ^{197}Au, which is very close to the UFF.

6.4.2. *Suppression factors*

A very convenient way to investigate the effects of the breakup channel on fusion of weakly bound systems is to look at suppression factors. Since their experimental fusion excitation functions at above-barrier energies can be approximated by the barrier penetration model cross section multiplied by a constant suppression factor, F_{CF} for CF and F_{TF} for TF, the influence of the low breakup threshold can be expressed by this single number. In the following, we mention some papers that adopt this procedure to perform systematic studies of CF and TF of weakly bound systems at energies above the barrier. They aim at correlating suppression factors with the target's mass or charge, and/or to the projectile breakup threshold energy. The target mass/charge dependence of F_{CF} for the ^{6,7}Li projectiles has been investigated in several recent papers [101,332,335,338,344]. They all find that the CF cross section is suppressed and that the suppression factor depends weakly on the target. It is between 0.60 and 0.70 for ^{6}Li projectile, and between 0.70 and 0.75 for ^{7}Li projectiles. The study considered the ^{90}Zr, ^{144}Sm, ^{159}Tb, ^{165}Ho, ^{208}Pb and ^{209}Bi targets and the data are from Refs. [69,101,180,269,328,332,335,336,398]. Thus, the CF suppression is found to be larger for ^{6}Li than for ^{7}Li.

Examples of suppression factors are given in Figs. 68 and 69. The left panel of Fig. 68 shows results of Ref. [332] for ^{6}Li projectiles. It investigates the dependence of the suppression factor on the target, plotting F_{CF} as a function of the product of the projectile's and target's atomic numbers, $Z_P Z_T$. The solid circles in red correspond to light systems, for which just TF was measured. One notices that ^{6}Li + ^{59}Co [227] is the only system that does not follow the systematic trend of the other systems. However, we remark that this point corresponds to TF, rather than CF. The right panel of Fig. 68 shows similar plots for ^{6,7}Li and other weakly bound projectiles. Now F_{CF} is given as a percentage. The behavior of the suppression factors for ^{6,7}Li projectiles [344] is similar to the one observed on the left panel.

The top panel of Fig. 69 shows results of a similar study for heavy targets, reported in Ref. [335]. We point out that in this case the suppression factor is defined in a different way. It corresponds to the suppression of the experimental cross section, rather than to its ratio with respect to the cross section of barrier penetration models. That is, it gives, in fact, $1 - F_{CF}$. The suppression for ^{6}Li projectiles is plotted as a function of the atomic number of the target. Their results are consistent with those shown in the previous figure. Suppression factors for collisions of ^{6}Li projectile on other targets [338] are also shown on the bottom panel of Fig. 69 and they agree with the results previously shown. For the ^{9}Be projectile, the situation is not so clear. Some papers investigated the dependence of F_{CF} on the target's charge [101,338,344,362], but the data did not show the constant behavior found for ^{6,7}Li. Data for several targets can be found in Refs. [269,342,284,337–339,361] and some examples are given in Figs. 68 and 69. We observe that the CF suppression factor for ^{124}Sn, ^{208}Pb and ^{209}Bi are of the order of 0.7, whereas for ^{144}Sm it is around 0.9. If one includes also the ^{89}Y [337] and ^{186}W [342] targets in the systematics, it is hard to draw any conclusion. This can be seen more clearly in Fig. 70, taken from the very recent work of Jha et al. [273]. These authors calculated ICF probabilities, which is roughly $1 - F_{CF}$. The dark region in Fig. 70 between the full (blue) curve and the dashed (red) curve corresponds to the region where the CF suppression is expected to be, from those calculations. The pink dotted–dashed curve in this figure is the result of an empirical prediction of Hinde et al. [215].

The behavior of F_{CF} for the not so weakly bound ^{11}B projectile was also investigated [338,344]. Data from Refs. [328,344] for the ^{159}Tb and ^{209}Bi targets are included on the right panels of Figs. 68 and 69. CF suppression factors of the order of 0.85 were found for both targets, in both works.

Now we discuss the dependence of the suppression of CF on the breakup threshold energy. As already shown in Fig. 62, Aguilera et al. [353] have found that the CF suppression factor for the ^{6}Li + ^{209}Bi is smaller (that is, larger suppression) than that for ^{8}Li + ^{208}Pb, which is smaller than that for ^{7}Li + ^{209}Bi. This agrees with the expectation that CF suppression increases as the threshold breakup energy decreases. Gasques et al. [344] plotted the ICF probability versus the breakup

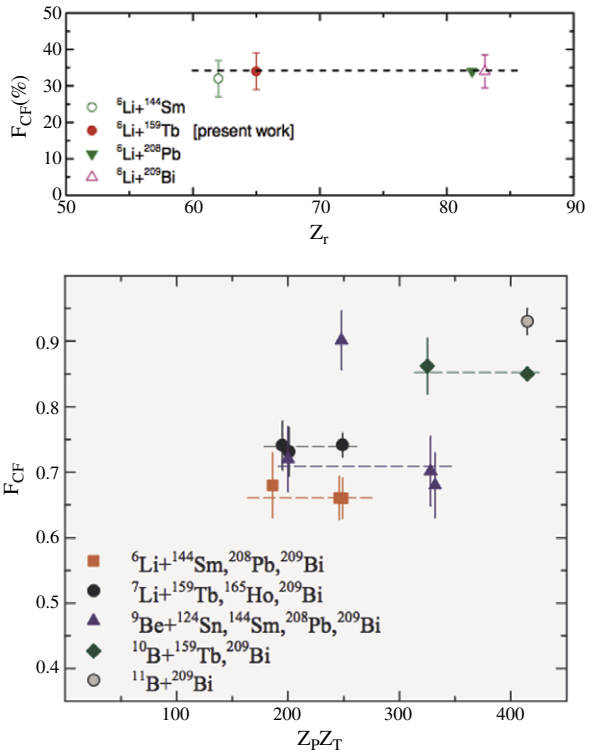

Fig. 69. (Color online) Top panel: CF suppression in collisions with ^{6}Li with very heavy targets, as a function of the atomic number of the target [335]. Note that in this case the suppression factor is defined as the missing percentage of the experimental cross section, with respect to that of the barrier penetration model; Bottom panel: similar to Fig. 68 [338].

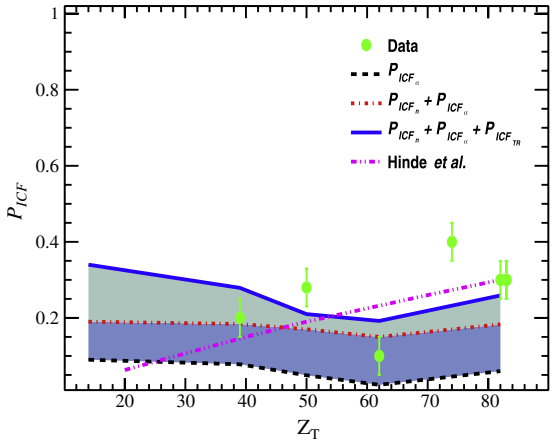

Fig. 70. (Color online) ICF probabilities for ^{9}Be projectiles as a function of the target's atomic number. The calculated probabilities are compared with probabilities determined from experimental data [273]. For detail, we refer to the original paper [273].

energy for different projectiles on similar heavy targets. Their results are shown on the top panel of Fig. 71. They found a linear behavior in a logarithmic scale, which means that the ICF probability decreases exponentially with the breakup threshold energy. Pradhan et al. [335], however, found a different behavior. Studying collisions of ^{6}Li, ^{7}Li and ^{10,11}B with ^{159}Tb, they concluded that the ICF probability decreases linearly with the breakup threshold energy. This is illustrated on the bottom panel of Fig. 71. Although the works of Gasques et al. [344] and Pradhan et al. [335] agree qualitatively, the quantitative dependence of the ICF probability on the breakup threshold has not been established.

At this point it is important to mention that the differences in the CF suppression under investigation are very small. Thus, they can be hardly noticed in traditional fusion excitation functions in logarithmic plots. One example is the recent work of Palshetkar et al. [96], where the authors compare results for different projectiles (^{6,7}Li, ^{6,8}He) on similar targets (^{197}Au and ^{198}Pt). Fig. 72 shows their results. They used the reduction method proposed by Canto et al. [160]. In the notation of the

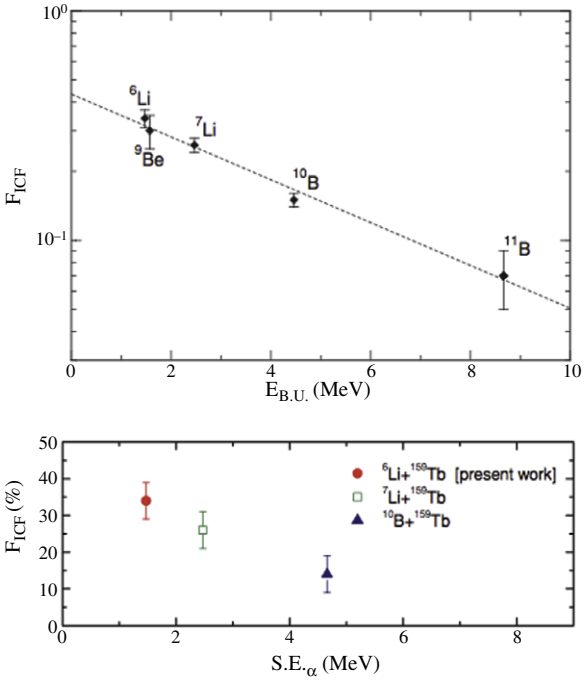

Fig. 71. (Color online) Top panel: ICF probabilities in collisions with different weakly bound projectiles with very heavy targets as a function of the projectiles' breakup threshold energies [344]; Bottom panel: ICF probability as a function of the breakup threshold energy [335].

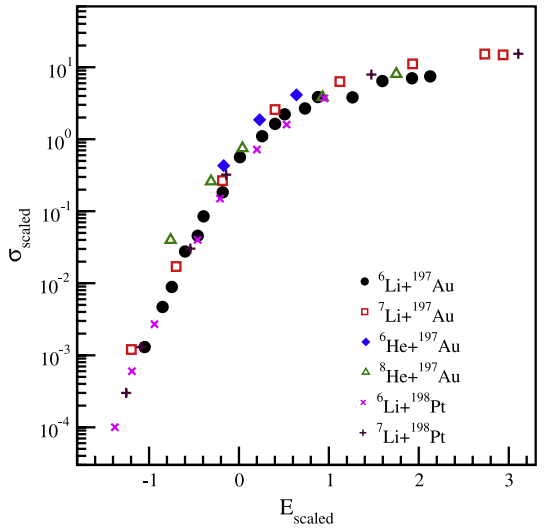

Fig. 72. (Color online) Comparison of scaled fusion cross sections for some stable and radioactive weakly bound projectiles. The scaled energies and cross sections are the dimensionless variables of fusion function reduction method of Refs. [160,161].
Source: The figure is from Ref. [96]. Details can be found in this paper.

previous section, E_{scaled} and σ_{scaled} correspond respectively to x and $\bar{F}_{\text{CF}}^{\text{exp}}$. Their conclusion is that the reduced CF excitation function does not have a significant dependence on the breakup threshold of the projectile. Although this conclusion is consistent with the results shown in this logarithmic plot, linear plots are more appropriate for this analysis.

Very recently, Wang et al. [399] performed a comprehensive investigation of the suppression of CF in collisions at energies slightly above the barrier. They considered collisions of the ^{6,7}Li, ^{9}Be, ^{10,11}B, ^{12,13}C and ^{16}O projectiles with several heavy targets, ranging from ^{89}Y to ^{209}Bi. To plot together results for collisions of a given projectile with different targets, the data were reduced by the method proposed by Canto et al. [160,161]. That is, the collision energies and the CF cross sections were transformed according to Eq. (131). Since couplings with bound channels do not play an important role in this energy range, it was not necessary to renormalize the fusion functions to eliminate their effects. The reduced data for each projectile were then compared with the universal fusion function of Eq. (133) and a suppression factor was determined. The dependence of

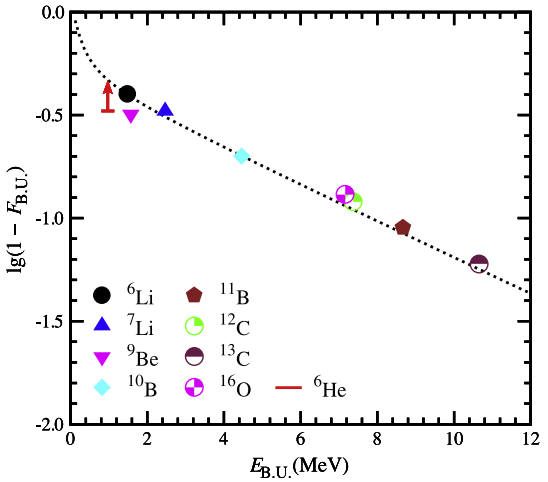

Fig. 73. (Color online) Comparison of the empirical function of Eq. (135) with the corresponding experimental results.
Source: This figure was taken from Ref. [399].

the suppression factors on the breakup threshold of the projectile was then investigated. They found the empirical equation,

$$\ln\left[1 - F_{\text{B.U.}}\right] = -0.76\ \exp\left[-\frac{0.29}{E_{\text{B.U.}}}\right] - 0.29\,E_{\text{B.U.}}, \tag{135}$$

where $F_{\text{B.U.}}$ and $E_{\text{B.U.}}$ stand respectively for the CF suppression factor and the breakup threshold. In Fig. 73 the curve corresponding to the above equation is compared with the experimental results.

We mention also the calculations of Sargsyan et al. [400], based on their quantum diffusion approach [296–298,401–403]. Comparing their predictions of the CF cross section with the available data, they fit the CF suppression factor. They considered collisions of ^{6,7}Li, ^{9}Be, ^{6,8}He and ^{11}B weakly bound projectiles at energies above the barrier. Their study of the CF suppression factor does not lead to a clear systematic behavior for all projectiles. For ^{6,7}Li it is nearly independent of the target, remaining around 0.50 for all ^{6}Li and in the range 0.60–0.70 for ^{7}Li. However, for ^{9}Be, there is no systematics trend. The suppression factor varies from 0.64 to 0.90. Similar situations are found for ^{6}He and ^{11}B. In the case of ^{6}He, the suppression factors for the ^{64}Zn, ^{197}Au and ^{209}Bi targets are respectively 0.40, 0.80 e 0.68. In the case of ^{11}B, they are 0.82 and 0.95, for the ^{209}Bi and ^{159}Tb targets, respectively.

Although the studies of the systematic behavior of the CF suppression factor discussed in this section indicate that the suppression does not depend on the mass or charge of the target, one should be careful about this conclusion. We remark that these studies were based on data for relatively heavy targets and for one of the lightest system investigated, ^{6}Li + ^{96}Zr [333], a smaller suppression was found. The suppression factor is 0.75, which corresponds to less suppression than that found for heavier targets. This might be the indication of a trend. Although only TF data are available for lighter systems, there is some evidence that the CF suppression factor for the ^{6}Li + ^{64}Ni system is of the order of 0.87 (13% suppression) [333]. Thus, the behavior of the suppression factor in collisions of weakly bound projectiles with light and medium mass targets is not fully established. For a reliable conclusion about this subject, new measurements of CF for lighter targets are required.

7. Summary and conclusions

We have presented an account of recent experimental and theoretical advances on near-barrier fusion reactions induced by weakly bound nuclei. In this endeavor other important processes which influence fusion, such as elastic scattering and breakup reactions are also reviewed. One important feature of the low-energy fusion of weakly bound nuclei, which includes halo nuclei, is the dominant role of the coupling to the breakup channel. This coupling seems to be responsible for suppression of fusion at above-barrier energies and, together with the static effect of the more diffuse density, to a slight enhancement at sub-barrier energies.

The usual Threshold Anomaly (TA) seems to be replaced by the Breakup Threshold Anomaly (BTA), which involves some increase in the imaginary part of the potential as the barrier is crossed as the energy is lowered, accompanied by a reduction of the attraction in the real part of the polarization potential. The important distinction between Total Fusion (TF) and Complete Fusion (CF) is discussed in light of the importance of Incomplete Fusion (ICF), the fusion of the fragment after breakup has occurred. Elastic scattering and breakup reactions are also discussed. Deep sub-barrier suppression of fusion, a subject of great interest during the last few years, is discussed and the role of the short distance repulsion of the ion–ion potential and of the compound nucleus are considered as potential causes of the suppression, with the latter being operative in the fusion of light systems.

From the theoretical perspective, we have gone at length in discussing the available theoretical methods do describe collisions of weakly bound nuclei. The Continuum Discretized Coupled Channels (CDCC) method is discussed in detail, both in calculations of direct reaction and in the evaluation of fusion cross sections. It is pointed out that the CDCC is not able to give individual cross sections for the ICF and CF processes. In general, it gives only the TF cross section, which is the sum of the contributions from the CF and ICF reaction mechanisms. This is because the CDCC is an effective two-body scattering theory, with breakup mocked up through a discretized continuum. We discuss means to avoid this shortcoming by using models that allow the identification of the ICF pieces, based on semiclassical or classical approximations. Recent advances in theory are reviewed, and future development are pointed out. We present also a brief discussion of the relevance of the information obtained from these fusion studies to nuclear astrophysics.

From the experimental side, we gave a full account of most of the measurements of fusion, elastic scattering (including BTA studies) and breakup reactions during the last decade. About 50 experimental works were reviewed. Several stable weakly bound projectiles, such as (^{6}Li, ^{7}Li, ^{9}Be, ^{10}B), unstable, one- and two-neutron halo projectiles (^{6}He, ^{8}He, ^{11}Be, ^{11}Li), one-proton halo projectiles (^{8}B, ^{17}F), and non-halo unstable projectile (^{8}Li, ^{7}B) have been studied in fusion and scattering measurements on several target nuclei spanning a wide range of mass. We gave a rather detailed account of the major findings of the analyses of these data. For this, we partially relied on the method of reducing the fusion and reaction cross sections to system-independent ones, in order to compare data for systems in different mass ranges. The conclusion reached points to the need to get more precise data in order to better pin down the relative importance of ICF, take the CDCC to its limit of validity, and get a better description of the ion–ion interaction. We consider these to be part of the future effort dedicated to the study of low energy fusion of weakly bound nuclei and we are happy to be part of this endeavor.

References

[1] J.F. Liang, C. Signorini, Int. J. Mod. Phys. E 14 (2005) 1121.
[2] N. Keeley, R. Raabe, N. Alamanos, J.L. Sida, Prog. Part. Nucl. Phys. 59 (2007) 579.
[3] N. Keeley, N. Alamanos, K.W. Kemper, K. Rusek, Prog. Part. Nucl. Phys. 63 (2009) 396.
[4] K. Hagino, N. Takigawa, Prog. Theor. Phys. 128 (2012) 1061.
[5] B.B. Back, H. Esbensen, C.L. Jiang, K.E. Rehm, Rev. Mod. Phys. 86 (2014) 317.
[6] L.F. Canto, P.R.S. Gomes, R. Donangelo, M.S. Hussein, Phys. Rep. 424 (2006) 1.
[7] L.F. Canto, M.S. Hussein, Scattering Theory of Molecules, Atoms and Nuclei, World Scientific Publishing Co. Pte. Ltd., 2013.
[8] I.J. Thompson, F.M. Nunes, Nuclear Reactions for Astrophysics: Principles, Calculation and Applications, first ed., Cambridge University Press, 2009.
[9] G.R. Satchler, Direct Nuclear Reactions, Oxford University Press, 1983.
[10] A. Diaz-Torres, I.J. Thompson, Phys. Rev. C 65 (2002) 024606.
[11] Y. Sakuragi, M. Yahiro, M. Kamimura, Prog. Theor. Phys. Suppl. 89 (1986) 136.
[12] N. Austern, Y. Iseri, M. Kamimura, M. Kawai, G. Rawitscher, M. Yashiro, Phys. Rep. 154 (1987) 125.
[13] T. Matsumoto, T. Kamizato, K. Ogata, Y. Iseri, E. Hiyama, M. Kamimura, M. Yahiro, Phys. Rev. C 68 (2003) 064607.
[14] F.M. Nunes, I.J. Thompson, Phys. Rev. C 59 (1999) 2652.
[15] I. Bray, Phys. Rev. Lett 89 (2002) 273201.
[16] I. Bray, A.T. Stelbovics, Phys. Rev. A 46 (1992) 6995.
[17] G. Schiwietz, Phys. Rev. A 42 (1990) 296.
[18] H. Feshbach, Ann. Phys. (NY) 19 (1962) 287; ibid 5 (1958) 357.
[19] I.J. Thompson, M.A. Nagarajan, J.S. Lilley, M.J. Smithson, Nucl. Phys. A 505 (1989) 84.
[20] L. Rodberg, R. Thaler, Introduction to the Quantum Theory of Scattering, Academic Press, N.Y., 1967.
[21] B.V. Carlson, T. Frederico, M.S. Hussein, H. Esbensen, S. Landowne, Phys. Rev. C 41 (1990) 933.
[22] H.W. Wyld, Mathematical Methods for Physics, Benjamin/Cummings, Reading, Mass, 1976.
[23] J. Lubian, F.M. Nunes, J. Phys. G: Nucl. Part. Phys. 34 (2007) 513.
[24] M.A. Nagarajan, C.C. Mahaux, G.R. Satchler, Phys. Rev. Lett. 54 (1985) 1136.
[25] D. Abriola, D. Digregorio, J.E. Testoni, A. Etchegoyen, M.C. Etchegoyen, J.O. Fernández Niello, A.M.J. Ferrero, S. Gil, A.O. Macchiavelli, A.J. Pacheco, J. Kittl, Phys. Rev. C 39 (1989) 546.
[26] M.S. Hussein, P.R.S. Gomes, J. Lubian, L.C. Chamon, Phys. Rev. C 73 (2006) 044610.
[27] N.C. Summers, F.M. Nunes, I.J. Thompson, Phys. Rev. C 73 (2006) 031603(R).
[28] N.C. Summers, F.M. Nunes, I.J. Thompson, Phys. Rev. C 74 (2006) 014606.
[29] R. de Diego, J.M. Arias, J.A. Lay, A.M. Moro, Phys. Rev. C 89 (2014) 064609.
[30] P. Descouvemont, M.S. Hussein, Phys. Rev. Lett 111 (2013) 082701.
[31] E.C. Pinilla, P. Descouvemont, Phys. Rev. C 89 (2014) 054615.
[32] M. Rodríguez-Gallardo, J.M. Arias, J. Gómez-Camacho, R.C. Johnson, A.M. Moro, I.J. Thompson, J.A. Tostevin, Phys. Rev. C 77 (2008) 064609.
[33] M. Rodríguez-Gallardo, J.M. Arias, J. Gómez-Camacho, A.M. Moro, I.J. Thompson, J.A. Tostevin, Phys. Rev. C 80 (2009) 051601.
[34] M. Rodríguez-Gallardo, A.M. Moro, Int. J. Mod. Phys. E 20 (2011) 947.
[35] T. Matsumoto, E. Hiyama, K. Ogata, Y. Iseri, M. Kamimura, S. Chiba, M. Yahiro, Phys. Rev. C 70 (2004) 061601.
[36] P. Descouvemont, T. Druet, L.F. Canto, M.S. Hussein, Phys. Rev. C 91 (2015) 024606.
[37] N. Keeley, K.W. Kemper, K. Rusek, Eur. Phys. J. A 50 (2014) 145.
[38] W.G. Love, T. Terasawa, G.R. Satchler, Nucl. Phys. A 291 (1977) 183.
[39] C.E. Thorn, M.J. Levine, J.J. Kolata, C. Flaum, P.D. Bond, J.C. Sens, Phys. Rev. Lett. 38 (1977) 384.
[40] A. Di pietro, V. Scuderi, A.M. Moro, L. Acosta, F. Amorini, M.J.G. Borge, P. Figuera, M. Fisichella, L.M. Fraile, J. Gomez-Camacho, H. Jeppesen, M. Lattuada, I. Martel, M. Milin, A. Musumarra, M. Papa, M.G. Pellegriti, F. Perez-Bernal, R. Raabe, G. Randisi, F. Rizzo, G. Scalia, O. Tengblad, D. Torresi, A.M. Vidal, D. Voulot, F. Wenander, M. Zadro, Phys. Rev. C 85 (2012) 054607.
[41] M. Mazzocco, C. Signorini, M. Romoli, A. De franesco, M. Di Pietro, E. Vardaci, K. Yoshida, R. Yoshida, A. Bonetti, A. De Rosa, T. Glodariu, A. Guglielmetti, G. Inglima, M. La Commara, B. Martin, D. Pierroutsakou, M. Sandoli, F. Soramel, L. Stroe, R. Kanungo, N. Khai, T. Motobayshi, T. Nomura, T. Ishikawa, H. Ishiyama, S. Jeong, H. Miyatake, M.H. Tanaka, I. Sugai, Y. Watanabe, Eur. Phys. J. A 28 (2006) 295.
[42] A. Di pietro, G. Randisi, V. Scuderi, L. Acosta, F. Amorini, M.J.G. Borge, P. Figuera, M. Fisichella, L.M. Fraile, J. Gomez-Camacho, H. Jeppesen, M. Lattuada, I. Martel, M. Milin, A. Musumarra, M. Papa, M.G. Pellegriti, F. Perez-Bernal, R. Raabe, F. Rizzo, D. Santonocito, G. Scalia, O. Tengblad, D. Torresi, A.M. Vidal, D. Voulot, F. Wenander, M. Zadro, Phys. Rev. Lett 105 (2010) 022701.
[43] K.C.C. Pires, R. Lichtenthäler, A. Lépine-Szily, V. Guimarães, P.N. De Faria, A. Barioni, D.R. Mendes junior, V. Morcelle, R. Pampa condori, M.C. Morais, J.C. Zamora, E. Crema, A.M. Moro, M. Rodríguez-Gallardo, M. Assunçao, J.M.B. Shorto, S. Mukherjee, Phys. Rev. C 83 (2011) 064603.

[44] E. Benjamim, A. Lépine-Sziy, D.M. Junior, R. Richtenthäler, V. Guimarẽs, P. Gomes, L. Chamon, M. Hussein, A. Moro, A. Arazi, I. Padron, J. Alcântara Nuñes, M. Assunção, A. Barioni, O.C. Jr, R. Denke, P. de Faria, K. Pires, Phys. Lett. B 647 (2007) 30.
[45] V. Morcelle, K.C.C. Pires, M. Rodríguez-Gallardo, R. Lichtenthäler, A. Lépine-Szily, V. Guimarães, P.N. Faria, D.R. Mendes junior, A.M. Moro, L.R. Gasques, E. Leistenschneider, R. Pampa condori, V. Scarduelli, M.C. Morais, A. Barioni, I.C. Zamora, J.M.B. Shorto, Phys. Lett. B 732 (2014) 228.
[46] P.N. De Faria, R. Lichtenthäler, K.C.C. Pires, A.M. Moro, A. Lépine-Szily, V. Guimarães, D.R. Mendes, A. Arazi, M. Rodríguez-Gallardo, A. Barioni, V. Morcelle, M.C. Morais, O. Camargo, J. Alcantara Nuñez, M. Assunçao, Phys. Rev. C 81 (2010) 044605.
[47] L. Standyło, L. Acosta, C. Angulo, R. Berjillos, J.A. Duenas, M.S. Golovkov, N. Keeley, T. Keutgen, I. Martel, M. Mazzocco, F. Perez-Bernal, A.M. Sánchez-Benítez, C. Signorini, M. Romoli, K. Rusek, R. Wolski, Phys. Rev. C 87 (2013) 064603.
[48] O.R. Kakuee, J. Rahighi, A.M. Sanchez-Benitez, M.V. Andrés, S. Cherubini, T. Davinson, W. Galster, J. Gomez-Camacho, A.M. Laird, M. Lamehi-Rachti, I. Martel, A.C. Shotter, W.B. Smith, J. Vervier, P.J. Woods, Nucl. Phys. A 728 (2003) 339.
[49] A.M. Sánchez-Benítez, D. Escrig, M.A.G. Álvarez, M.V. Andrés, C. Angulo, M.J.G. Borge, J. Cabrera, S. Cherubini, P. Demarelt, J.M. Espino, P. Figuera, M. Freer, J.E. Garí a Ramos, J. Gómez-Camacho, M. Gulino, O.R. Kakuee, I. Martel, C. Metelco, A.M. Moro, F. Pŕez-Bernal, J. Rahigi, K. Rusek, D. Smirnov, O. Tengblad, P. van Duppen, V. Ziman, Nucl. Phys. A 803 (2008) 30.
[50] L. Acosta, A.M. Sánchez-Benítez, M.E. Gómez, I. Martel, F. Pérez-Bernal, F. Pizarro, J. Rodríguez-Quintero, K. Rusek, M.A.G. Alvarez, M.V. Andrés, J.M. Espino, J.P. Fernández-García, J. Gómez-Camacho, A.M. Moro, C. Angulo, J. Cabrera, E. Casarejos, P. Demaret, M.J.G. Borge, D. Escrig, O. Tengblad, S. Cherubini, P. Figuera, M. Gulino, M. Freer, C. Metelko, V. Ziman, R. Raabe, I. Mukha, D. Smirnov, O.R. Kakuee, J. Rahighi, Phys. Rev. C 84 (2011) 044604.
[51] A. Lemasson, A. Navin, N. Keeley, M. Rejmund, S. Bhattacharyya, A. Shrivastava, D. Bazin, D. Beaumel, Y. Blumenfeld, A. Chatterjee, D. Gupta, G. de France, B. Jacquot, M. Labiche, R. Lemmon, V. Nanal, J. Nyberg, R.G. Pillay, R. Raabe, K. Ramachandran, J.A. Scarpaci, C. Simenel, I. Stefan, C.N. Timis, Phys. Rev. C 82 (2010) 044617.
[52] A. Diaz-Torres, A.M. Moro, Phys. Lett. B 733 (2014) 89.
[53] N. Keeley, N. Alamanos, K.W. Kemper, K. Rusek, Phys. Rev. C 82 (2010) 034606.
[54] T. Druet, P. Descouvemont, Eur. Phys. J. A 48 (2012) 147.
[55] M.V. Andrés, J. Gómez-Camacho, M.A. Nagarajan, Nucl. Phys. A 579 (1994) 273; Nucl. Phys. A 583 (1994) 817.
[56] J. Lubian, T. Correa, E.F. Aguilera, L.F. Canto, A. Gomez-Camacho, E.M. Quiroz, P.R.S. Gomes, Phys. Rev. C 79 (2009) 064605.
[57] E.F. Aguilera, E. Martinez-Quiroz, D. Lizcano, A. Gómez-Camacho, J.J. Kolata, L.O. Lamm, V. Guimarães, R. Lichtenthäler, O. Camargo, F.D. Becchetti, H. Jiang, P.A. Deyoung, P.J. Mears, T.L. Belyaeva, Phys. Rev. C 79 (2009) 021601.
[58] J.P. Fernández-García, M.A.G. Alvarez, A.M. Moro, M. Rodríguez-Gallardo, Phys. Lett. B 693 (2008) 310.
[59] M. Cubero, J.P. Fernández-García, M. Rodríguez-Gallardo, L. Acosta, M. Alcorta, M.A.G. Alvarez, M.J.G. Borge, L. Buchmann, C.A. Diget, H.A. Falou, B.R. Fulton, H.O.U. Fynbo, D. Galaviz, J. Gómez-Camacho, R. Kanungo, J.A. Lay, M. Madurga, I. Martel, A.M. Moro, I. Mukha, T. Nilsson, A.M. Sánchez-Benítez, A. Shotter, O. Tengblad, P. Walden, Phys. Rev. Lett. 109 (2012) 262701.
[60] R.J. Woolliscroft, B.R. Fulton, R.L. Cowin, M. Dasgupta, D.J. Hinde, C.R. Morton, A.C. Berriman, Phys. Rev. C 69 (2004) 044612.
[61] N. Yu, H.Q. Zhang, H.M. Jia, S.T. Zhang, M. Ruan, F. Yang, Z.D. Wu, X.X. Xu, C.L. Bai, J. Phys. G: Nucl. Part. Phys. 37 (2010) 075108.
[62] V.V. Sargsyan, G.G. Adamian, N.V. Antonenko, P.R.S. Gomes, Phys. Rev. C 87 (2013) 044611.
[63] V.V. Sargsyan, G.G. Adamian, N.V. Antonenko, P.R.S. Gomes, Phys. Rev. C 88 (2013) 044606.
[64] V.V. Sargsyan, G.G. Adamian, N.V. Antonenko, P.R.S. Gomes, Eur. Phys. J. A 50 (2014) 184.
[65] V.V. Sargsyan, G.G. Adamian, N.V. Antonenko, A. Diaz-Torres, P.R.S. Gomes, H. Lenske, Phys. Rev. C 90 (2014) 064601.
[66] V.V. Sargsyan, G.G. Adamian, N.V. Antonenko, A. Diaz-Torres, P.R.S. Gomes, H. Lenske, Eur. Phys. J. A 50 (2014) 168.
[67] V.V. Sargsyan, G.G. Adamian, N.V. Antonenko, W. Sheid, H.Q. Zhang, Eur. Phys. J. A 50 (2014) 71.
[68] A.B. Balantekin, A.J. De weerd, S. Kuyucak, Phys. Rev. C 54 (1996) 1853.
[69] Y.W. Wu, Z.H. Liu, C.J. Lin, H.Q. Zhang, M. Ruan, F. Yang, Z.C. Li, M. Trotta, K. Hagino, Phys. Rev. C 68 (2003) 044605.
[70] C.J. Lin, H.Q. Zhang, F. Yang, M. Ruan, Z.H. Liu, Y.W. Wu, X.K. Wu, P. Zhou, C.L. Zhang, G.L. Zhang, G.P. An, H.M. Jia, X.X. Xu, Nucl. Phys. A 787 (2007) 281c.
[71] D. Torresi, A. Di pietro, E. Strano, M. Zadro, P. Figuera, M. Fisichella, M. Lattuada, C. Maiolino, A. Musumarra, M.G. Pellegriti, D. Santonocito, V. Scuderi, Eur. Phys. J. Conf. 17 (2011) 16018.
[72] A. Di Pietro, P. Figuera, E. Strano, M. Fisichella, O. Goryunov, M. Lattuada, C. Maiolino, C. Marchetta, M. Milin, A. Musumarra, V. Ostashko, M.G. Pellegriti, V. Privitera, G. Randisi, L. Romano, D. Santonocito, V. Scuderi, D. Torresi, M. Zadro, Phys. Rev. C 87 (2013) 064614.
[73] P.R.S. Gomes, I. Padrón, M.D. Rodríguez, G.V. Martí, R.M. Anjos, J. Lubian, R.L. Neto, E. Crema, N. Added, L.C. Chamon, J.O.F. Niello, O.A. Capurro, A.J. Pacheco, J.E. Testoni, A. Arazi, M. Ramírez, M.S. Hussein, Phys. Lett. B 601 (2004) 20.
[74] P.R.S. Gomes, M.D. Rodríguez, G.V. Martí, I. Padron, L.C. Chamon, J.O. Fernández Niello, O.A. Capurro, A.J. Pacheco, J.E. Testoni, A. Arazi, M. Ramírez, R.M. Anjos, J. Lubian, R. Veiga, R. Liguori Neto, E. Crema, N. Added, C. Tenreiro, M.S. Hussein, Phys. Rev. C 71 (2005) 034608.
[75] P.R.S. Gomes, J. Lubian, L.F. Canto, Phys. Rev. C 79 (2009) 027606.
[76] A. Pakou, V. Soukeras, O. Sgouros, K. Zerva, Eur. Phys. J. A 50 (2014) 65.
[77] V.V. Sargsyan, G.G. Adamian, N.V. Antonenko, W. Sheid, H.Q. Zhang, Eur. Phys. J. A 50 (2014) 71.
[78] A. Diaz-Torres, G.G. Adamian, V.V. Sargsyan, N.V. Antonenko, Phys. Lett. B 739 (2014) 348.
[79] K. Hagino, N. Rowley, Phys. Rev. C 69 (2004) 054610.
[80] N. Rowley, N. Grar, M. Trotta, Phys. Rev. C 76 (2007) 044612.
[81] A.B. Balantekin, S.E. Koonin, J.W. Negele, Phys. Rev. C 28 (1983) 1565.
[82] N. Rowley, G.R. Satchler, P.H. Stelson, Phys. Lett. B 254 (1991) 25.
[83] A.B. Balantekin, N. Takigawa, Rev. Mod. Phys. 70 (1998) 77.
[84] H. Timmers, J.R. Leigh, M. Dasgupta, D.J. Hinde, R.C. Lemmon, J.C. Mein, C.R. Morton, J.O. Newton, N. Rowley, Nucl. Phys. A 584 (1995) 190.
[85] V.I. Zagrebaev, Phys. Rev. C 78 (2008) 047602.
[86] J. Lubian, T. Correa, P.R.S. Gomes, L.F. Canto, Phys. Rev. C 78 (2008) 064615.
[87] N. Keeley, Phys. Rev. C 80 (2009) 064614.
[88] C. Signorini, Z.H. Liu, Z.C. Li, K.E.G. Löbner, L. Müller, M. Ruan, K. Rudolph, F. Soramel, C. Zotti, A. Anddrighetto, L. Stroe, A. Vitturi, H.Q. Zhang, Euro. Phys. J. A 5 (1999) 7.
[89] K. Zerva, N. Patronis, A. Pakou, N. Alamanos, X. Aslanoglou, D. Filipescu, T. Glodariu, M. Kokkoris, M. La Commara, A. Lagoyannis, M. Mazzocco, N.G. Nicolis, D. Pierroutsakou, M. Romoli, K. Rusek, Phys. Rev. C 80 (2009) 017601.
[90] K. Zerva, A. Pakou, K. Rusek, N. Patronis, N. Alamanos, X. Aslanoglou, D. Filipescu, T. Glodariu, N. Keeley, M. Kokkoris, M. La Commara, A. Lagoyannis, M. Mazzocco, N.G. Nicolis, D. Pierroutsakou, M. Romoli, Phys. Rev. C 82 (2010) 044607.
[91] K. Zerva, A. Pakou, N. Patronis, P. Figuera, A. Musumarra, A. Di pietro, M. Fisichella, M. Lattuada, T. Lonnroth, M. Milin, V. Ostashko, M.G. Pellegriti, V. Scuderi, D. Stanko, E. Strano, D. Torresi, Eur. Phys. J. A 48 (2012) 102.
[92] M.M. Shaikh, S. Roy, S. Rajbanshi, M.K. Pradhan, A. Mukherjee, P. Basu, S. Pal, V. Nanal, R.G. Pillay, A. Shrivastava, Phys. Rev. C 91 (2015) 034615.
[93] M. Zadro, P. Figuera, A. Di pietro, M. Fisichella, M. Lattuada, T. Lönnroth, M. Milin, V. Ostashko, M.G. Pellegriti, V. Scuderi, D. Stanko, E. Strano, D. Torresi, Phys. Rev. C 87 (2013) 054606.
[94] D.R. Otomar, J. Lubian, P.R.S. Gomes, D.S. Monteiro, O.A. Capurro, A. Arazi, J.O. Fernández niello, J.M. Figueira, G.V. Martí, M.D. Heimann, A.E. Negri, A.J. Pacheco, V. Guimarães, L.C. Chamon, Phys. Rev. C 80 (2009) 034614.
[95] D.S. Monteiro, O.A. Capurro, A. Arazi, J.O. Fernández niello, J.M. Figueira, G.V. Martí, D.M.n. Heimann, A.E. Negri, A.J. Pacheco, V. Guimarães, D.R. Otomar, J. Lubian, P.R.S. Gomes, Phys. Rev. C 79 (2009) 014601.
[96] C.S. Palshetkar, S. Thakur, V. Nanal, A. Shrivastava, N. Dokania, V. Singh, V.V. Parkar, P.C. Rout, R. Palit, R.G. Pillay, S. Bhattacharyya, A. Chatterjee, S. Santra, K. Ramachandran, N.L. Singh, Phys. Rev. C 89 (2014) 024607.

[97] D. Patel, S. Mukherjee, B.K. Nayak, S.V. Suryanarayana, D.C. Biswas, E.T. Mirgule, Y.K. Gupta, L.S. Danu, B.V. John, A. Saxena, Phys. Rev. C 89 (2014) 064614.
[98] S. Mukherjee, B.K. Nayak, D.S. Monteiro, J. Lubian, P.R.S. Gomes, S. Appannababu, R.K. Choudhury, Phys. Rev. C 80 (2009) 014607.
[99] H.M. Jia, C.J. Lin, H.Q. Zhang, Z.H. Liu, N. Yu, F. Yang, F. Jia, X.X. Xu, Z.D. Wu, S.T. Zhang, C.L. Bai, Phys. Rev. C 82 (2010) 027602.
[100] A. Diaz-Torres, J. Phys. G: Nucl. Part. Phys. 37 (2010) 075109.
[101] P.K. Rath, S. Santra, N.L. Singh, R. Tripathi, V.V. Parkar, B.K. Nayak, K. Mahata, R. Palit, S. Kumar, S. Mukherjee, S. Appannababu, R.K. Choudhury, Phys. Rev. C 79 (2009) 051601(R).
[102] J.M. Figueira, J.O. Fernández Niello, D. Abriola, A. Arazi, O.A. Capurro, E. de Barbará, G.V. Martí, D.M. Heimann, A.E. Negri, A.J. Pacheco, I. Padrón, P.R.S. Gomes, J. Lubian, T. Correa, B. Paes, Phys. Rev. C 75 (2007) 017602.
[103] A. Pakou, N. Alamanos, G. Doukelis, A. Gillibert, G. Kalyva, M. Kokkoris, S. Kossionides, A. Lagoyannis, A. Musumarra, N. Patronis, C. Papachristodoulou, G. Perdikakis, D. Pierroutsakou, E.C. Pollacco, K. Rusek, Phys. Rev. C 69 (2004) 054602.
[104] M. Biswas, S. Roy, M. Sinha, M.K. Pradhan, A. Mukherjee, P. Basu, H. Majumdar, K. Ramachandran, A. Shrivastava, Nucl. Phys. A 802 (2008) 67.
[105] F.A. Souza, L.A.S. Leal, N. Carlin, M.G. Munhoz, R. Liguori Neto, M.M. de Moura, A.A.P. Suaide, E.M. Szanto, A. Szanto de Toledo, J. Takahashi, Phys. Rev. C 75 (2007) 044601.
[106] M. Zadro, P. Figuera, A.D. Pietro, F. Amorini, M. Fisichella, O. Goryunov, M. Lattuada, C. Maiolino, A. Musumarra, V. Ostashko, M. Papa, M.G. Pellegriti, F. Rizzo, D. Santonocito, V. Scuderi, D. Torresi, Phys. Rev. C 80 (2009) 064610.
[107] L. Fimiani, J.M. Figueira, G.V. Martí, E. J testoni, A.J. Pacheco, W.H.Z. Cárdenas, A. Arazi, O.A. Capurro, M.A. Cardona, P. Carnelli, E. de Barbará, D. Hojman, D. Martinez Heimann, A.E. Negri, Phys. Rev. C 86 (2012) 044607.
[108] H. Kumawat, V. Jha, B.J. Roy, V.V. Parkar, S. Santra, V. Kumar, D. Dutta, P. Shukla, L.M. Pant, A.K. Mohanty, R.K. Choudhury, S. Kailas, Phys. Rev. C 78 (2008) 044617.
[109] N.N. Deshmukh, S. Mukherjee, D. Patel, N.L. Singh, P.K. Rath, B.K. Nayak, D.C. Biswas, S. Santra, E.T. Mirgule, L.S. Danu, Y.K. Gupta, A. Saxena, R.K. Choudhury, R. Kumar, J. Lubian, C.C. Lopes, E.N. Cardozo, P.R.S. Gomes, Phys. Rev. C 83 (2011) 024607.
[110] A.M.M. Maciel, P.R.S. Gomes, J. Lubian, R.M. Anjos, R. Cabezas, G.M. Santos, C. Muri, S.B. Moraes, R.L. Neto, N. Added, N.C. Filho, C. Tenreiro, Phys. Rev. C 59 (1999) 2103.
[111] P.R.S. Gomes, I. Padrón, J.O. Fernández Niello, G.V. Martí, M.D. Rodríguez, O.A. Capurro, A.J. Pacheco, J.E. Testoni, A. Arazi, J. Lubian, R.M. Anjos, L.C. Chamon, E. Crema, M.S. Hussein, J. Phys. G 31 (2005) S1669.
[112] J.M. Figueira, J.O. Fernández Niello, A. Arazi, O.A. Capurro, P. Carnelli, L. Fimiani, G.V. Martí, D.M. Heimann, A.E. Negri, A.J. Pacheco, J. Lubian, D.S. Monteiro, P.R.S. Gomes, Phys. Rev. C 81 (2010) 024613.
[113] N. Keeley, S.J. Bennet, M.N. Clarke, B.R. Fulton, G. Tungate, P.V. Drumm, M.A. Nagarajan, J.L. Lilley, Nucl. Phys. A 571 (1994) 326.
[114] S. Santra, S. Kailas, K. Ramachandran, V.V. Parkar, V. Jha, B.J. Roy, P. Shukla, Phys. Rev. C 83 (2011) 034616.
[115] S. Dubey, S. Mukherjee, D.C. Biswas, B.K. Nayak, D. Patel, G.K. Prajapati, Y.K. Gupta, B.N. Joshi, L.S. Danu, S. Mukhopadhyay, B.V. John, V.V. Desai, S.V. Suryanarayana, R.P. Vind, N.N. Deshmukh, S. Appnnababu, P.M. Prajapati, Phys. Rev. C 89 (2014) 014610.
[116] J.M. Figueira, D. Abriola, J.O. Fernández Niello, A. Arazi, O.A. Capurro, E. de Barbará, G.V. Martí, D. Martínez heimann, A.J. Pacheco, J.E. Testoni, I. Padrón, P.R.S. Gomes, J. Lubian, Phys. Rev. C 73 (2006) 054603.
[117] N.N. Deshmukh, S. Mukherjee, B.K. Nayak, D.C. Biswas, S. Santra, E.T. Mirgule, S. Appannababu, D. Patel, A. Saxena, R.K. Choudhury, J. Lubian, P.R.S. Gomes, Eur. Phys. J. A 47 (2011) 118.
[118] J. Lubian, I. Padron, P.R.S. Gomes, A.M.M. Maciel, R.M. Anjos, S.B. Moraes, J.J.S. Alves, C. Muri, R. Liguori Neto, N. Added, Phys. Rev. C 64 (2001) 027601.
[119] L. Yang, C.J. Lin, H.M. Jia, F. Yang, Z.D. Wu, X.X. Xu, H.Q. Zhang, Z.H. Liu, P.F. Bao, L.J. Sun, N.R. Ma, Phys. Rev. C 89 (2014) 044615.
[120] P.R.S. Gomes, J. Lubian, B. Paes, V.N. Garcia, D.S. Monteiro, I. Padrón, J.M. Figueira, A. Arazi, O.A. Capurro, L. Fimiani, A.E. Negri, G.V. Martí, J. Fernández Niello, A. Gómez-Camacho, L.F. Canto, Nucl. Phys. A 828 (2009) 233.
[121] R.A.N. Oliveira, N. Carlin, R. Liguori Neto, M.M. de Moura, M.G. Munhoz, M.G. Del Santo, F.A. Souza, E.M. Szanto, A. Szanto de Toledo, A.A.P. Suaide, Nucl. Phys. A 856 (2011) 46.
[122] C. Signorini, A. Andrighetto, M. Ruan, J.Y. Guo, L. Stroe, F. Soramel, K.E.G. Löbner, L. Müller, D. Pierroutsakou, M. Romoli, K. Rudolph, I.J. Thompson, M. Trotta, A. Vitturi, R. Gernhäuser, A. Kastenmüller, Phys. Rev. C 61 (2000) 061603R.
[123] P.R.S. Gomes, R.M. Anjos, C. Muri, J. Lubian, I. Padrón, L.C. Chamon, R. Liguori neto, N. Added, J.O. Fernández niello, G.V. Marti, O.A. Capurro, A.J. Pacheco, J.E. Testoni, D. Abriola, Phys. Rev. C 70 (2004) 054605.
[124] C.S. Palshetkar, S. Santra, A. Shrivastava, A. Chatterjee, S.K. Pandit, K. Ramachandran, V.V. Parkar, V. Nanal, V. Jha, B.J. Roy, S. Kalias, Phys. Rev. C 89 (2014) 064610.
[125] L.C. Chamon, D. Pereira, M.S. Hussein, M.A. Candido ribeiro, D. Galetti, Phys. Rev. Lett. 79 (1997) 5218.
[126] L.C. Chamon, B.V. Carlson, L.R. Gasques, D. Pereira, C. de Conti, M.A.G. Alvarez, M.S. Hussein, M.A. Cândido Ribeiro, E.S. Rossi Jr, C.P. Silva, Phys. Rev. C 66 (2002) 014610.
[127] A.R. Garcia, J. Lubian, I. Padron, P.R.S. Gomes, T. Lacerda, V.N. Garcia, A. Gómez Camacho, E.F. Aguilera, Phys. Rev. C 76 (2007) 067603.
[128] Y. Kucuk, Nucl. Phys. A 927 (2014) 195.
[129] E.F. Aguilera, J.J. Kolata, F.D. Becchetti, P.A. de Young, J.D. Hinnefeld, A. Horvath, L.O. Lamm, H.Y. Lee, D. Lizcano, E. Martinez-Quiroz, P. Mohr, T.W. O'Donnell, D.A. Roberts, G. Rogachev, Phys. Rev. C 63 (2001) 061603(R).
[130] A. Gómez camacho, E.F. Aguilera, E. Martínez-Quiroz, P.R.S. Gomes, J. Lubian, L.F. Canto, Nucl. Phys. A 833 (2010) 156.
[131] A. Gómez camacho, E.F. Aguilera, P.R.S. Gomes, J. Lubian, Phys. Rev. C 84 (2011) 034615.
[132] A. Gomez camacho, E.F. Aguilera, J. Lubian, P.R.S. Gomes, J. Phys. G: Nucl. Part. Phys. 40 (2013) 035103.
[133] A. Gómez camacho, P.R.S. Gomes, J. Lubian, Phys. Rev. C 82 (2010) 067601.
[134] A. Gómez camacho, P.R.S. Gomes, J. Lubian, I. Padrón, Phys. Rev. C 77 (2008) 054606.
[135] A. Gómez camacho, P.R.S. Gomes, J. Lubian, E.F. Aguilera, I. Padrón, Phys. Rev. C 76 (2007) 044609.
[136] A. Gómez camacho, P.R.S. Gomes, J. Lubian, L.F. Canto, Phys. Rev. C 82 (2010) 014616.
[137] A. Gómez camacho, E.F. Aguilera, Phys. Rev. C 90 (2014) 064607.
[138] A. Gómez camacho, N. Yu, H.Q. Zhang, P.R.S. Gomes, H.M. Jia, J. Lubian, C.J. Lin, Phys. Rev. C 91 (2015) 044610.
[139] W.Y. So, T. Udagawa, K.S. Kim, S.W. Hong, B.T. Kim, Phys. Rev. C 81 (2010) 047604.
[140] W.Y. So, T. Udagawa, K.S. Kim, S.W. Hong, B.T. Kim, Phys. Rev. C 75 (2007) 024610.
[141] W.Y. So, T. Udagawa, K.S. Kim, S.W. Hong, B.T. Kim, Phys. Rev. C 76 (2007) 024613.
[142] B.T. Kim, W.Y. So, S.W. Hong, T. Udagawa, Phys. Rev. C 65 (2002) 044616.
[143] W.Y. So, S.W. Hong, B.T. Kim, T. Udagawa, Phys. Rev. C 69 (2004) 064606.
[144] W.Y. So, S.W. Hong, B.T. Kim, T. Udagawa, Phys. Rev. C 72 (2005) 064602.
[145] W.Y. So, K.S. Kim, Mod. Phys. Lett. A 26 (2011) 325.
[146] J.J. Kolata, V. Guimarães, D. Peterson, P. Santi, R. White-Stevens, P.A. De young, G.F. Peaslee, B. Hughey, B. Atalla, M. Kern, P.L. Jolivette, J.A. Zimmerman, M.Y. Lee, F.D. Becchetti, E.F. Aguilera, E. Martinez-Quiroz, J.D. Hinnefeld, Phys. Rev. Lett. 81 (1998) 4580.
[147] J.J. Kolata, V. Guimarães, D. Peterson, P. Santi, R. White-Stevens, J. von Schwarzenberg, J.D. Hinnefeld, E.F. Aguilera, E. Martinez-Quiroz, D.A. Roberts, F.D. Becchetti, M.Y. Lee, R.A. Kryger, Phys. Rev. C 57 (1998) R6.
[148] E.F. Aguilera, J.J. Kolata, F.M. Nunes, F.D. Becchetti, P.A. De young, M. Goupell, V. Guimarães, B. Hughey, M.Y. Lee, D. Lizcano, E. Martinez-Quiroz, A. Nowlin, T.W. O'donnell, G.F. Peaslee, D. Peterson, P. Santi, R. White-Stevens, Phys. Rev. Lett. 84 (2000) 5058.
[149] A. Lemasson, A. Shrivastava, A. Navin, M. Rejmund, N. Keeley, V. Zelevinsky, S. Bhattacharyya, A. Chatterjee, G. De france, B. Jacquot, V. Nanal, R.G. Pillay, R. Raabe, C. Schmitt, Phys. Rev. Lett. 103 (2009) 232701.
[150] K.C.C. Pires, R. Lichtenthäler, A. Lépine-Szily, V. Morcelle, Phys. Rev. C 90 (2014) 027605.

[151] A. Pakou, K. Rusek, N. Alamanos, X. Aslanoglou, M. Kokkoris, A. Lagoyannis, T.J. Mertzimekis, A. Musumarra, N.G. Nicolis, D. Pierroutsakou, D. Roubos, Eur. Phys. J. A 39 (2009) 187.
[152] A. Pakou, K. Rusek, N. Alamanos, X. Aslanoglou, S. Harissopulos, M. Kokkoris, A. Lagoyannis, T.J. Mertzimekis, A. Musumarra, N.G. Nicolis, C. Papachristodoulou, D. Pierroutsakou, D. Roubos, Phys. Rev. C 76 (2007) 054601.
[153] V.V. Parkar, K. Mahata, S. Santra, S. Kailas, A. Shrivastava, K. Ramachandran, A. Chatterjee, V. Jha, P. Singh, Nucl. Phys. A 792 (2007) 187.
[154] S. Santra, S. Kailas, V.V. Parkar, K. Ramachandran, V. Jha, A. Chatterjee, P.K. Rath, A. Parihari, Phys. Rev. C 85 (2012) 014612.
[155] P.N. De faria, R. Lichtenthäler, K.C.C. Pires, A.M. Moro, A. Lépine-Szily, V. Guimarães, D.R. Mendes, A. Arazi, A. Barioni, V. Morcelle, M.C. Morais, Phys. Rev. C 82 (2010) 034602.
[156] H. Kumawat, V. Jha, V.V. Parkar, B.J. Roy, S. Santra, V. Kumar, D. Dutta, P. Shukla, L.M. Pant, A.K. Mohanty, R.K. Choudhury, S. Kailas, Phys. Rev. C 81 (2010) 054601.
[157] A. Navin, V. Tripathi, Y. Blumenfeld, V. Nanal, C. Simenel, J.M. Casandjian, G. De france, R. Raabe, D. Bazin, A. Chatterjee, M. Dasgupta, S. Kailas, R.C. Lemmon, K. Mahata, R.G. Pillay, E.C. Pollacco, K. Ramachandran, M. Rejmund, A. Shrivastava, J.L. Sida, E. Tryggestad, Phys. Rev. C 70 (2004) 044601.
[158] P.R.S. Gomes, J. Lubian, I. Padrón, R.M. Anjos, Phys. Rev. C 71 (2005) 017601.
[159] J.M.B. Shorto, P.R.S. Gomes, J. Lubian, L.F. Canto, S. Mukherjee, L.C. Chamon, Phys. Letters B 678 (2009) 77.
[160] L.F. Canto, P.R.S. Gomes, J. Lubian, L.C. Chamon, E. Crema, J. Phys. G: Nucl. Part. Phys. 36 (2009) 015109.
[161] L.F. Canto, P.R.S. Gomes, J. Lubian, L.C. Chamon, E. Crema, Nucl. Phys. A 821 (2009) 51.
[162] J.J. Kolata, E.F. Aguilera, Phys. Rev. C 79 (2009) 027603.
[163] A. Barioni, V. Guimarães, A. Lépine-Szily, R. Lichtenthäler, D.R. Mendes, E. Crema, K.C.C. Pires, M.C. Morais, V. Morcelle, P.N. De faria, R.P. Condori, A.M. Moro, D.S. Monteiro, J.M.B. Shorto, J. Lubian, M. Assunçao, Phys. Rev. C 80 (2009) 034617.
[164] E.F. Aguilera, E. Martinez-Quiroz, D. Lizcano, A. Gómez-Camacho, J.J. Kolata, L.O. Lamm, V. Guimarães, R. Lichtenthäler, O. Camargo, F.D. Becchetti, H. Jiang, P.A. De Young, P.J. Mears, T.L. Belyaeva, Phys. Rev. C 79 (2009) 021601.
[165] C. Signorini, D. Pierroutsakou, B. Martin, M. Mazzocco, T. Glodariu, R. Bonetti, A. Guglielmetti, M. La Commara, M. Romoli, M. Sandoli, E. Vardaci, H. Esbensen, F. Farinon, P. Molini, C. Parascandolo, F. Soramel, S. Sidortchuk, L. Stroe, Eur. Phys. J. A 44 (2010) 63.
[166] E.F. Aguilera, I. Martel, A.M. Sánchez-Benítez, L. Acosta, Phys. Rev. C 83 (2011) 021601.
[167] M. Mazzocco, C. Signorini, D. Pierroutsakou, T. Glodariu, A. Boiano, C. Boiano, F. Farinon, P. Figuera, D. Filipescu, L. Fortunato, A. Guglielmetti, G. Inglima, M. La commara, M. Lattuada, P. Lotti, C. Mazzocchi, P. Molini, A. Musumarra, A. Pakou, C. Parascandolo, N. Patronis, M. Romoli, M. Sandoli, V. Scuderi, F. Soramel, L. Stroe, D. Torresi, E. Vardaci, A. Vitturi, Phys. Rev. C 82 (2010) 054604.
[168] J.C. Zamora, V. Guimarães, A. Barioni, A. Lépine-Szily, R. Lichtenthäler, P.N. De faria, D.R. Mendes, L.R. Gasques, J.M.B. Shorto, V. Scarduelli, K.C.C. Pires, V. Morcelle, E. Leistenschneider, R.P. Condori, V.A. Zagatto, M.C. Morais, E. Crema, Phys. Rev. C 84 (2011) 034611.
[169] J. Lei, J.S. Wang, S. Mukherjee, Q. Wang, R. Wada, Phys. Rev. C 86 (2012) 057603.
[170] X.P. Yang, G.L. Zhang, H.Q. Zhang, Phys. Rev. C 87 (2013) 014603.
[171] A. Pakou, D. Pierroutsakou, M. Mazzocco, L. Acosta, X. Aslanoglou, A. Boiano, C. Boiano, D. Carbone, M. Cavallaro, J. Grebosz, N. Keeley, M. La commara, C. Manea, G. Marquinez-Duran, I. Martel, C. Parascandolo, K. Rusek, A.M. Sánchez-Benítez, O. Sgouros, C. Signorini, F. Soramel, V. Soukeras, E. Stiliaris, E. Strano, D. Torresiv, A. Trzcinska, Y.X. Watanabe, H. Yamaguchi, Eur. Phys. J. A 51 (2015) 55.
[172] S. Mukherjee, N.N. Deshmukh, V. Guimarães, J. Lubian, P.R.S. Gomes, A. Barioni, S. Appannababu, C.C. Lopes, E.N. Cardozo, K.C.C. Pires, R. Lichtenthäler, A. Lépine-Szily, D.S. Monteiro, J.M.B. Shorto, P.N. De faria, E. Crema, V. Morcelle, M.C. Morais, R. Pampa condori, Eur. Phys. J. A 45 (2010) 23.
[173] V. Morcelle, R. Lichtenthäler, R. Linares, M.C. Morais, V. Guimarães, A. Lépine-Szily, P.R.S. Gomes, J. Lubian, D.R. Mendes junior, P.N. De faria, A. Barioni, L.R. Gasques, J.M.B. Shorto, K.C.C. Pires, J.C. Zamora, R.P. Condori, V. Scarduelli, J.J. Kolata, H. Amro, F.D. Becchetti, H. Jiang, E.F. Aguilera, D. Lizcano, E. Martinez-Quiroz, H. Garcia, Phys. Rev. C 89 (2014) 044611.
[174] C.Y. Wong, Phys. Rev. Lett. 31 (1973) 766.
[175] L.F. Canto, D.R. Mendes Junior, P.R.S. Gomes, J. Lubian, Phys. Rev. C 92 (2015) 014626.
[176] R. Serber, Phys. Rev. 72 (1947) 1114.
[177] M.S. Hussein, K.W. Mcvoy, Nucl. Phys. A 445 (1985) 124.
[178] G. Baur, C.A. Bertulani, Phys. Lett. B 74 (1986) 26.
[179] A. Winther, K. Alder, Nucl. Phys. A 319 (1979) 518.
[180] M. Dasgupta, D.J. Hinde, K. Hagino, S.B. Moraes, P.R.S. Gomes, R.M. Anjos, R.D. Butt, A.C. Berriman, N. Carlin, C.R. Morton, J.O. Newton, A. Szanto de Toledo, Phys. Rev. C 66 (2002) 041602(R).
[181] K. Hagino, M. Dasgupta, D.J. Hinde, Nucl. Phys. A 738 (2004) 475.
[182] A. Diaz-Torres, D.J. Hinde, J.A. Tostevin, M. Dasgupta, L.R. Gasques, Phys. Rev. Lett. 98 (2007) 152701.
[183] A. Diaz-Torres, Comput. Phys. Comm. 182 (2011) 1100.
[184] H.D. Marta, L.F. Canto, R. Donangelo, Phys. Rev. C 89 (2014) 034625.
[185] H.D. Marta, L.F. Canto, R. Donangelo, P. Lotti, Phys. Rev. C 66 (2002) 024605.
[186] H.D. Marta, L.F. Canto, R. Donangelo, Phys. Rev. C 78 (2008) 034612.
[187] J.J. Kolata, V. Guimarães, D. Peterson, P. Santi, R.H. White-Stevens, S.M. Vincent, F.D. Becchetti, M.Y. Lee, T.W. O'Donnell, D.A. Roberts, J.A. Zimmerman, Phys. Rev. C 63 (2001) 024616.
[188] M.S. Hussein, P.R.S. Gomes, J. Lubian, D.R. Otomar, L.F. Canto, Phys. Rev. C 88 (2013) 047601.
[189] D.R. Otomar, P.R.S. Gomes, J. Lubian, L.F. Canto, M.S. Hussein, Phys. Rev. C 87 (2013) 014615.
[190] Y. Kucuk, A.M. Moro, Phys. Rev. C 86 (2012) 034601.
[191] E. Cravo, R. Crespo, A.M. Moro, A. Deltuva, Phys. Rev. C 81 (2010) 031601(R).
[192] A. Deltuva, A.M. Moro, E. Cravo, F.M. Nunes, A.C. Fonseca, Phys. Rev. C 76 (2007) 064602.
[193] B. Mukeru, M.L. Lekala, A.S. Denikin, Nucl. Phys. A 935 (2015) 18.
[194] B. Mukeru, M.L. Lekala, A.S. Denikin, J. Phys. G: Nucl. Part. Phys. 42 (2015) 015109.
[195] A.J. Baltz, S.K. Kauffmann, N.K. Glendenning, K. Pruess, Phys. Rev. Lett 40 (1978) 20.
[196] L.F. Canto, R. Donangelo, M.S. Hussein, Nucl. Phys. A 529 (1991) 243.
[197] L.F. Canto, R. Donangelo, M.S. Hussein, M. Pato, Nucl. Phys. A 542 (1992) 131.
[198] M.V. Andrés, J. Gómez-Camacho, M.A. Nagarajan, Nucl. Phys. A 724 (2003) 113.
[199] L.F. Canto, R. Donangelo, M.S. Hussein, P. Lotti, Nucl. Phys. A 589 (1995) 117.
[200] M.S. Hussein, M.P. Pato, L.F. Canto, R. Donangelo, Phys. Rev. C 47 (1993) 2398.
[201] M.V. Andrés, J. Gomez-Camacho, M.A. Nagarajan, Nucl. Phys. A 583 (1995) C817.
[202] R.S. Mackintosh, N. Keeley, Phys. Rev. C 70 (2004) 024604.
[203] N. Keeley, K.W. Kemper, K. Rusek, Phys. Rev. C 65 (2001) 014601.
[204] N. Keeley, K.W. Kemper, K. Rusek, Phys. Rev. C 88 (2013) 017602.
[205] M.A. Franey, P.J. Ellis, Phys. Rev. C 23 (1981) 787.
[206] V.V. Parkar, V. Jha, S.K. Pandit, S. Santra, S. Kailas, Phys. Rev. C 87 (2013) 034602.
[207] N. Keeley, N. Alamanos, K. Rusek, K.W. Kemper, Phys. Rev. C 71 (2005) 014611.
[208] V.N. Garcia, J. Lubian, P.R.S. Gomes, A. Gomez-Camacho, L.F. Canto, Phys. Rev. C 80 (2009) 037602.
[209] P.R.S. Gomes, D.R. Otomar, T. Correa, L.F. Canto, J. Lubian, R. Linares, D.H. Luong, M. Dasgupta, D.J. Hinde, M.S. Hussein, J. Phys. G: Nucl. Part. Phys. 39 (2012) 115103.
[210] W.Y. So, K.S. Kim, K.S. Choi, M.-K. Cheoun, Phys. Rev. C 90 (2014) 054615.
[211] D.R. Otomar, J. Lubian, P.R.S. Gomes, T. Correa, J. Phys. G: Nucl. Part. Phys. 40 (2013) 125105.

[212] R. Rafiei, R. Du Rietz, D.H. Luong, D.J. Hinde, M. Dasgupta, M. Evers, A. Diaz-Torres, Phys. Rev. C 81 (2010) 024601.
[213] D.H. Luong, M. Dasgupta, D.J. Hinde, R. Du rietz, R. Rafieri, C.J. Lin, M. Evers, A. Diaz-Torres, Phys. Lett. B 695 (2011) 105.
[214] D.H. Luong, M. Dasgupta, D.J. Hinde, R. Du rietz, R. Rafiei, C.J. Lin, M. Evers, A. Diaz-Torres, Phys. Rev. C 88 (2013) 034609.
[215] D.J. Hinde, M. Dasgupta, B.R. Fulton, C.R. Morton, R.J. Wooliscroft, A.C. Berriman, K. Hagino, Phys. Rev. Lett. 89 (2002) 272701.
[216] A. Shrivastava, A. Navin, N. Keeley, K. Mahata, K. Ramachandran, V. Nanal, V.V. Parkar, A. Chatterjee, S. Kailas, Phys. Lett. B 633 (2006) 463.
[217] S. Santra, V.V. Parkar, K. Ramachandran, U.K. Pal, A. Shrivastava, B.J. Roy, B.K. Nayak, A. Chatterjee, R.K. Choudhury, S. Kailas, Phys. Lett. B 677 (2009) 139.
[218] F.A. Souza, N. Carlin, C. Beck, N. Keeley, A. Diaz-Torres, R. Liguori neto, C. Siqueira-Mello, M.M. de Moura, M.G. Munhoz, R.A.N. Oliveira, M.G. Del Santo, A.A.P. Suaide, E.M. Szanto, A. Szanto de Toledo, Eur. Phys. J. A 44 (2010) 181.
[219] O.A. Capurro, A.J. Pacheco, A. Arazi, J.M. Figueira, D. Martinez heimann, A.E. Negri, Nucl. Phys. A 849 (2011) 1.
[220] D. Martinez heimann, A.J. Pacheco, O.A. Capurro, A. Arazi, C. Balpardo, M.A. Cardona, P.F.F. Carnelli, E. De barbará, J.O. Fernández Niello, J.M. Figueira, D. Hojman, G.V. Martí, E.A. Negri, D. Rodrígues, Phys. Rev. C 89 (2014) 014615.
[221] D. Martinez heimann, A.J. Pacheco, O.A. Capurro, Nucl. Instrum. Methods Phys. Res. A 622 (2010) 642.
[222] D. Martinez heimann, A.J. Pacheco, O.A. Capurro, Nucl. Instrum. Methods Phys. Res. A 694 (2012) 313.
[223] A. Gómez camacho, A. Diaz-Torres, P.R.S. Gomes, J. Lubian, Phys. Rev. C 91 (2015) 014607.
[224] A. Shrivastava, A. Navin, A. Diaz-Torres, V. Nanal, K. Ramachandran, M. Rejmund, S. Bhattacharyya, A. Chatterjee, S. Kailas, A. Lemasson, R. Palit, V.V. Parkar, R.G. Pillay, P.C. Rout, Y. Sawant, Phys. Lett. B 718 (2013) 931.
[225] O.A. Capurro, A.J. Pacheco, A. Arazi, J.M. Figueira, D. Martinez heimann, A.E. Negri, Nucl. Phys. A 849 (2011) 1.
[226] A. Pakou, N. Alamanos, A. Gillibert, M. Kokkoris, S. Kossionides, A. Lagoyannis, N.G. Nicolis, C. Papachristodoulou, D. Patiris, D. Pierroutsakou, E.C. Pollacco, K. Rusek, Phys. Rev. Lett. 90 (2003) 202701.
[227] F.A. Souza, C. Beck, N. Carlin, N. Keeley, R. Liguori Neto, M.M. de Moura, M.G. Munhoz, M.G. del Santo, A.A.P. Suaide, E.M.A. Szanto, A. Szanto de Toledo, Nucl. Phys. A 821 (2009) 36.
[228] C. Signorini, M. Mazzocco, G.F. Prete, F. Soramel, L. Stroe, A. Andrigheto, I.J. Thompson, A. Vitturi, A. Brondi, M. Cinausero, D. Fabris, E. Fioretto, N. Gelli, J.Y. Guo, G. La rana, Z.H. Liu, F. Lucarelli, R. Moro, G. Nebbia, M. Trotta, E. Vardaci, G. Viesti, Euro. Phys. J. A10 (2001) 249.
[229] K.O. Pfeiffer, E. Speth, K. Bethege, Nucl. Phys. A 206 (1973) 545.
[230] A. Pakou, N.G. Nicolis, K. Rusek, N. Alamanos, G. Doukelis, A. Gillibert, G. Kalyva, M. Kokkoris, A. Lagoyannis, A. Musumarra, C. Papachristodoulou, G. Perdikakis, D. Pierroutsakou, E.C. Pollacco, A. Spyrou, C. Zarkadas, Phys. Rev. C 71 (2005) 064602.
[231] V. Tripathi, A. Navin, V. Nanal, R.G. Pillay, K. Mahata, K. Ramachandran, A. Shrivastava, A. Chatterjee, S. Kailas, Phys. Rev. C 72 (2005) 017601.
[232] L. Acosta, A.M. Sánchez-Benítez, M.E. Gómez, I. Martel, F. Pérez-Bernal, F. Pizarro, J. Rodríguez-Quintero, K. Rusek, M.A.G. Alvarez, M.V. Andrés, J.M. Espino, J.P. Fernández-García, J. Gómez-Camacho, A.M. Moro, C. Angulo, J. Cabrera, E. Casarejos, P. Demaret, M.J.G. Borge, D. Escrig, O. Tengblad, S. Cherubini, P. Figuera, M. Gulino, M. Freer, C. Metelko, V. Ziman, R. Raabe, I. Mukha, D. Smirnov, O.R. Kakuee, J. Rahighi, Phys. Rev. C 84 (2011) 044604.
[233] J.P. Fernández-García, M.A.G. Alvarez, A.M. Moro, M. Rodríguez-Gallardo, Phys. Lett. B 693 (2010) 310.
[234] J.P. Fernández-García, M. Cubero, M. Rodríguez-Gallardo, L. Acosta, M. Alcorta, M.A.G. Alvarez, M.J.G. Borge, L. Buchmann, C.A. Diget, H.A. Falou, B.R. Fulton, H.O.U. Fynbo, D. Galaviz, J. Gómez-Camacho, R. Kanungo, J.A. Lay, M. Madurga, I. Martel, A.M. Moro, I. Mukha, T. Nilsson, A.M. Sánchez-Benítez, A. Shotter, O. Tengblad, P. Walden, Phys. Rev. Lett. 110 (2013) 142701.
[235] A. Shrivastava, Y. Blumenfeld, N. Keeley, T. Zerguerras, T. Aumann, D. Bazin, M. Chromik, G.M. Crawley, T. Glasmacher, K.W. Kemper, F. Maréchal, D.J. Morrissey, T. Nakamura, A. Navin, E.C. Pollacco, D. Santonocito, B.M. Sherrill, T. Suomijärvi, M. Thoennessen, E. Tryggestad, R.L. Varner, Phys. Lett. B 596 (2004) 54.
[236] M. Dasgupta, L.R. Gasques, D.H. Luong, R. du Riet, R. Rafiei, D.J. Hinde, C.J. Lin, M. Evers, A. Diaz-Torres, Nucl. Phys. A 834 (2010) 147c.
[237] E.C. Kemble, Phys. Rev. 48 (1935) 549.
[238] D.L. Hill, J.A. Wheeler, Phys. Rev. 89 (1953) 1102.
[239] R.G. Stokstad, Y. Eisen, S. Kaplanis, D. Pelte, U. Smilansky, I. Tserruya, Phys. Rev. Lett. 41 (1978) 465.
[240] C.H. Dasso, S. Landowne, A. Winther, Nucl. Phys. A 405 (1983) 381.
[241] C.H. Dasso, S. Landowne, A. Winther, Nucl. Phys. A 407 (1983) 221.
[242] D.M. Andrade, M.S. Hussein, Phys. Rev. C 80 (2009) 034610.
[243] I.J. Thompson, Comput. Phys. Rep. 7 (1988) 167.
[244] O. Akyüz, A. Winther, in: R.A. Broglia, C.H. Dasso, R.A. Ricci (Eds.), Nuclear Structure of Heavy Ion Reaction, North Holland, 1981, in: proc. E. Fermi Summer School of Physics.
[245] P.R. Christensen, A. Winther, Phys. Lett. B 65 (1976) 19.
[246] J. Blocki, J. Randrup, W.J. Swiatecki, C.F. Tsang, Ann. Phys. 105 (1977) 427.
[247] R. Bass, Phys. Rev. Lett. 39 (1977) 265.
[248] G.R. Satchler, W.G. Love, Phys. Rep. 55 (1979) 183.
[249] G.F. Bertsch, J. Borysowicz, H. McManus, W.G. Love, Nucl. Phys. A 284 (1977) 399.
[250] N. Anantaraman, H. Toki, G.F. Bertsch, Nucl. Phys. 398 (1983) 269.
[251] S. Mişicu, H. Esbensen, Phys. Rev. Lett. 96 (2006) 112701.
[252] S. Mişicu, H. Esbensen, Phys. Rev. C 75 (2007) 034606.
[253] D.T. Khoa, W. von Ortzen, H.G. Bohlen, S. Ohkubo, J. Phys. G: Nucl. Part. Phys. 34 (2007) R111.
[254] L.F. Canto, P.R.S. Gomes, J. Lubian, M.S. Hussein, P. Lotti, Eur. Phys. J. A 50 (2014) 89.
[255] R. Keser, A.S. Umar, V.E. Oberacker, Phys. Rev. C 85 (2012) 044606.
[256] A.S. Umar, C. Simenel, V.E. Oberacker, Phys. Rev. C 89 (2014) 034611.
[257] C. Simenel, M. Dasgupta, D.J. Hinde, E. Williams, Phys. Rev. C 88 (2013) 064604.
[258] K. Washiyama, D. Lacroix, Phys. Rev. C 78 (2008) 024610.
[259] N. Takigawa, H. Sagawa, Phys. Lett. B 265 (1991) 23.
[260] M.S. Hussein, M.P. Pato, L.F. Canto, R. Donangelo, Phys. Rev. C 46 (1992) 377.
[261] N. Takigawa, M. Kuratani, H. Sagawa, Phys. Rev. C 47 (1993) R2470.
[262] C.H. Dasso, A. Vitturi, Phys. Rev. C 50 (1994) R12.
[263] K. Alder, A. Winther, Electromagnetic Excitations, North-Holland, Amsterdam, 1975.
[264] R.A. Broglia, S. Landowne, R.A. Malfliet, V. Rostokin, A. Winther, Phys. Rep. 11 (1974) 1.
[265] A. Romanelli, L.F. Canto, R. Donangelo, P. Lotti, Nucl. Phys. A 588 (1995) 71c.
[266] L.F. Canto, R. Donangelo, J.O. Rasmussen, P. Ring, M.A. Stoyer, Phys. Lett. B 248 (1990) 10.
[267] L.F. Canto, R. Donangelo, M.W. Guidry, A.R. Farhan, J.O. Rasmussen, P. Ring, M.A. Stoyer, Phys. Lett. B 241 (1990) 295.
[268] C.A. Bertulani, L.F. Canto, Nucl. Phys. A 539 (1992) 163.
[269] M. Dasgupta, P.R.S. Gomes, D.J. Hinde, S.B. Moraes, R.M. Anjos, A.C. Berriman, R.D. Butt, N. Carlin, J. Lubian, C.R. Morton, J.O. Newton, A. Szanto de Toledo, Phys. Rev. C 70 (2004) 024606.
[270] M. Boselli, A. Diaz-Torres, J. Phys. G: Nucl. Part. Phys. 41 (2014) 094001.
[271] K. Hagino, A. Vitturi, C.H. Dasso, S.M. Lenzi, Phys. Rev. C 61 (2000) 037602.
[272] A. Diaz-Torres, I.J. Thompson, C. Beck, Phys. Rev. C 68 (2003) 044607.
[273] V. Jha, V.V. Parkar, S. Kailas, Phys. Rev. C 89 (2014) 034605.
[274] I.J. Thompson, A. Diaz-Torres, Prog. of Theor. Phys. Suppl. 154 (2004) 69.
[275] C. Beck, N. Keeley, A. Diaz-Torres, Phys. Rev. C 75 (2007) 054605.

[276] K. Bodek, H. Hugi, J. Lang, R. Müller, E. Ungricht, K. Jankowski, W. Zipper, L. Jarczyk, A. Strzalkonski, G. Willim, H. Witala, Nucl. Phys. A 339 (1980) 353.
[277] N. Keeley, K. Rusek, Phys. Lett. B 427 (1998) 1.
[278] N. Keeley, K.W. Kemper, K. Rusek, Phys. Rev. C 66 (2002) 044605.
[279] K. Rusek, N. Keeley, K.W. Kemper, R. Raabe, Phys. Rev. C 67 (2003) 041604(R).
[280] K. Rusek, N. Alamanos, N. Keeley, V. Lapoux, A. Pakou, Phys. Rev. C 70 (2004) 014603.
[281] L.F. Canto, J. Lubian, P.R.S. Gomes, M.S. Hussein, Phys. Rev. C 80 (2009) 047601.
[282] S. Hashimoto, K. Ogata, S. Chiba, M. Yahiro, Prog. Theor. Phys. 122 (2009) 1291.
[283] L.F. Canto, P.R.S. Gomes, J. Lubian, M.S. Hussein, EPJ Web of Conferences, vol. 17, 2011, p. 01001.
[284] M. Dasgupta, D.J. Hinde, R.D. Butt, R.M. Anjos, A.C. Berriman, N. Carlin, P.R.S. Gomes, C.R. Morton, J.O. Newton, A. Szanto de Toledo, K. Hagino, Phys. Rev. Lett. 82 (1999) 1395.
[285] K. Yabana, T. Nakatsukasa, M. Ito, Few-Body Syst. 43 (2008) 247.
[286] M. Ito, K. Yabana, T. Nakatsukasa, M. Ueda, Nucl. Phys. A 787 (2006) 267c.
[287] K. Yabana, Prog. Theor. Phys. 97 (1997) 437.
[288] V.V. Sargsyan, Z. Kanokov, G.G. Adamian, N.V. Antonenko, W. Scheid, Phys. Rev. C 80 (2009) 034606.
[289] C.R. Morton, A.C. Berriman, M. Dasgupta, D.J. Hinde, J.O. Newton, K. Hagino, I.J. Thompson, Phys. Rev. C 60 (1999) 044608.
[290] D.J. Hinde, A.C. Berriman, M. Dasgupta, J.R. Leigh, J.C. Mein, C.R. Morton, J.O. Newton, Phys. Rev. C 60 (1999) 054602.
[291] B.B. Back, R.R. Betts, J.E. Gindler, B.D. Wilkins, S. Saini, M.B. Tsang, C.K. Gelbke, W.G. Lynch, M.A. Mcmahan, P.A. Baisden, Phys. Rev. C 32 (1985) 195.
[292] R. Bock, Y.T. Chu, M. Dakowski, A. Gobbi, E. Grosse, A. Olmi, H. Sann, D. Schwalm, Nucl. Phys. A 388 (1982) 334.
[293] D.J. Hinde, C.R. Morton, M. Dasgupta, J.R. Leigh, J.C. Mein, H. Timmers, Nucl. Phys. A 592 (1995) 271.
[294] L.F. Canto, Nucl. Phys. A 491 (1989) 337.
[295] Z. Kanokov, Y.V. Palchikov, G.G. Adamian, N.V. Antonenko, W. Scheid, Phys. Rev. E 71 (2005) 016121.
[296] V.V. Sargsyan, G.G. Adamian, N.V. Antonenko, W. Scheid, H.Q. Zhang, Phys. Rev. C 84 (2011) 064614.
[297] V.V. Sargsyan, G.G. Adamian, N.V. Antonenko, W. Scheid, C.J. Lin, H.Q. Zhang, Phys. Rev. C 85 (2012) 017603.
[298] V.V. Sargsyan, G.G. Adamian, N.V. Antonenko, W. Scheid, C.J. Lin, H.Q. Zhang, Phys. Rev. C 85 (2012) 037602.
[299] S. Yusa, K. Hagino, N. Rowley, Phys. Rev. C 88 (2013) 044620.
[300] S. Yusa, K. Hagino, N. Rowley, Phys. Rev. C 88 (2013) 054621.
[301] E. Piasecki, L. Świderski, W. Gawlikowicz, J. Jastrzębski, N. Keeley, M. Kisieliński, S. Kliczewski, A. Kordyasz, M. Kowalczyk, S. Khlebnikov, E. Koshchiy, E. Kozulin, T. Krogulski, T. Loktev, M. Mutterer, K. Piasecki, A. Piórkowska, K. Rusek, A. Staudt, M. Sillanpää, S. Smirnov, I. Strojek, G. Tiourin, W.H. Trzaska, A. Trzcińska, K. Hagino, N. Rowley, Phys. Rev. C 80 (2009) 054613.
[302] S. Yusa, K. Hagino, N. Rowley, Phys. Rev. C 82 (2010) 024606.
[303] S. Yusa, K. Hagino, N. Rowley, Phys. Rev. C 85 (2012) 054601.
[304] D. Agassi, C.M. Ko, H.A. Weidenmüller, Ann. Phys. 107 (1977) 140.
[305] D. Agassi, C.M. Ko, H.A. Weidenmüller, Phys. Rev. C 18 (1978) 223.
[306] C.M. Ko, D. Agassi, H.A. Weidenmüller, Ann. Phys. 117 (1979) 237.
[307] D. Agassi, C.M. Ko, H.A. Weidenmüller, Ann. Phys. 117 (1979) 407.
[308] V.I. Zagrebaev, Phys. Rev. C 64 (2001) 034606.
[309] V.A. Rachkov, A.V. Karpov, A.S. Denikin, V.I. Zagrebaev, Phys. Rev. C 90 (2014) 014614.
[310] A. Kumari, R. Kharab, Nucl. Phys. A 933 (2015) 93.
[311] C.L. Jiang, H. Esbensen, K.E. Rehm, B.B. Back, R.V.F. Janssens, J.A. Caggiano, P. Collon, J. Greene, A.M. Heinz, D.J. Henderson, I. Nishinaka, T.O. Pennington, D. Seweryniak, Phys. Rev. Lett. 89 (2002) 052701.
[312] C.L. Jiang, K.E. Rehm, R.V.F. Janssens, H. Esbensen, I. Ahmad, B.B. Back, P. Collon, C.N. Davids, J.P. Greene, D.J. Henderson, G. Mukherjee, R.C. Pardo, M. Paul, T.O. Pennington, D. Seweryniak, S. Sinha, Z. Zhou, Phys. Rev. Lett. 93 (2004) 012701.
[313] C.L. Jiang, K.E. Rehm, H. Esbensen, R.V.F. Janssens, B.B. Back, C.N. Davids, J.P. Greene, D.J. Henderson, C.J. Lister, R.C. Pardo, T. Pennington, D. Peterson, D. Seweryniak, B. Shumard, S. Sinha, X.D. Tang, I. Tanihata, S. Zhu, P. Collon, S. Kurtz, M. Paul, Phys. Rev. C 71 (2005) 044613.
[314] A.M. Stefanini, G. Montagnoli, R. Silvestri, S. Beghini, L. Corradi, S. Courtin, E. Fioretto, B. Guiot, F. Haas, D. Lebhertz, N. Mărginean, P. Mason, F. Scarlassara, R.N. Sagaidak, S. Szilner, Phys. Rev. C 78 (2008) 044607.
[315] C.L. Jiang, B.B. Back, H. Esbensen, J.P. Greene, R.V.F. Janssens, D.J. Henderson, H.Y. Lee, C.L. Lister, M. Notani, R.C. Pardo, N. Patel, K.E. Rehm, D. Seweryniak, B. Shumard, X. Wang, S. Zhu, S. Mișicu, P. Collon, X.D. Tang, Phys. Rev. C 78 (2008) 017601.
[316] A.M. Stefanini, G. Montagnoli, R. Silvestri, L. Corradi, S. Courtin, E. Fioretto, B. Guiot, F. Haas, D. Lebhertz, P. Mason, F. Scarlassara, S. Szilner, Phys. Lett. B 679 (2009) 95.
[317] C.H. Dasso, G. Pollarolo, Phys. Rev. C 68 (2003) 054604.
[318] M. Dasgupta, D.J. Hinde, A. Diaz-Torres, B. Bouriquet, C.I. Low, G.J. Milburn, J.O. Newton, Phys. Rev. Lett. 99 (2007) 192701.
[319] H. Esbensen, C.L. Jiang, A.M. Stefanini, Phys. Rev. C 82 (2010) 054621.
[320] T. Ichikawa, K. Hagino, A. Iwamoto, Phys. Rev. C 75 (2007) 057603.
[321] T. Ichikawa, K. Hagino, A. Iwamoto, Phys. Rev. Lett. 103 (2009) 202701.
[322] T. Ichikawa, K. Matsuyanagi, Phys. Rev. C 88 (2013) 011602(R).
[323] K. Hagino, N. Rowley, A.T. Kruppa, Comput. Phys. Comm. 123 (1999) 143.
[324] M. Ray, A. Mukherjee, M.K. Pradhan, R. Kshetri, M.S. Sarkar, R. Palit, I. Majumdar, P.K. Joshi, H.C. Jain, B. Dasmahapatra, Phys. Rev. C 78 (2008) 064617.
[325] M. Sinha, H. Majumdar, P. Basu, S. Roy, R. Bhattacharya, M. Biswas, M.K. Pradhan, S. Kailas, Phys. Rev. C 78 (2008) 027601.
[326] M. Sinha, H. Majumdar, R. Bhattacharya, P. Basu, S. Roy, M. Biswas, R. Palit, I. Mazumdar, P.K. Joshi, H.C. Jain, S. Kailas, Phys. Rev. C 76 (2007) 027603.
[327] P.K. Rath, S. Santra, N.L. Singh, B.K. Nayak, K. Mahata, R. Palit, K. Ramachandran, S.K. Pandit, A. Parihari, A. Pal, S. Appannababu, S.K. Sharma, D. Patel, S. Kailas, Phys. Rev. C 88 (2013) 044617.
[328] A. Mukherjee, S. Roy, M.K. Pradhan, M.S. Sarkar, P. Basu, B. Dasmahapatra, T. Bhattacharya, S. Bhatacharya, S.K. Basu, A. Chatterjee, V. Tripathi, S. Kailas, Phys. Lett. B 636 (2006) 91.
[329] R. Raabe, C. Angulo, J.L. Charvet, C. Jouanne, L. Nalpas, P. Figuera, D. Pierroutsakou, M. Romoli, J.L. Sida, Phys. Rev. C 74 (2006) 044606.
[330] M. Sinha, H. Majumdar, P. Basu, S. Roy, R. Bhattacharya, M. Biswas, M.K. Pradhan, R. Palit, I. Mazumdar, S. Kailas, Eur. Phys. J. A 44 (2010) 403.
[331] M.M. Shaikh, S. Roy, S. Rajbanshi, M.K. Pradhan, A. Mukherjee, P. Basu, S. Pal, V. Nanal, R.G. Pillay, A. Shrivastava, Phys. Rev. C 90 (2014) 024615.
[332] H. Kumawat, V. Jha, V.V. Parkar, B.J. Roy, S.K. Pandit, R. Palit, P.K. Rath, C.S. Palshetkar, S.K. Sharma, S. Thakur, A.K. Mohanty, A. Chatterjee, S. Kailas, Phys. Rev. C 86 (2012) 024607.
[333] S.P. Hu, G.L. Zhang, J.C. Yang, H.Q. Zhang, P.R.S. Gomes, J. Lubian, X.G. Wu, J. Zhong, C.Y. He, Y. Zheng, C.B. Li, G.S. Li, W.W. Qu, F. Wang, L. Zheng, L. Yu, Q.M. Chen, P.W. Luo, H.W. Li, Y.H. Wu, W.K. Zhou, B.J. Zhu, H.B. Sun, Phys. Rev. C 91 (2015) 044619.
[334] P.K. Rath, S. Santra, N.L. Singh, K. Mahata, R. Palit, B.K. Nayak, K. Ramachandran, V.V. Parkar, R. Tripathi, S.K. Pandit, S. Appannababu, N.N. Deshmukh, R.K. Choudhury, S. Kailas, Nucl. Phys. A 874 (2012) 14.
[335] M.K. Pradhan, A. Mukherjee, P. Basu, A. Goswami, R. Kshetri, S. Roy, P.R. Chowdhury, M.S. Sarkar, R. Palit, V.V. Parkar, S. Santra, M. Ray, Phys. Rev. C 83 (2011) 064606.
[336] A. Shrivastava, A. Navin, A. Lemasson, K. Ramachandran, V. Nanal, M. Rejmund, K. Hagino, T. Ichikawa, S. Bhattacharyya, A. Chatterjee, S. Kailas, K. Mahata, V.V. Parkar, R.G. Pillay, P.C. Rout, Phys. Rev. Lett. 103 (2009) 232702.
[337] C.S. Palshetkar, S. Santra, A. Chatterjee, K. Ramachandran, S. Thakur, S.K. Pandit, K. Mahata, A. Shrivastava, V.V. Parkar, V. Nanal, Phys. Rev. C 82 (2010) 044608.

[338] V.V. Parkar, R. Palit, S.K. Sharma, B.S. Naidu, S. Santra, P.K. Joshi, P.K. Rath, K. Mahata, K. Ramachandran, T. Trivedi, A. Raghav, Phys. Rev. C 82 (2010) 054601.
[339] P.R.S. Gomes, I. Padron, E. Crema, O.A. Capurro, J.O. Fernández Niello, A. Arazi, G.V. Martí, J. Lubian, M. Trotta, A.J. Pacheco, J.E. Testoni, M.D. Rodríguez, M.E. Ortega, L.C. Chamon, R.M. Anjos, R. Veiga, M. Dasgupta, D.J. Hinde, K. Hagino, Phys. Rev. C 73 (2006) 064606.
[340] Y.D. Fang, P.R.S. Gomes, J. Lubian, M.L. Liu, X.H. Zhou, D.R. Mendes Junior, N.T. Zhang, Y.H. Zhang, G.S. Li, J.G. Wang, S. Guo, Y.H. Qiang, B.S. Gao, Y. Zheng, X.G. Lei, Z.G. Wang, Phys. Rev. C 91 (2015) 014608.
[341] N.T. Zhang, Y.D. Fang, P.R.S. Gomes, J. Lubian, M.L. Liu, X.H. Zhou, G.S. Li, J.G. Wang, S. Guo, Y.H. Qiang, Y.H. Zhang, D.R. Mendes junior, Y. Zheng, X.G. Lei, B.S. Gao, Z.G. Wang, K.L. Wang, X.F. He, Phys. Rev. C 90 (2014) 024621.
[342] Y.D. Fang, P.R.S. Gomes, J. Lubian, X.H. Zhou, Y.H. Zhang, J.L. Han, M.L. Liu, Y. Zheng, S. Guo, J.G. Wang, Y.H. Qiang, Z.G. Wang, X.G. Wu, C.Y. He, Y. Zheng, C.B. Li, S.P. Hu, S.H. Yao, Phys. Rev. C 87 (2013) 024604.
[343] M. Dasgupta, D.J. Hinde, S.L. Sheehy, B. Bouriquet, Phys. Rev. C 81 (2010) 024608.
[344] L.R. Gasques, D.J. Hinde, M. Dasgupta, A. Mukherjee, R.G. Thomas, Phys. Rev. C 79 (2009) 034605.
[345] V. Scuderi, A. di Pietro, P. Figuera, M. Fisichella, F. Amorini, C. Angulo, G. Cardella, E. Casarejos, M. Lattuada, M. Milin, A. Musumarra, M. Papa, M.G. Pellegriti, R. Raabe, F. Rizzo, N. Skukan, D. Torresi, M. Zadro, Phys. Rev. C 84 (2011) 064604.
[346] Y.E. Penionzhkevich, R. Astabatyan, N. Demekhina, G. Gulbekian, R. Kalpakchieva, A.A. Kulko, S. Lukyanov, E.R. Markaryan, V. Maslov, Y.E.R. Muzychka, Y.T. Oganessian, R.V. Revenko, N.K. Skobelev, Y.G. Sobolev, D.A. Testov, T. Zholdybaev, Eur. Phys. J. A 31 (2007) 185.
[347] S.M. Lukyanov, Y.E. Penionzhkevich, R. Astabatyan, N. Demekhina, Z. Dlouhy, M.P. Ivanov, R. Kalpakchieva, A.A. Kulko, E.R. Markaryan, V. Maslov, R.V. Revenko, N.K. Skobelev, V.I. Smirnov, Y.G. Sobolev, W. Trazka, S.V. Khlebnikov, Phys. Lett. B 670 (2009) 321.
[348] R. Wolski, I. Martel, L. Standylo, L. Acosta, J.L. Aguado, C. Angulo, R. Bejillos, J.P. Bolivar, J.A. Duenas, M.S. Golovkov, T. Keutgen, M. Mazzocco, A. Padilla, A.M. Sáchez-Benítez, C. Signorini, M. Romoli, K. Rusek, Eur. Phys. J. A 47 (2011) 111.
[349] A.M. Vinodkumar, W. Loveland, R. Yanez, M. Leonard, L. Yao, P. Bricault, M. Dombsky, P. Kunz, J. Lassen, A.C. Morton, D. Ottewell, D. Preddy, M. Trinczek, Phys. Rev. C 87 (2013) 044603.
[350] D.J. Hinde, M. Dasgupta, Phys. Rev. C 81 (2010) 064611.
[351] A. Pakou, E. Stiliaris, D. Pierroutsakou, N. Alamanos, A. Boiano, C. Boiano, D. Filipescu, T. Glodariu, J. Grebosz, A. Guglielmetti, M. La commara, M. Mazzocco, C. Parascandolo, K. Rusek, A.M. Sánchez-Benítez, C. Signorini, O. Sgouros, F. Soramel, V. Soukeras, E. Strano, L. Stroe, N. Toniolo, D. Torresi, K. Zerva, Phys. Rev. C 87 (2013) 014619.
[352] E.F. Aguilera, P. Amador-Valenzuela, E. Martinez-Quiroz, D. Lizcano, P. Rosales, H. García-Martínez, A. Gómez-Camacho, J.J. Kolata, A. Roberts, L.O. Lamm, G. Rogachev, V. Guimarães, F.D. Becchetti, A. Villano, M. Ojaruega, M. Febbraro, Y. Chen, H. Jiang, P.A. de Young, G.F. Peaslee, C. Guess, U. Khadka, J. Brown, J.D. Hinnefeld, L. Acosta, E.S. Rossi Jr, J.F.P. Huiza, T.L. Belyaeva, Phys. Rev. Lett. 107 (2011) 092701.
[353] E.F. Aguilera, E. Martinez-Quiroz, P. Rosales, J.J. Kolata, P.A. de Young, G.F. Peaslee, P. Mears, C. Guess, F.D. Becchetti, J.H. Lupton, Y. Chen, Phys. Rev. C 80 (2009) 044605.
[354] E. Martinez-Quiroz, E.F. Aguilera, D. Lizcano, P. Amador-Valenzuela, H. García-Martínez, J.J. Kolata, A. Roberts, L.O. Lamm, G. Rogachev, V. Guimarães, F.D. Becchetti, A. Villano, M. Ojaruega, M. Febbraro, Y. Chen, H. Jiang, P.A. de Young, G.F. Peaslee, Phys. Rev. C 90 (2014) 014616.
[355] P.R.S. Gomes, M.D. Rodríguez, G.V. Martí, I. Padron, L.C. Chamon, J.O. Fernández Niello, O.A. Capurro, A.J. Pacheco, J.E. Testoni, A. Arazi, M. Ramírez, R.M. Anjos, J. Lubian, R. Veiga, R. Liguori Neto, E. Crema, N. Added, C. Tenreiro, M.S. Hussein, Phys. Rev. C 71 (2005) 034608.
[356] I. Padrón, P.R.S. Gomes, R.M. Anjos, J. Lubian, C. Muri, J.J.S. Alves, G.V. Marti, M. Ramirez, A.J. Pacheco, O.A. Capurro, J.O. Fernández Niello, J.E. Testoni, D. Abriola, M.R. Spinella, Phys. Rev. C 66 (2002) 044608.
[357] A. Mukherjee, U. Datta pramanik, S. Chattopadhyay, M. Saha sakar, A. Goswami, P. Basu, S. Bhatacharya, S. Sen, M.L. Chatterjee, B. Dasmahapatra, Nucl. Phys. A 596 (1996) 299.
[358] A. Mukherjee, U. Datta Pramanik, S. Chattopadhyay, M. Saha Sakar, A. Goswami, P. Basu, S. Bhatacharya, S. Sen, M.L. Chatterjee, B. Dasmahapatra, Nucl. Phys. A 635 (1998) 305.
[359] A. Mukherjee, U. Datta Pramanik, S. Chattopadhyay, M. Saha Sakar, A. Goswami, P. Basu, S. Bhatacharya, S. Sen, M.L. Chatterjee, B. Dasmahapatra, Nucl. Phys. A 645 (1999) 13.
[360] A. Mukherjee, M. Dasgupta, D.J. Hinde, H. Timmers, R. Butt, P.R.S. Gomes, Phys. Lett. B 526 (2002) 295.
[361] P.R.S. Gomes, I. Padrón, E. Crema, O.A. Capurro, J.O.F. Niello, G.V. Martí, A. Arazi, M. Trotta, J. Lubian, M.E. Ortega, A.J. Pacheco, M.D. Rodriguez, J.E. Testoni, R.M. Anjos, L.C. Chamon, M. Dasgupta, D.J. Hinde, K. Hagino, Phys. Lett. B 634 (2006) 356.
[362] P.R.S. Gomes, R. Linares, J. Lubian, C.C. Lopes, E.N. Cardozo, B.H.F. Pereira, I. Padrón, Phys. Rev. C 84 (2011) 014615.
[363] S.B. Moraes, P.R.S. Gomes, J. Lubian, J.J.S. Alves, R.M. Anjos, M.M. Sant'Anna, I. Padrón, C. Muri, R. Liguori Neto, N. Added, Phys. Rev. C 61 (2000) 064608.
[364] G.V. Martí, P.R.S. Gomes, M.D. Rodriguez, J.O. Fernández Niello, O.A. Capurro, A.J. Pacheco, J.E. Testoni, M. Ramirez, A. Arazi, I. Padrón, R.M. Anjos, J. Lubian, E. Crema, Phys. Rev. C 71 (2005) 027602.
[365] V. Fekou-Youmbi, S.J.L.N. Alamanos, F. Auger, D. Bazin, B.C.C. Cabot, A. Cunsolo, A. Foti, A. Gillibert, A. Lépine, M. Lewitowicz, R. Liguori Netto, W. Mittig, E. Pollacco, P. Roussel-Chomaz, C. Volant, Y. Yong Feng, Nucl. Phys. A 583 (1995) 811c.
[366] A.S. Fomichev, I. David, Z. Dlouhy, S.M. Lukyanov, Y.T. Oganessian, Y.Z. Penionzkevich, V.P. Perelygin, N.K. Skobelev, O.B. Tarasov, R. Wolski, Z. Phys. A 351 (1995) 129.
[367] A. Yoshida, C. Signorini, T. Fukuda, Y. Watanabe, N. Aoi, M. Hirai, M. Ishihara, H. Kobinata, Y. Mozoi, L. Muller, Y. Nagashima, J. Nakano, T. Nomura, Y.H. Pu, F. Scarlassara, Phys. Lett. B 389 (1996) 457.
[368] M. Trotta, J.L. Sida, N. Alamanos, A. Andreyev, F. Auger, D.L. Balabanski, C. Borcea, N. Coulier, A. Drouart, D.J.C. Durand, G. Georgiev, A. Gillibert, J.D. Hinnefeld, M. Huyse, C. Jouanne, V. Lapoux, A. Lépine, A. Lumbroso, F. Marie, A. Musumarra, G. Neyens, S. Ottini, R. Raabe, S. Ternier, P. van Duppen, K. Vyvey, C. Volant, R. Wolski, Phys. Rev. Lett. 84 (2000) 2342.
[369] R. Raabe, J.L. Sida, J.L. Chavet, N. Alamanos, C. Angulo, J.M. Casandjian, S. Courtin, A. Drouart, C. Durand, P. Figuera, A. Gillibert, S. Heinrich, C. Jouanne, V. Lapoux, A. Lépine, A. Masumarra, L. Nalpas, D. Pierroutsakou, M. Romoli, K. Rusek, M. Trotta, Nature 431 (2004) 823.
[370] A. di Pietro, P. Figuera, F. Amorini, C. Angulo, G. Cardella, S. Cherubini, T. Davinson, D. Leanza, J. Lu, H. Mahmud, M. Milin, A. Musumarra, A. Ninane, M. Papa, M.G. Pellegriti, R. Raabe, F. Rizzo, C. Ruiz, A.C. Shotter, N. Soic, S. Tudisco, L. Weissman, Phys. Rev. C 69 (2004) 044613.
[371] Y.E. Penionzhkevich, Y.A. Muzychka, S.M. Lukyanov, R. Kalpakchieva, N.K. Skobelev, V.P. Pelelygin, Z. Dlouhy, Eur. Phys. J. A A13 (2002) 123.
[372] C. Signorini, Z.H. Liu, A. Yoshida, T. Fukuda, Z.C. Li, K.E.G. Löbner, R. Müller, Y.H. Pu, K. Rudolph, F. Soramel, C. Zotti, J.L. Sida, Eur. Phys. J. A 2 (1998) 227.
[373] J.P. Bychowski, P.A. de Young, B.B. Hilldore, J.D. Hinnefeld, A. Vida, F.D. Becchetti, J. Lupton, T.W. O'Donnell, J.J. Kolata, G. Rogachev, M. Hencheck, Phys. Lett. B 596 (2004) 26.
[374] P.A. de Young, P.J. Mears, J.J. Kolata, E.F. Aguilera, F.D. Becchetti, Y. Chen, M. Cloughesy, H. Griffin, C. Guess, J.D. Hinnefeld, H. Jiang, S.R. Jones, U. Khadka, D. Lizcano, E. Martinez-Quiroz, M. Ojaniega, G.F. Peaslee, A. Pena, J. Rieth, S. Vandendriessche, J.A. Zimmerman, Phys. Rev. C 71 (2005) 051601(R).
[375] P.R.S. Gomes, L.F. Canto, J. Lubian, M.S. Hussein, Phys. Lett. B 695 (2011) 320.
[376] M.A. Cândido Ribeiro, L.C. Chamon, D. Pereira, M.S. Hussein, D. Galetti, Phys. Rev. Lett. 78 (1997) 3270.
[377] F.H. Ruddy, B.D. Pate, Nucl. Phys. A 127 (1969) 305.
[378] Y.E. Penionzhkevich, V.I. Zagrebaev, S.M. Lukyanov, R. Kalpakchieva, Phys. Rev. Lett. 96 (2006) 162701.
[379] V.I. Zagrebaev, Phys. Rev. C 67 (2003) 061601(R).
[380] M.S. Basunia, H.A. Shugart, A.R. Smith, E.B. Norman, Phys. Rev. C 75 (2007) 015802.
[381] A. Chatterjee, A. Navin, A. Shrivastava, S. Bhattacharyya, M. Rejmund, N. Keeley, V. Nanal, J. Nyberg, R.G. Pillay, K. Ramachandran, I. Stefan, D. Bazin, D. Beaumel, Y. Blumenfeld, G. de France, D. Gupta, M. Labiche, A. Lemasson, R. Lemmon, R. Raabe, J.A. Scarpaci, C. Simenel, C. Timis, Phys. Rev. Lett. 101 (2008) 032701.

[382] C. Signorini, A. Yoshida, Y. Watanabe, D. Pierroutsakou, L. Stroe, T. Fukuda, M. Mazzocco, N. Fukuda, Y. Mizoi, M. Ishihara, H. Sakurai, A. Diaz-Torres, K. Hagino, Nucl. Phys. A 735 (2004) 329.
[383] K.E. Rehm, H. Esbensen, C.L. Jiang, B.B. Back, F. Borasi, B. Harss, R.V.F. Janssens, V. Nanal, J. Nolen, R.C. Pardo, M. Paul, P. Reiter, R.E. Segel, A. Sonzogni, J. Uusitalo, A.H. Wuosmaa, Phys. Rev. Lett. 81 (1998) 3341.
[384] J. Rangel, J. Lubian, P.R.S. Gomes, B.V. Carlson, L.C. Chamon, A. Gomez Camacho, Eur. Phys. J. A 49 (2013) 57.
[385] K. Kalita, S. Verma, R. Singh, J.J. Das, A. Jhingan, N. Madhavan, S. Nath, T. Varughese, P. Sugathan, V.V. Parkar, K. Mahata, K. Ramachandran, A. Shrivastava, A. Chatterjee, S. Kailas, S. Barua, P. Basu, H. Majumdar, M. Sinha, R. Bhattacharya, A.K. Sinha, Phys. Rev. C 73 (2006) 024609.
[386] M. Beckerman, M. Salomaa, A. Sperduto, H. Enge, J. Ball, A. Dirienzo, S. Gazes, Y. Chen, J.D. Molitoris, M. Nai-feng, Phys. Rev. Lett. 45 (1980) 1472.
[387] R.A. Broglia, C.H. Dasso, S. Landowne, A. Winther, Phys. Rev. C 27 (1983) 2433.
[388] R.J. Woolliscroft, N.M. Clarke, B.R. Fulton, R.L. Cowin, M. Dasgupta, D.J. Hinde, C.R. Morton, A.C. Berriman, Phys. Rev. C 68 (2003) 014611.
[389] C. Signorini, Eur. Phys. J. A A13 (2002) 129.
[390] V. Guimarães, R. Lichtenthäler, O. Camargo, A. Barioni, M. Assunçao, J.J. Kolata, H. Amro, F.D. Becchetti, H. Jiang, E.F. Aguilera, D. Lizcano, E. Martines-Quiroz, H. Garcia, Phys. Rev. C 75 (2007) 054602.
[391] O. Camargo, V. Guimarães, R. Lichtenthäler, V. Scarduelli, J.J. Kolata, C.A. Bertulani, H. Amro, F.D. Becchetti, H. Jiang, E.F. Aguilera, D. Lizcano, E. Martinez-Quiroz, H. Garcia, Phys. Rev. C 78 (2008) 034605.
[392] J.J. Kolata, V.Z. Goldberg, L.O. Lamm, M.G. Marino, C.J. O'Keeffe, G. Rogachev, E.F. Aguilera, H. Garcia-Martinez, E. Martinez-Quiroz, P. Rosales, F.D. Becchetti, T.W. O'Donnell, D.A. Roberts, J.A. Brown, P.A. de Young, J.D. Hinnefeld, S.A. Shaheen, Phys. Rev. C 65 (2002) 054616.
[393] F. Pühlhofer, Nucl. Phys. A 280 (1977) 267.
[394] A. Gavron, Phys. Rev. C 21 (1980) 230.
[395] H.Q. Zhang, C.J. Lin, F. Yang, H.M. Jia, X.X. Xu, Z.D. Wu, F. Jia, S.T. Zhang, Z.H. Liu, A. Richard, C. Beck, Phys. Rev. C 82 (2010) 054609.
[396] V.V. Sargsyan, A.S. Zubov, G.G. Adamian, N.V. Antonenko, S. Heinz, Phys. Rev. C 88 (2013) 054609.
[397] R.A. Kuzyakin, V.V. Sargsyan, G.G. Adamian, N.V. Antonenko, E.E. Saperstein, S.V. Tolokonnikov, Phys. Rev. C 85 (2012) 034612.
[398] I.J. Thompson, M.A. Nagarajan, J.A. Lilley, M.J. Smithson, Nucl. Phys. A 505 (1989) 84.
[399] B. Wang, W.J. Zhao, P.R.S. Gomes, E.G. Zhao, S.G. Zhou, Phys. Rev. C 90 (2014) 034612.
[400] V.V. Sargsyan, G.G. Adamian, N.V. Antonenko, W. Scheid, H.Q. Zhang, Phys. Rev. C 86 (2012) 054610.
[401] V.V. Sargsyan, G.G. Adamian, N.V. Antonenko, W. Scheid, H.Q. Zhang, Phys. Rev. C 85 (2012) 024616.
[402] V.V. Sargsyan, G.G. Adamian, N.V. Antonenko, W. Scheid, H.Q. Zhang, Phys. Rev. C 86 (2012) 014602.
[403] V.V. Sargsyan, G.G. Adamian, N.V. Antonenko, W. Scheid, H.Q. Zhang, Phys. Rev. C 86 (2012) 034614.